

JYU DISSERTATIONS 773

Marlom Ramalho

**The Nuances of β^- Decay:
Theoretical Computations and
Their Applications for Beyond the
Standard Model Physics**



UNIVERSITY OF JYVÄSKYLÄ
FACULTY OF MATHEMATICS
AND SCIENCE

JYU DISSERTATIONS 773

Marlom Ramalho

**The Nuances of β^- Decay:
Theoretical Computations and
Their Applications for Beyond the
Standard Model Physics**

Esitetään Jyväskylän yliopiston matemaattis-luonnontieteellisen tiedekunnan suostumuksella
julkisesti tarkastettavaksi yliopiston Ylistönrinteen salissa Kem4
huhtikuun 26. päivänä 2024 kello 12.

Academic dissertation to be publicly discussed, by permission of
the Faculty of Mathematics and Science of the University of Jyväskylä,
in Ylistönrinne, auditorium Kem4, on April 26, 2024 at 12 o'clock noon.



JYVÄSKYLÄN YLIOPISTO
UNIVERSITY OF JYVÄSKYLÄ

JYVÄSKYLÄ 2024

Editors

Ilari Maasilta

Department of Physics, University of Jyväskylä

Ville Korkiakangas

Open Science Centre, University of Jyväskylä

Copyright © 2024, by author and University of Jyväskylä

ISBN 978-952-86-0124-1 (PDF)

URN:ISBN:978-952-86-0124-1

ISSN 2489-9003

Permanent link to this publication: <http://urn.fi/URN:ISBN:978-952-86-0124-1>

ABSTRACT

Ramalho, Marlom

The nuances of β^- decay: Theoretical Computations and their applications for Beyond the Standard Model physics

This dissertation encompasses a series of six articles, accompanied by an introductory discourse, centered on the intricacies of beta decays and the utilization of the nuclear shell model in computational analysis. The overarching objective is to elucidate various beta decay methodologies as pathways to unearth novel insights in the realm of physics beyond the standard model.

The initial segment of research delves into an in-depth examination of ^{92}Rb beta-spectral shapes, scrutinizing the legitimacy of employing approximations for forbidden non-unique decays within the summation method. This analysis is pertinent to the reactor antineutrino anomaly, suggesting potential resolutions or improvements to the spectral shoulder conundrum and bridging the gap between theoretical summation approaches and observed experimental fluxes.

Subsequent investigations are geared towards the implementation of computed beta spectra in calibrating background radiation for rare-event experiments, particularly focusing on the Radon decay chain in subterranean settings. An exhaustive analysis of the $^{212-214}\text{Pb-Bi-Po}$ decay chain has been undertaken, marking significant progress in addressing the challenge of underground background radiation. A notable discovery in this segment is the sensitivity of spectral shapes to the small relativistic nuclear matrix element (sNME), a parameter that poses computational challenges within the confines of the nuclear shell model's valence space framework. Inspired by this sensitivity, the research extends to study the impact of varying g_A and sNME values on ^{99}Tc , an adjacent isotope to potential neutrinoless double beta decay candidates ^{100}Mo and ^{96}Zr . Observations of dependency on the dual solutions of sNME catalyzed further exploration across a spectrum of isotopes linked to the reactor antineutrino anomaly, assessing the predictive accuracy of beta spectral shapes in relation to sNME and weak-axial coupling.

The culmination of this work applies the developed methodologies to assist in the quest for determining the (anti)neutrino's mass, leveraging the nuclear shell model alongside our computational predictions of half-lives.

Keywords: beta decay, nuclear shell model, beta spectral shape, forbidden non-unique, weak axial coupling, small nuclear matrix element.

TIIVISTELMÄ (ABSTRACT IN FINNISH)

Ramalho, Marlom

The nuances of β^- decay: Theoretical Computations and their applications for Beyond the Standard Model physics

Tämä väitöskirja sisältää kuusi julkaisua ja johdanto-osan, joka keskittyy ytimen beetahajoamisen ominaisuuksien kuvailuun ja ytimen kuorimalliin osana sen yksityiskohtaista laskennallista analyysiä. Työn kantavana teemana on tarkastella erilaisia beetahajoamiseen liittyviä menetelmiä, joiden käyttö mahdollistaa uusien näkökulmien avaamisen ytimen standardimallin ulkopuolisen fysiikan tarkastelulle.

Tutkimuksen ensimmäinen osa syventyy ytimen ^{92}Rb beetaspektrien muotojen perusteelliseen tarkasteluun pyrkien vastaamaan kysymykseen tiettyjen likimääräis-
menetelmien käytön oikeutuksesta tarkasteltaessa kiellettyjä ei-uniikkeja hajoamia beetaspektrien summausmenetelmän yhteydessä. Tämä analyysi on merkityksellinen reaktoriantineutriinoanomalian kannalta, ehdottaen antineutriinospektrissä esiintyvän "olkapään" arvoitukseen liittyviä mahdollisia ratkaisuja ja paraneltuja menetelmiä näiden ratkaisujen löytämiseksi. Näin pyrkimyksenä on rakentaa siltaa summausmenetelmän tulosten ja mitatun antineutriinovuon välille.

Seuraavat tutkimukset suuntautuvat laskettujen beetaspektrien hyväksikäyttöön harvinaisia hajoamia mittaavien kokeiden taustasäteilyyn liittyvässä kalibroinnissa, keskittyen erityisesti maanalaislaboratorioissa esiintyvän radonin radioaktiiviseen hajoamisketjuun. Tätä silmällä pitäen on suoritettu $^{212}\text{--}^{214}\text{Pb}$ -Bi-Po hajoamisketjun perusteellinen analyysi, mikä merkitsee huomattavaa edistystä maanalaisen taustasäteilyn tuoman haasteen ratkaisemisessa. Tähän liittyen on huomattu, että beetaspektrien muoto voi riippua ns. pienestä relativistisesta ydinmatriisielementistä (sNME), jonka tarkka laskeminen ytimen kuorimallin valenssi-
avaruuksissa on todella haastavaa. Tämän riippuvuuden innoittamana tutkimusta on laajennettu tarkastelemalla aksiaalikytkentävoimakkuuden g_A ja matriisielementin sNME vaikutusta ytimen ^{99}Tc beetaspektriin. Kyseinen ydin on neutriinottomalla kaksoisbeetahajoamisella mahdollisesti purkautuvien ydinten ^{100}Mo ja ^{96}Zr välitömässä läheisyydessä. Havaittu matriisielementtiin sNME liittyvä kaksiselitteisyys johti lisätutkimuksiin läpi reaktoriantineutriinoanomaliaan liittyvien isotooppien kirjon, pyrkimyksenä valottaa beetaspektrien muodon ennustettavuuden tarkkuutta suhteessa sNME:hen ja g_A :han.

Eräs työn huipentumana on, että työssä kehitetyt menetelmät auttavat myös (anti)neutriinon massan määrittämisessä hyödyntäen ytimen kuorimallia ja sillä saatuja ennusteita beetasiirtymien puoliintumisajoille.

Avainsanat: beetahajoaminen, ytimen kuorimalli, beetaspektrin muoto, kielletty ei-uniikki, heikko aksiaalikytkentä, pieni ydinmatriisielementti.

Author	Marlom Ramalho Department of Physics University of Jyväskylä Finland
Supervisor	Professor Jouni Suhonen Department of Physics University of Jyväskylä Finland
Reviewers	Professor Praveen Srivastava Department of Physics Indian Institute of Technology Roorkee India Professor Osvaldo Civitarese Department of Physics Universidad Nacional de La Plata Argentina
Opponent	Dr. Xavier Mougeot Université Paris-Saclay, CEA, List Laboratoire National Henri Becquerel (LNE-LNHB) France

PREFACE

I am deeply grateful to the University of Jyväskylä and Professor Jouni Suhonen for providing me with the remarkable opportunity to conduct state-of-the-art research within such a dynamic group. The collaboration with Ge Zhuang, Tommi Eronen, and other members of the experimental group has been exceptionally productive. The synergy between the experimental and theoretical groups at our University is extraordinary and certainly something to be nurtured.

The financial support from the Doctoral School of the University of Jyväskylä was invaluable, providing the foundation for several years of focused research.

I want to stress how important the support from my supervisor Jouni Suhonen has been for this whole project, never ceasing with new creative directives for us to pursue, his enthusiasm, friends and colleagues in need of some theoretical computations-it was never a dull moment

Pursuing research in Nuclear Physics, particularly in the realm of radioactivity, has been a dream of mine for over a decade. Connecting this passion with the intriguing field of beyond the standard model research has further motivated my academic pursuits.

I extend my appreciation to Professors Praveen Srivastava and Osvaldo Civitarese for their thorough review of my thesis manuscript, and a special thanks to Dr. Xavier Mougeot for accepting the role of the opponent on the defense day.

I would like to thank Prof. Antonio Carlos Pedroza, for his support in my physicist career and Prof. Oyanarte Portilho, who inspired me to pursue research in the field of Nuclear Physics.

Last but certainly not least, my heartfelt thanks go to my family for their lifelong support. A special thanks to Siobhan, my anchor and greatest supporter, whose presence has been indispensable throughout this journey.

Jyväskylä, January 2024,
Marlom Ramalho

LIST OF INCLUDED ARTICLES

This thesis consists of an introductory part and of the following publications:

- [I] **Analysis of the total β -electron spectrum of ^{92}Rb : Implications for the reactor flux anomalies**
M Ramalho et al., *Phys. Rev. C*. 106, 2 (Aug. 2022) 024315, DOI: 10.1103/PhysRevC.106.024315.
- [II] **Computed total β -electron spectra for decays of Pb and Bi in the $^{220,222}\text{Rn}$ radioactive chains**
M Ramalho and J Suhonen, *Phys. Rev. C*. 109, 1 (Jan. 2024) 014326, DOI: 10.1103/PhysRevC.109.014326.
- [III] **Shell-model treatment of the β decay of ^{99}Tc**
M. Ramalho and J. Suhonen, *Submitted to Il Nuovo Cimento C and to ArXiv* (Nov. 2023) 2312.07448, DOI: 10.48550/arXiv.2312.07448.
- [IV] **g_A -sensitive β spectral shapes in the mass $A = 86 - 99$ region assessed by the nuclear shell model**
Marlom Ramalho and Jouni Suhonen, *Phys. Rev. C*. 109, 3 (Mar. 2024) 034321, DOI: 10.1103/PhysRevC.109.034321.
- [V] **High-precision measurement of a low Q value for allowed β^- -decay of ^{131}I related to neutrino mass determination**
T Eronen et al., *Phys. Lett. B* 830, 137135 (July 2022), DOI: 10.1016/j.physletb.2022.137135.
- [VI] **β^- decay Q-value measurement of ^{136}Cs and its implications for neutrino studies**
Z Ge et al., *Phys. Rev. C*. 108, 4 (Oct. 2023) 045502, DOI: 10.1103/PhysRevC.108.045502.

The author performed all the theoretical computations for the articles [I, II, III, IV, V, VI] and contributed to the writing of the original draft of these publications on the theoretical aspect. The author also developed his own codes for the beta spectral shapes computations and updated the codes to address atomic exchange corrections.

CONTENTS

ABSTRACT

TIIVISTELMÄ

LIST OF INCLUDED ARTICLES

1	INTRODUCTION	1
2	THEORETICAL FRAMEWORK	4
2.1	Beta Decay	4
2.2	Nuclear Many Body Theory - Effective Potentials	7
2.3	Nuclear Shell Model	8
2.4	Beta Shapes and its dependencies	14
3	ARTICLE ANALYSES AND DISCUSSIONS	17
3.1	The Antineutrino Anomaly	17
3.2	Computed Spectra for Rn background	24
3.3	Technetium-99 spectra as a probe for the weak-axial coupling	30
3.4	Beta Shape sensitivity on g_A and s_{NME}	35
3.5	Neutrino Studies via Beta Decays	40
4	SUMMARY	44

REFERENCES

INCLUDED ARTICLES

1 INTRODUCTION

The theoretical framework for β -decays has its origins in the work of Fermi in 1934 [1]. Since then, the theory has evolved through numerous contributions addressing its various aspects. Despite these advancements, the theory remains incomplete. A notable example of ongoing development is the significant impact of atomic exchange effects on the computed beta spectral shapes and half-lives. This phenomenon is of importance even in the most simplistic cases of allowed decays, as can be seen as recently as those in 2023 [2], particularly, for low electron energies. While the foundational aspects of β -decay theory have evolved significantly since Fermi's time, contemporary research confronts new challenges, particularly in the realm of forbidden decays.

Forbidden β -decays, particularly non-unique decays, present computational challenges. Approximations to their shape factors, as elucidated in [3], offer a method for calculating these decay shapes. However, the application of these approximations is not uniformly successful. Even when forbidden unique approximations with the same ΔJ are employed as a surrogate for the complete first forbidden non-unique decays, they often fail to accurately reproduce the experimental beta spectrum, a limitation also documented in [3].

The complexities inherent in β -decay analysis primarily stem from two distinct sources: corrections related to nuclear interactions with atomic electrons (such as atomic exchange corrections and screening effects), and the accurate depiction of nuclear wave functions. The former can be seen as an extension and refinement of Fermi's original theory, encompassing secondary yet significant effects that were initially overlooked. The latter, however, delves into the intricacies, or in the case of heavy nuclei, the impossibility, of applying a perfect many-body theory to adequately represent nuclear structure. Understanding these complexities leads us to examine the current methodologies and computational tools employed in β -decay studies, which often involve approximations due to the intricate nature of nuclear interactions.

At present, the methodologies employed to tackle the complexities of nuclear wave function representation in β -decay studies primarily involve approximative computations. These methods often overlook detailed nuclear structure. Notable among these are the use of *Geant4* [4], with its dedicated radioactive decay module,

and *Betashape* [5]. *Betashape*, in particular, offers a more comprehensive approach by incorporating experimentally known beta shapes from its database when available. These tools are valuable and generally suffice when the exact precision of the beta shape is not the principal focus of the study.

The landmark discovery that confirmed neutrino oscillations, propelling physics beyond the standard model (BSM), has significantly amplified the pursuit of BSM physics through rare event-experiments (REE). Among these experiments is the search for dark matter in the Universe by detecting Weakly Interacting Massive Particles (WIMP) scattering. Concurrently, investigations into neutrinoless double beta decays (NDBD) are intensifying, aiming to unravel the fundamental nature of neutrinos – specifically, to determine whether they are Dirac or Majorana particles. The potential discovery of neutrinos as Majorana particles would represent a groundbreaking advancement in the field of physics.

Discrepancies between theoretical predictions and experimental observations of neutrinos generated in nuclear reactor fission have revealed a notable mismatch [6, 7]. This mismatch, evident in the number of neutrinos detected, has spurred various hypotheses, one of which posits the existence of a sterile neutrino flavor [8]—a type of neutrino that does not interact via the weak force. This divergence between the expected and observed neutrino flux across multiple experiments has been termed the 'Reactor Antineutrino Anomaly' (RAA).

Researchers investigating the underlying causes of the Reactor Antineutrino Anomaly (RAA) have identified the use of incomplete calculations, approximations and the **Pandemonium Effect** as a potential factor contributing to the observed discrepancy [9, 10]. This recognition has led to a surge in high-precision beta spectrum experiments, notably employing the Total Absorption Gamma Spectroscopy (TAGs) method. These efforts aim to ascertain the true origin of the RAA with greater accuracy and detail and has already contributed substantially to its objectives.

To overcome the constraints of traditional approximations, employing advanced many-body theory computations is crucial. Theoretical models like the Nuclear Shell Model (NSM), proton-neutron quasi-particle random phase approximation (pnQRPA), and Microscopic Quasiparticle-Phonon Model (MQPM) are often used. These models are particularly vital in the study of medium to heavy nuclei, where the great number of interacting particles create complex behaviors. A significant challenge in applying these methods, however, is the substantial computational power required. This requirement for high computational resources is, in fact, the primary reason behind the reliance on simpler approximations in many studies.

Recent advancements in computational power have led to a notable increase in the popularity and capability of Shell model computations. These advancements have enabled significant reductions in computational truncation, leading to a more true-to-the-heart physics. A key factor contributing to this progress is the resurgence of codes designed for parallel computing, which are well-suited for High Performance Computing (HPC) environments. Notable examples of such environments include LUMI and Mahti, which allow users to simultaneously utilize up to 200 nodes, each with 128 cores, for a single computational job. This enhancement in computational resources has been crucial to the development of the research presented in this

dissertation.

This thesis delves into the intricate aspects of β decay computations using the Nuclear Shell Model (NSM), with a particular emphasis on the effective weak-axial coupling, which is essential for both β and double- β decays. It explores the recent methodological innovation of employing the small-Nuclear Matrix Element (sNME) to refine half-life computations, thereby enhancing the reliability of β spectra. Additionally, the thesis examines the significance of atomic exchange corrections and assesses the interplay of the complex factors that influence the broader challenges faced in Beyond the Standard Model (BSM) physics research aforementioned.

2 THEORETICAL FRAMEWORK

In this chapter, we present an overview of the theoretical formalism underpinning the research conducted in this work. The structure is as follows: We begin with a brief introduction to beta decays, discussing the foundational concepts in Section 2.1. This is followed by an exploration of the challenges and approaches in nuclear many-body theory, outlined in Section 2.2.

Subsequently, we delve into the intricacies of the nuclear shell model, which forms the cornerstone of our computational analysis, in Section 2.3. The peculiarities and nuances of beta spectral shapes, a critical aspect of beta decay studies, are examined in Section 2.4 where we finally underscore the importance of the weak axial coupling and the small nuclear matrix element, two pivotal factors in our analysis.

2.1 Beta Decay

Beta decay represents a fundamental process in nuclear physics, where an unstable atomic nucleus transforms into a more stable configuration. This decay process is pivotal in understanding nuclear structure, nuclear forces, and particle physics. At its core, beta decay is a manifestation of the weak force, one of the four fundamental forces in nature.

In beta decay, a nucleus emits a beta particle, which can be either an electron (β^-) or a positron (β^+), along with an antineutrino ($\bar{\nu}_e$) or a neutrino (ν_e), respectively. The decay can be understood as a transformation of a nucleon:

– β^- Decay:



In beta minus decay, a neutron (n) is transformed into a proton (p), releasing an electron (e^-) and an electron antineutrino ($\bar{\nu}_e$). This process increases the atomic number by one while keeping the atomic mass number unchanged.

– β^+ Decay:



Beta plus decay involves the conversion of a proton into a neutron, with the emission of a positron (e^+) and an electron neutrino (ν_e). Here, the atomic number decreases by one, but the mass number remains constant.

We shall focus solely on β^- decay throughout this work and shall therefore mean β^- decay, for all forward mentions of β decay.

Beta decay strictly adheres to the conservation laws of charge, energy, and momentum. The conservation of charge is outlined in Equations 1 and 2. In the context of energy conservation, the decay energy, denoted as the Q value, is derived from the difference in binding energies between the parent and daughter nuclei.

The energy conservation in beta decay processes alone is governed by the equations:

$$Q_{\beta^-} = (m_n - m_p - m_{e^-})c^2, \quad (3)$$

for beta-minus decay, and

$$Q_{\beta^+} = (m_p - m_n - m_{e^+})c^2, \quad (4)$$

for beta-plus decay, where m_n , m_p , m_{e^-} and m_{e^+} are respectively neutron's, proton's, electron and positron's masses and c , the speed of light. These equations indicate that the energy released in beta-minus decay is positive, signifying that such decays are energetically favorable and can occur spontaneously, as in the case of free neutrons. Conversely, for beta-plus decays the energy released is negative, implying that these decays require an external energy input to proceed and typically occur within atomic nuclei where the energy deficit can be compensated.

In beta-minus decay, the energy released is partitioned among the electron (e^-), the antineutrino ($\bar{\nu}_e$), and the daughter nucleus. This distribution of energy among the decay products gives rise to the continuous spectrum characteristic of beta decay, in contrast to the discrete energy emissions observed in α and γ decays.

The conservation of angular momentum and parity between the parent and daughter nuclei, as well as the electron and antineutrino, dictates the nature and 'forbiddenness' of the decay. These properties are summarized in Table 1. Here, ΔJ represents the change in total angular momentum, with J being the total angular momentum of a many-nucleon state. For leptons ΔJ stems from the coupling of their relative orbital angular momentum L and total spin S , for instance, $L = 0$ for leptons in an 's' state.

Forbidden decays are further classified as either unique or non-unique, which has implications for the complexity of the Nuclear Matrix Elements (NMEs) associated with their respective wave functions. A more detailed exploration of these complexities will be addressed in subsequent sections and is comprehensively covered in Chapter 7 of [11].

The β spectrum is defined by the probabilities of electron emission with energies between W_e to $W_e + dW_e$. The construction of the spectra is due to the energy distribution between the electron and the antineutrino. These probabilities however can be expressed as:

Transition	L	ΔJ	$\Delta\pi$
Allowed Fermi	0	0	0
Allowed Gamow–Teller	0	0, 1	0
First-Forbidden (parity change)	1	0, 1, 2	1
Second-Forbidden (no parity change)	2	2, 3	0
Third-Forbidden (parity change)	3	3, 4	1
Fourth-Forbidden (no parity change)	4	4, 5	0

TABLE 1. Summary of beta decay transitions with angular momentum and parity change characteristics.

$$P(W_e) = \frac{G_F}{(\hbar c)^6} \cdot \frac{C(W_e)}{2\pi^3 \hbar} \cdot p_e c \cdot W_e (W_0 - W_e)^2 \cdot F_0(Z, W_e), \quad (5)$$

where G_F is the Fermi coupling constant, Z is the atomic number of the daughter nucleus, p_e is the momentum of the electron, and $F_0(Z, W_e)$ is the Fermi function, which accounts for the Coulomb interaction between the emitted electron and the daughter nucleus. The term $C(W_e)$, known as the shape factor, encompasses the details of the nuclear structure, and W_0 denotes the endpoint energy of the electron spectrum. It is important to note that Equation 5 does not include corrections for radiative, atomic exchange, and atomic screening effects. These are considered as multiplicative corrections to the above expression.

The complexity of the beta decay process is then encapsulated in the shape factor $C(W_e)$, which integrates nuclear structure information and determines the spectral shape. A deeper examination of the shape factor and its implications for beta decay will be discussed in subsequent sections.

Upon establishing the probability distribution of electron emission energies, one can integrate over all possible values of W_e up to the endpoint energy to obtain the integrated shape function \tilde{C} . This integration is performed as follows:

$$\tilde{C} = \int_1^{w_0} C(w_e) p w_e (w_0 - w_e)^2 F_0(Z, w_e) dw_e, \quad (6)$$

where the lowercase w_e and w_0 are the kinematic scaled W_e , W_0 by $m_e c^2$. The integral encapsulates the nuclear structure information, inclusive of all the Nuclear Matrix Elements (NMEs) contained in the shape factor. For allowed decays, the computation simplifies as the shape factor $C(w_e) \approx 1$. However, the scenario becomes considerably more complex for forbidden decays. For instance, first-forbidden unique decays involve calculations with only one NME, but, non-unique forbidden decays entail multiple NMEs, adding layers of complexity to the computation.

The integrated shape factor, \tilde{C} , is instrumental in the determination of a beta decay's half-life. The half-life can be computed using the direct relationship given by:

$$t_{1/2} = \frac{\kappa}{\tilde{C}}, \quad (7)$$

where κ is a constant encompassing several natural constants, numerically evaluated as $\kappa = 6289$ s [12]. The half-life of a beta decay is one of the most significant

quantities of interest. It encapsulates the decay's kinetics and is directly influenced by the shape factor, which, as we have seen, is determined by the intricate details of nuclear structure and the transition type. Hence, the shape factor not only shapes the beta spectrum but also critically influences the half-life, underscoring its importance in beta decay studies.

2.2 Nuclear Many Body Theory - Effective Potentials

One of the most significant challenges in nuclear physics is understanding the interactions within a system of many bodies governed by electromagnetic, weak, and strong forces. Consider a simple nucleus denoted by A_ZX_N , where A is the total number of nucleons, Z is the number of protons, and N is the number of neutrons. The complexity of interactions in such a system, even for a relatively small A , poses what is known as the nuclear many-body problem. This problem is exacerbated by the fact that nucleons are not elementary particles but are composed of quarks and gluons that interact with each other. At its core, the nuclear many-body problem can be encapsulated by the Hamiltonian:

$$H = T + V, \quad (8)$$

where T represents the kinetic energy of the nucleons and V is the potential energy arising from their interactions:

$$T = \sum_{i=1}^A t(x_i), \quad (9)$$

$$V = \sum_{i<j} v(x_i, x_j) = \frac{1}{2} \sum_{i \neq j} v(x_i, x_j). \quad (10)$$

In these expressions, $t(x_i)$ denotes the kinetic energy of an individual nucleon with spatial and spin coordinates x_i , and $v(x_i, x_j)$ represents the interaction potential between a pair of nucleons in states x_i and x_j .

While an exact solution to the many-body problem in nuclear physics remains out of reach, significant strides have been made through the use of nuclear mean field approximations. These methods greatly simplify the issue by considering nucleons to move in an average potential field as if they were free particles. This average field is synthesized from the collective effect of all nucleons in the nucleus. Corrections are then applied for the missing interactions between pairs of nucleons, using what is known as a residual interaction.

Despite its inherent approximations, the mean field approach has become an indispensable tool for unraveling the complexities of the nuclear many-body problem, a fact that is underscored by the findings presented in this work.

The mean field approximation methods build upon the experimentally observed properties and symmetries of nuclei to devise a simplified, yet surprisingly effective, Hamiltonian to tackle the many-body problem. The emergence of 'magic numbers'

suggests a shell structure within the nucleus, mirroring the electronic shells found in atoms. This insight has been pivotal to the formulation of nuclear shell models. Specifically, this symmetry permits a focus on nucleons at the Fermi surface and in the valence space, while the remaining nucleons are considered part of a 'frozen' core, thereby markedly reducing the computational burden.

The crux of these methods lies then in formulating an appropriate Hamiltonian that reflects the nuclear property or phenomenon under investigation. This is typically achieved by calibrating the model against a range of experimental data. The process involves selecting a suitable model space and adjusting the parameters of the Hamiltonian until it closely aligns with the empirical observations. Such a methodology has been pivotal in enhancing our understanding of nuclear structure and the underlying forces governing nuclear phenomena.

Having outlined the importance of constructing an effective Hamiltonian, we will now transition to an in-depth exploration of the primary mean-field method employed in this study: the Nuclear Shell Model. This model is predicated on the shell-like behavior observed within the nucleus, analogous to the electrons in an atom. The upcoming section will elucidate how this model is applied to describe nuclear phenomena, detailing its implementation and the insights it provides into the intricate workings of nuclear systems.

2.3 Nuclear Shell Model

The interacting Nuclear Shell Model (NSM) is currently one of the most prominent approaches to nuclear structure, largely owing to the vast array of Hamiltonians embedded within its coded frameworks, such as *NuShellX@MSU* [13] and *KSHELL* [14]—both utilized in the studies presented herein. This approach has gained momentum with the increasing accessibility of High-Performance Computing (HPC) resources like Mahti and LUMI at the Finnish CSC IT Center for Science.

Furthermore, alternative computational tools such as *ANTOINE* [15] and *BIGSTICK* [16] are also noteworthy. Although these codes are adept at computing level schemes, they are somewhat restricted in their output of additional properties, which will be discussed later in this section. We note however, that these are not exhaustive of all NSM codes.

One of the intricate challenges within NSM is the derivation of practical Hamiltonians for calculations. Nonetheless, these codes typically include several ready-to-use Hamiltonians, with *NuShellX@MSU* offering a particularly extensive assortment, thereby establishing itself as a robust instrument for nuclear structure analysis.

In the context of nuclear interactions, model spaces are conceptual frameworks designed to replicate the physical behavior of the target nuclei. These spaces are delineated by distinguishing between active and inert orbitals. Specifically, proton and neutron orbitals located beneath a defined 'magic number' are treated as a 'closed core'. This core is considered inert, meaning it does not engage in configuration

mixing and remains constant throughout the calculation.

Contrastingly, the orbitals that lie above the closed core and within the designated valence space are dynamically involved in the nuclear structure calculations. They are the 'active' components that participate in configuration mixing and determine the nuclear properties being investigated. Any orbitals beyond the valence space are similarly treated as part of the closed core, effectively simplifying the model.

Table 2 outlines a selection of model spaces as implemented in the *NuShellX@MSU* software. Within this table, the valence spaces are indicated by marked boxes, signifying their active role in the computational process, while the unmarked boxes represent orbitals that are not included in the interaction calculations.

Model Space	1p1/2	1p3/2	1d3/2	1d5/2	2s1/2	1f7/2	1f5/2	2p3/2	2p1/2	1s1/2
P	☒	☒	☐	☐	☐	☐	☐	☐	☐	☐
PPN	☒	☒	☐	☐	☐	☐	☐	☐	☐	☐
SD	☐	☐	☒	☒	☒	☐	☐	☐	☐	☐
PSD	☒	☒	☒	☒	☒	☐	☐	☐	☐	☐
SPSDPF	☒	☒	☒	☒	☒	☒	☒	☒	☒	☒
D3F7	☐	☐	☒	☐	☐	☒	☐	☐	☐	☐
HASP	☐	☐	☒	☐	☒	☒	☐	☒	☐	☐

TABLE 2. A few of *NuShellX*'s nuclear model spaces and their corresponding orbitals

With the model spaces delineated, we focus on the single-particle energies (SPEs), which are integral to the one-body component of the nuclear interaction. These SPEs are crucial for accurately predicting observables. In the occupation number representation, the one-body operator T is given by:

$$T = \sum_{i=1}^A t(x_i) = \sum_{\alpha\beta} t_{\alpha\beta} c_{\alpha}^{\dagger} c_{\beta}, \quad (11)$$

where $t_{\alpha\beta}$ is defined as:

$$t_{\alpha\beta} \equiv \langle \alpha | T | \beta \rangle = \int \phi_{\alpha}^{*}(x) t(x) \phi_{\beta}(x) d^3r, \quad (12)$$

and the SPEs are represented by $t_{\alpha\alpha}$, the diagonal elements of the one-body operator.

Once the model space is established, single-particle energies (SPEs) for each orbital are adjusted to match experimental data relevant to the mass region of interest. This fitting process typically aims to replicate known level schemes or other experimentally known properties. For instance, within the "SD" model space as delineated in Table 2 and using the *USDA* interaction [17], the SPEs for the orbitals 1d3/2, 1d5/2, and 2s1/2 are set at 1.9798 MeV, -3.9436 MeV, and -3.0612 MeV, respectively.

In addition to the SPEs, the nuclear interactions encompass the Two-body Matrix Elements (TBMEs), which account for the two-body contributions in the nuclear

system. These elements are represented in the occupation number representation as follows:

$$V = \frac{1}{2} \sum_{\alpha\beta\gamma\delta} \bar{v}_{\alpha\beta\gamma\delta} c_{\alpha}^{\dagger} c_{\beta}^{\dagger} c_{\delta} c_{\gamma}, \quad (13)$$

where the matrix element $\bar{v}_{\alpha\beta\gamma\delta}$ is defined by the integral:

$$\bar{v}_{\alpha\beta\gamma\delta} = \int \phi_{\alpha}^{\dagger}(x_1) \phi_{\beta}^{\dagger}(x_2) v(x_1, x_2) \phi_{\gamma}(x_1) \phi_{\delta}(x_2) d^3r_1 d^3r_2. \quad (14)$$

These TBMEs are crucial in determining the proton-proton, proton-neutron, and neutron-neutron interactions within the nucleus and are fundamental to the efficacy of a Hamiltonian. Different TBMEs are employed for each specific interaction in the codes such as *NuShellX@MSU* and *KSHELL*. For a comprehensive discussion on TBMEs, outlining an example: the Surface Delta Interaction (SDI), readers are referred to Chapter 8 in [11].

Upon fine-tuning the Hamiltonians to a specific region of isotopes, the Nuclear Shell Model (NSM) can be applied to compute various nuclear properties. These include level schemes, electromagnetic properties like magnetic dipole (M1) moments and electric quadrupole (E2) moments, as well as one-body transition densities (OBTDs). OBTDs are particularly important for computing processes such as beta decays and electromagnetic transitions, such as γ -emission.

One of the most frequently pursued observables in NSM calculations is the nuclear level scheme. Figure 1 illustrates the calculated level schemes for the isotopes ^{99}Tc and ^{99}Ru , using the Hamiltonians *jj45pnb* and *glekpn*, respectively in [III]. There, one can note that even if the agreement of the order of J^{π} is slightly mixed, the levels are reproduced efficiently. These Hamiltonians have been adjusted to align with experimental data, offering a more accurate representation of nuclear structures in the region. The validation of these interactions against experimental data is discussed in the works of Lisetskiy et al. [18] and Mach et al. [19], highlighting the relevance of these interactions for the studied region.

NuShellX@MSU and *KSHELL* have been instrumental in the investigations conducted in this work. Their selection was based not only on their widespread use in the field but also on specific features that make them particularly apt for the studies undertaken here. The following two subsections will delve into the unique aspects of these codes, including their computational efficiency, user-friendliness, applicable model spaces, and the diversity of physical observables they can calculate. This detailed exploration is intended to serve as a practical guide for future researchers in the field of nuclear shell model computations, offering insights into the operational nuances and capabilities of *NuShellX@MSU* and *KSHELL*. Readers whose interests lie outside the specifics of these computational tools may opt to bypass the next two subsections, focusing instead on the broader findings and implications of the current research.

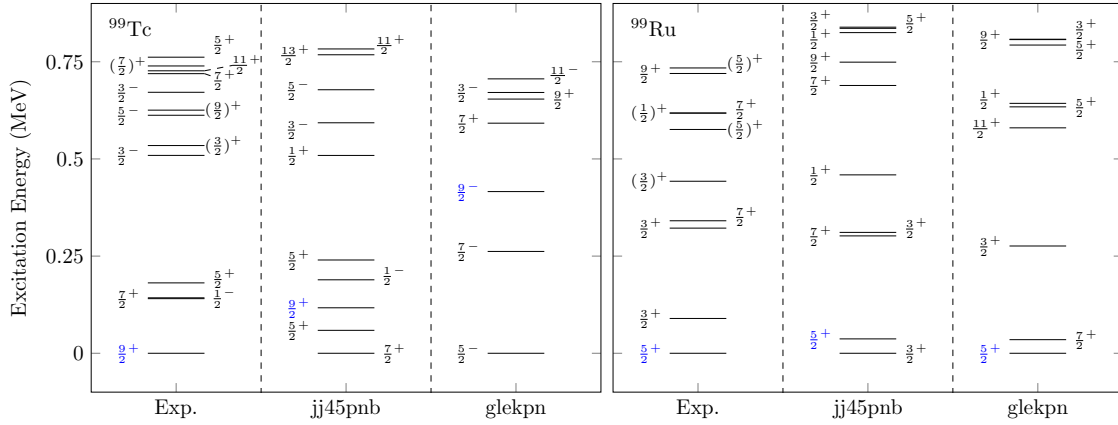


FIGURE 1. Energy level schemes for ^{99}Tc and ^{99}Ru with their corresponding NSM-computed values using the interactions $jj45pnb$ and $glekpn$. Experimental data are taken from the ENSDF [20] evaluation. Levels in blue are the initial and final states for the second forbidden decay of interest. Reprinted from [III] with APS copyrights.

2.3.1 NuShellX@MSU Software

NuShellX@MSU represents the latest advancement in a series of Nuclear Shell Model (NSM) codes developed by Alex Brown and colleagues, succeeding its predecessors MultiShell (unpublished) and OXBASH [21]. The introduction of *NuShellX@MSU* [13] has significantly broadened accessibility to nuclear theory research, evidenced by its widespread adoption. As of the date of this dissertation, the starting paper on *NuShellX@MSU* has garnered over 580 citations, underscoring its prominence as a computational tool in NSM studies.

One of the software's key strengths is its user-friendly interface, which facilitates ease of use and shortens the learning curve for nuclear physicists. The installation process is streamlined, particularly for users familiar with LINUX or Windows' environment variables.

From a performance standpoint, *NuShellX@MSU* is highly optimized for efficient CPU utilization. It leverages OpenMP processes to enable parallel computations across multiple CPU cores, often maximizing the CPU usage to its full potential for each computation.

In terms of capabilities, *NuShellX@MSU* allows the calculating of the angular momentum J and parities of nuclei, whilst also computing their excitation energies. It also generates wavefunctions for each state of a nucleus, categorized by their J^π values. This capability is instrumental in constructing comprehensive nuclear level scheme structures.

Furthermore, the software simplifies the calculation of γ transition strengths between states, a feature that is integrated as an option into its user interface. This combination of user-friendliness and robust computational power makes *NuShellX@MSU* an indispensable tool in contemporary nuclear physics theoretical research.

Embedded within the user interface of *NuShellX@MSU* are functionalities that extend beyond the computation of single nuclei properties. One may also

run the computation for adjacent nuclei, which is crucial for beta decay studies, encompassing both β^- and β^+ processes. This can then involve calculating the overlap of wavefunctions between an initial state nucleus ${}^A_Z X_N$ in a J_i^π state and a final state nucleus ${}^A_{Z+1} X_{N-1}$ in a J_f^π state. This capability is especially important for determining One-Body Transition Densities (OBTD) using the many rank operators. The output, a well-organized text file that elucidates critical data and paves the way for comprehensive beta decay studies, including the efficient computation of half-lives and beta decay shapes.

Despite these strengths, *NuShellX@MSU* faces computational limitations, primarily dictated by the processing capabilities of the hardware in use. The software's intense CPU utilization implies that computational capacity is inherently restricted by the number of cores and their processing speed within a single CPU. Memory usage is another critical factor; high memory demand in a single computer can constrain computations.

To mitigate these limitations, a common practice involves truncating the model space, either by fixing a certain number of nucleons in specific orbitals or by restricting nucleon occupancy in others. This approach, while practical, can potentially compromise the accuracy of the physical model. One has to proceed with caution with such truncations as they can significantly alter beta decay shapes and half-lives, highlighting the need for caution in employing these computational strategies.

In the context of contemporary hardware capabilities, even considering the best processors currently available, such as the AmpereOne Family with up to 192 cores and memory limitations, these remain a bottleneck. This means that the ultimate computational boundary for *NuShellX@MSU* is defined by the maximum capacity of a **single computer**. In practical terms, this often limits the software to computations of an individual state at a time of a specific angular momentum J and parity π , thus defining the current computational horizon for *NuShellX@MSU*.

In conclusion, *NuShellX@MSU* excels in managing up to medium-to-heavy nuclear structure computations with its user-friendly interface and extensive Hamiltonian library, making it an ideal choice for beginners in Nuclear Shell Model computations. The primary challenges of *NuShellX@MSU* emerge in the realm of extremely heavy computations or comprehensive full-blown beta decay calculations. These scenarios often necessitate the evaluation of numerous J^π states and decay processes, pushing the software to its computational limits. Nevertheless, for a wide range of nuclear structure studies, *NuShellX@MSU* stands out as a valuable and accessible tool in the field of nuclear physics.

2.3.2 KSHELL Software

The code *KSHELL*, introduced in 2019 by Noritaka Shimizu at the University of Tsukuba [14], represents a significant advancement in nuclear physics computation softwares. Designed to address the computational limitations of *NuShellX@MSU*, it leverages both OpenMP and MPI (Message Passing Interface) packages. This dual approach enables the simultaneous use of multiple computers or nodes for a single

calculation, thereby greatly enhancing its computational power.

While *KSHELL* boasts an even more streamlined user interface than *NuShellX@MSU*, its installation process presents certain challenges. The software requires specific Linux packages that are not standard in all systems. Additionally, users might need to modify the ‘makefile’ to compile the software correctly, a task that may prove daunting for those not well-versed in Linux environments.

KSHELL excels in its predictive capabilities for nuclear states. It is able to compute the quantum numbers (J and parities) even without defining the J and parities of these states. This feature is particularly useful for identifying the lowest energy levels in a nucleus, offering more reliable level spectrum computations as compared to methods that pre-specify expected J ’s and parities.

The software also includes an intuitive option for calculating key electromagnetic properties, such as magnetic dipole (M1) and electric quadrupole (E2) moments. Additionally, *KSHELL* simplifies the computation of all γ transition strengths for a given nucleus with a simple option in the setup, a feature that proves extremely useful in nuclear physics research, especially when assessing the feasibility of a Hamiltonian as can be seen in [III, IV].

Another advantage of *KSHELL* is the flexibility it offers in adjusting parameters. Users can easily modify effective charges, harmonic oscillator properties, and other computational parameters. Furthermore, the output for level schemes includes information on the average occupancy of the orbitals, providing a quick and deep insight into the behavior of each state calculated. This combination of predictive power, ease of parameter adjustment, and detailed output makes *KSHELL* a powerful tool in the arsenal of theoretical nuclear physicists.

KSHELL distinguishes itself with additional scripts that significantly enhance its functionality. These scripts allow for detailed analysis of wavefunctions, including occupancy numbers and the configuration mixing contribution for each state. A particularly useful feature is a script that facilitates the conversion of Hamiltonians from other nuclear shell model codes into the format used by *KSHELL*. This capability enables users to combine the extensive Hamiltonian library of *NuShellX* with the computational strengths of *KSHELL*.

Furthermore, *KSHELL* includes scripts for automatically generating graphical representations of gamma emission cascades predicted by level scheme computations. This feature, which can be labor-intensive to perform manually, adds considerable value to the software.

One complication of *KSHELL* is in the output format for one-body transition densities (OBTDs), particularly when used in beta decay studies. The output is organized by tensor ranks rather than the more intuitive classification of J and parities. This necessitates additional coding or manual conversion to reformat the data into a more user-friendly structure. However, for research not requiring detailed OBTD analysis, this issue can be ignored.

The integration of Message Passing Interface (MPI) in *KSHELL* represents a significant advancement in parallel computing for nuclear shell model calculations. This feature extends the software’s computational capabilities beyond the single-node limit of *NuShellX*, allowing it to harness the collective power of multiple computing

nodes. The primary advantage of this approach is the scalability it offers, with the computational horizon now defined by the aggregate resources of the available nodes, including their memory, CPU cores, and clock speeds.

For instance, as detailed in the *KSHELL* manual, the computation of the ground-state energy of ^{56}Ni within the ‘pf’ shell model space can be performed in a mere 53 seconds. This calculation, which encompasses approximately one billion M-scheme dimensions, was achieved using 144 nodes with a total of 8064 CPU cores. Such a feat underscores the dramatic computational efficiency of *KSHELL* when leveraging advanced parallel computing techniques.

The advent of high-performance computing (HPC) clusters like Mahti and LUMI, operated by the Finnish IT Center for Science (CSC), further expands these capabilities. These HPC clusters offer up to 200 nodes, each equipped with 128 cores (or 256 threads) and 256 GBs of memory per node. For extensive projects requiring even greater computational resources, exceptions can be granted, thus allowing for scalability of computations in the NSM field to previously unattainable horizons.

In conclusion, NSM computations using *KSHELL* benefit significantly from the ability to convert Hamiltonian formats between *NuShellX@MSU* and *KSHELL*, facilitating the sharing of extensive Hamiltonian libraries across these software platforms. The incorporation of both MPI and OpenMP in *KSHELL* enhances its computational capacity, making it a robust tool for large-scale nuclear shell model calculations.

However, the software’s installation process, particularly on supercomputers where users do not have full control over the system packages, presents a notable challenge. This aspect potentially limits *KSHELL*’s accessibility, especially for less experienced users or those without the necessary system privileges. Additionally, *KSHELL*’s output format for beta decay computations, which is organized by ranks rather than by J and parity, may require further processing for some applications, adding a layer of complexity to its use.

Given these considerations, while *KSHELL*’s advanced capabilities make it an ideal choice for demanding computations that exceed the scope of *NuShellX@MSU*, its installation challenges and the necessity for high-performance computing resources position it as a more suitable option for experienced users in the field. *KSHELL*’s optimal utilization is therefore in scenarios requiring extensive computational power, where its advanced features can be fully leveraged.

2.4 Beta Shapes and its dependencies

In the computation of beta decay characteristics, such as decay shapes and half-lives, a key component is the One-body Transition Density (OBTD). These densities are integral in calculating the Nuclear Matrix Elements (NMEs), which are essential for understanding and computing the decay process. The detailed methodology for computing OBTDs is outlined in Chapter 2.3.

For the calculation of beta decay NMEs, one may employ the following formula:

$$\mathcal{M}_{K L s}^{(N)} = \frac{\sqrt{4\pi}}{\hat{J}_i} \sum_{pn} m_{K L s}^{(N)}(pn) (\Psi_f || [c_p^\dagger \tilde{c}_n]_K || \Psi_i), \quad (15)$$

for both the axial and vector components of the NMEs. Here, $m_{K L s}^{(N)}(pn)$ represents the single-particle matrix element, which involves the proton orbital 'p' and neutron orbital 'n'. The term $(\Psi_f || [c_p^\dagger \tilde{c}_n]_K || \Psi_i)$ denotes the one-body transition density, derived from the computational steps previously described. In this context, 'K' indicates the forbiddenness level of the decay (with 0 signifying allowed decays, 1 first forbidden, and so forth). The symbols Ψ_f and Ψ_i represent the wavefunctions of the daughter and parent nuclei, respectively.

For this work, the computation of the beta-decay Nuclear Matrix Elements is facilitated by a C++ script developed at the University of Jyväskylä by M. T. Mustonen and M. Haranen. This code adheres to the formalisms outlined in [11] and in the work of Behrens and Buhning [22], with my own contributions that include the implementation of the associated Laguerre Polynomial of third order. Additionally, the code incorporates further Coulomb corrections to enhance the accuracy of the matrix elements.

The shape factor, which encapsulates the Nuclear Matrix Elements (NMEs), incorporates contributions from the axial part, vector part, and a mixed component of both. Consequently, the shape factor can be articulated as follows:

$$C(w_e) = g_V^2 C_V(w_e) + g_A^2 C_A(w_e) + g_V g_A C_{VA}(w_e). \quad (16)$$

For the vector components, we adopt the CVC-compatible value of $g_V = 1.0$ for the weak vector coupling.

This expression distinctly highlights the dependence of the shape on the weak-axial coupling g_A . This decoupling reveals that, although all spectral shapes are influenced by g_A , not all necessarily exhibit a strong dependency.

The uncertainty in the exact value of the effective weak-axial coupling constant g_A^{eff} presents a significant challenge. While the value for a free neutron decay is well-established at 1.27, in more complex systems, this value tends to be quenched, a phenomenon that is also demonstrated in the current work.

Numerous studies underscore the necessity of determining a reliable value for g_A^{eff} [23, 24] and thus the novel Spectrum Shape Method (SSM) has emerged as a potent tool for accurately determining the value of the weak-axial coupling. Recent efforts in this direction include the works of Bodenstern-Dresler *et al.* [25], Kostensalo *et al.* [26], and Leder *et al.* [27]. These studies not only highlight the significance of g_A^{eff} but also pave the way for a more nuanced understanding of weak interactions in complex nuclear systems.

The spectral shapes are significantly influenced by the Nuclear Matrix Elements. Among these, the small relativistic Nuclear Matrix Element (sNME) is particularly of importance. Accurately predicting the sNME value using the NSM poses a challenge, as the sNME accumulates contributions from outside the major shells at the Fermi surfaces thus the NSM fails to adequately account for these contributions.

Notably, the value of the sNME is not arbitrary either. Under the principle of the Conserved Vector Current (CVC), as proposed in Behrens and Bühring's hypothesis [22], the sNME is linked to the large vector NME (l-NME). This connection allows for an estimation of the sNME using the following relation:

$${}^V\mathcal{M}_{KK-11}^{(0)} = \left(\frac{(-M_n c^2 + M_p c^2 + W_0) \cdot R}{\hbar c} + \frac{6}{5} \alpha Z \right) \times {}^V\mathcal{M}_{KK0}^{(0)}, \quad (17)$$

where ${}^V\mathcal{M}_{KK-11}^{(0)}$ represents the sNME, and ${}^V\mathcal{M}_{KK0}^{(0)}$ the l-NME. In this equation, K denotes the order of forbiddenness. The terms M_n and M_p are the masses of the neutron and proton, respectively, while W_0 is the decay's endpoint energy. \hbar is the reduced Planck constant, α the fine-structure constant, and c the speed of light. The atomic number of the daughter nucleus is denoted by Z , and the nuclear radius, given as $R = 1.2A^{1/3}$ fm [11] (where A is the nuclear mass number).

The computation of the l-NME can be performed with a higher degree of reliability using the NSM. This is primarily because the main contributions to the l-NME originate from the major shell or shells where the nucleon Fermi surfaces are situated. These regions are well within the analytical reach of the NSM, facilitating accurate calculations.

Furthermore, it is important to note that the sNME has a significant influence on the shape factor, in the vector components of the shape factor. This influence is manifest in both vector terms in Equation 16.

The intricate dependencies of beta decay shapes and half-lives on various uncertain factors underline the critical need for continued research in this domain. A key focus of such research is the effective weak axial coupling constant, g_A^{eff} . Its precise determination is crucial, given its significant influence on β and double- β decay processes.

Additionally, the dependence of the spectral shape on the sNME is a subject of keen interest. The difficulty in precisely estimate sNME further justifies the need for thorough research. These factors collectively pave the way for the work presented in this dissertation, underscoring its significance in advancing our understanding of nuclear beta decay processes.

3 ARTICLE ANALYSES AND DISCUSSIONS

This chapter is dedicated to presenting our contributions in the field, building upon the theoretical framework outlined in the preceding chapter. The discussions here not only delve into our findings but also explore the prospective future developments in these areas.

We commence this chapter in Section 3.1 by addressing the reactor antineutrino anomaly. This section presents our approach to tackling this issue, as done in our work [I] where we apply the novel approach of a full-blown β -decay analysis to this problem. The focus then shifts to the central theme of our research – the weak-axial coupling and the effects of small relativistic nuclear matrix elements (sNMEs) on the beta decay shapes of forbidden non-unique transitions. This discussion is outlined in Sections 3.2, 3.3 and 3.4, where we highlight our contributions through the studies presented in [II, III, IV]. These findings are not only crucial for beyond the standard model experiments but also provide deeper insights into the intricacies of beta decays.

Finally, Section 3.5 discusses how advancements in our understanding of beta decays can significantly impact research on neutrino topics. This section includes our work on low-Q value nuclides, particularly focusing on the studies conducted in [V, VI]. Each of these sections collectively demonstrates the depth of our research endeavors and their implications in the wider context of nuclear and particle physics.

3.1 The Antineutrino Anomaly

Studies in neutrino oscillations within the three-flavour mixing framework have unveiled notable anomalies, particularly regarding the postulated existence of a sterile neutrino flavour, which ostensibly does not interact with conventional matter. This anomaly primarily stems from discrepancies observed between the antineutrino fluxes reported in reactor antineutrino experiments such as RENO [28], Double Chooz [29], and Daya Bay [30], and those predicted by the Huber-Muller (HM) conversion model [31, 32], which is based on data from the 1980s. These discrepancies are twofold: a noticeable reduction in the experimentally observed flux compared to the

model predictions, and the emergence of an unexpected spectral peak in the 4-7 MeV antineutrino energy range. The former has been termed the Reactor Antineutrino Anomaly (RAA), while the latter is often referred to as the 'spectral shoulder' or the 'bump'. Although sterile neutrinos have been hypothesized to account for the flux variations, the 'bump' remains an aspect yet to be fully elucidated.

Another method employed to address this issue is the summation method (SM), which bases its approach on nuclear fission yield data and β -spectral shapes. This methodology, initially introduced by [33], has been subsequently refined and expanded upon in various studies [34–37]. The SM, however, is fraught with complexities, including a heavy reliance on existing experimental data for fission yields, the influence of the *Pandemonium Effect*, and the necessity for accurate β -spectral shapes, as discussed in Chapter 2.

The *Pandemonium Effect* can be effectively mitigated using coincidence techniques like Total Absorption Gamma Spectroscopy (TAGs). TAGs method is particularly effective in adding data points only when a β and a γ -emission occur (almost) simultaneously, or exclusively in the case of a β emission, indicative of a ground-state transition. This has catalyzed a series of experimental endeavours employing the TAGs method, notable examples include studies by [9, 10]. These experiments have been instrumental in providing more accurate β -decay branching ratios, which are essential for the robustness of summation methods.

To address the challenges associated with reliance on β -spectral shapes, particularly in the context of forbidden unique and non-unique decay approximations, Kostensalo et al. [38] conducted an insightful analysis using 36 critical individual decays pertinent to the Reactor Antineutrino Anomaly (RAA) phenomenon. Their study notably contributed to partially addressing the intricacies of the spectral shoulder or 'bump'. This research served as a catalyst for further exploration in this domain. Consequently, we embarked on an advanced study focusing on one of the most significant isotopes implicated in the RAA, ^{92}Rb . Our approach entailed a comprehensive computational analysis of all transitions in the high-Q decay from ^{92}Rb to ^{92}Sr . Despite the inherent complexities of this task, the outcomes, as demonstrated in our work [I], have been rewarding, offering new insights into the nuances of this phenomenon.

3.1.1 NSM Computation

In pursuit of beta spectral shapes, we adhered to the methodologies delineated in Chapter 2. The initial step involved computing the level schemes for both ^{92}Rb and ^{92}Sr , utilizing the *NuShellX@MSU* software. For these computations, we selected two interactions, *glepn* and *glekpn* [19], both of which are suited for the study's region. The associated model spaces for these interactions are detailed in Table 3.

To optimize the computational process, we implemented truncations in the orbital configurations. Specifically, in the case of the *glekpn* interaction, the proton orbital $\pi 1f7/2$ and the neutron orbital $\nu 1g9/2$ were treated as closed shells, populated with their maximum nucleon capacities (8 and 10, respectively). This approach was influenced and justified by the shell closures at magic numbers 28 and 50. Similarly,

3.1.2 Weak-axial coupling and charge - TAGs

Upon obtaining the level schemes and wave functions, the next phase involves calculating the One-Body Transition Densities (OBTDs) and the Nuclear Matrix Elements (NMEs) for the relevant decays. These decays encompass allowed, first forbidden unique, and non-unique transitions integral to our comprehensive analysis. The computational process requires operators of ranks 0, 1, and 2. Notably, rank 2 operators, which are pseudotensors, facilitate pure-axial transitions and involve a singular NME, thereby categorizing them as unique. In contrast, ranks 0 and 1, representing pseudoscalar and pseudovector transitions, respectively, are contingent on both axial and vector components. Consequently, they necessitate multiple NMEs and exhibit heightened sensitivity to the wave functions.

A critical aspect of $\Delta J = 0$ transitions is the amplification of the weak-axial component by the weak-axial charge $g_A(\gamma_5)$, attributed to the mesonic enhancement current. This enhancement is particularly salient for our study, given the high experimental branching ratio of 87.5(1.75)% for ground-state to ground-state transitions, as reported in the TAGs data from A. Algora's group. The weak-axial charge is expressed as:

$$g_A(\gamma_5) = \varepsilon_{\text{MEC}} \times g_A, \quad (18)$$

where ε_{MEC} denotes the mesonic enhancement. In their systematic investigation of medium-to-heavy isotopes, Kostensalo et al. [39] established a straightforward relationship for the enhancement values:

$$\varepsilon_{\text{MEC}} = 1.576 + 2.08 \times 10^{-3} A, \quad (19)$$

applicable for an effective g_A^{eff} approximately equal to 0.7. This implies that our computational analysis must consider both g_A^{eff} and ε_{MEC} in pairs to ensure precise and accurate results for the task at hand.

Leveraging the TAGs data from Algora's team, which measured the decay branching ratios for ^{92}Rb 's decay devoid of the Pandemonium Effect, we set these measurements as benchmarks for our computed branching ratios. This approach ensures a higher degree of accuracy and reliability in our results.

To ascertain the most probable values for the weak-axial coupling g_A^{eff} along with the mesonic enhancement factor ε_{MEC} , we developed a script that evaluates various pairs of $[g_A^{\text{eff}}, \varepsilon_{\text{MEC}}]$ to reproduce the experimentally observed branchings for defined clusters of states. These clusters, as outlined in Table II in [I], comprise groups of computed states whose individual branchings are aggregated for comparison with experimental data. The pairs yielding results within a 2.5% relative error margin for the primary ground-state to ground-state branching and within 25% for subsequent clusters were identified as viable 'solutions'. This systematic approach revealed patterns in the solution sets, as illustrated in Figure 3.

Based on this methodology, we selected the pairs of $[g_A^{\text{eff}}, \varepsilon_{\text{MEC}}]$ values [1.106, 1.3] and [1.083, 1.57] for the interactions $glekpn$ and $glepn$, respectively. These pairs were chosen due to their minimal relative errors in replicating the main ground-state branching ratio, thus ensuring the highest fidelity to the experimental data.

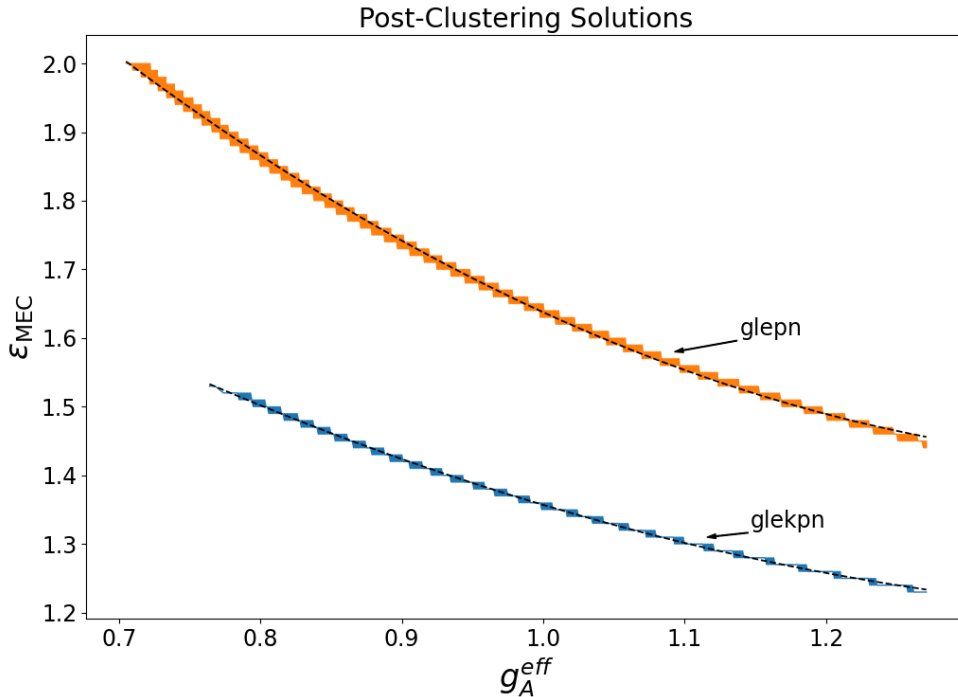


FIGURE 3. Solution pairs obtained through the clustering method, fitting the experimental branching ratios from TAGs data. Arrows indicate the solutions selected for this study.

3.1.3 Full-blown β decay spectra

Having established the weak-axial coupling constants and charges, we were poised to compute the β spectral shapes for all allowed and first forbidden unique and non-unique decays. Given the high- Q nature of this decay, the Q -window encompasses a vast array of transitions. To facilitate a clearer presentation of the spectral decomposition, we employed the clustering method. This approach divides the transitions into three distinct clusters: Cluster 1, consisting solely of the ground state to ground state decay; Cluster 2, encompassing states listed in Table II in [I]; and Cluster 3, which includes all remaining transitions.

Figure 4 presents the results for the interaction $glekpn$, illustrating the progression from partial clusters to the total electron spectrum.

We proceeded to contrast our computed nuclear-structured beta spectrum, which rigorously addresses forbidden decays, with the simplified allowed approximations. This was done using the experimental branching ratios acquired from the TAGs experiments. Such a comparison, illustrated in Figure 5a), with the relative deviation depicted in b), is pivotal in highlighting the significance of accurately treating forbidden decays as opposed to relying on surrogate allowed decays, even with correct decay branchings.

The deviation, especially apparent at lower electron energies (corresponding to higher antineutrino energies), underscores a significant discrepancy. Considering that the cross-section for antineutrino detection in telescopes is proportional to the

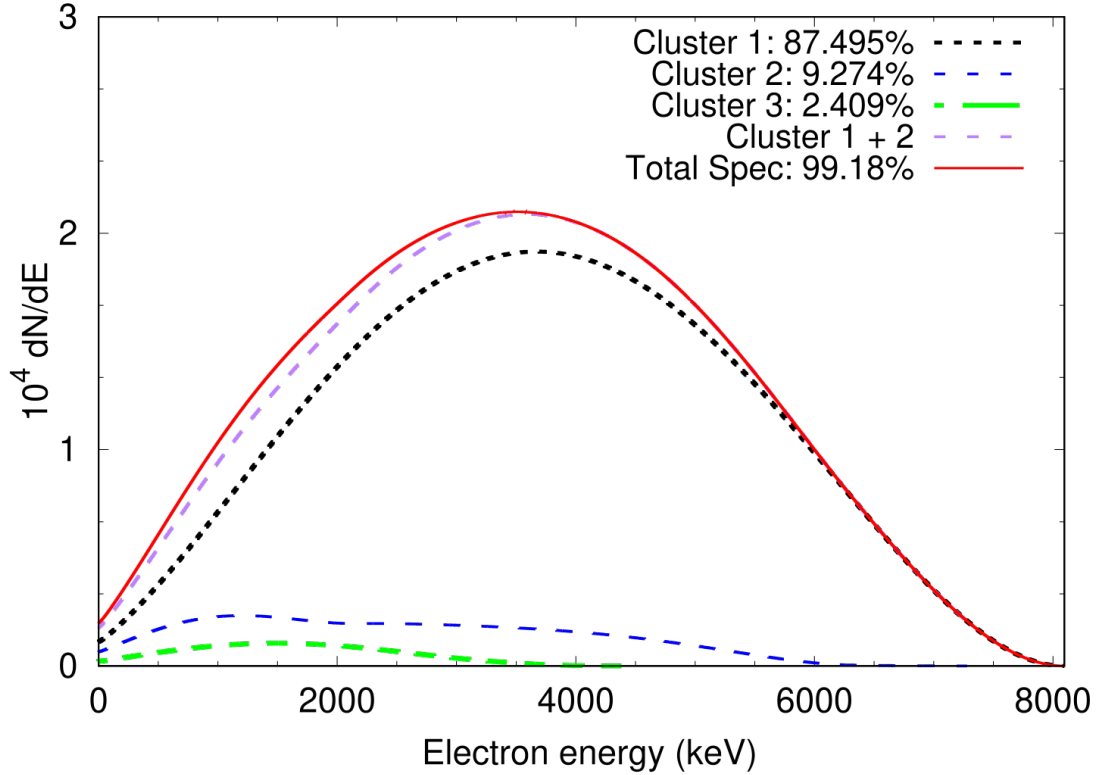


FIGURE 4. Total β -electron spectra for the decay of ^{92}Rb computed using the *glekpn* interaction. The figure demonstrates the build-up from individual clusters to the total spectrum. Reprinted from [I] with APS copyrights.

antineutrino energy and momentum [40], a reduction in high-energy antineutrinos implies a consequent decrease in flux detection at these energies.

The expected impact on the Inverse Beta Decay (IBD) detection in antineutrino telescopes is estimated to range from a 2.6 to 4.6% drop, relative to the allowed approximation for the TAS spectrum. In the context of ^{92}Rb , given its known fission yield of 4.8%, this translates to an estimated reduction of 0.13 to 0.22% in the overall antineutrino reactor anomaly.

3.1.4 Conclusion and outlook

This investigation, while centered on a single isotope within the extensive array implicated in the Reactor Antineutrino Anomaly (RAA), provides critical insight. It underscores that substituting an allowed transition for a forbidden one, even when experimental branching ratios are accurately determined and free from the Pandemonium effect, is insufficient for a comprehensive resolution of the anomaly. Accurate nuclear-structured computations, despite their complexity and computationally-intensive nature, are indispensable for addressing this challenge.

A significant portion of our work was dedicated to the determination of the weak-axial coupling constant $g_{\text{A}}^{\text{eff}}$ and its enhancement. Although our methodology is substantiated by experimental data, it highlights the urgent need for additional experiments focused on ascertaining the $g_{\text{A}}^{\text{eff}}$ value specifically for this mass region.

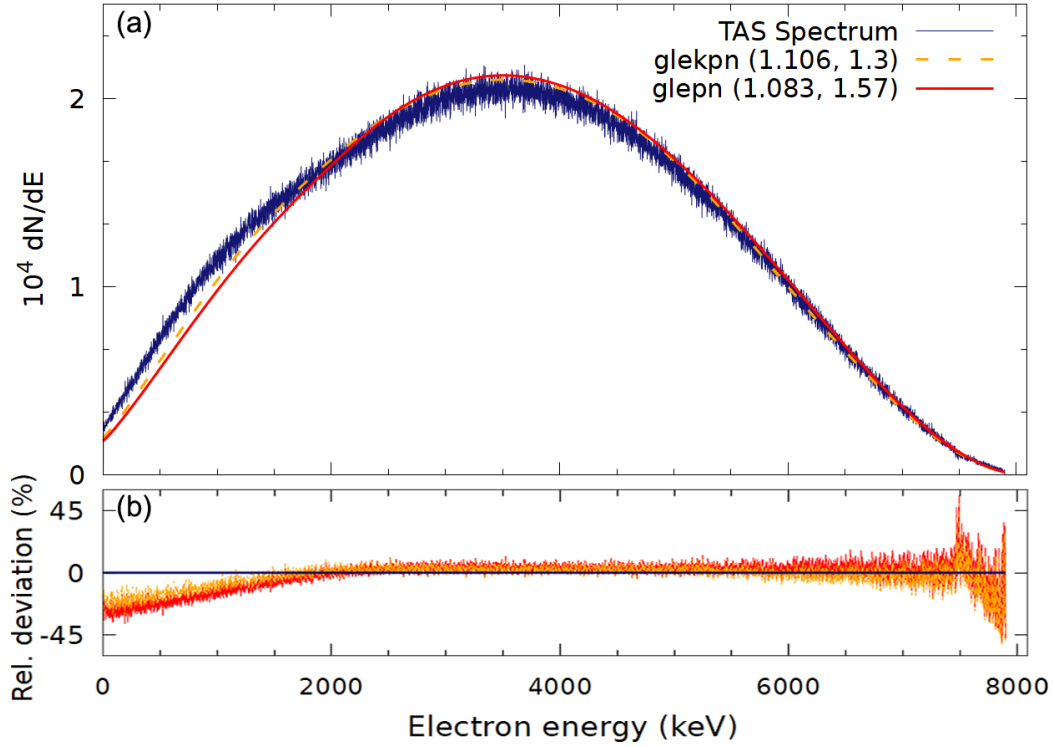


FIGURE 5. Comparative analysis of the total β -electron spectra for ^{92}Rb 's decay computed using the *glekpn* interaction, against the allowed approximations. Part a) displays the computed spectra, while part b) shows the relative deviation. Reprinted from [I] with APS copyrights.

The ambiguity of the solution pairs in our study indicates that almost any combination within our pair pool could be valid, emphasizing the need for further experimental clarification.

Since this study's completion in 2022, recent advancements [2], including our own work [III, IV], have revealed the significance of atomic exchange corrections, particularly in the lower electron energy spectrum. These findings will inevitably influence our future beta spectral shape computations and potentially bring new perspectives to RAA research. In 2023, we began incorporating the small Nuclear Matrix Element (sNME) into our beta spectral shape calculations, a development whose impact is explored in the forthcoming Sections 3.2, 3.3, 3.4. This addition represents yet another avenue to deepen our understanding of the RAA.

Looking ahead, there are several isotopes that hold promise for advancing our knowledge in this area, including, but not limited to, ^{90}Rb , ^{94}Y , ^{96}Y , ^{140}Xe , and ^{140}Cs . Continued research on these isotopes is expected to further illuminate the underlying mechanisms of the reactor antineutrino anomaly.

3.2 Computed Spectra for Rn background

In recent years, numerous liquid Xenon experiments [41, 42] have been developed and are operational, focusing on the search for rare events such as dark matter, evidence of neutrino oscillations, and neutrinoless double-beta decays. The challenge in these experiments lies in differentiating the signals of rare events from more common occurrences like gamma emissions or beta decays. Although various methods are employed to segregate these signals from the primary events of interest, certain scenarios necessitate detector calibration to eliminate extraneous phenomena, particularly when physical purification is impractical. This necessity arises in cases where the interference may originate from the detector’s construction materials, isotopic characteristics (e.g., xenon’s double beta decay), or even ambient underground radiation.

One strategy to mitigate or eliminate these unwelcome signals involves calibrating the detector using theoretical input, such as precise gamma emission energies or beta spectral shapes. However, this approach can be challenging when dealing with beta decays that do not fall into the categories of either allowed or first forbidden unique types. The continuous nature of beta spectra further complicates matters, particularly when comprehensive spectral data is not readily available.

However, complexities arise when beta decays are dependent on intricate nuclear structures, as is the case with first forbidden non-unique transitions. For these scenarios, precise calculations of Nuclear Matrix Elements (NMEs) are paramount for accurately computing the beta spectrum, as demonstrated in [43] for a single transition. Oversimplifying these decays by treating them as allowed or first forbidden unique transitions can lead to over-calibration, potentially masking the detection of rare events. In contrast, a comprehensive, full-scale computation of the nuclear structure, which inherently includes the calculation of NMEs, is the most reliable and preferred method.

Presently, beta decay calculations often utilize software like *Geant4* [4], equipped with a radioactive decay module. This module, however, incorporates simplifications that could result in over-calibration due to the absence of a detailed nuclear structure computation, unlike what would be achieved using a Nuclear Shell Model (NSM) or a Proton-Neutron Quasi-Particle Random Phase Approximation (pnQRPA). Therefore, such software might not be ideally suited for tasks demanding precision in nuclear structure analysis.

Earth’s background radiation predominantly stems from four natural decay chains: Thorium, Neptunium, Uranium, and Actinium. These chains, abundant in long-lived isotopes, undergo continuous decay processes, emitting α , β , and γ radiation. The most significant source of uncertainty in these emissions is the β^- decay, characterized by the shared energy distribution between the electron and the antineutrino. These decay chains hold particular importance in underground experiments. Specifically, in liquid Xenon detectors, the most prominent low-energy contributions are from isotopes $^{212-214}\text{Pb-Bi-Po}$, which are decay products of $^{220-222}\text{Rn}$, a noble gas, as elucidated in [43].

Recognizing the significance of this challenge, we embarked on an extensive project to thoroughly analyze the decay chains starting from $^{212-214}\text{Pb}$. This ambitious endeavor involves generating a complete beta decay spectrum for each transition within these chains.

Moreover, our spectral analysis is currently being applied to the PandaX experiment [41], specifically focusing on the decay chain of $^{214}\text{Pb-Bi}$. The preliminary results from this study have shown promising potential in reducing the background radiation in underground experiments. This success has further motivated our comprehensive investigation into the full $^{220-222}\text{Rn}$ beta decay chains, as detailed in our recent work [II].

3.2.1 NSM Computation

The computational analysis was conducted using *NuShellX@MSU*'s interaction, specifically employing the *khpe* Hamiltonian interaction [44]. We then adapted this interaction for use with *KSHELL* by utilizing the provided script for conversion between the two codes. The *khpe* interaction is optimally designed for studying isotopes in the mass region around $A = 208 - 212$, making it well-suited for the isotopes of interest in our study. The model space employed in these computations, with ^{208}Pb as the closed core, is detailed in Table 4. Notably, no truncations were necessary within the specified model space for these calculations.

Model Space	1h9/2	2f7/2	2f5/2	3p3/2	3p1/2	1i13/2	1i11/2	2g9/2	2g7/2	3d5/2	3d3/2	4s1/2	1j15/2
jj67pn	☒	☒	☒	☒	☒	☒	☒	☒	☒	☒	☒	☒	☒

TABLE 4. Model spaces used for the $^{212-214}\text{Pb-Bi-Po}$ decay chain. The model space *jj67pn* is used with the interaction *khpe*. Blue boxes denote proton orbitals, and red for the neutron orbitals.

With the selected computational framework in place, we proceeded to calculate the level schemes for the isotopes $^{212-214}\text{Pb-Bi-Po}$. This step is crucial as it serves as a verification of the robustness and applicability of the chosen Hamiltonian. We compared our computational results with the experimentally available data, which is illustrated in Figure 6 for the daughter isotopes in the decay chain. The comparison revealed a commendable correspondence with the experimental data, bolstering our confidence in the reliability of our approach and encouraging further pursuit of this line of investigation.

3.2.2 Weak-axial coupling and sNMEs

The value for the weak-axial coupling constant, g_A^{eff} , was determined based on a previous study in the same mass region utilizing the same interaction. Following the findings of Haselschwardt et al. [43], we adopted $g_A^{\text{eff}}=0.85$. Given the prominence of $\Delta J = 0$ transitions in the decays of $^{212-214}\text{Pb}$, the mesonic enhancement factor ε_{MEC} plays a crucial role in our study. Consequently, we undertook an analysis to

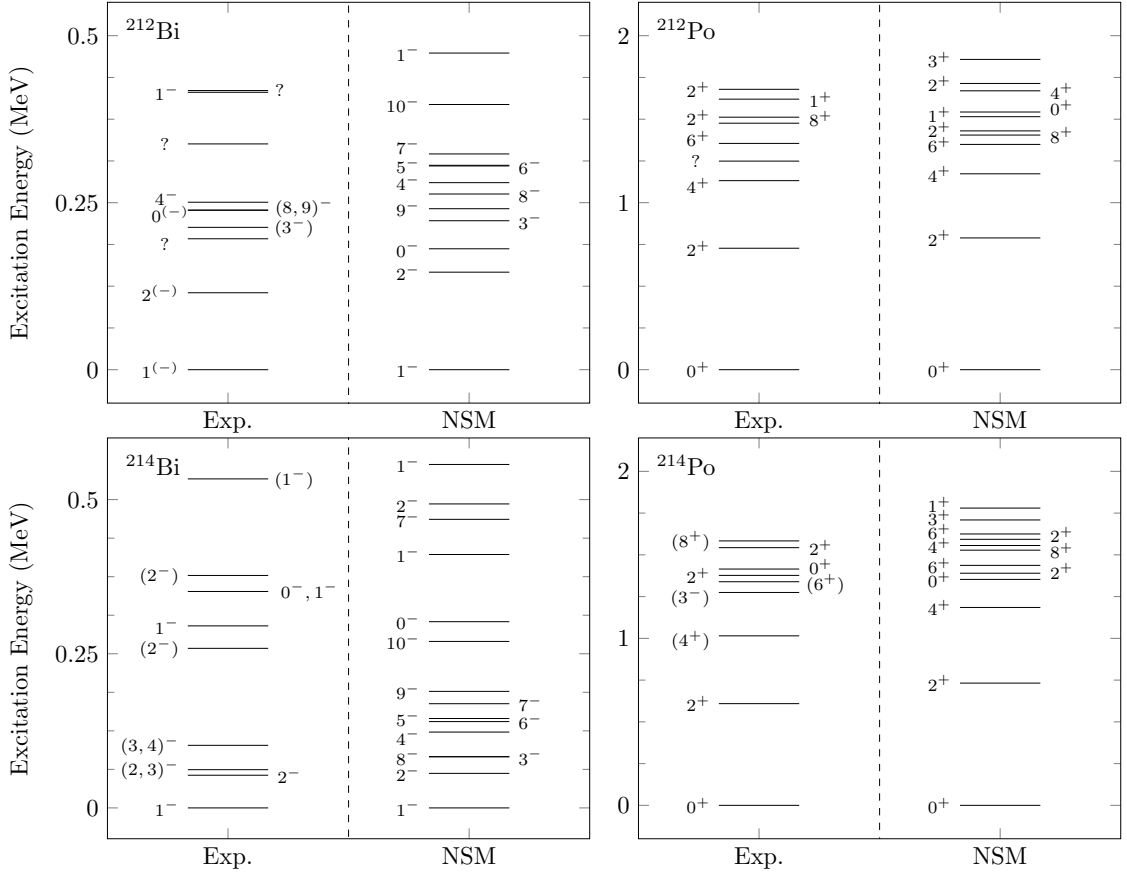


FIGURE 6. Comparative analysis of the level schemes for the β^- -decay daughters ^{212}Bi , ^{214}Bi , ^{212}Po , and ^{214}Po , calculated using the Hamiltonian *khpe*. Parentheses indicate uncertainties in parity and spin-parity assignments. The evaluated data for comparison is sourced from [20]. Reprinted from [II] with APS copyrights.

investigate the dependence of the half-lives on both g_{Λ}^{eff} and ε_{MEC} for these isotopes, leading to the derivation of two distinct curves presented in Figure 1 of [II].

In our analysis, points were deemed solutions if the relative error between the computed and experimentally observed branchings was less than 0.1%. Additionally, we referenced a study by Warburton [45], which explored the same region using a nearly unquenched value of $g_{\Lambda}^{\text{eff}}=1.25$. This approach resulted in a considerably lower value for ε_{MEC} . Both our findings and Warburton's are compared in Figure 1 of [II]. Although there is a general agreement between the two studies, it is important to note that our analysis was specifically focused on the $^{212-214}\text{Pb}$ isotopes, while Warburton's study encompassed a broader range of isotopes within the region, accounting for the minor discrepancies observed between the two analyses.

Having established the weak-axial coupling and charge, we embarked on the subsequent phase of our research: the small Nuclear Matrix Element (sNME) analysis. As elucidated in Chapter 2, while the Nuclear Shell Model (NSM) efficiently handles the large NME (l-NME), it falls short in accurately processing the sNME. To overcome this limitation, we adopted the approach outlined in [12, 26, 46], fitting the sNME value to reproduce the experimentally known partial half-lives for the significant

branchings in the decays under study. It is noteworthy that the sNME, owing to its pseudovector nature, is only relevant in forbidden non-unique decays with non-zero angular momentum couplings. This distinction excludes decays with transitions from $J = 0$ to $J = 0$, thereby separating the determination of the ϵ_{MEC} for the isotopes $^{212-214}\text{Pb}$ from the sNME analysis.

Additionally, the sNME exerts a quadratic influence on the calculation of partial half-lives. Consequently, this often results in either two potential solutions for a given Branching Ratio (BR) or, in some cases, no solutions if the computational output fails to align with the experimental partial half-lives.

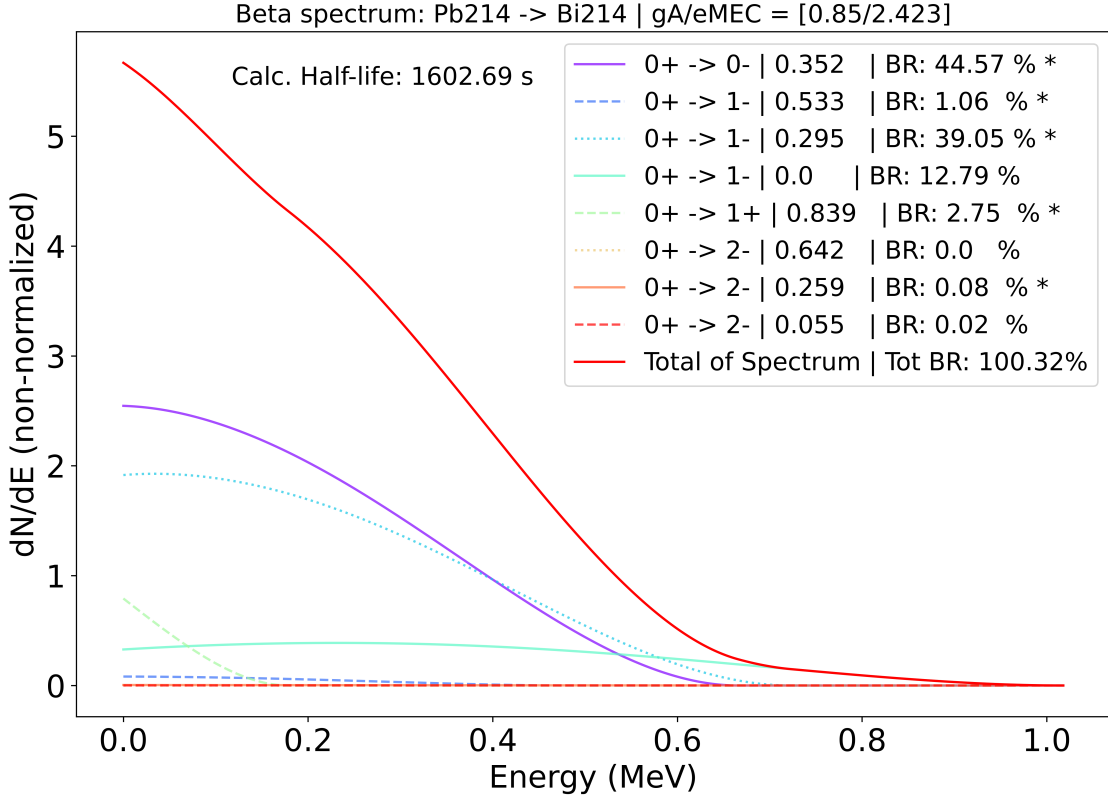


FIGURE 7. Spectral decomposition for the decay of ^{214}Pb , conducted using the Hamiltonian $khpe$ and sNMEs aligned closely with the CVC-predicted values. Asterisks indicate levels matched with the evaluated data from [20].

3.2.3 Beta Spectra and the sNME Dependency

In our computational process, we meticulously addressed each individual transition predicted by the Nuclear Shell Model (NSM) for the decays of isotopes $^{212-214}\text{Pb-Bi-Po}$. A critical step in this approach involved aligning the NSM-predicted level schemes with the energies documented in available experimental data. This adjustment is essential due to the sensitivity of beta decay shapes and half-lives to the endpoint energy.

For each transition within the decay chain, allowed and first forbidden unique

transitions were computed to match the branching ratios as per the evaluations, owing to the well-known nature of their shape factors. However, for the first forbidden non-unique transitions, we utilized the two potential solutions for the sNME to calibrate our computations with the experimental Branching Ratios (BR).

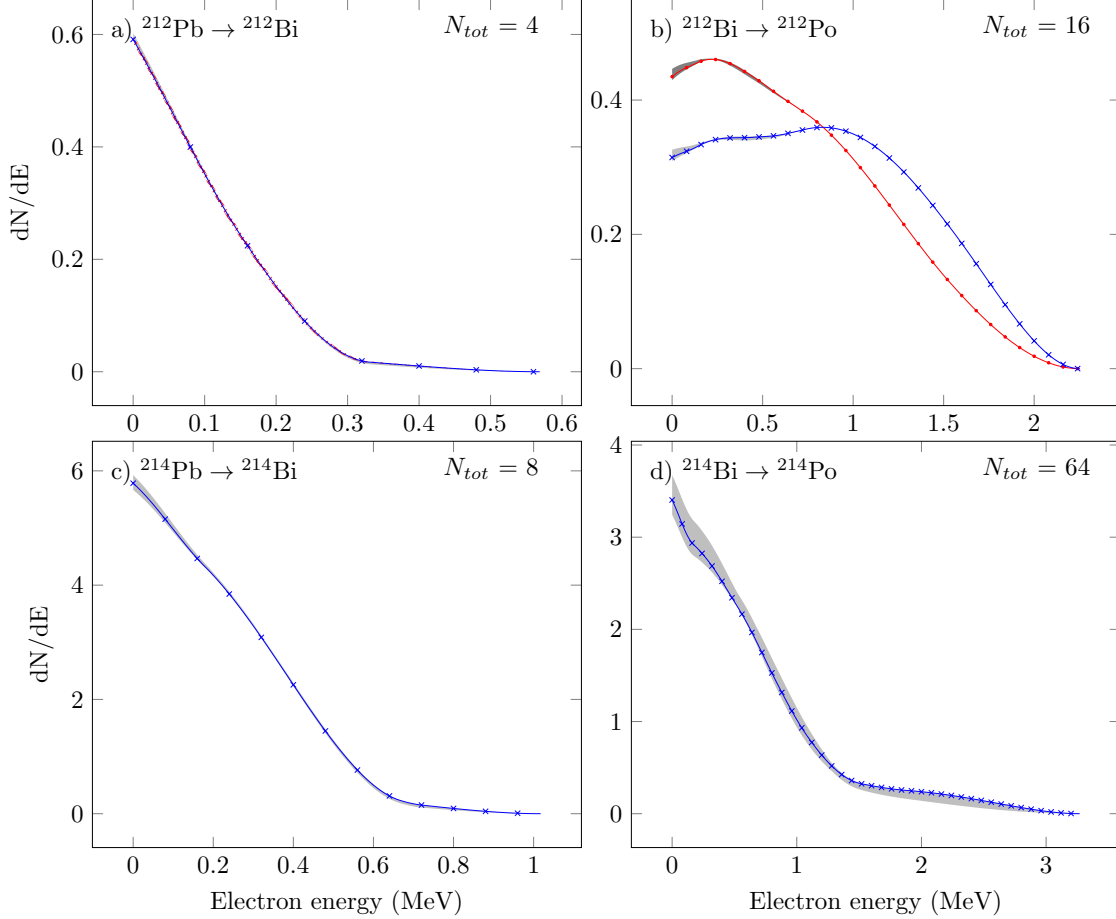


FIGURE 8. Computed total β spectra and their dependencies on the selection of the sNME. The crossed-blue curves represent spectra constructed using the sNME value closer to the Conserved Vector Current (CVC) predicted value for each transition. The gray-hatched regions illustrate the range of curves derived from the total number of transitions (N_{tot}). Reprinted from [II] with APS copyrights. Detailed explanations are provided in the corresponding figure description in the article.

To exemplify our approach, we present the spectral decomposition of the total beta electron shape for the decay of ^{214}Pb , utilizing sNMEs proximate to the CVC-predicted values. This strategy is elaborated upon in Chapter 2, where the CVC-value serves as a reference point. In this context, we have designated the spectral shapes derived from sNMEs closest to the CVC predictions as the 'optimum curve'. The decomposition of this spectrum is depicted in Figure 7.

The inherent multiplicity of sNME solutions implies that each potential final state in a beta decay process can yield two distinct beta electron shapes, both of which align with the experimental partial half-lives. Consequently, for a decay

involving N transitions, we encounter a total of 2^N spectra that are consistent with the experimental partial half-life. This exponential increase in potential spectra adds a layer of complexity to the characterization of the total electron spectra shapes. However, selecting the 'optimal curve' significantly reduces this ambiguity, providing a more definitive depiction of the spectral shape.

In our final analysis, we incorporate the transitions examined in Figure 8. Within this figure, the blue curves represent the 'optimal curve', while the shaded areas encompass the remaining $2^N - 1$ potential spectra.

As previously discussed in Chapter 2, the electron spectra shapes are not only influenced by the small Nuclear Matrix Element (sNME) in terms of half-life but also in their overall form. This study has revealed a marked divergence in the spectral shapes of two specific transitions in panel b) of ^{212}Bi 's decay. These distinct transitions contribute to a bifurcation of the grey-hatched area, underscoring the significant impact of the sNME on spectral shapes. For a more detailed examination of these transitions, refer to Figure 4 in [II].

3.2.4 Conclusion and Outlooks

The critical need for precise nuclear-structured computations was clearly demonstrated in the previous Section 3.1. The same is true for underground experiments seeking to detect rare Beyond the Standard Model (BSM) events, which require accurate beta spectral shape calculations.

The challenge in underground experiments and Xenon detectors, where physical removal of potential 'contaminants' is unfeasible, necessitates reliance on theoretical calculations and additional experimental data. This underscores the significance of our current research.

Our work reveals that the computation of spectral shapes entails numerous subtleties. The complexity of these computations can be mitigated with increased availability of experimental data. The methodology employed for the sNME depends on evaluation data for partial half-lives, endpoint energies, and level schemes, among other factors. Consequently, we advocate for the initiation and execution of new experiments to further this research area.

This study contributes to the evolving understanding of the dependence of shape factors on Nuclear Matrix Elements (NMEs), particularly focusing on the small Nuclear Matrix Element (sNME). The notable influence of the sNME on the overall spectral shapes exemplifies an area of continuous development in the field, as explored in our study [IV] and outlined in Section 3.4. We anticipate that future research will further expand on these insights.

Lastly, it is imperative to revisit these analyses in light of recent advancements in atomic exchange corrections. Additionally, a comprehensive assessment of all background beta radiation from Earth's natural decay chains—Thorium, Neptunium, Uranium, and Actinium—is crucial for the accuracy and reliability of numerous BSM physics experiments globally.

3.3 Technetium-99 spectra as a probe for the weak-axial coupling

In the quest to uncover Beyond the Standard Model (BSM) physics, the detection of neutrinoless double beta decays ($0\nu\beta\beta$) holds the potential to reveal that neutrinos are Majorana particles, a groundbreaking discovery in the realm of BSM phenomena [47]. One of the primary challenges in these experiments is the variability in Nuclear Matrix Elements (NMEs) predictions across different models, the sensitivity of double beta decay to the uncertain effective value of the weak axial coupling constant g_A raised to the fourth power, and the ambiguity surrounding intermediate states in the decay process. A novel method to investigate these intermediate states involves Ordinary Muon Captures (OMCs), as exemplified in the study of ^{136}Ba [48]. This approach aims to enhance our understanding of NMEs and the behavior of the effective g_A in the high momentum exchange region, thereby facilitating more precise half-life predictions for $0\nu\beta\beta$ decay candidates.

Another strategy to elucidate this matter involves deepening our knowledge of the effective weak axial coupling constant g_A^{eff} , particularly in isotopes like ^{100}Mo and ^{96}Zr , which are prime candidates for $0\nu\beta\beta$ decay. Our research contributes to this effort by examining the beta decay of $^{99}\text{Tc}(9/2^+) \rightarrow ^{99}\text{Ru}(5/2^+)$ using our Nuclear Shell Model (NSM) framework.

This specific transition, being a second forbidden non-unique beta decay, is replete with NMEs, making its precise computational analysis challenging. Our objective is to employ two distinct interactions within the NSM to predict their spectral shapes, thereby determining their sensitivity to the value of g_A^{eff} . Unlike previous studies referenced in this context, our focus here is on a single transition, where the values of g_A^{eff} and sNME are the primary variables under investigation.

The major interest of this current work is to check the dependence of the beta spectral shapes on both g_A^{eff} and sNME simultaneously and if such dependence is shown, inspire new Spectral Shape Method (SSM) studies such as [12, 49] and also for fourth-forbidden decays [25, 50, 51].

If results are positive and new experiments are devised to determine which value of g_A^{eff} is feasible for the used interaction(s), one can then try compute with much more reliability, the $0\nu\beta\beta$ half-lives for both ^{100}Mo and ^{96}Zr , using the same Hamiltonian, and the now much more reliable value for the fourth-power dependency of the g_A^{eff} . This information is crucial for determining the necessary material amounts and detector sensitivity required to measure such elusive events in current and future experiments, this inspired us to proceed with our work [III].

The principal aim of this research is to investigate the interdependence of beta spectral shapes on both the effective weak axial coupling constant g_A^{eff} and the small Nuclear Matrix Element (sNME). This exploration is crucial to ascertain whether such dependencies are pronounced enough to warrant further investigations using the Spectral Shape Method (SSM), as seen in previous studies [12, 49] and those focusing on fourth-forbidden decays [25, 50, 51].

Should our results affirmatively indicate a significant dependence, they could potentially catalyze new experimental endeavors aimed at pinpointing the precise

value of g_A^{eff} for the interactions employed. This could facilitate an improved computation of the $0\nu\beta\beta$ decay half-lives for isotopes such as ^{100}Mo and ^{96}Zr using the same Hamiltonian. Crucially, a more reliable determination of the fourth-power dependency of g_A^{eff} is vital for accurately predicting these half-lives. Such knowledge is indispensable in analyzing the requisite quantity of material and sensitivity of detectors needed to detect these elusive events in both current and future experiments. This prospect has been the driving force behind our work [III].

3.3.1 NSM Computation

The computational analyses central to this study were carried out using the *KSHELL* software, leveraging the interactions *jj45pnb* [18] and *glekpn* [19]. These interactions, specifically tailored for the mass region encompassing $A = 94 - 98$, were originally configured for *NuShellX@MSU* and subsequently adapted for *KSHELL* using the conversion script included within the software. This adaptation was crucial to ensure the effective utilization of *KSHELL*'s capabilities in our analysis.

Model Space	2s1/2	1d3/2	1f7/2	2p3/2	1f5/2	2p1/2	1g9/2	1g7/2	2d5/2	2d3/2	3s1/2	1h11/2
JJ45PN	□	□	□	⊠	⊠	⊠	⊠	⊠	⊠	⊠	⊠	⊠
GLEKPN	□	□	⊠	⊠	⊠	⊠	⊠	⊠	⊠	⊠	⊠	□

TABLE 5. Model spaces used for the $^{99}\text{Tc-Ru}$ decay in [III]. Black checked boxes denote both proton and neutron orbitals at play; blue, denote only proton orbitals and red, only neutron orbitals. The empty boxes before the valence space are part of the closed core, as described in Chapter 2.

The employed model spaces for the interactions *jj45pnb* and *glekpn* are detailed in Table 5, adhering to the color-coded format established in preceding tables. A strategic truncation was implemented for the $0f_{5/2}$ orbital in both interactions, allowing for the occupancy of 4 to 6 nucleons. Additionally, inspired by the magic numbers, we maintained a fixed occupancy for the proton orbital $\pi 1f_{7/2}$ and the neutron orbital $\nu 1g_{9/2}$ at 8 and 10 nucleons, respectively, in the *glekpn* interaction. These truncations were essential given the computational complexity posed by the large number of active nucleons in the valence space of the isotope under study. Notably, the advanced parallel computing capabilities of *KSHELL* were indispensable for this analysis, employing 80 nodes with 128 CPU cores each for simultaneous computations.

Upon defining the model spaces and interactions, our focus shifted to calculating the level schemes and Electromagnetic properties such as the Magnetic Dipole (M1) and Electric Quadrupole (E2). This step served as a preliminary assessment of the Hamiltonians' robustness. The resulting level schemes are illustrated in Figure 9, where the *jj45pnb* interaction shows a commendable alignment with the ENDSF evaluation, while *glekpn* demonstrates average performance. Furthermore, a comparison of the calculated electromagnetic properties with experimental values, as

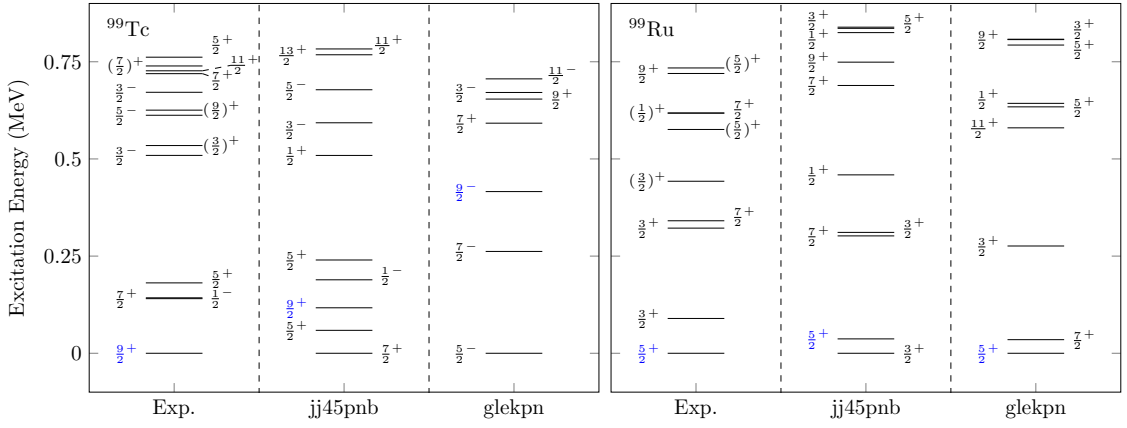


FIGURE 9. Energy level schemes for ^{99}Tc and ^{99}Ru with their corresponding NSM-computed values using the interactions $jj45pnb$ and $glekpn$. Experimental data are taken from the ENSDF [20] evaluation. Levels in blue are the initial and final states relevant for this work. Reprinted from [III] reproduced under the license CC BY 4.0.

presented in Table I of our work [III], revealed remarkable consistency for $jj45pnb$ and satisfactory results for $glekpn$. This methodology of comparing electromagnetic properties has since become a foundational aspect of our Hamiltonian validation process.

In summary, the dual-method approach employed for testing has indicated that the $jj45pnb$ interaction appears more suited for the specific requirements of our current study. However, to ensure a comprehensive analysis, we will continue to examine both $jj45pnb$ and $glekpn$ interactions throughout the entirety of our work. This balanced approach allows for a robust evaluation and ensures that our conclusions are grounded in a thorough comparative analysis of the interactions.

3.3.2 Beta spectral shapes and the weak-axial coupling dependency

Given that our study primarily aims to ascertain plausible values for the effective weak axial coupling constant g_A^{eff} , we advanced to the critical step of determining the small Nuclear Matrix Element (sNME) values that accurately replicate the experimentally known half-life for this specific transition. Mirroring the methodology outlined in the previous Section 3.2, the singular focus on one transition in this instance simplifies our task to identifying only two potential sNME values, corresponding to each considered g_A^{eff} value.

Our pursuit involved methodically exploring a range of g_A^{eff} values, spanning from 0.8 to 1.20, while discerning which values of sNME align with the observed experimental half-life. This systematic process is comprehensively detailed in Table II of our publication [III]. Notably, the Conserved Vector Current (CVC) value remains constant across all g_A^{eff} values but varies between the two interactions due to their differing calculations for the large Nuclear Matrix Element (1-NME). Each combination presented in Table II successfully reproduces the experimental half-life, yet results in distinct beta spectral shapes.

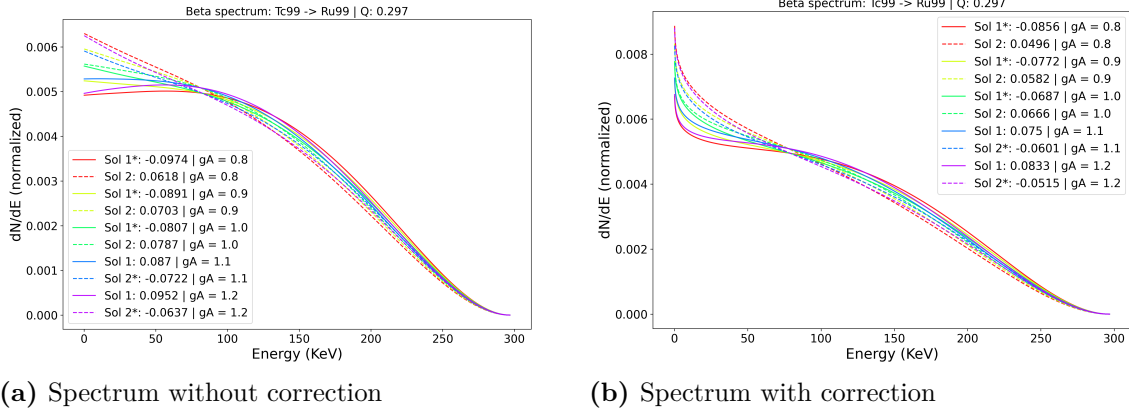


FIGURE 10. Comparative spectra analysis with regards to the enhanced allowed atomic exchange correction with the interaction $jj45pnb$. Sol. 1 and 2 refer to the two sNME solutions. The asterisks denotes the closest sNME to the CVC-value.

In this investigation, we have integrated the latest advancements in the atomic exchange correction for the Fermi function, as elaborated in [2]. Although primarily developed for allowed decays, we deemed its implementation pertinent, given the low endpoint energy of this specific decay, which could significantly influence the results. Figure 10 presents a comparative analysis using the $jj45pnb$ interaction, illustrating the notable differences when the correction is applied versus when it is not.

This atomic exchange correction impacts both the half-life calculations and the spectral shapes, leading to variances in the derived sNME values necessary to replicate the experimental half-life, contingent on the application of the correction. Recent experimental data specific to this isotope, as reported in [52], demonstrate spectral characteristics more closely aligning with the corrected scenario depicted in Figure 10b). This finding reinforces our decision to proceed with incorporating this correction in our analyses. Notably, the correction's effect appears to be particularly significant at lower electron energies, specifically below 50 keV.

Ultimately, our analysis extends to a side-by-side comparison of the beta spectral shapes for both interactions, factoring in the atomic exchange corrections. This comparative visualization is presented in Figure 11.

The results from these computations substantiate the existence of a dependency on the effective weak axial coupling constant g_A^{eff} for both interactions. Particularly notable is the influence of the sNME on the shape of the spectral curves in the case of the $glekpn$ interaction, echoing the findings discussed in Section 3.2. This observation underscores the significance of both the g_A^{eff} value and the sNME in determining the precise shape of the beta spectrum.

3.3.3 Conclusion and outlook

The relevance of this study to the pursuit of phenomena beyond the standard model, particularly in the context of neutrinoless double-beta decay ($0\nu\beta\beta$), is evident. The observed dependency on the effective weak axial coupling constant g_A^{eff} across both interactions underscores the imperative for experimental investigations of this decay.

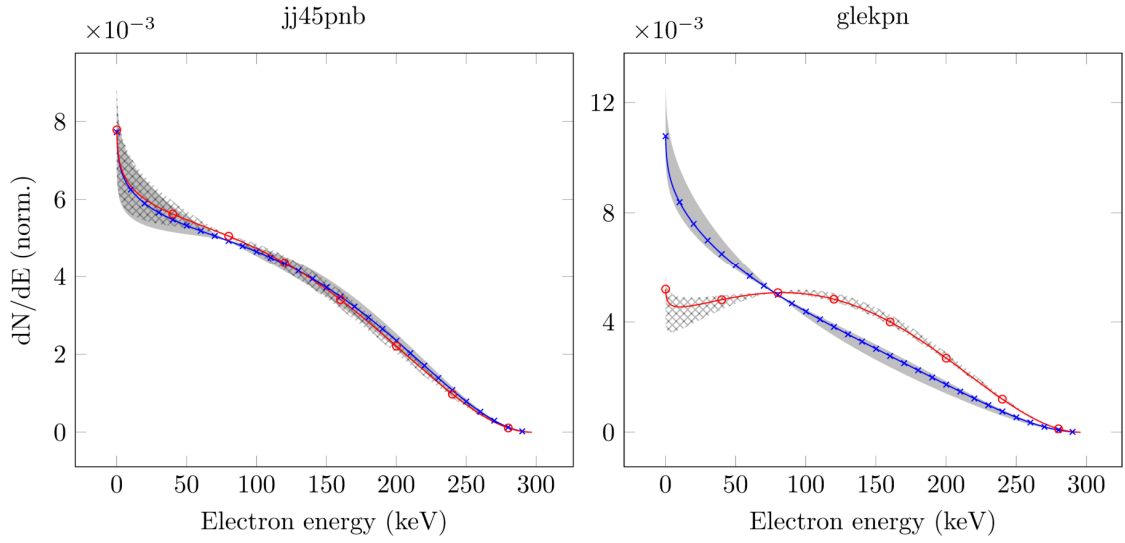


FIGURE 11. Computed β spectral shapes for the decay transition $^{99}\text{Tc}(9/2^+) \rightarrow \text{Ru}(5/2^+)$ utilizing the Hamiltonians $jj45pnb$ (left panel) and $glekpn$ (right panel). The crossed-blue curves represent the sNME values closest to the CVC-predicted value, while the circled-red curves indicate the sNME values farthest from it, assuming $g_A^{\text{eff}} = 1.0$. The gray-hatched (gray-crossed) areas reflect the range of spectral shapes corresponding to g_A^{eff} values from 0.8 to 1.2, with sNME values chosen closest to (farthest from) the CVC values. Figure from [III] reproduced under the license CC BY 4.0.

Such empirical endeavors, potentially employing the Spectral Shape Method (SSM), could ascertain feasible values for the weak-axial coupling. Should experimental outcomes align with theoretical predictions, this would provide robust justification for utilizing these Hamiltonians—or the most accurate among them—with the validated g_A^{eff} values in modeling $0\nu\beta\beta$ decays of isotopes like ^{100}Mo and ^{96}Zr . Given their proximity to the isotope studied in our work, these isotopes stand to benefit immensely from enhanced half-life predictions, thereby enriching the research landscape in this domain.

The inclusion of the allowed atomic exchange correction has emerged as an integral component of our computational methodology, prompting its application in subsequent studies, as will be detailed in Section 3.4. This development naturally raises questions about the potential differences that might arise from employing first-forbidden atomic exchange corrections.

Further investigations encompassing neighboring isotopes of $0\nu\beta\beta$ decay candidates are warranted. Such studies should ideally be paralleled—or indeed, informed—by experimental research aimed at validating or challenging the suitability of the Hamiltonians employed in these complex analyses.

3.4 Beta Shape sensitivity on g_A and sNME

In the preceding sections, we have highlighted the significance of accurate beta spectral shape calculations, especially in light of the Antineutrino Anomaly discussed in Section 3.1. We’ve also looked at the role of these calculations in the detection of rare events as mentioned in Section 3.2, and their potential to inform our understanding of weak-axial coupling in relation to isotopes near those undergoing double-beta decay, which was the focus of Section 3.3.

Building on these insights, the current section seeks to determine whether these spectral shapes depend on the effective weak-axial coupling constant g_A^{eff} and the small Nuclear Matrix Element (sNME) values. Our choice of isotopes is strategic, targeting those (or nearby those) with direct relevance to the Reactor Antineutrino Anomaly (RAA) and neutrinoless double-beta decay ($0\nu\beta\beta$) candidates.

The goal of this integrated approach, which incorporates the application of the allowed atomic exchange correction, is laid out in [IV]. We aim to identify isotopes that could be key to future Spectral Shape Method (SSM) experiments. Such isotopes would be instrumental in refining our predictions for beta spectral shapes in the mass region $A=86 - 99$ and in improving the accuracy of the weak-axial coupling’s quenched value for isotopes in this mass range.

3.4.1 NSM Computation

The computational endeavours underpinning this investigation were conducted via the *KSHELL* platform, which engaged the interactions *jj45pnb* [18] and *glekpn* [19]. These interactions, honed for the mass region under study, were initially formatted

for use with *NuShellX@MSU* and were subsequently converted for compatibility with *KSHELL* utilizing the software’s included scripted tools. Notably, the interaction *glekpn* features a triad of single-particle energy (SPE) sets, enabling us to accommodate the broad spectrum of nuclear masses integral to our research. For a comprehensive exposition of these SPE sets, the reader is referred to our detailed account in [IV], particularly Table I therein.

In alignment with the methodologies delineated in Section 3.3, the model spaces employed remain consistent, as detailed in Table 6. The model space truncations were selectively applied due to the diversity of isotopes encompassed within this study. For all computations utilizing *glekpn*, the valence spaces were modified to incorporate the $\pi 0f_{7/2}$ orbital into the closed core framework. Similarly, the $\nu 0g_{9/2}$ orbital was assimilated as a fixed component of the closed core, honoring the magic number-influenced truncation strategy.

Model Space	2s1/2	1d3/2	1f7/2	2p3/2	1f5/2	2p1/2	1g9/2	1g7/2	2d5/2	2d3/2	3s1/2	1h11/2
JJ45PN	□	□	□	⊗	⊗	⊗	⊗	⊗	⊗	⊗	⊗	⊗
GLEKPN	□	□	⊗	⊗	⊗	⊗	⊗	⊗	⊗	⊗	⊗	□

TABLE 6. Employed model spaces for the mass range $A=86 - 99$ as delineated in [IV]. Black checkmarks represent orbitals active for both protons and neutrons; blue checkmarks signify proton-only orbitals, and red for neutron-only orbitals. Unmarked boxes preceding the valence space constitute the inert core, consistent with the descriptions offered in Chapter 2.

The *jj45pnb* calculations, conversely, mandated distinct truncations due to the M -scheme dimensions, occasionally surpassing 10^{10} : For isotopes with mass $A = 95$, a restriction was imposed on the $\pi 0f_{5/2}$ orbital to host between 4 to 6 protons. For $A = 97$, a dual truncation approach was employed: the $\nu 0h_{11/2}$ orbital was limited to a maximum of 6 neutrons, and the $\pi 0f_{5/2}$ orbital was constrained to accommodate 3 to 6 protons. The remainder of the isotopes analyzed with *jj45pnb* were processed without further truncations.

This series of calculations represented some of the most computationally demanding tasks our team has ever undertaken, often harnessing the full computational power of 200 nodes, each equipped with 128 CPU cores, dedicated to a singular isotope’s analysis. The adoption of *KSHELL*, renowned for its MPI + OpenMP parallelization capabilities, proved to be pivotal in this intensive computational effort.

The level schemes for states of particular interest in the transitions were meticulously constructed and subsequently compared with the available experimental data. This comparative analysis is presented in Table II of [IV]. Therein, we assessed not only the states directly implicated in the beta spectral shape study but also those states with corresponding electromagnetic properties documented in the evaluation data. The consistency of these properties with experimental observations provides a compelling validation of our methodologies, thereby reinforcing the foundation upon which we continue to build our study.

3.4.2 Results and Categories

In the pursuit of refining our understanding of beta spectral shapes, we have studied each of the following transitions:

- $^{86}\text{Br} (1^-) \rightarrow ^{86}\text{Kr} (0^+)$,
- $^{87}\text{Br} (5/2^-) \rightarrow ^{87}\text{Kr} (7/2^+)$,
- $^{87}\text{Kr} (5/2^+) \rightarrow ^{87}\text{Rb} (3/2^-)$,
- $^{93}\text{Y} (1/2^-) \rightarrow ^{93}\text{Zr} (3/2^+)$,
- $^{95}\text{Sr} (1/2^+) \rightarrow ^{95}\text{Y} (3/2^-)$,
- $^{97}\text{Zr} (1/2^+) \rightarrow ^{97}\text{Nb} (3/2^-)$,
- $^{99}\text{Mo} (1/2^+) \rightarrow ^{99}\text{Tc} (3/2^-)$,
- $^{99}\text{Tc} (9/2^+) \rightarrow ^{99}\text{Ru} (5/2^+)$.

In line with the methodologies established in Section 3.3, we explored a range of effective weak-axial coupling values, $g_{\text{A}}^{\text{eff}}$, ranging from 0.8 to 1.20. For each increment within this spectrum, we endeavored to identify the corresponding small Nuclear Matrix Element (sNME) values that align with experimental branching ratios. The Conserved Vector Current (CVC) theorem provided a pivotal reference point, as delineated by Equation 17, allowing us to evaluate the sNMEs for each transition and respective interaction.

Table III in [IV] delineates the options of sNME values extrapolated from our computations across the varied $g_{\text{A}}^{\text{eff}}$ landscape. Analogous to the precedents set in [III], these are the sNME values that enable the accurate reproduction of experimental partial half-lives, although often with the distinct beta spectral shapes engendered by each unique sNME and $g_{\text{A}}^{\text{eff}}$ pairing. This meticulous examination functions as a measure for the beta spectral shape's susceptibility to the nuances of $g_{\text{A}}^{\text{eff}}$ and sNME.

Upon completing the beta spectral shapes computations, we discerned that the transitions could be classified into four distinct categories:

Category I encompasses transitions that exhibit sensitivity to both g_{A} and sNME. This category includes the transitions $^{86}\text{Br}(1^-) \rightarrow ^{86}\text{Kr}(0^+)$, $^{87}\text{Kr}(5/2^+) \rightarrow ^{87}\text{Rb}(3/2^-)$, and $^{93}\text{Y}(1/2^-) \rightarrow ^{93}\text{Zr}(3/2^+)$ for both Hamiltonians; $^{97}\text{Zr}(1/2^+) \rightarrow ^{97}\text{Nb}(3/2^-)$ and $^{99}\text{Mo}(1/2^+) \rightarrow ^{99}\text{Tc}(3/2^-)$ for the Hamiltonian *jj45pnb*; and $^{99}\text{Tc}(9/2^+) \rightarrow ^{99}\text{Ru}(5/2^+)$ for the Hamiltonian *glekpn*.

Category II consists of transitions with a pronounced g_{A} dependency but a minimal sNME influence. These transitions are $^{97}\text{Zr}(1/2^+) \rightarrow ^{97}\text{Nb}(3/2^-)$ and $^{99}\text{Mo}(1/2^+) \rightarrow ^{99}\text{Tc}(3/2^-)$ for the Hamiltonian *glekpn*, and $^{99}\text{Tc}(9/2^+) \rightarrow ^{99}\text{Ru}(5/2^+)$ for the Hamiltonian *jj45pnb*.

Category III is characterized by transitions that show a minor sensitivity to g_{A} but a significant response to the sNME. The sole transition in this category is $^{95}\text{Sr}(1/2^+) \rightarrow ^{95}\text{Y}(3/2^-)$.

Category IV comprises transitions with negligible sensitivity to both g_{A} and sNME. Within this category falls the transition $^{87}\text{Br}(5/2^-) \rightarrow ^{87}\text{Kr}(7/2^+)$.

For illustrative purposes, Figure 12 presents a single transition from each category, thereby encapsulating the essence of the above classifications.

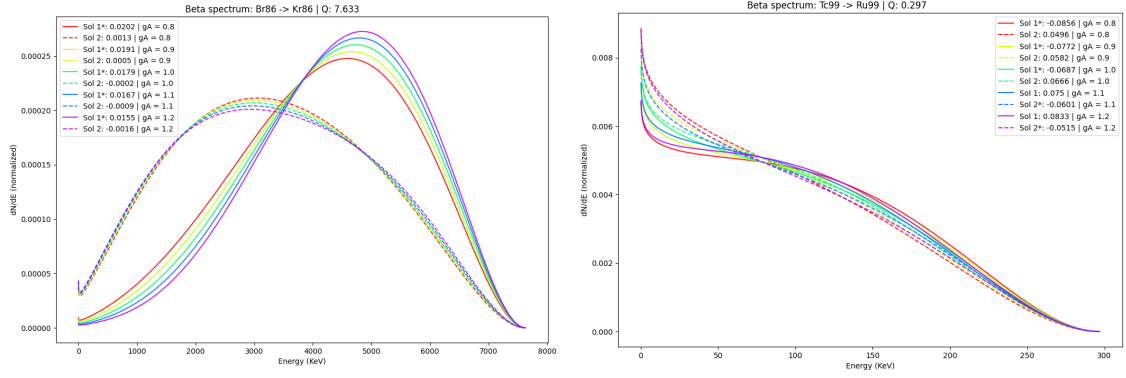
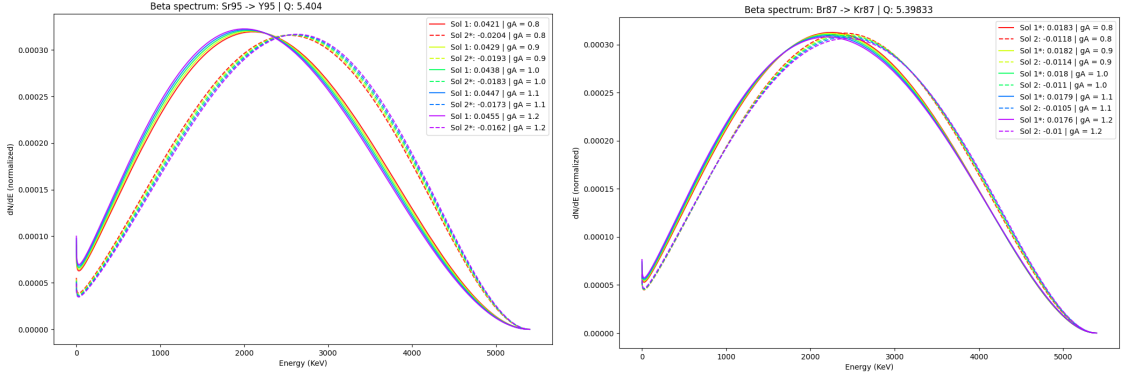
(a) Category I: $^{86}\text{Br}(1^-) \rightarrow ^{86}\text{Kr}(0^+)$ (b) Category II: $^{99}\text{Tc}(9/2^+) \rightarrow ^{99}\text{Ru}(5/2^+)$ (c) Category III: $^{95}\text{Sr}(1/2^+) \rightarrow ^{95}\text{Y}(3/2^-)$ (d) Category IV: $^{87}\text{Br}(5/2^-) \rightarrow ^{87}\text{Kr}(7/2^+)$

FIGURE 12. Examples for computed β spectral shapes for the analyses mentioned in the text for each category using the interaction $jj45pnb$. Sol. 1 and 2 denote the two possible solutions for the sNME for a given g_A^{eff} within the range of 0.8 to 1.2. The asterisk denote the option closest to the CVC-computed value. Lines are distinguished by their solutions with a solid line or dashed line

3.4.3 Conclusion and outlook

The findings underscored in our investigations emphasize the crucial role of rigorous nuclear structure computations in generating beta spectra for addressing both the Reactor Antineutrino Anomaly (RAA) and research into rare event experiments (REE). The methodology we have adopted in this work is pivotal, as it contributes to the production of trustworthy computational results, which in turn, bolsters the reliability of the Hamiltonians applied to these phenomena.

Particularly in the context of calculating half-lives for neutrinoless double-beta decay ($0\nu\beta\beta$) candidates, a detailed examination of the validity of the Hamiltonians and the anticipated values for the weak-axial coupling is indispensable. This is due to the exceedingly elusive nature of such decays if they do occur. Nonetheless, the potential implications of detecting $0\nu\beta\beta$ are profound, with the possibility of significantly advancing our comprehension of the Standard Model. Hence, the justification for our rigorous approach is clear, underscoring the necessity for expanded research into other isotopes neighboring those that are candidates for $0\nu\beta\beta$ decay.

Our computational analyses have identified several instances where the beta spectral shape is influenced by either or both the weak-axial coupling (g_A^{eff}) and the small nuclear matrix elements (sNMEs). Each category identified through our research has specific implications for various areas of study.

Category I exemplifies the critical nature of beta decay studies. The sensitivity of these transitions to both g_A^{eff} and sNMEs highlights the need for more detailed experimental investigations to determine these parameters accurately.

Category II presents ideal candidates for applying the Spectral Shape Method (SSM) since the impact of sNMEs on the spectral shape can be considered negligible whilst allowing for precise half-life predictions using sNME fitting without the concern of shape alteration. Further enhancing our understanding of the correct value for the quenching in the region.

Category III is instrumental in deciding which sNME solution to adopt, particularly in scenarios where experimental measurement of the beta spectra is not feasible, such as in the case of rapidly decaying fission by-products. This category provides the confidence to select sNME values closest to or farthest from the Conserved Vector Current (CVC) value when predicting beta spectra.

Finally, Category IV acts as a benchmark for testing the robustness of Hamiltonians. Since these transitions show little sensitivity to variations in g_A^{eff} and sNME, they can be used to validate the accuracy of Hamiltonian predictions against experimental shapes, thereby eliminating doubts about whether discrepancies arise from incorrect values of g_A^{eff} or sNME.

As we look to the horizon of nuclear physics research, a possible strategic approach emerges for enhancing the reliability of theoretical models used to describe beta decay processes. This strategy involves a sequential analysis of transitions within neighboring isotopes, each characterized by the forbiddenness for the decay but varying in their sensitivity to the weak-axial coupling (g_A^{eff}) and small nuclear matrix elements (sNMEs).

The first step in this comprehensive research plan is to focus on Category IV transitions. These serve as a litmus test for the suitability of a given Hamiltonian. Should the Hamiltonian accurately predict experimental shapes, it could then be deemed reliable for further studies.

Next, attention shifts to Category III isotopes to ascertain whether the sNME aligns closer to or further from the Conserved Vector Current (CVC) value. This determination builds upon the confirmed Hamiltonian, setting the stage for more precise spectral shape predictions.

The third phase exploits Category II transitions to refine the value of g_A^{eff} . By minimizing the impact of sNME variability, this step aims to pinpoint g_A^{eff} with greater accuracy for the mass region.

Finally, with a validated Hamiltonian, a well-defined sNME, and a precisely determined g_A^{eff} , one can tackle Category I isotopes with newfound confidence. This methodical process improves reliability in the prediction of beta spectral shapes for these isotopes, including for application on the half-life of a potential $0\nu\beta\beta$ decay candidate, should the analysis be neighboring one candidate.

3.5 Neutrino Studies via Beta Decays

In yet another directive for beta decays applied for Beyond the Standard Model (BSM) physics, the determination of (anti)neutrino's mass is of great importance. Following the discovery of oscillative three-flavored neutrinos, it is established that the three flavors have different masses. However, only their mass differences are known, necessitating experimental determination of at least one of the masses. Stellar observations combined with cosmological models provide an upper limit on the sum of the neutrino masses, currently estimated to be around $\sim 0.12 \text{ eV}/c^2$ [53].

Several methods have been proposed to pinpoint the neutrino mass, notably involving nuclear β and double- β decays [54, 55]. The β -decay methods are grounded in nuclear decay kinematics, where the neutrino mass is deduced from precise measurements of spectral shape distortion near the endpoint of the emitted electrons in the decay. Given that only a small fraction of β -decay events occur near this endpoint, it is advantageous to study decays with as low a Q value as possible [56]. The lower the Q value, the greater the fraction of events occurring near the endpoint.

Among the notable experiments in this area is the KATRIN experiment, which utilizes tritium (^3H) and has a ground-state-to-ground-state Q value of 18.6 keV [57]. Additionally, ^{187}Re presents an even smaller Q value of about 2.5 keV [58], making it a compelling subject for such studies.

The nucleus of ^{163}Ho boasts the lowest known ground-state-to-ground-state electron-capture Q value, approximately 2.8 keV [59, 60]. In contrast, the rhenium experiment focuses on the β transition $^{187}\text{Re}(5/2^+) \rightarrow ^{187}\text{Os}(1/2^-)$, a first-forbidden unique decay. This decay possesses the lowest known ground-state-to-ground-state β -decay Q value of $2.492(30)_{\text{stat}}(15)_{\text{sys}}$ keV [58, 61]. The Q value of the rhenium decay is nearly an order of magnitude smaller than that of the tritium decay. Despite their very low Q values, these decay cases still confront the challenge that only a tiny fraction of decays occur close to the endpoint. Moreover, understanding the spectrum shape near the endpoint is crucial. To detect a distortion indicative of the mass of a (anti)neutrino, a significant amount of events is required, coupled with excellent background suppression and a thorough understanding of detector systematics.

Recently, decays from ground state to excited state (gs-to-es) have also been recognized as a viable method for addressing the (anti)neutrino mass issue. These decays' endpoint energy can range between negative and positive values, considering the experimental uncertainty. This uncertainty led the team of scientists at JYFL [62] to remeasure many ground-state to ground-state decay cases where precision was critical, thereby enhancing the accuracy of these energy uncertainties and discovering new candidates for the study in the process. Such research endeavors are feasible owing to the high precision afforded by Penning-Trap measurements. An additional nuance of gs-to-es experiments involves gating the electrons emitted in the beta decay by detecting the known gamma radiation for the excited state of interest.

In our collaborative efforts, as detailed in [V, VI], we have focused on the pivotal role of spectral studies in the context of neutrino mass determination. This

section aims to highlight the significance of our progress in spectral studies for ongoing and future investigations in this domain.

Our research encompasses the analysis of two notable neutrino-mass study candidates: the allowed β^- -decay of ^{131}I ($7/2^+$) transitioning to ^{131}Xe ($9/2^+$), and the first-forbidden unique transition of $^{136}\text{Cs}(5^+)$ to $^{136}\text{Ba}(3^-)$, both being ground-state to excited-state studies.

While various methods have been utilized to ascertain the half-lives of these isotopes, our focus here is specifically on the insights gained through our nuclear shell model computations. These calculations not only enhance our understanding of the nuclear structure involved in these transitions but also contribute significantly to the precision required in neutrino mass measurement studies.

3.5.1 NSM Computation

The computational framework for this study was anchored in the *NuShellX@MSU* software. In light of their proximate mass numbers, we employed the same effective interaction, *sn100pn*, previously used for delineating the characteristics of ^{132}Sn [63]. This interaction, with ^{100}Sn as a closed core, was pivotal in our analysis. The specifics of the model space utilized are outlined in Table 7.

Model Space	1g9/2	2p1/2	1f5/2	1g7/2	2d5/2	2d3/2	3s1/2	1h11/2
jj55pn	□	□	□	⊗	⊗	⊗	⊗	⊗

TABLE 7. Model spaces used for the allowed β^- -decay ^{131}I ($7/2^+$) \rightarrow ^{131}Xe ($9/2^+$) and the first-forbidden unique transition $^{136}\text{Cs}(5^+) \rightarrow ^{136}\text{Ba}(3^-)$. The model space *jj55pn* is used with the interaction *sn100pn*. Symbols follow the previous similar Tables.

Our Nuclear Shell Model (NSM) calculations successfully predicted most of the level energies within a 100 keV margin of the corresponding experimental energies for states below 1 MeV of excitation energy in ^{131}Xe . Notably, the computed excitation energy for the state of interest, $9/2^+$, was 937.0 keV, aligning closely with the experimentally determined energy of 971.22(13) keV. Similarly, for $^{136}\text{Ba}(3^-)$, our calculated energy was 2708 keV, in reasonable agreement with the experimentally documented value of 2532.653(23) keV. This level of precision is particularly commendable for higher energy excited states in NSM computations.

3.5.2 Half-lives and the weak-axial coupling

In our investigations involving the decays of ^{131}I and ^{136}Cs , the half-lives were computed, incorporating various scenarios of the weak-axial coupling, g_A^{eff} . For ^{131}I , we only employed the unquenched value of g_A^{eff} to estimate the swiftest plausible decay scenario. In contrast, for ^{136}Cs , we explored a range of g_A^{eff} values, spanning from 0.8 to 1.2, to derive a more realistic approximation of the half-life.

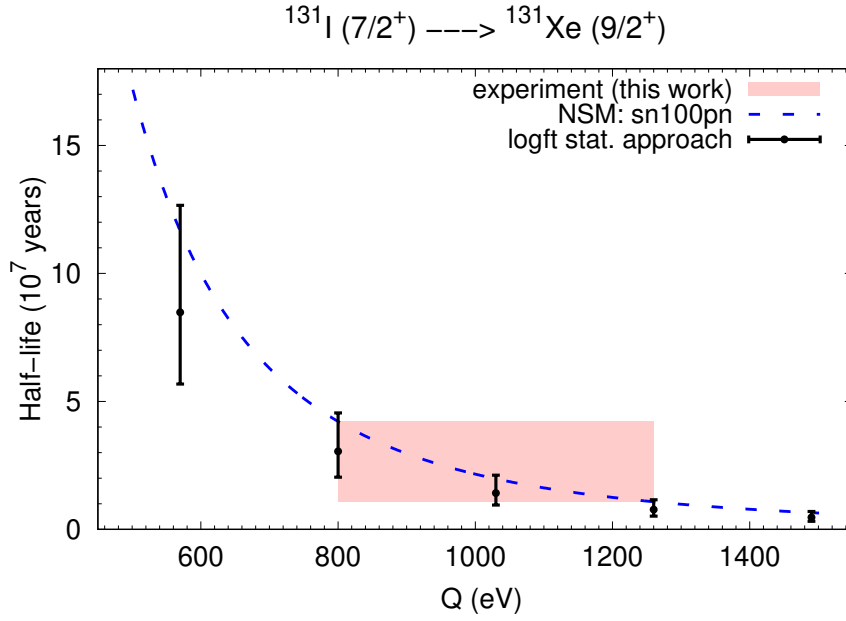


FIGURE 13. Shell-model computed half-life as a function of the Q value in blue and the corresponding predicted half-life range for the decay to the $9/2^+$ state, in the rectangle. The points with uncertainties in black are estimates of the half-life assuming the measured Q value 1.03 keV (central point) up to 2σ errors, based on a $\log ft$ value deduced using the allowed β transitions to the lower three states in ^{131}Xe . Reprinted from [V] with APS copyrights.

It is pertinent to note that these studies did not incorporate all the advanced computational tools we later developed, particularly concerning the atomic exchange correction. Our understanding of the significance of this correction has evolved, and in our more recent publications, we have diligently implemented these advancements to enhance the accuracy of our computational models.

In our comprehensive analyses, the variations in the weak-axial coupling, g_A^{eff} , and the uncertainties in the decay energy played a crucial role in estimating the half-lives of ^{131}I and ^{136}Cs . For the allowed β^- decay of ^{131}I , the half-life was estimated to be in the range of $1.97^{+2.24}_{-0.89} \times 10^7$ years, as illustrated in Figure 13. Similarly, for the first-forbidden unique decay of ^{136}Cs , the half-life was approximated to be $2.1^{+1.6}_{-0.8} \times 10^{12}$ years.

These estimations underscore the impact of variable weak-axial couplings and the significance of precise energy measurements in the realm of nuclear physics, particularly in studies aimed at understanding neutrino properties and their role in the broader context of particle physics.

3.5.3 Conclusion and outlook

The investigations into the β decays of ^{131}I and ^{136}Cs , as detailed in our studies [V, VI], provide valuable insights into the potential for future experiments aimed at determining the mass of (anti)neutrinos. These cases are particularly noteworthy due

to their significantly low Q values of 1.03(23) keV and 4.18(45) keV for the allowed and first forbidden unique decays, respectively, which are markedly less than the 18.6 keV Q value in the KATRIN experiment [57].

A key challenge in these ground-state to excited-state (gs-to-es) decay studies is the extremely low branching ratio compared to standard ground-state to ground-state (gs-to-gs) decays. This necessitates a larger volume of material to ensure sufficient event counts for reliable statistical analysis. Additionally, while uncertainties in spectral shapes may arise in the case of first forbidden unique decays, these concerns are less pronounced than in forbidden non-unique decays. For unique transitions, spectral shapes are better understood and involve a single Nuclear Matrix Element (NME).

To further refine our studies, implementation of atomic exchange corrections is anticipated. Additionally, testing the applied Hamiltonians against known partial half-lives of the isotopes and extending our analysis to neighboring isotopes using the same Hamiltonian would greatly enhance the validity of our results. Ideally, these neighboring isotopes should have experimentally measured branching ratios to affirm and accurately determine the value of the weak-axial coupling g_A^{eff} , for the mass region.

Our collaborative efforts thus demonstrate the extensive applicability of Nuclear Shell Model (NSM) computations in advancing the search for new physics beyond the standard model, highlighting the broad scope and potential of these studies in the field of nuclear and particle physics.

4 SUMMARY

In this dissertation, we have explored the intricate nuances of beta electron spectra, underlining their critical role in various aspects of research for beyond the standard model (BSM) physics, including the Reactor Antineutrino Anomaly (RAA), Rare-Event Experiments (REE), and for theoretical computations of double beta decay. Our focus has been on demonstrating the indispensability of nuclear-structured computations for accurately modeling beta spectral shapes.

For the RAA, we emphasized the complexities involved in full-blown beta spectral composition, particularly for the major contributors to the anomaly. In the context of REE, we established that robust computations of beta spectral shapes are essential for effectively managing background radiation, and we have made significant strides towards this goal. Lastly, in preparation for future experiments aimed at determining the mass of (anti)neutrinos, we highlighted how nuclear shell model computations emerge as a potent tool.

A recurring theme throughout this work is the need for precise computations of beta spectral shapes. This requirement is often linked to the challenges of computing first forbidden non-unique cases due to the multitude of nuclear matrix elements and their sensitivity to the weak-axial coupling and small nuclear matrix elements. Our consistent methodology in computing spectral shapes has strengthened our confidence in the reliability of our future research, as evidenced by the increasing complexity and sophistication of our analyses, culminating in the advanced studies presented in [IV].

The thesis commenced with an investigation into the reactor antineutrino anomaly, scrutinizing the effectiveness of summation methods that approximate complex forbidden non-unique decays. Our findings suggest that precise nuclear-structured NME computation, as opposed to simpler approximations, could potentially explain the spectral shoulder observed in nuclear fission reactors by considering the major contributing isotopes.

Progressing further, we tackled isotopes relevant to rare-event experiments, focusing on background radiation arising from Earth's decay chains. Here, our accurate nuclear-structured beta spectral shapes demonstrated a dependence on small nuclear matrix elements. This led to an investigation of the sNMEs in ^{99}Tc 's

decay, aiming to enhance our understanding of neighboring double beta decaying isotopes ^{100}Mo and ^{96}Zr , and to test our methodologies in predicting beta spectral shapes. The observed dependency on both sNME and weak-axial coupling inspired further exploration into a wider range of isotopes, encompassing those relevant to RAA and neighboring isotopes.

Parallel to this, we applied our methodology to predict the half-lives of candidates for antineutrino mass studies, offering a potentially cost-effective approach to avoid repeating experiments with different isotopes due to the lack of theoretical research.

In conclusion, our work demonstrates that many of the current major research directions in BSM physics can be effectively addressed through nuclear physics approaches similar to those employed in this thesis. This underscores the anticipation of more research in this field, including future works by the author of this thesis.

REFERENCES

- [1] Enrico Fermi, Tentativo di una Teoria Dei Raggi, *Il Nuovo Cimento* 11, 1 (Jan. 1934) 1–19, DOI: 10.1007/bf02959820.
- [2] O Nițescu, S Stoica and F Šimkovic, Exchange correction for allowed β decay, *Phys. Rev. C* 107, 2 (Feb. 2023) 025501, DOI: 10.1103/PhysRevC.107.025501.
- [3] X Mougeot, Reliability of usual assumptions in the calculation of β and ν spectra, *Phys. Rev. C Nucl. Phys.* 91, 5 (May 2015) 055504, DOI: 10.1103/PhysRevC.91.055504.
- [4] S Agostinelli et al., Geant4—a simulation toolkit, *Nucl. Instrum. Methods Phys. Res. A* 506, 3 (July 2003) 250–303, DOI: 10.1016/s0168-9002(03)01368-8.
- [5] Xavier Mougeot, BetaShape: A new code for improved analytical calculations of beta spectra, *EPJ Web Conf.* 146 (Sept. 2017) 12015, DOI: 10.1051/epjconf/201714612015.
- [6] A. A. Aguilar-Arevalo et al., Significant Excess of Electronlike Events in the MiniBooNE Short-Baseline Neutrino Experiment, *Phys. Rev. Lett.* 121, 22 (Sept. 2018) 221801, DOI: 10.1103/PhysRevLett.121.221801.
- [7] G. Mention, M. Fechner, T. Lasserre, T. A. Mueller, D. Lhuillier, M. Cribier and A. Letourneau, Reactor antineutrino anomaly, *Phys. Rev. D* 83, 7 (Jan. 2011) 073006, DOI: 10.1103/PhysRevD.83.073006.
- [8] Johnathon R. Jordan, Yonatan Kahn, Gordan Krnjaic, Matthew Moschella and Joshua Spitz, Severe Constraints on New Physics Explanations of the MiniBooNE Excess, *Phys. Rev. Lett.* 122, 8 (Nov. 2019) 081801, DOI: 10.1103/PhysRevLett.122.081801.
- [9] Muriel Fallot, Status of the prediction of reactor anti-neutrino spectra, *J. Phys. Conf. Ser.* 598 (Apr. 2015) 012003, DOI: 10.1088/1742-6596/598/1/012003.
- [10] G A Alcalá et al., Beta spectrum shape studies for the predictions of the antineutrino spectrum from reactors, *EPJ Web Conf.* 284 (May 2023) 08001, DOI: 10.1051/epjconf/202328408001.
- [11] J. Suhonen, *From Nucleons to Nucleus: Concepts of Microscopic Nuclear Theory*, Springer, Berlin, 2007, DOI: 10.1007/978-3-540-48861-3.
- [12] Anil Kumar, Praveen C Srivastava and Jouni Suhonen, Second-forbidden nonunique β^- decays of $^{59,60}\text{Fe}$ candidates for g_{Λ} sensitive electron spectral-shape measurements, *Eur. Phys. J. A* 57, 7 (July 2021), DOI: 10.1140/epja/s10050-021-00540-6.
- [13] B A Brown and W D M Rae, The shell-model code NuShellX@MSU, *Nucl. Data Sheets* 120 (June 2014) 115–118, DOI: 10.1016/j.nds.2014.07.022.
- [14] Noritaka Shimizu, Takahiro Mizusaki, Yutaka Utsuno and Yusuke Tsunoda, Thick-restart block Lanczos method for large-scale shell-model calculations, *Comput. Phys. Commun.* 244 (Nov. 2019) 372–384, DOI: 10.1016/j.cpc.2019.06.011.

- [15] E. Caurier and F. Nowacki, Present status of shell model techniques, *Acta Physica Polonica B* 30 (Jan. 1999).
- [16] Calvin W Johnson, W Erich Ormand, Kenneth S McElvain and Hongzhang Shan, BIGSTICK: A flexible configuration-interaction shell-model code (Jan. 2018) 1801.08432, DOI: 10.48550/arXiv.1801.08432.
- [17] B Alex Brown and W A Richter, New USD Hamiltonians for the sd shell, *Phys. Rev. C Nucl. Phys.* 74, 3 (Sept. 2006) 034315, DOI: 10.1103/PhysRevC.74.034315.
- [18] A F Lisetskiy, B A Brown, M Horoi and H Grawe, New T=1 effective interactions for the f5/2,p3/2, p1/2, g9/2 model space: Implications for valence-mirror symmetry and seniority isomers, *Phys. Rev. C Nucl. Phys.* 70, 4 (Oct. 2004) 044314, DOI: 10.1103/PhysRevC.70.044314.
- [19] H. Mach, E. K. Warburton, R. L. Gill, R. F. Casten, J. A. Becker, B. A. Brown and J. A. Winger, Meson-exchange enhancement of the first-forbidden $^{96}\text{Y}^g(0^-) \rightarrow ^{96}\text{Zr}^g(0^+)$ β transition: β decay of the low-spin isomer of ^{96}Y , *Phys. Rev. C* 41 (June 1990) 226–242, DOI: 10.1103/PhysRevC.41.226.
- [20] From ENSDF database Available at <http://www.nndc.bnl.gov/ensarchivals/> (Nov. 2023).
- [21] B Alex et al. Brown, Oxbash for Windows PC, *MSU-NSCL report*, 1289 (Jan. 2004).
- [22] H. Behrens and W. Bühring, *Electron Radial Wave Functions and Nuclear Beta Decay*, Clarendon, Oxford, 1982, DOI: 10.1016/0029-5582(63)90290-6.
- [23] M Haaranen, P C Srivastava and J Suhonen, Forbidden non-unique β decays and effective values of weak coupling constants, *Phys. Rev. C.* 93, 3 (Mar. 2016) 034308, DOI: 10.1103/PhysRevC.93.034308.
- [24] M Haaranen, J Kotila and J Suhonen, Spectrum-shape method and the next-to-leading-order terms of the β -decay shape factor, *Phys. Rev. C.* 95, 2 (Feb. 2017) 024327, DOI: 10.1103/PhysRevC.95.024327.
- [25] Lucas Bodenstern-Dresler et al., Quenching of g_A deduced from the β -spectrum shape of ^{113}Cd measured with the COBRA experiment, *Phys. Lett. B* 800 (Jan. 2020) 135092, DOI: 10.1016/j.physletb.2019.135092.
- [26] Joel Kostensalo, Jouni Suhonen, Juliane Volkmer, Stefan Zatschler and Kai Zuber, Confirmation of g_A quenching using the revised spectrum-shape method for the analysis of the ^{113}Cd β -decay as measured with the COBRA demonstrator, *Phys. Lett. B* 822 (Nov. 2021) 136652, DOI: 10.1016/j.physletb.2021.136652.
- [27] A F Leder et al., Determining g_A/g_V with high-resolution spectral measurements using a LiInSe2 bolometer, *Phys. Rev. Lett.* 129, 23 (Dec. 2022) 232502, DOI: 10.1103/PhysRevLett.129.232502.
- [28] J K Ahn et al., Observation of reactor electron antineutrinos disappearance in the RENO experiment, *Phys. Rev. Lett.* 108, 19 (May 2012) 191802, DOI: 10.1103/physrevlett.108.191802.

- [29] Y Abe et al., Improved measurements of the neutrino mixing angle ϑ_{13} with the Double Chooz detector, *J. High Energy Phys.* 2014, 10 (Oct. 2014), DOI: 10.1007/JHEP10%282014%29086.
- [30] F P An et al., Measurement of the reactor antineutrino flux and spectrum at Daya Bay, *Phys. Rev. Lett.* 116, 6 (Feb. 2016) 061801, DOI: 10.1103/PhysRevLett.116.061801.
- [31] P. Huber, Determination of antineutrino spectra from nuclear reactors, *Phys. Rev. C* 84, 2 (June 2011) 024617, DOI: 10.1103/PhysRevC.84.024617.
- [32] Th. A. Mueller et al., Improved predictions of reactor antineutrino spectra, *Phys. Rev. C* 83, 5 (Dec. 2011) 054615, DOI: 10.1103/PhysRevC.83.054615.
- [33] R W King and J F Perkins, Inverse beta decay and the two-component neutrino, *Phys. Rev.* 112, 3 (Nov. 1958) 963–966, DOI: 10.1103/physrev.112.963.
- [34] F T Avignone, S M Blakenship and C W Darden, Theoretical Fission-Antineutrino Spectrum and Cross Section of the Reaction ${}^3\text{He}(\bar{\nu}_e, e^+){}^3\text{H}$, *Phys. Rev.* 170, 4 (June 1968) 931–934, DOI: 10.1103/PhysRev.170.931.
- [35] P Vogel, G K Schenter, F M Mann and R E Schenter, Reactor antineutrino spectra and their application to antineutrino-induced reactions. II, *Phys. Rev. C Nucl. Phys.* 24, 4 (Oct. 1981) 1543–1553, DOI: 10.1103/physrevc.24.1543.
- [36] O Tengblad, K Aleklett, R Von Dincklage, E Lund, G Nyman and G Rudstam, Integral gn-spectra derived from experimental β -spectra of individual fission products, *Nucl. Phys. A* 503, 1 (Oct. 1989) 136–160, DOI: 10.1016/0375-9474(89)90258-3.
- [37] G Rudstam, P I Johansson, O Tengblad, P Aagaard and J Eriksen, Beta and gama spectra of short-lived fission products, *At. Data Nucl. Data Tables* 45, 2 (July 1990) 239–320, DOI: 10.1016/0092-640x(90)90009-9.
- [38] L. Hayen, J. Kostensalo, N. Severijns and J. Suhonen, First-forbidden transitions in reactor antineutrino spectra, *Phys. Rev. C* 99, 3 (Mar. 2019) 031301, DOI: 10.1103/PhysRevC.99.031301.
- [39] J. Kostensalo and J. Suhonen, Mesonic enhancement of the weak axial charge and its effect on the half-lives and spectral shapes of first-forbidden $J^+ \leftrightarrow J^-$ decays, *Physics Letters B* 781 (Apr. 2018) 480–484, DOI: 10.1016/j.physletb.2018.02.053.
- [40] Anna C Hayes and Petr Vogel, Reactor neutrino spectra, *Annu. Rev. Nucl. Part. Sci.* 66, 1 (Oct. 2016) 219–244, DOI: 10.1146/annurev-nucl-102115-044826.
- [41] Chen Cheng et al., Search for light dark matter-electron scattering in the PandaX-II experiment, *Phys. Rev. Lett.* 126, 21 (May 2021) 211803, DOI: 10.1103/physrevlett.126.211803.
- [42] E Aprile et al., Double-weak decays of Xe124 and Xe136 in the XENON1T and XENONnT experiments, *Phys. Rev. C* 106, 2 (Aug. 2022) 024328, DOI: 10.1103/PhysRevC.106.024328.

- [43] S J Haselschwardt, J Kostensalo, X Mougeot and J Suhonen, Improved calculations of β decay backgrounds to new physics in liquid xenon detectors, *Phys. Rev. C* 102, 6 (Dec. 2020) 065501, DOI: 10.1103/PhysRevC.102.065501.
- [44] E K Warburton and B A Brown, Appraisal of the Kuo-Herling shell-model interaction and application to $A=210$ -212 nuclei, *Phys. Rev. C Nucl. Phys.* 43, 2 (Feb. 1991) 602–617, DOI: 10.1103/PhysRevC.43.602.
- [45] E K Warburton, First-forbidden β decay in the lead region and mesonic enhancement of the weak axial current, *Phys. Rev. C Nucl. Phys.* 44, 1 (July 1991) 233–260, DOI: 10.1103/physrevc.44.233.
- [46] Joel Kostensalo, Eligio Lisi, Antonio Marrone and Jouni Suhonen, Cd113 β -decay spectrum and g_A quenching using spectral moments, *Phys. Rev. C* 107, 5 (May 2023) 055502, DOI: 10.1103/PhysRevC.107.055502.
- [47] S. M. Bilenky and C. Giunti, Neutrinoless double-beta decay: A probe of physics beyond the Standard Model, *International Journal of Modern Physics A* 30, 04n05 (Feb. 2015) 1530001, DOI: 10.1142/s0217751x1530001x.
- [48] P. Gimeno et al., Ordinary Muon Capture on ^{136}Ba : Comparative Study Using the Shell Model and pnQRPA, *Universe* 9, 6 (June 2023) 270, DOI: 10.3390/universe9060270.
- [49] Anil Kumar, Praveen C Srivastava, Joel Kostensalo and Jouni Suhonen, Second-forbidden nonunique β - decays of ^{24}Na and ^{36}Cl assessed by the nuclear shell model, *Phys. Rev. C* 101, 6 (June 2020), DOI: 10.1103/PhysRevC.101.064304.
- [50] J. Kostensalo, M. Haaranen and J. Suhonen, Electron spectra in forbidden β decays and the quenching of the weak axial-vector coupling constant g_A , *Phys. Rev. C* 95, 4 (Apr. 2017) 044313, DOI: 10.1103/PhysRevC.95.044313.
- [51] J. Kostensalo and J. Suhonen, g_A -driven shapes of electron spectra of forbidden β decays in the nuclear shell model, *Phys. Rev. C* 96, 2 (Aug. 2017) 024317, DOI: 10.1103/PhysRevC.96.024317.
- [52] Michael Paulsen et al., High precision measurement of the ^{99}Tc β spectrum (Sept. 2023), DOI: 10.48550/arXiv.2309.14014.
- [53] N. Aghanim et al., Planck 2018 results VI. Cosmological parameters, *Astron. Astrophys.* 641 (Sept. 2020) A6, DOI: 10.1051/0004-6361/201833910.
- [54] Frank T. Avignone, Steven R. Elliott and Jonathan Engel, Double beta decay, Majorana neutrinos, and neutrino mass, *Rev. Mod. Phys.* 80, 2 (Apr. 2008) 481, DOI: 10.1103/revmodphys.80.481.
- [55] H. Ejiri, J. Suhonen and K. Zuber, Neutrino-nuclear responses for astro-neutrinos, single beta decays and double beta decays, *Phys. Rep.* 797 (Mar. 2019) 1, DOI: 10.1016/j.physrep.2018.12.001.
- [56] E. Ferri et al., The Status of the MARE Experiment with ^{187}Re and ^{163}Ho Isotopes, *Phys. Procedia* 61 (Mar. 2015) 227–231, DOI: 10.1016/j.phpro.2014.12.037.

- [57] E. G. Myers, A. Wagner, H. Kracke and B. A. Wesson, Atomic Masses of Tritium and Helium-3, *Phys. Rev. Lett.* 114, 1 (Jan. 2015), DOI: 10.1103/physrevlett.114.013003.
- [58] D. A. Nesterenko et al., Direct determination of the atomic mass difference of ^{187}Re and ^{187}Os for neutrino physics and cosmochronology, *Phys. Rev. C* 90, 4 (Oct. 2014) 042501(R), DOI: 10.1103/physrevc.90.042501.
- [59] S. Eliseev et al., Direct Measurement of the Mass Difference of ^{163}Ho ^{163}Dy Solves the Q -Value Puzzle for the Neutrino Mass Determination, *Phys. Rev. Lett.* 115, 6 (Aug. 2015), DOI: 10.1103/physrevlett.115.062501.
- [60] P. C.-O. Ranitzsch et al., Characterization of the ^{163}Ho Electron Capture Spectrum: A Step Towards the Electron Neutrino Mass Determination, *Phys. Rev. Lett.* 119, 12 (Sept. 2017) 122501, DOI: 10.1103/physrevlett.119.122501.
- [61] M. Shamsuzzoha Basunia, Nuclear Data Sheets for $A=193$, *Nucl. Data Sheets* 143 (July 2017) 1–381, DOI: 10.1016/j.nds.2017.08.001.
- [62] J. S. E. Wieslander et al., Smallest Known Q Value of Any Nuclear Decay: The Rare β^- Decay of $^{115}\text{In}(9/2^+) \rightarrow ^{115}\text{Sn}(3/2^+)$, *Phys. Rev. Lett.* 103, 12 (Sept. 2009) 122501, DOI: 10.1103/PhysRevLett.103.122501.
- [63] B. A. Brown, N. J. Stone, J. R. Stone, I. S. Towner and M. Hjorth-Jensen, Magnetic moments of the 2 states around ^{132}Sn , *Physical Review C* 71, 4 (Apr. 2005), DOI: 10.1103/physrevc.71.044317.

ORIGINAL PAPERS

I

ANALYSIS OF THE TOTAL β -ELECTRON SPECTRUM OF ^{92}RB : IMPLICATIONS FOR THE REACTOR FLUX ANOMALIES








by

Ramalho, M and Suhonen, J and Kostensalo, J and Alcalá, G A and Algora, A and
Fallot, M and Porta, A and Zakari-Issoufou, A-A

Phys. Rev. C **106**, **2**, 024315 (2022).

DOI: 10.1103/PhysRevC.106.024315

Reproduced with kind permission of American Physical Society.

Analysis of the total β -electron spectrum of ^{92}Rb : Implications for the reactor flux anomaliesM. Ramalho ^{1,*} J. Suhonen ^{1,†} J. Kostensalo ² G. A. Alcalá ³ A. Algora ^{3,4} M. Fallot ⁵
A. Porta,⁵ and A.-A. Zakari-Issoufou ⁵¹*Department of Physics, University of Jyväskylä, P.O. Box 35, FI-40014, Jyväskylä, Finland*²*Natural Resources Institute Finland, Yliopistokatu 6B, FI-80100 Joensuu, Finland*³*Instituto de Física Corpuscular, CSIC-Universitat de València, E-46071 València, Spain*⁴*Institute for Nuclear Research (Atomki), H-4001 Debrecen, Hungary*⁵*SUBATECH, CNRS/IN2P3, IMT Atlantique, Nantes Université, F-44307 Nantes, France*

(Received 22 March 2022; accepted 1 August 2022; published 16 August 2022)

We present here a microscopic nuclear-structure calculation of a β -electron spectrum including all the β -decay branches of a high Q -value reactor fission product contributing significantly to the reactor antineutrino energy spectrum. We perform large-scale nuclear shell-model calculations of the total electron spectrum for the β^- decay of ^{92}Rb to states in ^{92}Sr using a computer cluster. We exploit the β -branching data of a recent total absorption γ -ray spectroscopy (TAGS) measurement to determine the effective values of the weak axial-vector coupling, g_A , and the weak axial charge, $g_A(\gamma_5)$. By using the TAGS data we avoid the bias stemming from the pandemonium effect which is a systematic error biasing the usual β -decay measurements. We take fully into account all the involved allowed and forbidden β transitions, in particular the first-forbidden nonunique ones which have earlier been shown to be relevant in the context of the reactor-antineutrino flux anomaly and the unexplained spectral shoulder, the “bump,” the former one having been interpreted as one of the strongest evidence for the existence of sterile neutrinos. Here we are able to present quantitative evidence for the relevance of forbidden nonunique β^- decays in a total β spectrum of a fission product, in this case ^{92}Rb , which is one of the major contributors to the total reactor antineutrino spectral shape. We demonstrate that taking the forbidden spectral shapes fully into consideration leads for ^{92}Rb to a 2.6%–4.6% reduction in the expected inverse β -decay rate at the reactor antineutrino telescopes. We also confirm by our calculation of a total β -electron spectrum that the forbidden transitions can contribute to the formation of the spectral bump in the reactor-antineutrino flux profile.

DOI: [10.1103/PhysRevC.106.024315](https://doi.org/10.1103/PhysRevC.106.024315)**I. INTRODUCTION**

Neutrino-oscillation experiments and the subsequent analyses of their outcomes in the three-flavor framework have produced precision data on the mixing angles and magnitudes of the neutrino-mass splittings [1–3]. The three-flavor mixing framework was, however, challenged by the results of the reactor-antineutrino experiments RENO [4], Double Chooz [5], and Daya Bay [6]. When the measured antineutrino flux was compared with the predicted flux calculated using the standard Huber-Mueller (H-M) conversion method [7,8] based on the cumulative β -electron spectra measured by Schreckenbach *et al.* in the 1980s [9–12], two flux anomalies were recorded: a deficit of the measured flux relative to the predicted flux, coined the “reactor flux anomaly,” or the “reactor antineutrino anomaly” (RAA) [13], and an unexpected spectral shoulder or “bump,” an extra increase in the measured number of antineutrinos between 4 and 7 MeV of antineutrino energy. The significance of the RAA reaches up to 2.8σ [14]

and depends on the adopted flux model [15]. The flux deficit has been hypothesized to be due to oscillations to a fourth neutrino flavor which does not interact with ordinary matter and is thus called a sterile neutrino. Sterile neutrinos have also been suggested as a potential solution to the so-called gallium anomaly [16], and such neutrinos are currently under a very active experimental search [17]. Furthermore, no explanation has been found for the spectral-bump anomaly within the H-M model.

An alternative to the H-M model is the summation method where all the individual beta branches are summed to produce the total β -electron spectrum nucleus by nucleus through the plethora of fission products of the reactor fuel. This model, originally proposed by King and Perkins [18] and further elaborated by others [19–22], is the only one able to access the various components of the total antineutrino flux and the related spectral shape. This method relies fully on the available nuclear data on fission yields, combined with the β -decay data on the fission products. The complications associated with the application of this method are the incompleteness of the nuclear data bases, their uncertainties, and systematic errors such as the pandemonium effect [23]. This effect is due to the limited efficiency of germanium detectors. Because γ -rays

*madeoliv@jyu.fi

†jouni.t.suhonen@jyu.fi

from high-energy nuclear levels may not be detected owing to efficiency issues, an underestimation of the β branchings to these states is produced. This, in turn, results in an overestimation of the high-energy part of the antineutrino spectrum in reactors.

The pandemonium effect can be circumvented in two ways: First, experimentally the weak β branches can be detected by total absorption γ -ray spectroscopy (TAGS), thus enabling the prediction of a more reliable antineutrino flux for the nuclear reactors. Hitherto, several TAGS measurement campaigns have led to numerous corrections to nuclear data regarding β -decay branches of relevant isotopes for the RAA [24–29]. Second, the correct β branchings could, in principle, be computed by using a suitable nuclear model, such as the nuclear shell model (NSM) with its several available Hamiltonians applicable to the key nuclei involved in the building of the total antineutrino flux. In this work we combine these two approaches and use the TAGS-measured branching data on the β decay of the 0^- ground state of ^{92}Rb to excited states in ^{92}Sr to guide our NSM calculations. The ^{92}Rb nucleus is one of the major contributors to the total antineutrino spectrum in nuclear reactors and the value of the important branching to the ^{92}Sr ground state has been independently verified by Rasco *et al.* [30]. We also compute the nuclear matrix elements (NMEs) involved in the forbidden nonunique β transitions, thus avoiding the previously used approximations where these transitions had been substituted by unique forbidden β transitions or allowed Gamow-Teller and Fermi transitions which all have universal β -electron spectral shapes. To our knowledge, the present work is the first one to venture a theoretical description of the total β -electron spectrum of a fission product with branchings to a large number of possible final states. Such a study gives important information on the contributions of the first-forbidden β decays to total β -electron spectra and eventually their importance in the reactor-antineutrino and bump anomalies.

The earlier studies such as the H-M model used allowed and forbidden unique β transitions as surrogates for forbidden nonunique β transitions, mostly due to computational difficulties. Doubts about the validity of this procedure were voiced by Hayes *et al.* [31] and Fang *et al.* [32]. In Hayen *et al.* [33,34] it was quantitatively shown by NSM calculations of key individual β transitions that the replacement of the nonunique β transitions by unique and allowed β transitions may lead to serious flaws in the estimations of the reactor antineutrino fluxes. This model, the “HKSS flux model” (coined as such by Berryman *et al.* [15]) has implications for both the RAA [15] and the spectral bump [33,34].

The first reasonable step in a full-blown nuclear-model analysis of the total antineutrino flux from nuclear reactors would be to try to compare the computed individual total β spectra with the TAGS-measured ones nucleus by nucleus. However, the corresponding nuclear-structure calculations face two specific complications: The first is related to the effective quenched value of the weak axial-vector coupling g_A^{eff} , and the second is related to the uncertain value of the weak axial charge $g_A^{\text{eff}}(\gamma_5)$, relevant for the first-forbidden nonunique β transitions without change in the nuclear angular momentum (i.e., the so-called $\Delta J = 0$ transitions). For more

information on the values of these couplings and how they vary from nucleus to nucleus and β transition to β transition, see Refs. [35–39]). The electron spectral shapes have been found to be sometimes very sensitive to the value of g_A^{eff} [38,40–45]. The weak axial charge $g_A^{\text{eff}}(\gamma_5)$, on the other hand, is enhanced by the meson-exchange currents [46–49] and the value of the related enhancement factor, ε_{MEC} , as also its effects on β -electron spectra, has lately been systematically studied by Kostensalo *et al.* [39].

Since both g_A^{eff} and ε_{MEC} possibly influence the β -electron spectra, a reasonable way to fix their values has to be found. In the present work we use the TAGS-measured branchings to groups of final states to determine the values of these two quantities. At the same time we keep an eye on the consistency with the systematics of Ref. [39] for ε_{MEC} . For the vector part, as also for the allowed Fermi transitions, we adopt the conservation of vector current–protected (CVC-protected) value $g_V = 1.0$ for the weak vector coupling.

The present article is organized as follows: First, in Sec. II, the adopted theoretical framework is briefly highlighted including a short introduction to the electron spectral shapes and an account of the involved shell-model calculations. We report and discuss the obtained results in Sec. III and draw conclusions in Sec. IV.

II. THEORETICAL FRAMEWORK

Here we describe briefly the theory framework used in the calculations, both the beta-decay formalism and the shell-model Hamiltonian.

A. Beta spectral shapes

The branching ratio of a transition to a particular final state in ^{92}Sr can be obtained from the corresponding partial half-life, which can be written as

$$t_{1/2} = \kappa / \tilde{C}, \quad (1)$$

where $\kappa = 6289$ s is a collection of natural constants [50] and the integrated shape function reads

$$\tilde{C} = \int_0^{w_0} C(w_e) p w_e (w_0 - w_e)^2 F_0(Z, w_e) dw_e. \quad (2)$$

In the above expression, $F_0(Z, w_e)$, with Z being the proton number of the daughter nucleus, is the usual Fermi function taking into account the final-state Coulomb distortion of the wave function of the emitted electron and $w_0 = W_0/m_e c^2$, $w_e = W_e/m_e c^2$, and $p = p_e c/m_e c^2 = (w_e^2 - 1)^{1/2}$ are kinematic quantities scaled dimensionless by the electron rest mass $m_e c^2$. Here p_e and W_e are the momentum and energy of the emitted electron, respectively, and W_0 is the beta endpoint energy, which for the ground-state transition defines the β -decay Q value. The shape factor is $C(w_e) \approx 1$ for allowed transitions [51] and it is quite a complicated combination of leptonic phase-space factors and NMEs, as described in detail in Ref. [52] and recently in Refs. [40,41].

In the present work, the needed β -decay formalism includes the allowed β decays (Fermi and Gamow-Teller) and the first-forbidden ones. The higher-forbidden β -decay

TABLE I. Level scheme of ^{92}Rb for the states with experimentally determined spin-parity. The known experimental states are compared with those computed using the two NSM Hamiltonians. The data were taken from Nuclear Data Sheets [55].

J^π	Expt. Energy (MeV)	$glepn$ (MeV)	$glekpn$ (MeV)
0^-	0.000	0.000	1.430
1^-	0.142	0.263	0.189
3^-	0.284	0.566	0.341

transitions are strongly suppressed and contribute a negligible amount to the summed electron spectral shape. The allowed decays are associated with a universal spectral shape, independent of the NMEs. This simple spectral shape, corresponding to $C(w_e) \approx 1$ in (2), has been extensively discussed in Ref. [51]. The first-forbidden β transitions are associated with tensor operators of rank 0 (0^-), 1 (1^-), and 2 (2^-) [36,37,52]. The pseudotensor 2^- transitions are pure axial-vector transitions and include only one NME and thus have a universal electron spectral shape. The pseudovector 1^- and pseudoscalar 0^- transitions have both vector and axial-vector components and depend on more than one NME, thus being sensitive to details of nuclear structure through the initial and final nuclear wave functions. For the vector part, as also for the allowed Fermi transitions, we adopt the CVC-protected value $g_V = 1.0$ for the weak vector coupling. The pseudoscalar 0^- transitions are pure axial vector and depend on the weak axial charge $g_A(\gamma_5)$, in addition to g_A . These are the $\Delta J = 0$ transitions and their decay rate depends on the value of the enhancement factor ϵ_{MEC} , multiplying the $g_A(\gamma_5)$ term. Again, more than one NME is involved so that these transitions are nuclear-structure sensitive. Since in the present case the initial state of β decay is 0^- , the pseudoscalar transitions go to 0^+ states, the pseudovector transitions to 1^+ states and the pseudotensor transitions to 2^+ states. Here it should be noted that, for initial states with nonzero angular momentum, the situation is more complicated and more than one of these transition types may contribute for a given final state, with interesting consequences, as demonstrated in Refs. [33,34].

B. Shell-model calculations

The NSM calculations were performed using the software NUSHELLX@MSU [53]. The interactions used in this work were $glekpn$ and $glepn$, all originally designed to access the spectroscopy of ^{96}Y and ^{96}Zr in Ref. [54]. Thus, the single-particle energies were fit to a nuclear region suitable for the present studies. The single-particle model space for $glekpn$ consists of the proton orbitals $1f_{5/2}$, $2p_{3/2}$, $2p_{1/2}$, and $1g_{9/2}$, with $1f_{7/2}$ as a closed shell, and the neutron orbitals $1g_{7/2}$, $2d_{5/2}$, $2d_{3/2}$, and $3s_{1/2}$, with $1g_{9/2}$ as a closed shell. The $glepn$ has the single-particle model space with the proton orbitals $2p_{3/2}$, $1f_{5/2}$, $2p_{1/2}$, $1g_{9/2}$, and $3s_{1/2}$ while for neutrons all shells up to $1g_{9/2}$ are filled and the orbitals $3s_{1/2}$, $2d_{5/2}$, and $2d_{3/2}$ form the valence space. This setup enabled us to compute the level energies of ^{92}Rb (see Table I) and ^{92}Sr (see Table II). For ^{92}Rb only the lowest three states have an unambiguously assigned spin-parity. The corresponding $glepn$ -computed and $glekpn$ -

TABLE II. Clustering of states of ^{92}Sr for the determination of possible values of the pair $[g_A^{\text{eff}}, \epsilon_{\text{MEC}}]$. Parentheses indicate uncertainty in parity and/or angular momentum. The columns $glekpn$ and $glepn$ are the adopted interactions and their corresponding predicted energy schemes. Superscript numbers above each interaction's level schemes indicates the cluster in which the corresponding state has been assigned in determination of the pairs. The experimental level energies of ^{92}Sr were taken from Nuclear Data Sheets [55].

Energy (keV)	J^π	$glekpn$	$glepn$
0.0	0^+	0^1	0^1
814.98	2^+	1102^2	848^2
1384.79	2^+	1926^2	1793^2
1778.33	$2^{(+)}$	2341	2074^2
2053.9	(2^+)		2347
2088.39	$0^{(+)}$		
2140.82	1^+	2405^2	2552^2
2765.7	0^+	2863^2	2924
2783.6	$[2^+]^a$	2974	3011
2820.89	$([2^+], 1)^b$	3513^2	3437^2

^aState predicted by both interactions but of experimentally unknown parity and spin.

^bSquare brackets denote interactions' spin-parity prediction.

computed states are given for comparison in Table I. Notably, the $glepn$ interaction reproduces quite nicely the energies of the corresponding experimental states, but for $glekpn$ the 0^- state is quite high in energy and the ground state is a 2^- state. This is not unusual for typical shell-model Hamiltonians trying to predict state energies in odd-odd nuclei. In these nuclei one has to cope with an extremely high density of states so that prediction of a correct level sequence is more luck than a general rule. In the experimental spectrum there are a lot of states, above those listed in the table, with the ambiguous spin-parity assignment “ $(1, 2^-)$.” Also, in both computed spectra there are a lot of 1^- , 2^- , and 3^- states at low energies. As can be seen in Table II, the level scheme of ^{92}Sr could be reproduced within a few hundreds of keV accuracy. For ^{92}Sr , both interactions manage to predict the correct level sequence, which is easier than for ^{92}Rb since the state density in an even-even nucleus is much less than in an odd-odd one.

After the level schemes were produced for both NSM interactions, the β^- -decay transitions from the 0^- ground state of ^{92}Rb to the 0^+ , 1^+ , 2^+ , and 1^- states in ^{92}Sr were computed for further studies of the β feeding of ^{92}Sr . For the ground-state-to-ground-state decay energy we adopted the experimental value $Q = 8.095$ MeV.

III. RESULTS

Here we describe the flow of the calculations and the subsequent analyses. The predicted decay branchings, partial half-lives, and electron spectral shapes are dependent on the available endpoint energies (equal to the Q value for the ground-state transition, taken from experiment in the present work) and the values of g_A^{eff} and ϵ_{MEC} (the latter for $\Delta J = 0$ transitions). This means that a reasonable theoretical description of all these aspects is a demanding task, and we have

chosen to tackle the related problems in a way described in the following.

A. Determination of the values of the axial couplings

Our assessment of the values of g_A^{eff} and ε_{MEC} utilizes the TAGS-measured branching data by suitably clustering the final states in ^{92}Sr . This clustering includes the strong transition to the ground state as cluster number 1 and cluster 2 includes transitions to several excited states, as shown in Table II for each of the interactions used in the present calculations. All final states in the table correspond to first-forbidden transitions. Concerning the *glekpn* interaction, the 2^+ states at energies 1384.79 and 1778.33 keV were a bit problematic since excessively large branchings to these states were predicted by the calculations. We then opted for the 0^+ states at 2088.39 and 2527.18 keV to be used for determination of the values of the weak couplings for this interaction. Such differences between the results obtained by using the two shell-model Hamiltonians are not so surprising considering their different valence spaces, single-particle energies, and effective two-body interaction matrix elements. While it is true that selecting different final states in group 2 for the two interactions biases the choice of values of the weak couplings g_A^{eff} and ε_{MEC} , resulting in two different sets of these parameters, this only implies that the different Hamiltonians used in the calculations necessitate different effective values of these weak couplings.

Since all the individual branchings in cluster 2 are small and thus liable to large relative errors, we chose to sum up all the individual branchings to produce a larger summed branching which is easier to compare with the corresponding sum of the computed branchings. This procedure dampens the variations in the computed individual branchings among the two interactions used in the calculations. Since the branching corresponding to the ground-state-to-ground-state transition is large and best known we set a criterion of 2.5% relative error for the corresponding computed branching. For cluster 2 we adopted a less restrictive criterion of 25% relative error in the computed sum branching. We then searched for values of $[g_A^{\text{eff}}, \varepsilon_{\text{MEC}}]$ pairs satisfying both of the mentioned criteria by varying g_A^{eff} within the range from 0.2 to 1.27 and ε_{MEC} in the range between 0.7 and 2.0. In all these calculations we use the experimentally known excitation energies of the involved final states in order to treat correctly the lepton phase space with an accurate endpoint energy.

The obtained values of the pair were found to follow a regular pattern for each interaction. The patterns are reproduced by the polynomial regressions

$$\varepsilon_{\text{MEC}} = 0.572(4)g_A^2 - 1.755(3)g_A + 2.539(9), \quad (3)$$

$$\varepsilon_{\text{MEC}} = 1.003(2)g_A^2 - 2.948(4)g_A + 3.582(8), \quad (4)$$

for *glekpn* and *glepn*, respectively. For the former, it correctly predicts the pattern in the range $g_A^{\text{eff}} = 0.76$ – 1.27 and the latter $g_A^{\text{eff}} = 0.70$ – 1.27 . Lastly, from the pool of solutions we picked one $[g_A^{\text{eff}}, \varepsilon_{\text{MEC}}]$ combination for each interaction with the least relative branching error, below or equal to 0.25%, for the ground-state-to-ground-state decay branch. The obtained $[g_A^{\text{eff}}, \varepsilon_{\text{MEC}}]$ combinations were [1.106, 1.3] and [1.083, 1.57]

for *glekpn* and *glepn*, respectively. The corresponding range, $\varepsilon_{\text{MEC}} = 1.3$ – 1.6 , for the mesonic enhancement factor is compatible with that found for the corresponding mass region in Ref. [39] for values $g_A^{\text{eff}} = 0.7$ – 1.0 . Here it has to be pointed out that the presently obtained range $g_A^{\text{eff}} \approx 1.0$ – 1.1 does not represent only the $0^- \rightarrow 0^+$ transition but also transitions to 1^+ and 2^+ states, contrary to the analysis in Ref. [39]. Furthermore, the solutions in the lower and upper limits of g_A^{eff} introduce variations from the selected solution's total branching ranging from a minimum 0.7% to a maximum of 3.8%. The effects on the total spectral shape by these variations are quite small, and in the reasonable physical range $g_A^{\text{eff}} = 0.9$ – 1.2 even negligible. Due to this insensitivity to a reasonable variation in the values of the axial couplings and the fact that the major player in the parameter determination, the ground-state transition, has small experimental error bars in its measured branching, the experimental error bars in the measured branchings of groups 1 and 2 have a negligible impact on the computed spectral shapes. This indicates that our results concerning the total electron spectral shape are quite robust.

B. Computation of the electron spectral shapes

With the selected combinations of the weak couplings we can proceed with our calculations of the NMEs and their corresponding half-lives and electron spectra. We include in the calculations all allowed and first-forbidden transitions but leave out the higher-forbidden ones due to their strong hindrance and negligible contribution. Most of the final states within the Q window have not been included in the fitting procedure. The allowed Fermi and Gamow-Teller decays to the 0^- and 1^- states have a universal electron spectral shape and can thus be treated exactly by using the TAGS-measured branchings, thus minimizing the computational error related to these decays.

The first-forbidden transitions, beyond the states included in cluster 2, pose a source of uncertainty in our calculations as their precise state energies are experimentally unresolved, leading to uncertainties in the associated endpoint energies, branchings, and therefore their electron spectral shapes. The related error can be analyzed via comparison of the TAGS-measured total branching ratio and the corresponding computed one for transitions to the energy region containing the unresolved states.

Additionally, one can check the robustness of the spectral-shape prediction by adding (removing) a uniform amount of 250 keV to (from) the computed endpoint energies of the unresolved states. These shifts are reasonable considering the uncertainties in the level energies of the known states in groups 1 and 2, but this is just a nomenclature and does not mean that all the levels should shift uniformly, but rather in random, in any realistic scenario. By this nomenclature of uniform shifts we want to produce the maximal impact on the computed spectral shapes to see how robust our predictions are in this respect. The related effects are shown in Fig. 1 for the *glekpn* interaction where, for convenience, the area under the curves is normalized to unity to produce the same total half-life for each case. From the lower panel of the figure one

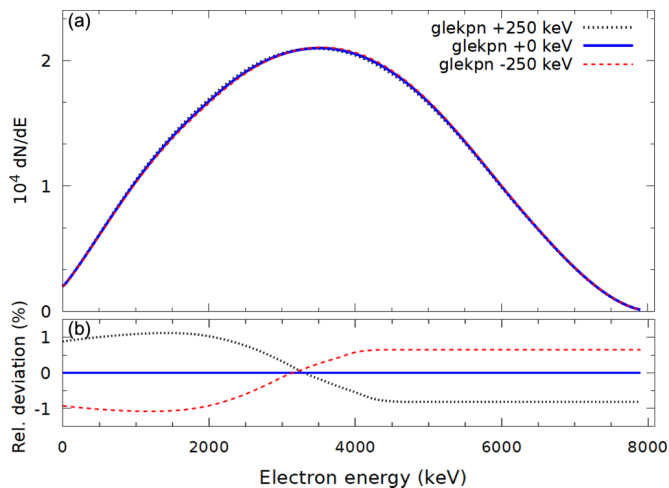


FIG. 1. (a) Analysis of the effects of uniformly over- or under-predicting by 250 keV (the dotted and dashed lines, respectively) the *glekpn*-computed endpoint energies (solid line) of the unresolved states. The horizontal axis indicates the electron kinetic energy and the vertical axis is given in arbitrary units such that the total area under the curves is normalized to unity (upper panel). (b) Plot of the relative deviation in percent. The semistraight lines after 4000 keV are due to the normalization to unity.

can see that the effects of these shifts are at a sub-percent level indicating that the unresolved states do not contribute significantly to the total spectral shape. The same is true for the *glepn* interaction. The related robust theory description can be seen from the variation of the total branching ratio to the unresolved states which now becomes $2.40^{+0.82}_{-0.63}\%$ and $2.26^{+0.70}_{-0.55}\%$ for *glekpn* and *glepn*, respectively, in good agreement with the TAGS-measured branching $2.81^{+1.32}_{-0.98}\%$.

C. Total electron spectral shape

After all these procedures and checks of robustness, we are ready to proceed to combine the calculated NMEs and phase-space factors into electron spectral shapes. In Fig. 2 we show the decomposition of the total electron spectral shape, again for the *glekpn* interaction. It can be seen that the dominant component is the first-forbidden nonunique decay to the ground state (cluster 1) and then come the first-forbidden of cluster 2 plus allowed transitions, with known experiment-based Q values. The smallest contribution comes from cluster 3, containing the rest of the states, including the unresolved first-forbidden transitions. The small contribution of the states in cluster 3 is clearly seen as the difference between the cumulative curves with solid line (total spectrum) and dotted line (total minus cluster 3), the deviations showing up below some 3.5 MeV of electron kinetic energy. For the *glepn* interaction a similar pattern is recorded. The percentages shown in the figure are the computed contributions to the measured total half-life. Since our calculations only include transitions to states of spins 0, 1, and 2, leaving out the higher-forbidden transitions, our calculations underpredict the total half-life by the missing 0.82%.

As a final step, we compare the computed total sum spectra with the one obtained from a simulation employing the ^{92}Rb

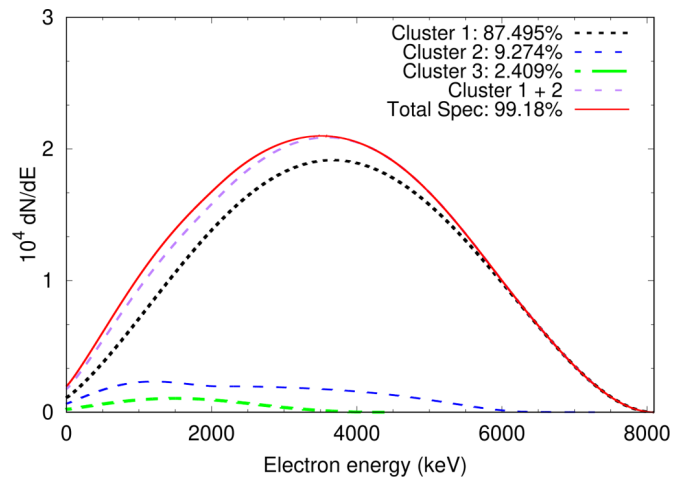


FIG. 2. The *glekpn*-computed total spectrum and its decomposition into contributions from the ground-state transition (cluster 1), the known forbidden (cluster 2) plus allowed transitions and the unresolved transitions (cluster 3). The cluster build-up to the total spectrum (clusters 1,2 and 3 combined) is also shown.

beta branchings from the TAGS measurements. In the TAGS spectrum, we exclusively use allowed shapes for all transitions from the parent ground state to the lowest and highest discrete and (continuum-like) high-density daughter energy states, respectively. The Fermi function correction based on Evans [56] was added to all transitions. This comparison is depicted in Fig. 3, where the TAGS result is denoted the “TAS” Spectrum. The area under each curve is the same since the same total half-life was obtained for each case. For convenience, this area is normalized to one in the figure. The lower panel of the figure gives the relative deviation of the curves in percent. We have tested that switching all the NSM-computed spectral

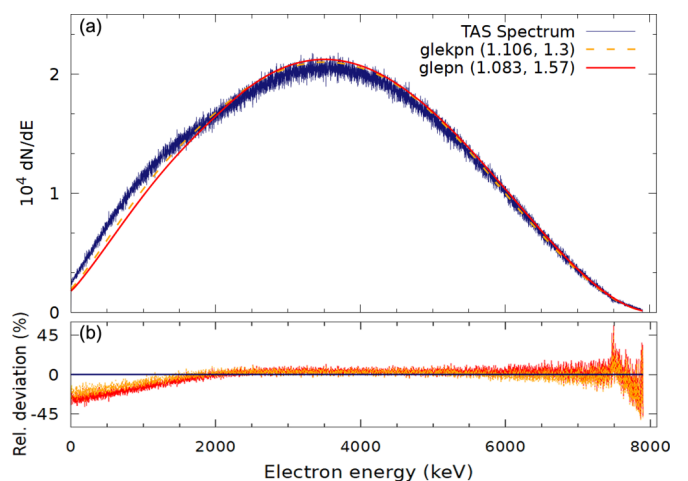


FIG. 3. (a) Comparison of the simulated TAGS total beta spectrum (thick fuzzy line) with those computed by using the shell-model interactions *glekpn* (dashed curve) and *glepn* (line). The horizontal axis indicates the electron kinetic energy and the vertical axis is given in arbitrary units such that the total area under the curves is normalized to unity. (b) Relative deviation in percent of the computed spectral curves (fuzzy line) from the simulated TAGS curve.

shapes allowed, i.e., making the “all-allowed” approximation in the total NSM-computed spectral shape reproduces the “TAS spectrum” of Fig. 3. Both the simulated TAGS spectrum and the all-allowed NSM spectrum are based on the TAGS-measured branchings, so that their coincidence can be used as a check of the consistency of the NSM calculations. It can be seen that abandoning the allowed approximation for the first-forbidden decay transitions of clusters 1 and 2, makes a clear difference, and the spectral shape changes in a similar way relative to the allowed approximation for the two interactions. The main differences are at low electron kinetic energies, below 2 MeV, where the interactions predict a clear deficit in the number of electrons, and in intermediate energies, between 2 and 4 MeV, where the interactions predict a slight excess of electrons.

The shell-model calculations predict a smaller number of low energy electrons than the TAGS analysis based on allowed transitions. This would mean less higher energy antineutrinos, which can have an outsized effect on the number of detected antineutrinos in antineutrino telescopes, since the cross section is roughly proportional to $E_e p_e$ [57], where E_e is the energy and p_e the momentum of the produced positron. Simulating the NSM-based and TAGS-based antineutrino spectra we found that the expected inverse beta decay (IBD) rate is 2.6% smaller for the *glekpn*-based and 4.6% smaller for the *glepn*-based antineutrino spectrum than for the TAGS-based one. While these results indicate that the allowed approximation leads to an over estimation of a couple of percent in the IBD rate they most importantly demonstrate the uncertainties related to the prediction of IBD rates for antineutrinos from fission fragments relevant for the reactor-flux anomalies. Furthermore, our “by-the-eye” analyses indicate that taking fully into account the first-forbidden β transitions leads in the case of the ^{92}Rb decay to a flux deficit at antineutrino energies above 6 MeV and to a flux excess in the energy interval 4–6 MeV. Thus ^{92}Rb could be conjectured to contribute to the emergence of the spectral bump in the reactor-antineutrino flux. Making this a bit more quantitative, we can use the fission yield 4.8% of ^{92}Rb and our computed reduction of 2.6%–4.6% in the IBD rate to produce an estimated reduction of 0.13%–0.22% in the total reactor-antineutrino flux by ^{92}Rb alone. This means that only a more comprehensive analysis, including a number of other nuclei contributing to the antineutrino flux, can verify quantitatively the impact of the first-forbidden transitions to the RAA and the spectral bump.

IV. CONCLUSIONS

In this work we report on the first computation of the shape of a total electron spectrum related to beta-decay transitions

to final states within a full decay Q window. Specifically, we calculate the total electron spectral shape related the β^- transitions from the 0^- ground state of ^{92}Rb to excited states in ^{92}Sr within the full Q window of 8.095 MeV. All relevant allowed and first-forbidden beta transitions are included and data on measured excitation energies of the final states and the TAGS-measured beta branching ratios are used as guidelines to adjust the values of the involved weak axial-vector and axial-charge couplings. Ultimately, these type of calculations for the most important fission products in nuclear reactors will pave the way to a better understanding of the reactor antineutrino spectra and the related flux and bump anomalies. By calculating the total electron spectral shape we have been able to demonstrate in a robust way that the first-forbidden β^- transitions can significantly affect this shape for a given fission product, in this case for ^{92}Rb , a major contributor to the reactor-antineutrino spectral shape. These corrections were shown to lead to a decrease of 2.6%–4.6% in the expected IBD rate thus demonstrating the percent-scale impact on the predicted antineutrino detection rates in antineutrino telescopes. We could also show that the decay of ^{92}Rb potentially contributes to the RAA by some 0.13%–0.22% reduction in the flux. Furthermore, “by-the-eye” inspection shows qualitatively that ^{92}Rb could contribute to the formation of the bump in the reactor-antineutrino flux profile. This said, one has to keep in mind that ^{92}Rb is only one of the so many fission products contributing to the total antineutrino flux from reactors. Based on the decay study of this one sole nucleus it is hard to make quantitative conclusions about the impact of the forbidden β transitions on the total antineutrino spectrum. Here one would need to proceed step by step, treating the most prominent flux contributors ^{90}Rb , ^{94}Y , ^{96}Y , ^{140}Xe , ^{140}Cs , . . . , one after another, as also suggested in Ref. [58]. This we leave for future work.

ACKNOWLEDGMENTS

We acknowledge the support by the Academy of Finland under the Contract No. 318043 and grants for computer resources from the Finnish Grid and Cloud Infrastructure (persistent identifier urn:nbn:fi:research-infras-2016072533). Colleagues from SUBATECH and Spain would like to thank the Master Projects TAGS, Jyvaskyla and OPALE from CNRS/in2p3, the CNRS IRN ASTRANUCAP, the NEEDS/NACRE project, the CHANDA and SANDA European projects, the University of Nantes, and the region Pays de Loire for their contributions to the funding of the TAGS experiments.

- [1] P. De Salas, D. Forero, M. Tórtola, and J. Valle, *Phys. Lett. B* **782**, 633 (2018).
 [2] F. Capozzi, E. Lisi, A. Marrone, and A. Palazzo, *Prog. Part. Nucl. Phys.* **102**, 48 (2018).

- [3] I. Esteban, M. C. Gonzalez-Garcia, A. Hernandez-Cabezudo, M. Maltoni, and T. Schwetz, *J. High Energy Phys.* **01** (2019) 106.
 [4] J. K. Ahn *et al.* (RENO Collaboration), *Phys. Rev. Lett.* **108**, 191802 (2012).

- [5] Y. Abe *et al.* (Double Chooz Collaboration), *J. High Energy Phys.* **10** (2014) 086.
- [6] B. Pal *et al.* (Daya Bay Collaboration), *Phys. Rev. Lett.* **116**, 161801 (2016).
- [7] P. Huber, *Phys. Rev. C* **84**, 024617 (2011).
- [8] T. A. Mueller *et al.*, *Phys. Rev. C* **83**, 054615 (2011).
- [9] K. Schreckenbach, H. R. Faust, F. von Feilitzsch, A. A. Hahn, K. Hawerkamp, and J. L. Vuilleumier, *Phys. Lett. B* **99**, 251 (1981).
- [10] F. von Feilitzsch, A. A. Hahn, and K. Schreckenbach, *Phys. Lett. B* **118**, 162 (1982).
- [11] K. Schreckenbach, G. Colvin, W. Gelletly, and F. von Feilitzsch, *Phys. Lett. B* **160**, 325 (1985).
- [12] A. A. Hahn, K. Schreckenbach, W. Gelletly, F. von Feilitzsch, G. Colvin, and B. Krusche, *Phys. Lett. B* **218**, 365 (1989).
- [13] G. Mention, M. Fechner, T. Lasserre, T. A. Mueller, D. Lhuillier, M. Cribier, and A. Letourneau, *Phys. Rev. D* **83**, 073006 (2011).
- [14] S. Gariazzo, C. Giunti, M. Laveder, and Y. F. Li, *J. High Energy Phys.* **06** (2017) 135.
- [15] J. M. Berryman and P. Huber, *Phys. Rev. D* **101**, 015008 (2020).
- [16] J. Kostensalo, J. Suhonen, C. Giunti, and P. C. Srivastava, *Phys. Lett. B* **795**, 542 (2019).
- [17] S. Schopmann, *Universe* **7**, 360 (2021).
- [18] R. W. King and J. F. Perkins, *Phys. Rev.* **112**, 963 (1958).
- [19] F. T. Avignone, S. M. Blakenship, and C. W. Darden, *Phys. Rev.* **170**, 931 (1968).
- [20] P. Vogel, G. K. Schenter, F. M. Mann, and R. E. Schenter, *Phys. Rev. C* **24**, 1543 (1981).
- [21] O. Tengblad, K. Aleklett, R. Von Dincklage, E. Lund, G. Nyman, and G. Rudstam, *Nucl. Phys. A* **503**, 136 (1989).
- [22] G. Rudstam, P. I. Johansson, O. Tengblad, P. Aagaard, and J. Eriksen, *At. Data Nucl. Data Tables* **45**, 239 (1990).
- [23] J. C. Hardy, L. C. Carraz, B. Jonson, and P. G. Hansen, *Phys. Lett. B* **71**, 307 (1977).
- [24] A. Algora *et al.*, *Phys. Rev. Lett.* **105**, 202501 (2010).
- [25] M. Fallot *et al.*, *Phys. Rev. Lett.* **109**, 202504 (2012).
- [26] A. A. Zakari-Issoufou, M. Fallot, A. Porta, A. Algora, J. L. Tain, E. Valencia, S. Rice, V. Bui, S. Cormon, M. Estienne, J. Agramunt, J. Aysto, M. Bowry, J. A. Briz, R. Caballero-Folch, D. Cano-Ott, A. Cucoanes, V. V. Elomaa, T. Eronen, E. Estevez, G. F. Farrelly, A. R. Garcia, W. Gelletly, M. B. Gomez-Hornillos, V. Gorlychev, J. Hakala, A. Jokinen, M. D. Jordan, A. Kankainen, P. Karvonen, V. S. Kolhinen, F. G. Kondev, T. Martinez, E. Mendoza, F. Molina, I. Moore, A. B. Perez-Cerdan, Z. Podolyak, H. Penttila, P. H. Regan, M. Reponen, J. Rissanen, B. Rubio, T. Shiba, A. A. Sonzogni, and C. Weber (IGISOL Collaboration), *Phys. Rev. Lett.* **115**, 102503 (2015).
- [27] E. Valencia *et al.*, *Phys. Rev. C* **95**, 024320 (2017).
- [28] S. Rice *et al.*, *Phys. Rev. C* **96**, 014320 (2017).
- [29] V. Guadilla *et al.*, *Phys. Rev. Lett.* **122**, 042502 (2019).
- [30] B. C. Rasco *et al.*, *Phys. Rev. Lett.* **117**, 092501 (2016).
- [31] A. C. Hayes, J. L. Friar, G. T. Garvey, G. Jungman, and G. Jonkmans, *Phys. Rev. Lett.* **112**, 202501 (2014).
- [32] D. L. Fang and B. A. Brown, *Phys. Rev. C* **91**, 025503 (2015).
- [33] L. Hayen, J. Kostensalo, N. Severijns, and J. Suhonen, *Phys. Rev. C* **99**, 031301(R) (2019).
- [34] L. Hayen, J. Kostensalo, N. Severijns, and J. Suhonen, *Phys. Rev. C* **100**, 054323 (2019).
- [35] J. Engel and J. Menéndez, *Rep. Prog. Phys.* **80**, 046301 (2017).
- [36] J. T. Suhonen, *Front. Phys.* **5**, 55 (2017).
- [37] H. Ejiri, J. Suhonen, and K. Zuber, *Phys. Rep.* **797**, 1 (2019).
- [38] J. Suhonen and J. Kostensalo, *Front. Phys.* **7**, 29 (2019).
- [39] J. Kostensalo and J. Suhonen, *Phys. Lett. B* **781**, 480 (2018).
- [40] M. Haaranen, P. C. Srivastava, and J. Suhonen, *Phys. Rev. C* **93**, 034308 (2016).
- [41] M. Haaranen, J. Kotila, and J. Suhonen, *Phys. Rev. C* **95**, 024327 (2017).
- [42] J. Kostensalo, M. Haaranen, and J. Suhonen, *Phys. Rev. C* **95**, 044313 (2017).
- [43] J. Kostensalo and J. Suhonen, *Phys. Rev. C* **96**, 024317 (2017).
- [44] L. Bodenstein-Dresler *et al.* (COBRA Collaboration), *Phys. Lett. B* **800**, 135092 (2020).
- [45] J. Kostensalo, J. Suhonen, J. Volkmer, S. Zatschler, and K. Zuber, *Phys. Lett. B* **822**, 136652 (2021).
- [46] K. Kubodera, J. Delorme, and M. Rho, *Phys. Rev. Lett.* **40**, 755 (1978).
- [47] J. Delorme, *Nucl. Phys. A* **374**, 541 (1982).
- [48] E. K. Warburton, *Phys. Rev. C* **44**, 233 (1991).
- [49] K. Kubodera and M. Rho, *Phys. Rev. Lett.* **67**, 3479 (1991).
- [50] A. Kumar, P. C. Srivastava, and J. Suhonen, *Eur. Phys. J. A* **57**, 225 (2021).
- [51] J. Suhonen, *From Nucleons to Nucleus: Concepts of Microscopic Nuclear Theory* (Springer-Verlag, Berlin, Heidelberg, Springer, Gaithersburg, 20899, 2007).
- [52] H. Behrens and W. Bühring, *Electron Radial Wave Functions and Nuclear Beta-decay (International Series of Monographs on Physics)* (Clarendon Press, Oxford, 1982).
- [53] B. A. Brown and W. D. M. Rae, *Nucl. Data Sheets* **120**, 115 (2014).
- [54] H. Mach, E. K. Warburton *et al.*, *Phys. Rev. C* **41**, 226 (1990).
- [55] C. M. Baglin, *Nucl. Data Sheets* **113**, 2187 (2012).
- [56] R. Evans, *The Atomic Nucleus* (McGraw-Hill Publishing Company, Ltd., 1955).
- [57] A. C. Hayes and P. Vogel, *Annu. Rev. Nucl. Part. Sci.* **66**, 219 (2016).
- [58] A. A. Sonzogni, T. D. Johnson, and E. A. McCutchan, *Phys. Rev. C* **91**, 011301(R) (2015).

II

COMPUTED TOTAL β -ELECTRON SPECTRA FOR DECAYS OF PB AND BI IN THE $^{220,222}\text{RN}$ RADIOACTIVE CHAINS

by



Ramalho, M and Suhonen, J

Phys. Rev. C **109**, 1, 014326 (2024).

DOI: 10.1103/PhysRevC.109.014326

Reproduced with kind permission of American Physical Society.

Computed total β -electron spectra for decays of Pb and Bi in the $^{220,222}\text{Rn}$ radioactive chains

M. Ramalho ^{1,*} and J. Suhonen ^{1,2,†}

¹*Department of Physics, University of Jyväskylä, P.O. Box 35, FI-40014 Jyväskylä, Finland*

²*International Centre for Advanced Training and Research in Physics (CIFRA), P.O. Box MG12, 077125 Bucharest-Magurele, Romania*



(Received 25 September 2023; revised 7 November 2023; accepted 3 January 2024; published 25 January 2024)

The radon radioactivity is an unavoidable background in present and future underground experiments attempting to detect the neutrinoless double β decay, WIMP-nucleus interactions in direct dark-matter searches, etc. In particular, the $^{220,222}\text{Rn}$ radioactive chains lead to β^- decays of $^{212,214}\text{Pb}$ and $^{212,214}\text{Bi}$, notorious backgrounds in the mentioned experiments. In this paper, we compute the total β -electron spectral shapes of these decays by including next-to-leading-order terms and other correction factors in the β spectral shape. The studied β^- decays involve strong allowed and first-forbidden β transitions, the nonunique first-forbidden transitions being nuclear-structure dependent through the numerous involved nuclear matrix elements (NMEs). We compute these NMEs by using the nuclear shell model with the *khpe* Hamiltonian. This Hamiltonian renders a very nice description of the level energies of the daughter nuclei $^{212,214}\text{Bi}$ and $^{212,214}\text{Po}$ of the mentioned mother nuclei. We adopt experimental endpoint energies and engage the small relativistic NMEs (sNME), to accurately describe the measured branching ratios, a necessary prerequisite for a precise description of the total β spectra. We also discuss the uncertainties of our computed spectra and hope that these computations will be of help for present and future rare-decays and dark-matter experiments.

DOI: [10.1103/PhysRevC.109.014326](https://doi.org/10.1103/PhysRevC.109.014326)

I. INTRODUCTION

β decay is a fundamental nuclear process in which a nucleus undergoes a transmutation by emitting a β particle (electron or positron) and a neutrino or antineutrino [1,2]. The study of β -decay spectra provides valuable insights into the underlying nuclear structure and the properties of the involved isotopes. In particular, the investigation of β spectral shapes for isotopes such as $^{212,214}\text{Pb}$ and $^{212,214}\text{Bi}$ holds great importance due to their contributions to backgrounds in various scientific measurements, including double- β -decay and dark-matter detection experiments.

To accurately interpret experimental data and distinguish potential double- β and dark-matter signals from background noise, a comprehensive understanding of the β spectral shapes of isotopes like $^{212,214}\text{Pb}$ and $^{212,214}\text{Bi}$ is crucial. These isotopes are part of the background problem emerging from the radon radioactivity, in this case from the $^{220,222}\text{Rn}$ radioactive chains. The spectral shape refers to the distribution of electron energies emitted in the β -decay process. The total β spectrum is the sum of β -electron spectral shapes corresponding to individual β -decay transitions. Computation of this total spectral shape is quite demanding and experimental β -endpoint energies (in the case of β^- decay the maximum energy of the emitted electron allowed by the available decay energy and its sharing with the emitted electron antineutrino) have to be used. In addition, it should be preferable to reproduce the measured branching ratios as accurately as possible. For the

presently discussed decays, they have been evaluated and can be found in the ENSDF database [3]. The experiment-based evaluated ground-state-to-ground-state endpoint energies (Q values) vary between $Q = 0.5691(18)$ – $3.269(11)$ MeV for the discussed nuclei (see the AME2020 database [4]) making the calculation of the total β spectra a challenge since it is quite hard to reliably describe all the decay transitions within Q windows of this size. As far as we know, there have been only a few attempts to compute total β spectra within decay Q windows in the range of several MeV, see [5].

In the present computations we use the formalism outlined in [6,7], including the next-to-leading-order terms in the β spectral shape. With this formalism, we are able to compute both the allowed and forbidden transitions involved in the decays $^{212,214}\text{Pb} \rightarrow ^{212,214}\text{Bi}$ and $^{212,214}\text{Bi} \rightarrow ^{212,214}\text{Po}$. The first-forbidden β transitions are particularly important in these decays, consisting of both unique and nonunique transitions. The allowed and unique first-forbidden transitions have universal β spectral shapes but the nonunique transitions depend on nuclear structure through the nuclear matrix elements (NMEs). We compute these NMEs by using the nuclear shell model (NSM) with a well-established Hamiltonian. By varying the value of one of these NMEs, the so-called small relativistic vector NME (sNME) close to its CVC (conserved vector current) value [1], we can reproduce the available data for all the numerous branching ratios involved in the studied total β spectra. In addition, the used Hamiltonian yields quite nice energy spectra within the decay Q window for the involved daughter nuclei $^{212,214}\text{Bi}$ and $^{212,214}\text{Po}$.

Recent advancements in experimental techniques, such as cryogenic calorimeters and solid-state NMR spectroscopy,

*madeoliv@jyu.fi

†jouni.t.suhonen@jyu.fi

have enabled precise measurements of individual β spectral shapes [8]. These techniques offer high-resolution spectra and improved sensitivity, allowing for a more detailed analysis of the decay process. For instance, the ACCESS (Array of Cryogenic Calorimeters to Evaluate Spectral Shapes) project aims to establish a novel technique for precision measurements of forbidden β decays, which can serve as important benchmarks for nuclear-physics calculations and background studies in astroparticle physics experiments [8]. Individual β^- spectra have already been measured and analyzed for ^{113}Cd [9–11] and ^{115}In [12].

The total spectral shapes with multi-MeV Q windows still offer a grand challenge for the experiments, but the recent advances made in the β -electron detectors [13] offer presently a possibility for the measurements of the total β -electron spectra for β decays with multi-MeV Q values.

Our article is organized as follows. In Sec. II the adopted theoretical framework is briefly summarized by introducing the β -electron spectral shapes, and the related NMEs and their computation through the NSM. The results are presented and discussed in Sec. III, and the conclusions are drawn in Sec. IV.

II. THEORETICAL FRAMEWORK

Nuclear β decays are mediated via weak interactions and are a nuclear disintegration process in which the atomic number of the decaying nucleus changes by one. Our current focus involves only β^- decays and it consists of a neutron transmuting into a proton emitting an electron and an electron antineutrino ($\bar{\nu}_e$) within a nuclear environment:

$$n \rightarrow p + e^- + \bar{\nu}_e.$$

In the following, we describe the theory of β -electron spectral shapes, and the effective values of the weak axial coupling g_A and weak-axial charge $g_A(\gamma_5)$. Furthermore, the NSM, alongside its effective interaction and its model space shall be discussed.

A. β spectral shapes

The branching ratio of a transition to a particular final state in the daughter isotope can be obtained from the corresponding partial half-life which can be written as

$$t_{1/2} = \kappa / \tilde{C}, \quad (1)$$

where $\kappa = 6289$ s is a collection of natural constants [7] and the integrated shape function reads

$$\tilde{C} = \int_0^{w_0} C(w_e) p w_e (w_0 - w_e)^2 F_0(Z, w_e) dw_e. \quad (2)$$

In this expression, $F_0(Z, w_e)$, with Z as the proton number of the daughter nucleus, is the usual Fermi function taking into account the final-state Coulomb distortion of the wave function of the emitted electron and

$$w_0 = \frac{W_0}{m_e c^2}, \quad w_e = \frac{W_e}{m_e c^2}, \quad p = \frac{p_e c}{m_e c^2} = \sqrt{w_e^2 - 1} \quad (3)$$

are the kinematic quantities scaled dimensionless by the electron rest mass $m_e c^2$. Here, p_e and W_e are the momentum and energy of the emitted electron, respectively, and W_0 is the β

endpoint energy, which for the ground-state transitions defines the β -decay Q value. The shape factor $C(w_e)$ contains the Fermi and Gamow-Teller NME for allowed transitions [2] and in general it is a complex combination of leptonic phase-space factors and NME, as described in detail in [1] and recently in [6,14].

For the current work, the main focus involves both first-forbidden unique and nonunique β^- decays. The unique decays have a universal spectral shape, as have the allowed decays, and correspond to $C(w_e)$ being proportional to a single NME in Eq. (2), as has been extensively discussed in [2]. Higher-forbidden β -decay transitions are strongly suppressed and contribute negligibly to the summed electron spectral shape and are thus not of interest in the current work.

First-forbidden β transitions are associated with tensor operators of rank 0, 1, and 2 [1,15,16]. The pseudoscalar $\Delta J = 2$ transitions with a change in parity are pure axial-vector transitions and include only one NME. These transitions are called first-forbidden unique and have a universal electron spectral shape. The pseudovector $\Delta J = 1$ and pseudoscalar $\Delta J = 0$ transitions with a change in parity are transitions that have both vector and axial-vector components and depend on more than one NME, thus being sensitive to details of nuclear structure through the initial and final nuclear wave functions. They are called first-forbidden nonunique. For the vector part and the allowed Fermi transitions, we adopt the CVC-compatible value $g_V = 1.0$ for the weak vector coupling.

The $\Delta J = 0$ transitions depend on the weak axial charge $g_A(\gamma_5)$, in addition to g_A . In this work, we will refer to the effective g_A^{eff} as simply g_A and it should not be confused with its free-nucleon value $g_A^{\text{free}} = 1.27$. Only these particular transitions and their decay rates depend on the value of the so-called mesonic enhancement factor ε_{MEC} , related to g_A as follows:

$$g_A(\gamma_5) = \varepsilon_{\text{MEC}} \times g_A. \quad (4)$$

The mesonic enhancement factor with values of $g_A \approx 0.7$ have been shown to follow the pattern

$$\varepsilon_{\text{MEC}} = 1.576 + 2.08 \times 10^{-3} A \quad (5)$$

in medium to heavy nuclei [17]. For heavy nuclei with a free-nucleon g_A , the mesonic enhancement factor can be as high as $\varepsilon_{\text{MEC}} \approx 2.0$ – 2.2 [18]. However, the magnitude of the mesonic enhancement depends on the model, interaction used, and the selected value of g_A .

B. Nuclear shell-model calculations

The NSM calculations were performed using the software KHELL [19] with the Hamiltonian $khpe$ [20] found in NUSHELLX@MSU [21]. This interaction and the participant single-particle energies were originally designed to access the level schemes of the mass region $A = 204$ – 212 and were also used for ^{212}Pb , of interest in this work.

The model space consists of the ^{208}Pb closed core and a valence space consisting of the proton $\pi(1h_{9/2})$, $\pi(2f_{7/2})$, $\pi(2f_{5/2})$, $\pi(3p_{3/2})$, $\pi(3p_{1/2})$, and $\pi(1i_{13/2})$ orbitals and neutron $\nu(1i_{11/2})$, $\nu(2g_{9/2})$, $\nu(2g_{7/2})$, $\nu(3d_{5/2})$, $\nu(3d_{3/2})$, $\nu(4s_{1/2})$,

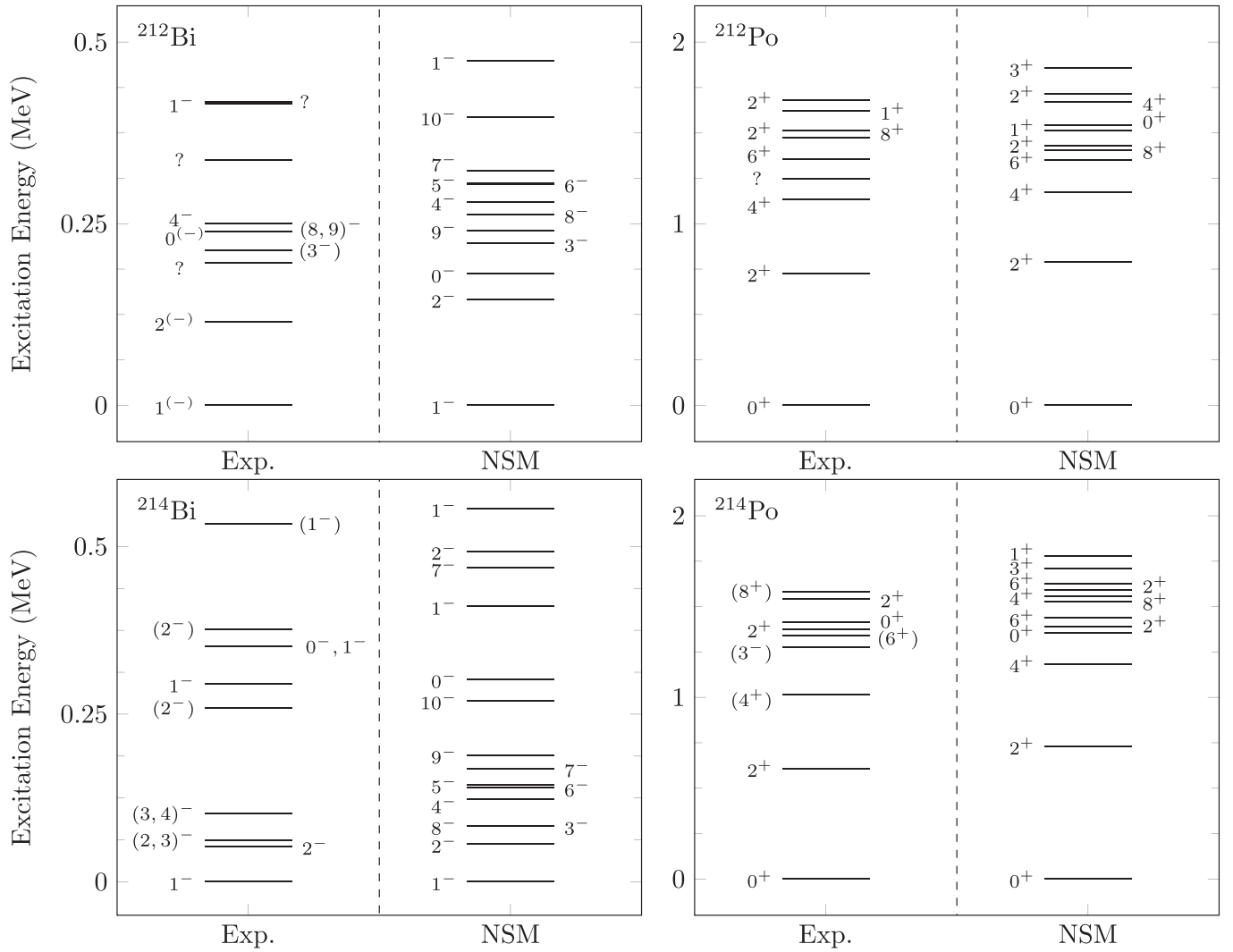


FIG. 1. Computed level schemes for the β^- -decay daughters ^{212}Bi , ^{214}Bi , ^{212}Po , and ^{214}Po using the Hamiltonian $khpe$. A comparison with the available data is performed with the parentheses denoting uncertainty in parity and spin-parity assignments. The evaluated data are gathered from [3].

and $\nu(1j_{15/2})$ orbitals. No truncations were made within the said valence space. This setup enabled us to compute $^{212}\text{Pb-Bi}$, $^{214}\text{Pb-Bi}$, $^{212}\text{Bi-Po}$, and $^{214}\text{Bi-Po}$ level schemes. The daughter level schemes can be seen in Fig. 1.

For ^{212}Bi (^{212}Po) the energies of the three (four) key levels in terms of β feeding (see Table II) are very well described

TABLE I. Allowed transitions involved in our total β -spectrum analyses. The evaluated [3] branching ratios are reproduced by fitting the values of the Fermi and/or Gamow-Teller NME since the β shapes of allowed decays are universal.

En. (MeV)	J^π	B.R
$^{214}\text{Pb}(0^+) \rightarrow \text{Bi}$		
0.839	1^+	2.75(8)%
$^{214}\text{Bi}(1^-) \rightarrow \text{Po}$		
1.995	1^-	1.192(21)%
2.448	1^-	2.78(6)%

and the maximum deviation between the experimental and computed level energies is some 60 keV (100 keV), see the upper two panels of Fig. 1 and Table II. For ^{214}Bi (lower left panel of Fig. 1) the deviation between the experimental and computed energies of the four key levels is below some 150 keV, see Table II. In Table II we have chosen the 351 keV level to be of spin-parity 0^- since it is strongly preferred by the NSM calculation: For the ^{212}Pb decay the evaluation [3] confirms angular momentum 0 for the daughter state corresponding to the large branching, 81.5%. Similar behavior could be expected for ^{214}Pb , only two neutrons away from ^{212}Pb . In addition, the choice of 0^- spin-parity guarantees a match between the numbers of the evaluated and computed 0^- and 1^- states below 0.5 MeV in ^{214}Bi . Moreover, the choice of the 0^- spin-parity also allows the chosen ε_{MEC} to fit perfectly the branchings of both strong transitions (there is no sNME to be used for the fit, see Table II).

The spectrum of ^{214}Po (lower right panel of Fig. 1) extends to higher energies than those depicted in Fig. 1. However,

TABLE II. Values of the small vector NME (sNME, columns 5 and 6) for each decay and individual transition (evaluation excitation energy, computed excitation energy, spin-parity of the final state, and the branching to this state are reported in columns 1, 2, 3, and 4, respectively) of interest in this work (i.e., having a non-negligible branching). These values reproduce the experimental branching ratio of the given transition. The numbers with an asterisk (*) denote the sNME closer to the CVC-predicted one (last column) and are the choice for the crossed-blue curves of Fig 3. The data for the excitation energies are taken from the evaluation [3]. It should be noted that for the ^{212}Bi decay the total branching to β^- transitions is 64.06%.

Eval. En. (MeV)	Comp. En. (MeV)	J^π	B.R.	sNME ⁽¹⁾	sNME ⁽²⁾	CVC
$^{212}\text{Pb}(0^+) \rightarrow \text{Bi}$						
0.238	0.181	0^-	81.5(10)% ^a	—	—	—
0.000	0.000	1^-	13.7(10)%	-0.0916	-0.0278*	0.0982
0.415	0.474	1^-	5.01(7)%	0.3448*	0.0293	0.6264
$^{214}\text{Pb}(0^+) \rightarrow \text{Bi}$						
0.351	0.302	0^-	44.5(7)% ^{a,c}	—	—	—
0.295	0.411	1^-	39.0(5)%	-0.4404*	-0.0890	-0.6002
0.000	0.000	1^-	12.7(9)%	-0.1182	-0.0076*	0.0924
0.533	0.673	1^-	1.063(18)%	0.0882	-0.0244*	-0.4945
0.259	0.493	2^-	0.075(20)% ^f	—	—	—
$^{212}\text{Bi}(1^-) \rightarrow \text{Po}$						
0.000	0.000	0^+	55.37(12)%	0.0075*	-0.0261	0.0458
0.727	0.789	2^+	4.47(11)%	-0.0209*	-0.0010	-0.0373
1.620	1.515	1^+	1.86(4)%	0.0855*	0.0380	0.0709
1.512	1.430	2^+	1.44(4)%	0.0844	0.0426*	0.0103
1.806	1.881	2^+	0.66(3)% ^b	0.0028	0.0693*	0.0449
$^{214}\text{Bi}(1^-) \rightarrow \text{Po}^e$						
0.000	0.000	0^+	19.2(4)%	-0.0080	0.0080*	0.0387
1.729	1.791	2^+	17.5(10)%	0.1140*	0.0453	0.0990
1.764	1.780	1^+	16.9(11)%	0.0869	0.0376*	0.0498
1.847	1.807	2^+	8.16(5)%	-0.0442*	0.0104	-0.0720
1.377	1.390	2^+	7.22(8)%	-0.0225*	-0.0523	-0.0298
2.118	2.066	1^+	4.33(4)% ^b	0.0489*	0.0124	0.1249
1.543	1.593	2^+	3.09(4)% ^b	-0.0361*	-0.0132	-0.0892
2.017	2.026	0^+	2.459(15)% ^b	0.0378*	-0.0001	0.0275
2.010	1.994	2^+	1.433(11)%	-0.0605*	-0.0324	-0.0501
1.415	1.353	0^+	0.90(5)% ^b	0.0232	0.0124*	0.0126
2.204	2.209	1^+	5.56(5)% ^d	0.0026	—	0.0101
2.728	2.833	1^+	0.542(22)% ^d	-0.0166	—	-0.0675

^aFitted to the experimental half-life using only ε_{MEC} . Does not participate in the sNME fitting process.

^bTransition with beta-spectrum shape independent of the sNME, small branching ratio, or both. Does not contribute to differences in the total spectral shape.

^cThe NSM calculations strongly prefer the spin-parity assignment 0^- out of the two choices 0^- , 1^- offered by the ENSDF [3] evaluation.

^dDoes not reproduce the ENSDF [3] branching. The value chosen is the one in which the branching is minimized, thus only one sNME value is indicated. NSM branchings are then 7.57% and 2.59%, respectively.

^eAnother 33 transitions were considered in the spectrum and their total branching corresponds to 9.59%, with their major contributions within the electron energies of 0 to 500 keV.

^fThere are no sNME/l-NME values for forbidden unique transitions. The fit was done by changing the associated NME.

we compare the experimental and computed energies of the levels fed by first-forbidden transitions, and relevant for the computation of the total β spectrum, in Table II. From Fig. 1 and Table II one can see that all the measured multipole states J^π below some 1.7 MeV of excitation are described very well by the NSM. In turn, Table II indicates that above 1.7 MeV the correspondence of the computed and experimental energies is still fabulously good. Also, the level schemes for the (grand)mother nuclei ^{212}Pb and ^{214}Pb are well described by the presently used Hamiltonian.

After the level schemes were produced for the discussed isotopes, the β^- -decay transitions from the ^{212}Pb , ^{214}Pb ,

^{212}Bi , and ^{214}Bi , in their corresponding ground states, 0^+ , 0^+ , $1^{(-)}$, and 1^- , to the states of their correspondent daughters ^{212}Bi , ^{214}Bi , ^{212}Po , and ^{214}Po , were computed. All the possible decay transitions from allowed transitions up to first-forbidden unique and nonunique were investigated within the decays Q windows. Thus, for the decays starting from a 0^+ state, the daughter states $0^{+,-}$, $1^{+,-}$, 2^- were considered, and for the parent nuclei having a 1^- ground state, the daughter states $0^{+,-}$, $1^{+,-}$, $2^{+,-}$, and 3^+ were included.

We adopted the following Q values for all our computations: $Q = 0.5691(18)$, $1.018(11)$, $2.2515(17)$, $3.269(11)$ MeV, respectively, for ^{212}Pb , ^{214}Pb , ^{212}Bi , and ^{214}Bi , as

taken from the mass evaluation [4]. Lastly, for the excited states that most contribute experimentally to the total β^- spectrum, i.e., for those transitions having the highest experimental branching ratios, the computations used the best available endpoint energies by adopting the evaluated excitation energies [3] instead of the computed ones. This was done due to the high β^- -decay rates sensitivity to the available endpoint energy. Here, we note that the allowed decays studied were fit to the experimental branchings by adjusting the values of the Fermi and/or Gamow-Teller NME. This is possible since the β spectral shapes of allowed transitions are universal and thus we can take these decays exactly into account in our total spectral-shape calculations. The spin-parities and branchings of these transitions can be seen in Table I.

III. RESULTS

Here, we detail the steps involved in the calculations. The predicted decay branchings, partial half-lives, and electron spectral shapes depend on the available endpoint energies, equal to the Q value for the ground-state transition, taken from the evaluations [3,4] in the present work. There is also a dependence on the values of g_A^{eff} and ε_{MEC} , the latter solely for $\Delta J = 0$ transitions. To have a reasonable theoretical description of the β spectral shapes, one must choose how to best approach systematically the values of g_A^{eff} and ε_{MEC} . We have done so in the following manner.

A. Determination of the values of the axial couplings

Assessing the proper values of g_A^{eff} and ε_{MEC} is rather cumbersome, as reviewed in [16,22]. However, for our current study, previous works shed light on these values. In a previous study Haselschwardt *et al.* [23] performed NSM calculations of the β decay of ^{214}Pb using the same interaction *khpe*. There, the value of $g_A^{\text{eff}} = 0.85$ was selected as the most reasonable one and hence we use the same value in the present calculations, as well.

Next, for determining the value of ε_{MEC} , we took the two ε_{MEC} -dependent transitions in ^{212}Pb and ^{214}Pb , from 0^+ to 0^- , with the experimental branching ratios of 81.5(1)% and 44.5(7)%, respectively, and calculated their half-lives for a range of $g_A^{\text{eff}} = 0.70$ –1.35, and for ε_{MEC} ranging from 0.8 to 2.7. We then took all the $(g_A^{\text{eff}}, \varepsilon_{\text{MEC}})$ combinations reproducing the evaluation's partial half-lives for the considered transitions within a relative error of less or equal to 0.1%. The resulting values of these parameters are depicted in Fig. 2. For comparison, the value of the $(g_A^{\text{eff}}, \varepsilon_{\text{MEC}})$ doublet from a previous analysis, using the value $g_A = 1.25$, of Warburton [24], is also shown in the figure. From the curve and its error range, for our choice $g_A^{\text{eff}} = 0.85$, we obtain the enhancement-factor range $\varepsilon_{\text{MEC}} = 2.437 \pm 0.014 \pm 0.003$ (If we consider the uncertainties in Q value, branching ratio, and total half-life).

B. Dependency of the β spectral shapes on the value of the sNME

The small relativistic NME, sNME, has been found to play an important role in combined studies of β spectral shapes

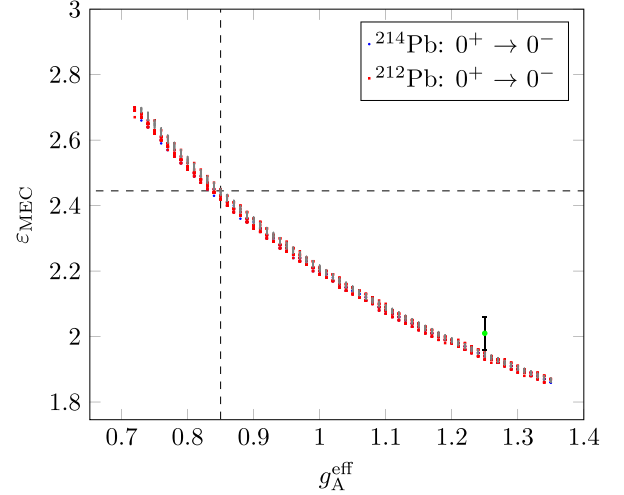


FIG. 2. Value of the enhancement factor ε_{MEC} as a function of g_A^{eff} for 0^+ to 0^- decays of experimental branchings of 81.5(1)% and 44.5(7)% [3] in ^{212}Pb and ^{214}Pb , respectively. Only solutions matching the experimental branchings within 0.1% relative error are plotted. The dashed lines point to our current choice for ^{214}Pb . The grey dots present the results when uncertainties in the Q value, branching, and total half-life are considered for the ^{212}Pb decay. The green dot with its error bars corresponds to the previous analysis of Warburton [24], however, our analysis is not directly comparable to it since in [24] many more transitions than our two were considered.

and branching ratios (partial half-lives) [7,10,11]. In these works the sNME has been used as a fitting parameter, together with g_A^{eff} and ε_{MEC} in order to yield both correct beta spectral shapes and branching ratios simultaneously. In the nuclear-structure calculations, the sNME gathers contributions outside the nucleon major shell(s) where the proton and neutron Fermi surfaces lie. Due to the limitation of the NSM valence space to these shells only, the value of the sNME turns out to be zero in the NSM calculations. The value of the sNME cannot be completely arbitrary since in an ideal case (infinite valence spaces, perfect nuclear many-body theory) the value of the sNME is tied to the value of the so-called large vector NME, 1-NME, by the CVC (conserved vector current) hypothesis [1]. The value of the 1-NME can be rather reliably computed by the NSM since the main contributions to it stem from the major shell(s) where the nucleon Fermi surfaces lie, thus being well accessible for the NSM.

Based on what was said above, one can have a good estimate of the proper value of the sNME by computing its CVC value using the formula (10.69) of [1], where the form factors have been replaced by the NMEs according to the definition (9) of [6], leading to

$${}^V \mathcal{M}_{KK-11}^{(0)} = \left(\frac{(-M_n c^2 + M_p c^2 + W_0) \cdot R}{\hbar c} + \frac{6}{5} \alpha Z \right) \times {}^V \mathcal{M}_{KK0}^{(0)}, \quad (6)$$

where the left side of the equation is the sNME, the last term on the right is the 1-NME, and K denotes the order of forbiddenness, with $K = 1$ denoting the first-forbidden decays. The quantities M_n and M_p denote neutron and proton masses, respectively. W_0 is the available endpoint energy

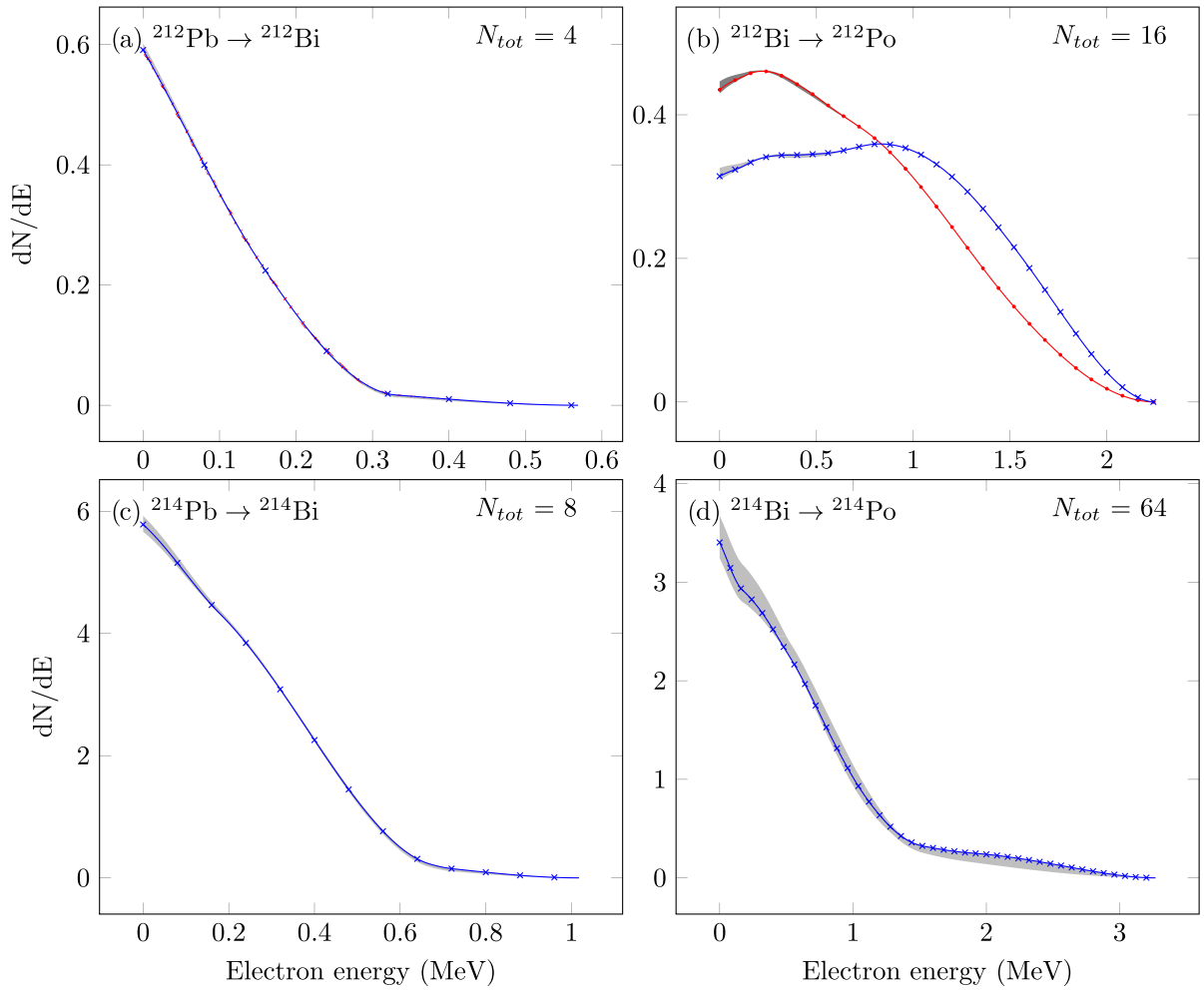


FIG. 3. Computed total β spectra and their dependencies on the choice of the sNME. The crossed-blue curves are those constructed by adopting the value closer to the CVC value for the sNME of an individual transition. The gray-hatched regions denote the span of the curves obtained through the N_{tot} (displayed at the top-right corner of each panel) different combinations of the two possible values of sNMEs listed in Table II. The dotted-red curve in (b) uses the value of the sNME further away from its CVC value for the important $^{212}\text{Bi} \rightarrow ^{212}\text{Po}(\text{g.s.})$ transition, the gray-hatched region being constructed as for the crossed-blue curve. In (a), an error budget, considering the uncertainties of the crossed-blue curve in the Q value, branchings, and total half-life, is presented by the red-dashed region. These spectral shapes are available from the authors at request. For more information see the text.

for the decay, \hbar the reduced Planck constant, α is the fine-structure constant, and c the speed of light. Lastly, Z is the atomic number of the daughter nucleus, and $R = 1.2A^{1/3}$ is the nuclear radius in fm [2], A being the nuclear mass number.

In our calculations, we adopt the approach of fitting the sNME such that each individual β^- transition with non-negligible experimental branching can be reproduced in terms of the branching ratio. There is a quadratic dependency of the computed branching ratios (partial half-lives) on the value of the sNME and hence two values of the sNME, for each decay transition, reproduce the experimental branching corresponding to this transition. One of these two sNMEs is closer to the CVC value of the sNME and thus offers a way to define the “optimal” β spectral shape: Choosing always the sNME closer to its CVC value produces the most probable total spectral shape, depicted as crossed-blue “CVC” curves in Fig. 3. The

through-the-fit obtained values for the sNMEs are displayed in Table II. As seen in the table, in most cases the selected sNME for the CVC curve is notably closer to the CVC value of sNME than the other solution, making the selection justifiable and the CVC spectrum a robust choice.

The sNME fitting produces two beta spectral curves for each transition. As mentioned above, the CVC curve uses those sNME values closer to their CVC values. The other possible curves are obtained by taking all the $2^N - 1$ combinations of the values of the sNME, N denoting the number of transitions considered. The number $N_{tot} = 2^N$ is indicated at the top-right corner of each panel of Fig. 3 and ranges from 4 (^{212}Pb decay) to 64 (^{214}Bi decay, where only the 12 most important transitions as shown in Table II were taken into the sNME variation analysis). Here, it is important to note that all decays in ^{214}Bi that are energetically allowed and predicted by the NSM are accounted for,

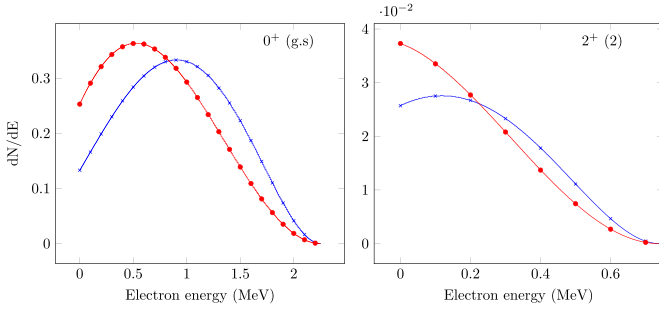


FIG. 4. β spectral shapes of the two transitions that are mostly affected by the choice between the two possible values of the sNME in Table II. These are the transitions from ^{212}Bi to the ground state (left panel) and the second excited 2^+ state (right panel) in ^{212}Po . The crossed-blue (dotted-red) curve represents the choice closer (farther) from the CVC value of the sNME.

therefore some possibly relevant states, such as those with energies 2.482 MeV (1.192%), 2.192 MeV (0.866%), and 1.890 MeV (1.589%), are accounted for. However, these states were not fitted using the sNME method since their ENSDF spin assignments were not definitive and their energies were not unequivocally predicted by the NSM level schemes so they could not be reliably identified. These states are, instead, included in the 33 transitions that are not displayed in Table II and account for a total of 9.59% of the total half-life.

All the 2^N curves form the gray-hatched region around the “optimal” CVC curve. A notable exception is the decay of ^{212}Bi where two curves appear in panel b) of Fig. 3. In addition to the crossed-blue CVC curve, there appears a dotted-red curve and its gray-hatched region. This curve is obtained by picking the value $\text{sNME} = -0.0261$ instead of the value $\text{sNME} = 0.0075^*$ (which is closer to the CVC value $\text{sNME} = 0.0458$) in the first line of the $^{212}\text{Bi} \rightarrow ^{212}\text{Po}$ decay in Table II. The gray-hatched region then emerges as in the case of the CVC curve.

The two curves in panel b) of Fig. 3 are presented in order to show that the value of the sNME can have a drastic effect on the β spectral shape. This effect is the strongest for the decay of ^{212}Bi to the ground state and the second 2^+ state (at an excitation energy of 1.512 MeV) in ^{212}Po , as shown in Fig. 4. In terms of the total β spectrum, panel b) of Fig. 3, the effect of the ground-state transition is the more important one owing to its much larger branching 55.37(12)% as compared to 1.44(4)% of the 2^+_2 state.

Lastly, considering the effect of the ENSDF evaluation’s uncertainty in the Q value, branching ratios, and total half-life on the CVC curve of the $^{212}\text{Pb} \rightarrow ^{212}\text{Bi}$ decay, as seen in panel a) of Fig. 3, produces a negligible difference in the spectral shape. However, due to the additive nature of experimental uncertainties the effect is expected to be stronger, the more curves the analysis involves and the higher the relative error in the Q value, making the most susceptible the $^{212}\text{Bi} \rightarrow ^{212}\text{Po}$ decay due to the 1.080% relative error in the Q value (versus the 0.3162% for the $^{212}\text{Pb} \rightarrow ^{212}\text{Bi}$ decay) and $^{214}\text{Bi} \rightarrow ^{214}\text{Po}$ due to the large number of curves. However, as shown by the error analysis of the $^{212}\text{Pb} \rightarrow ^{212}\text{Bi}$ decay, we do not

expect that the cumulative effect of the uncertainties in the Q values, branching ratios, and total half-lives on the presently discussed β spectral shapes are so large as to compete with the uncertainty associated with the selection of the values of the sNME. We have thus omitted the corresponding tedious analyses for the $^{212,214}\text{Bi}$ and ^{214}Pb decays.

IV. CONCLUSIONS

We believe that the present systematic study of β spectral shapes of key Pb and Bi nuclei in the ^{220}Rn and ^{222}Rn chains could be useful to the large underground experiments that struggle with background spectra from these chains. The ^{222}Rn and ^{220}Rn nuclei α decays to ^{218}Po and ^{216}Po , which then once again α decays to ^{214}Pb and ^{212}Pb , respectively, and from there the presently studied β^- decays emerge. It is almost impossible to get rid of these contaminants in the rare-events experiments, such as neutrino and dark-matter experiments. The continuous nature of β^- decays and their β electron shapes is a severe challenge in the calibration of the experimental set-ups since one has been relying on software such as GEANT4 [25] with its radioactive decay module or BETASHAPE [26] in the simulations of β decays. The problem with these methods is that they do not take into account the important part played by the nuclear structure in the form of nuclear matrix elements. These softwares can implement measured β spectral shapes but use allowed β shapes or forbidden unique β shapes as surrogates for non-unique decays. This can be dangerous since the non-unique β decays can be extremely dependent on the NMEs and thus affect strongly the calibration of the rare-events experiments.

We believe that the current study can help solve the calibration issue for the β decays of the Pb and Bi nuclei in the ^{220}Rn and ^{222}Rn decay chains. This study has inherent uncertainties: The proper values of g_A^{eff} , ε_{MEC} , and sNME. However, for the presently studied β decays there is no strong dependence of the β spectral shapes on the values of g_A^{eff} and ε_{MEC} , only the fitted branchings depend on them. The dependence of the β spectral shapes on sNME is there, but it is quite moderate for the decays of $^{212,214}\text{Pb}$ and ^{214}Bi , as can be seen in Fig 3, panels (a), (c), and (d). In this figure, panel (b) serves only as an example of the possibility for a large variation of the total spectral shape when even one individual transition, with a large branching, has a strong dependency on the value of the sNME. But even in this case the CVC-based crossed-blue line, with little uncertainty, is the one which should be taken as a paradigm. In any case, our computed spectral shapes make these total β spectra worth studying using experiments like [13]. In addition, the β spectra of individual transitions, listed in Table II, form interesting objects of study using other types of spectral-shape measurements, like ACCESS [8]. By these experiments, a lot can be learned about the appropriate values of the key parameters of β -shape calculations.

Lastly, we note that the present analyses are model dependent: In this case, we use the Hamiltonian $khpe$. However, we believe that this Hamiltonian nicely captures the physics of the involved nuclei, since the level schemes are well reproduced and this particular effective interaction was designed precisely

for the presently studied nuclear region. Further investigations of nuclei and interactions in this particular nuclear region could further shed light on the reliability of the computed β spectral shapes that are important for rare-events experiments.

ACKNOWLEDGMENT

We acknowledge the support by CSC – IT Center for Science, Finland, for the generous computational resources.

-
- [1] H. Behrens and W. Bühring, *Electron Radial Wave Functions and Nuclear Beta-Decay*, International Series of Monographs on Physics (Clarendon Press, Oxford, UK, 1982).
- [2] J. Suhonen, *From Nucleons to Nucleus: Concepts of Microscopic Nuclear Theory* (Springer-Verlag, Berlin/Heidelberg and Springer, Gaithersburg MD, 2007).
- [3] From ENSDF database as of Nov. 2023, version available at <http://www.nndc.bnl.gov/ensarchivals/>.
- [4] M. Wang, W. Huang, F. Kondev, G. Audi, and S. Naimi, *Chin. Phys. C* **45**, 030003 (2021).
- [5] M. Ramalho, J. Suhonen, J. Kostensalo, G. A. Alcalá, A. Algora, M. Fallot, A. Porta, and A.-A. Zakari-Issoufou, *Phys. Rev. C* **106**, 024315 (2022).
- [6] M. Haaranen, J. Kotila, and J. Suhonen, *Phys. Rev. C* **95**, 024327 (2017).
- [7] A. Kumar, P. C. Srivastava, and J. Suhonen, *Eur. Phys. J. A* **57**, 225 (2021).
- [8] L. Pagnanini, G. Benato, P. Carniti, E. Celi, D. Chiesa, J. Corbett, I. Dafinei, S. Di Domizio, P. Di Stefano, S. Ghislandi *et al.* (ACCESS Collaboration), *Eur. Phys. J. Plus* **138**, 445 (2023).
- [9] L. Bodenstern-Dresler, Y. Chu, D. Gehre, C. Gössling, A. Heimbald, C. Herrmann, R. Hodak, J. Kostensalo, K. Kröniger, J. Küttler *et al.* (COBRA Collaboration), *Phys. Lett. B* **800**, 135092 (2020).
- [10] J. Kostensalo, J. Suhonen, J. Volkmer, S. Zatschler, and K. Zuber, *Phys. Lett. B* **822**, 136652 (2021).
- [11] J. Kostensalo, E. Lisi, A. Marrone, and J. Suhonen, *Phys. Rev. C* **107**, 055502 (2023).
- [12] A. F. Leder, D. Mayer, J. L. Ouellet, F. A. Danevich, L. Dumoulin, A. Giuliani, J. Kostensalo, J. Kotila, P. de Marcillac, C. Nones, V. Novati, E. Olivieri, D. Poda, J. Suhonen, V. I. Tretyak, L. Winslow, and A. Zolotarova, *Phys. Rev. Lett.* **129**, 232502 (2022).
- [13] V. Guadilla, A. Algora, M. Estienne, M. Fallot, W. Gelletly, A. Porta, L.-M. Rigalleau, and J.-S. Stutzmann, [arXiv:2305.13832](https://arxiv.org/abs/2305.13832) [physics.ins-det].
- [14] M. Haaranen, P. C. Srivastava, and J. Suhonen, *Phys. Rev. C* **93**, 034308 (2016).
- [15] H. Ejiri, J. Suhonen, and K. Zuber, *Phys. Rep.* **797**, 1 (2019).
- [16] J. T. Suhonen, *Front. Phys.* **5**, 55 (2017).
- [17] J. Kostensalo and J. Suhonen, *Phys. Lett. B* **781**, 480 (2018).
- [18] K. Kubodera and M. Rho, *Phys. Rev. Lett.* **67**, 3479 (1991).
- [19] N. Shimizu, T. Mizusaki, Y. Utsuno, and Y. Tsunoda, *Comput. Phys. Commun.* **244**, 372 (2019).
- [20] E. K. Warburton and B. A. Brown, *Phys. Rev. C* **43**, 602 (1991).
- [21] B. A. Brown and W. D. M. Rae, *Nucl. Data Sheets* **120**, 115 (2014).
- [22] J. Suhonen and J. Kostensalo, *Front. Phys.* **7**, 29 (2019).
- [23] S. J. Haselschwardt, J. Kostensalo, X. Mougeot, and J. Suhonen, *Phys. Rev. C* **102**, 065501 (2020).
- [24] E. K. Warburton, *Phys. Rev. C* **44**, 233 (1991).
- [25] S. Agostinelli, J. Allison, K. Amako, J. Apostolakis, H. Araujo, P. Arce, M. Asai, D. Axen, S. Banerjee, G. Barrand *et al.*, *Nucl. Instrum. Methods Phys. Res. A* **506**, 250 (2003).
- [26] X. Mougeot, *Appl. Radiat. Isot.* **201**, 111018 (2023).

III

SHELL-MODEL TREATMENT OF THE β DECAY OF ^{99}TC

by

Ramalho, M and Suhonen, J

arXiv (Submitted to Il Nuovo Cimento C) **2312.07448**, (2023).

DOI: arXiv:2312.07448

Reproduced with kind permission of Società Italiana di Fisica.

Shell-model treatment of the β decay of ^{99}Tc

M. RAMALHO⁽¹⁾ and J. SUHONEN⁽¹⁾⁽²⁾

⁽¹⁾ *Department of Physics, University of Jyväskylä, P.O. Box 35, FI-40014, Jyväskylä, Finland*

⁽²⁾ *International Centre for Advanced Training and Research in Physics (CIFRA), P.O. Box MG12, 077125 Bucharest-Magurele, Romania*

Summary. — In the present paper we treat the second-forbidden non-unique (2nd-nu) ground-state-to-ground-state β^- decay $^{99}\text{Tc}(9/2^+) \rightarrow ^{99}\text{Ru}(5/2^+)$, with a 100% branching ratio, within the framework of the nuclear shell model (NSM). The energy spectrum of the electrons emitted in this β -decay transition (β -electron spectrum) is sensitive to the wave functions of the involved initial ($9/2^+$) and final ($5/2^+$) nuclear ground states through the many involved nuclear matrix elements (NME). The β -electron spectrum of this transition is potentially indicative of the effective value, g_A^{eff} , of the weak axial coupling, g_A , of crucial importance for extraction of information on beyond-the-standard-model physics from the results of the present and future rare-events experiments. We describe the β spectral shape of this decay by using a state-of-the-art β -decay formalism and compute the many involved NME using the well established NSM Hamiltonians *jj45pnb* and *glekpn*. We have found a strong dependence of the β spectral shape on the value of g_A making it a good candidate for determination of the value of g_A^{eff} through comparison with the corresponding experimental β spectral shape. We have also found an interesting dependence of the β spectral shape on the value of the so-called small relativistic vector NME, sNME, used to match the computed half-life with the measured one.

1. – Introduction

Rare-events experiments typically look for beyond-the-standard-model (BSM) physics by, e.g., measuring rare nuclear β decays, double β decays, and (anti)neutrino and WIMP (weakly interacting massive particle) scatterings off nuclei in searches for astrophysical neutrinos and cold dark matter of the Universe. In recent years, a booming interest in these experiments has concentrated on studies of β electrons (electrons emitted in β^- decays) and their energy distributions, the so-called β -electron spectra. Experimental and/or theoretical information on these spectra is crucial for, e.g., resolving the anomalies related to the antineutrino flux from nuclear reactors and for resolving the common backgrounds in the rare-events experiments themselves. Also, pinning down the effective

values of weak couplings is a considerable incentive for those present and future β -decay experiments able to tackle the spectral shapes of β electrons, see the review [1].

Nuclear β decays vary in complexity: from allowed to highly forbidden ones [2, 3]. Like in the case of allowed β decays, also in the case of forbidden unique β decays the lepton phase space can be separated from the nuclear part, resulting in a universal β spectral shape, independent of nuclear-structure details [2]. Of special interest for the rare-events experiments are the forbidden non-unique β decays for which the β spectral shapes can be strongly nuclear-structure dependent through several nuclear matrix elements (NME). The values of these NME are non-trivially determined by the wave functions of the initial and final states of a β -decay transition.

In addition to the many NME, the (partial) half-life of a forbidden non-unique β transition depends on the values of the weak vector and axial-vector couplings, g_V and g_A [3]. In atomic nuclei, the CVC (conserved vector current) hypothesis sets the value $g_V = 1.0$, whereas the PCAC (partially conserved axial-vector current) hypothesis leads only to the so-called effective value of g_A , recently discussed in the reviews [1, 4, 5]. On the other hand, the so-called bare-nucleon value $g_A = 1.27$ stems from data on the decay of an isolated neutron. Typically, the effective value of g_A is quenched relative to the bare-nucleon value which can have drastic effects on the sensitivity estimates of rare-events experiments trying to detect the neutrinoless double beta decay [6, 7], of crucial importance in the search for the BSM physics. Only in rare cases there is an enhancement of g_A present [8].

As discussed in [9, 10], information on the value of g_A can be gained by using the so-called spectrum-shape method (SSM). Use of SSM requires a β -electron spectrum with a notable g_A dependence in its shape. In this case information on the effective value of g_A can be gained through the comparison of computed template β spectra, for different g_A values, with the measured one in the aim to find a match. Such SSM analyses of β -spectral shapes of individual β^- transitions have been done recently for the fourth-forbidden non-unique β decays of ^{113}Cd and ^{115}In in [11, 12, 13].

An additional ingredient in the theoretical analyses of β spectral shapes is the so-called small relativistic vector NME, the sNME, used to fix the measured (partial) half-life in the so-called enhanced SSM [14, 15]. In spite of its smallness, sNME can influence the (partial) half-lives and shapes of β -electron spectra quite strongly, see [12, 16, 17]. The sNME gathers its major contributions outside the proton (neutron) valence major shell that contains the proton (neutron) Fermi surface making it hard to be calculated in many nuclear models.

In the present paper we investigate the g_A and sNME dependence of the second-forbidden non-unique (2nd-nu) β^- decay of the $9/2^+$ ground state of ^{99}Tc to the $5/2^+$ ground state of ^{99}Ru , with a branching ratio of 100%.

2. – Theoretical Background

2.1. NSM Hamiltonians. – The NSM calculations were performed using the software KSHELL [18] with the interactions *jj45pnb* [19] and *glekpn* [20] with the set of single-particle energies fit for the mass region of $A = 94 - 98$. Their model spaces consist of the proton $0f_{5/2}^{(2)}-1p_{3/2}-1p_{1/2}-1g_{9/2}$ orbitals and the neutron $0g_{7/2}-1d_{5/2}-1d_{3/2}-2s_{1/2}-0h_{11/2}$ orbitals for *jj45pnb*, as well as $0f_{7/2}^{(1)}-0f_{5/2}^{(2)}-1p_{3/2}-1p_{1/2}-1g_{9/2}$ proton orbitals and $0g_{9/2}^{(1)}-0g_{7/2}-1d_{5/2}-1d_{3/2}-2s_{1/2}$ neutron orbitals for *glekpn*. The restrictions in the orbital occupations are imposed in order to reduce the computational burden. We believe,

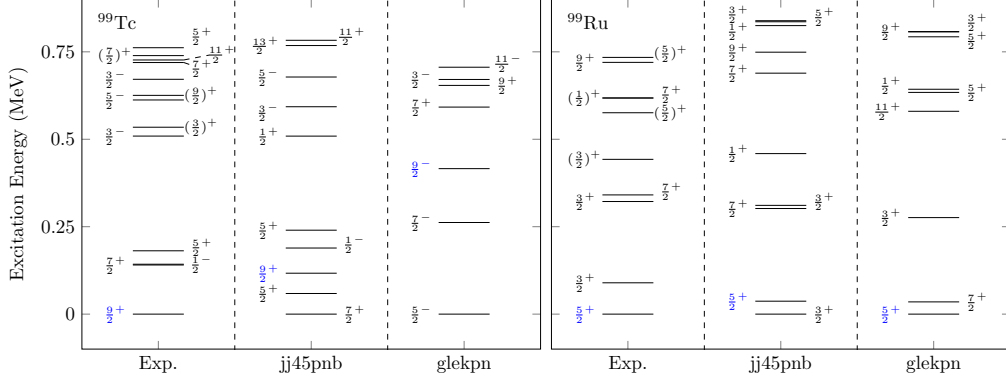


Fig. 1.: Energy level schemes for ^{99}Tc and ^{99}Ru with their corresponding NSM-computed values using the interactions $jj45pnb$ and $glekpn$. Experimental data are taken from the ENSDF [21] evaluation. Levels in blue are the initial and final states relevant for this work.

however, that these posed limitations do not affect much the wave functions of the initial and final ground states, relevant for the present work.

With the considered truncations we have calculated the excitation spectra for both interactions and compare them with the experimental spectrum in Fig 1. It can be seen that the $jj45pnb$ Hamiltonian works, overall, much better than the $glekpn$ one, in particular for the ground state of ^{99}Tc .

To further assess the reliability of the Hamiltonians employed, we have analyzed the magnetic dipole and electric quadrupole moments of the ^{99}Tc and ^{99}Ru ground states. The analysis can be seen in Table I, where once again the $jj45pnb$ Hamiltonian does better overall than the $glekpn$ Hamiltonian.

2.2. β spectral shapes and half-lives. – The half-life of a β transition can be obtained from $t_{1/2} = \kappa/\tilde{C}$, where κ is a constant [14, 15] and \tilde{C} is the integrated shape function C ,

⁽¹⁾ Orbital fixed with maximum amount of nucleons, e.g, 8 for $0f_{7/2}$.

⁽²⁾ Orbital with at least 4 particles.

TABLE I.: Comparison of experimental and theoretical ($jj45pnb$ and $glekpn$ Hamiltonians) nuclear magnetic dipole (in units of nuclear magneton) and electric quadrupole (in units of barns) moments for ^{99}Tc and ^{99}Ru , for the experimental ground states and their correspondents in theory.

	$^{99}\text{Tc}(9/2^+)$			$^{99}\text{Ru}(5/2^+)$		
	Exp.	jj45pnb	glekpn	Exp.	jj45pnb	glekpn
μ (μ_N)	+5.678(2)	+5.662	+5.4160	-0.641(5)	-0.2875	+1.0826
Q (b)	-0.129(6)	+0.0218	+0.2428	+0.079(4)	-0.0018	-0.3222

TABLE II.: Values of the small relativistic NME emerging from the fitting procedure for the $^{99}\text{Tc}(9/2^+) \rightarrow \text{Ru}(5/2^+)$ decay. The sNME values (1) and (2) shown reproduce the experimental half-life for their given $g_{\text{A}}^{\text{eff}}$.

jj45pnb - CVC = -0.1705			glekpn - CVC = -0.0080		
$g_{\text{A}}^{\text{eff}}$	sNME ⁽¹⁾	sNME ⁽²⁾	$g_{\text{A}}^{\text{eff}}$	sNME ⁽¹⁾	sNME ⁽²⁾
0.8	0.0496	-0.0856	0.8	0.1042	-0.0311
0.9	0.0582	-0.0772	0.9	0.1091	-0.0257
1.0	0.0666	-0.0687	1.0	0.1140	-0.0202
1.1	0.0750	-0.0601	1.1	0.1189	-0.0148
1.2	0.0833	-0.0515	1.2	0.1237	-0.0093

full of phase-space factors and NMEs in the next-to-leading-order expansion, as discussed in detail in [9, 10]. Our calculations employ screening, radiative, and atomic exchange corrections. The most essential to the current study, due to its small β -decay Q value, is the atomic exchange correction which was originally derived for allowed β decays [22]; the effects of this correction are the most important for electron energies below 50 keV.

The complexity of the shape function C can, however, be cast in a very simple dependence on the weak couplings by writing

$$(1) \quad C(w_e) = g_{\text{V}}^2 C_{\text{V}}(w_e) + g_{\text{A}}^2 C_{\text{A}}(w_e) + g_{\text{V}} g_{\text{A}} C_{\text{VA}}(w_e),$$

where w_e is the total (mass plus kinetic) energy of the emitted electron. The variation of the shape of the β -electron spectrum with the value of g_{A} comes from the subtle interference of the combined vector $C_{\text{V}}(w_e)$ and axial $C_{\text{A}}(w_e)$ parts with the mixed vector-axial part $C_{\text{VA}}(w_e)$ [9].

For the currently studied 2nd-nu decay transition $^{99}\text{Tc}(9/2^+) \rightarrow ^{99}\text{Ru}(5/2^+)$ we take the CVC-compatible value $g_{\text{V}} = 1.0$ for the weak vector coupling, and explore the impact of the quenched $g_{\text{A}}^{\text{eff}}$ values, ranging from 0.8 – 1.2 (see Table II), on the β spectral shape.

2.3. Small relativistic Nuclear Elements. – An important contributor to the β spectral shape and the half-life is the small relativistic NME (sNME) [12, 15, 16, 17]. In these works, by fitting the value of the sNME, alongside with $g_{\text{A}}^{\text{eff}}$, one is able to reproduce both the β spectral shape and the half-life of a β transition. The computation of the value of the sNME is a challenge for the NSM. This is why its CVC value (also presented in Table II) can be used as a reference [3]. It should be noted, though, that the CVC value represents an "ideal", pertaining to a perfect many-body theory, which is not the case for NSM, mainly due to its restricted proton and neutron valence spaces.

Following the philosophy adopted in [12, 15, 16, 17], we search for the values of the sNME that reproduce the experimental half-life of the $^{99}\text{Tc}(9/2^+) \rightarrow \text{Ru}(5/2^+)$ transition. Since the β -decay rate has a quadratic dependency on the sNME, two solutions are usually found for each value of $g_{\text{A}}^{\text{eff}}$, as presented in Table II.

3. – Results for the β spectral shapes

The β -decay transition of interest, $^{99}\text{Tc}(9/2^+) \rightarrow \text{Ru}(5/2^+)$, is 2nd-nu and is sensitive to the Q value of the decay. Thus, to ensure reliability of our β spectral-shape calcula-

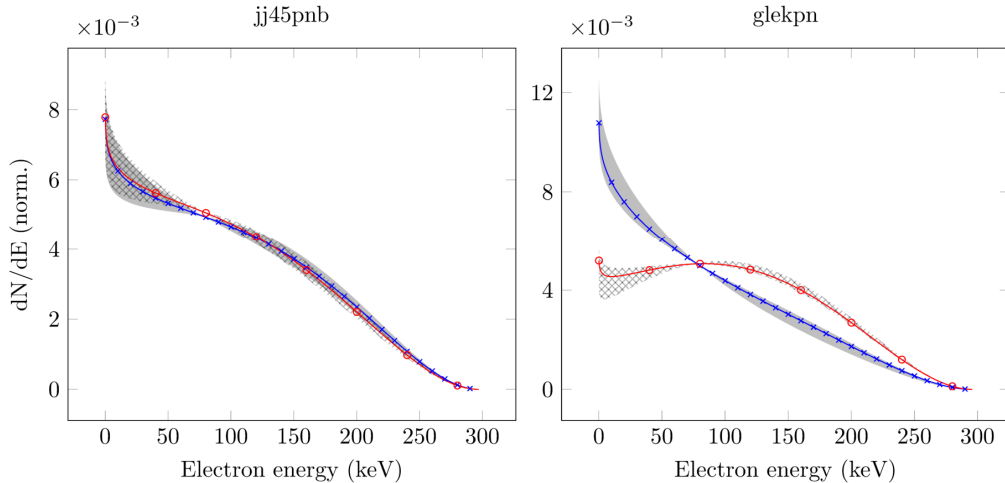


Fig. 2.: Computed β spectral shapes for the decay transition $^{99}\text{Tc}(9/2^+) \rightarrow \text{Ru}(5/2^+)$ using the Hamiltonians $jj45pnb$ (left panel) and $glekpn$ (right panel). The crossed-blue curves correspond to the fitted sNME closest to the CVC-value and the circled-red to the farthest (see Table II), with $g_A^{\text{eff}} = 1.0$. The gray-hatched (gray-crossed) area corresponds to the range $g_A^{\text{eff}} = 0.8 - 1.2$ with all the fitted sNME values chosen closest to (farthest from) the corresponding CVC values. All curves are normalized to unit area under them.

tions, we have fixed the energy difference of the initial $9/2^+$ and final $5/2^+$ state by the experimental Q value. We plot our results for the β spectral shapes of this transition in Fig. 2. There the crossed-blue (circled-red) curves correspond to a typical moderately quenched value $g_A^{\text{eff}} = 1.0$ [4] and the fitted sNME value closer to (farther from) its CVC value, see Table II. The gray-hatched (gray-crossed) area, in turn, corresponds to the range $g_A^{\text{eff}} = 0.8 - 1.2$ with all the sNME values chosen closest to (farthest from) the corresponding CVC values, the sNME values being shown in Table II. Interestingly enough, the two different options for the sNME value (the two different hatched regions in Fig. 2) sometimes produce drastically different shapes, as can be seen for $glekpn$, a pattern also recorded in [17]. As for the interaction $jj45pnb$, both hatched regions overlap nicely and there seems not to be any strong dependency of the β spectral shape on the choice of the value of sNME.

Since the β spectral shapes produced by the two interactions clearly disagree, it is hard to judge which one of the shapes is the more realistic one. Based on both the level schemes in Fig. 1 and the magnetic and electric moments of Table I it is tempting to say that the $jj45pnb$ Hamiltonian is better suited for these particular nuclei. Furthermore, looking at a recently measured experimental β spectral shape for this transition in [23], especially in their Fig. 5, one can see a striking resemblance of it to the spectral shapes for both fitted sNME^(1,2) of the $jj45pnb$ Hamiltonian (see Table II) and a bit less striking for the solution sNME⁽²⁾ for the $glekpn$ Hamiltonian. However, only a proper comparison with data will allow us to draw any definite conclusions concerning the effective value of the axial coupling and the proper value of sNME. This we leave as a future exercise.

4. – Summary and conclusions

We have performed shell-model calculations of the β spectral shape related to the second-forbidden non-unique β^- -decay transition $^{99}\text{Tc}(9/2^+) \rightarrow ^{99}\text{Ru}(5/2^+)$, with a 100% branching ratio. We use a state-of-the-art β -decay formalism and compute the many involved NME using the well established NSM Hamiltonians *jj45pnb* and *glekpn*. When compared with future available data, the β -electron spectrum of this transition is potentially indicative of the effective value of the weak axial coupling, g_A , of crucial importance for extraction of information on beyond-the-standard-model physics from the results of the present and future rare-events experiments. We also point out the important role played by the small relativistic vector matrix element, used to reproduce the measured half-life of the transition, in shaping the β -electron spectrum.

5. – Acknowledgments

We acknowledge the support by CSC – IT Center for Science, Finland, for the generous computational resources, which were essential to this project.

REFERENCES

- [1] Ejiri, H., Suhonen, J., and Zuber, K., *Phys. Rep.*, **797** (2019) 1.
- [2] Suhonen, J., *From Nucleons to Nucleus: Concepts of Microscopic Nuclear Theory*, Springer, Berlin, 2007.
- [3] Behrens, H. and Bühring, W., *Electron Radial Wave Functions and Nuclear Beta-decay*, Clarendon Press, Oxford, 1982.
- [4] Suhonen, J., *Front. Phys.*, **5** (2017) 55.
- [5] Suhonen, J. and Kostensalo, J., *Front. Phys.*, **7** (2019) 29.
- [6] Engel, J. and Menéndez, J., *Rep. Prog. Phys.*, **60** (2017) 046301.
- [7] Agostini, M. et al., *Rev. Mod. Phys.*, **95** (2023) 025002.
- [8] Kostensalo, J. and Suhonen, J., *Phys. Lett. B*, **781** (2018) 480.
- [9] Haaranen, M., Srivastava, P. C., and Suhonen, J., *Phys. Rev. C*, **93** (2016) 034308.
- [10] Haaranen, M., Kotila, J., and Suhonen, J., *Phys. Rev. C*, **95** (2017) 024327.
- [11] Bodenstern-Dresler, L. et al. (The COBRA Collaboration), *Phys. Lett. B*, **800** (2020) 135092.
- [12] Kostensalo, J., Suhonen, J., Volkmer, J., Zatschler, S., and Zuber, K., *Phys. Lett. B*, **822** (2021) 136652.
- [13] Leder, A. F. et al., *Phys. Rev. Lett.*, **129** (2022) 232502.
- [14] Kumar, A., Srivastava, P. C., Kostensalo, J., and Suhonen, J., *Phys. Rev. C*, **101** (2020) 064304.
- [15] Kumar, A., Srivastava, P. C., and Suhonen, J., *Eur. Phys. J. A*, **57** (2021) 225.
- [16] Kostensalo, J., Lisi, E., Marrone, A., and Suhonen, J., *Phys. Rev. C*, **107** (2023) 055502.
- [17] Ramalho, M. and Suhonen, J., Submitted to *Phys. Rev. C* (2023).
- [18] Shimizu, N. et al., *Comp. Phys. Comm.*, **244** (2019) 372.
- [19] Lisetskiy, A. F., Brown, B. A., Horoi, M., and Grawe, H., *Phys. Rev. C*, **70** (2004) 044314.
- [20] Mach, H. and Warburton, E. K. et al., *Phys. Rev. C*, **41** (1990) 226.
- [21] From ENSDF database as of Nov, 2023. Version available at <http://www.nndc.bnl.gov/ensarchivals/>.
- [22] Nitescu, O., Stoica, S., and Simkovic, F., *Phys. Rev. C*, **107** (2023) 025501.
- [23] Paulsen, M. et al., arXiv:2309.14014 [nucl-ex].

IV

g_A -SENSITIVE β SPECTRAL SHAPES IN THE MASS $A = 86 - 99$ REGION ASSESSED BY THE NUCLEAR SHELL MODEL

by



Ramalho, M and Suhonen, J

Phys. Rev. C **109**, **3**, 034321 (2024).

DOI: 10.1103/PhysRevC.109.034321

Reproduced with kind permission of American Physical Society.

g_A -sensitive β spectral shapes in the mass $A = 86$ – 99 region assessed by the nuclear shell model

Marlom Ramalho ^{1,*} and Jouni Suhonen ^{1,2,†}

¹*Department of Physics, University of Jyväskylä, P.O. Box 35, FI-40014, Jyväskylä, Finland*

²*International Centre for Advanced Training and Research in Physics (CIFRA), P.O. Box MG12, 077125 Bucharest-Magurele, Romania*



(Received 13 December 2023; accepted 1 March 2024; published 29 March 2024)

Recent years have witnessed an expanding interest in experimental studies of β electrons (electrons emitted in β^- decay transitions) and their energy distributions, the so-called β -electron spectra. These experiments have been focused mainly on β transitions with electron spectra sensitive to the effective value of the weak axial coupling g_A . In the present paper we make an extensive search for g_A sensitive β spectral shapes in the $A = 86$ – 99 region using the nuclear shell model with the well established Hamiltonians *glekpn* and *jj45pnb*, designed to render a good description of the spectroscopic properties of nuclei in this mass region. We have found eight β^- decay transitions with various degrees of g_A sensitivity. Moreover, these transitions are also important in pinning down the value of the so-called small relativistic vector nuclear matrix element. In addition, some of the corresponding mother nuclei are important contributors to the antineutrino flux from nuclear reactors. All this means that the found β transitions are potentially of great interest for future rare-events experiments.

DOI: [10.1103/PhysRevC.109.034321](https://doi.org/10.1103/PhysRevC.109.034321)

I. INTRODUCTION

Rare-events experiments typically look for beyond-the-standard-model (BSM) physics by, e.g., measurements of rare nuclear β decays and double β decays. Lately, a booming interest in these experiments has concentrated on studies of β electrons (electrons emitted in β^- decays) and their energy distributions, the so-called β -electron spectra. Experimental and/or theoretical information on these spectra is crucial, e.g., for resolving the anomalies related to the antineutrino flux from nuclear reactors [1,2], and for resolving the common backgrounds in the rare-events experiments themselves [3]. Also, pinning down the effective values of weak couplings is a considerable incentive for those present and future β -decay experiments able to tackle the spectral shapes of β electrons. In particular, determination of the effective value of the weak axial coupling g_A is needed for the estimation of the sensitivities of experiments trying to measure the neutrinoless double beta ($0\nu\beta\beta$) decay since the $0\nu\beta\beta$ half-life is proportional to the inverse fourth power of g_A [4–6]. The implications of detection of this decay mode are fundamental as discussed in the recent reviews [7–10].

Nuclear β decays vary in complexity, from allowed to highly forbidden ones: In the allowed Fermi and Gamow-Teller decays no orbital angular momentum is transferred to the emitted leptons [11], whereas in the forbidden decays [12] a nonzero orbital angular momentum is transferred. As in the case of allowed β decays, also in the case of forbidden unique

β decays the lepton phase space can be separated from the nuclear part, resulting in a universal β spectral shape, independent of nuclear-structure details [11]. Of special interest for the rare-events experiments are the forbidden nonunique β decays for which the β spectral shapes can be strongly nuclear-structure dependent through several nuclear matrix elements (NME). These NME depend, in turn, on the structure of the wave functions of the states involved in a β -decay transition.

In addition to the many NME, the (partial) half-life of a forbidden nonunique β transition depends on the so-called effective value of g_A , recently discussed in the reviews [5,6,8]. As discussed in these reviews, the effective value of g_A is quenched relative to the bare-nucleon value $g_A = 1.27$. Only in rare cases, for first-forbidden β -decay transitions with change in parity and no change in angular momentum, is there an enhancement of g_A present [13]. As mentioned earlier, pinning down the effective value of g_A is of crucial importance for quantifying the impact on the BSM physics stemming from the gained data of rare-events experiments. As discussed in [14,15], this information can be gained by using the so-called spectrum-shape method (SSM). Use of SSM requires a β -electron spectrum with a notable g_A dependence in its shape. In this case information on the effective value of g_A can be gained through the comparison of computed template β spectra, for different g_A values, with the measured one with the aim to find a match. Such SSM analyses of β -spectral shapes of individual β^- transitions have been done recently for the fourth-forbidden nonunique β decays of ^{113}Cd and ^{115}In in [16–18]. An enhanced version SSM (enhanced SSM) was introduced in [19,20] and the spectral moments method (SMM) in [21]. Measurements of the ^{113}Cd and ^{115}In β

*madeoliv@jyu.fi

†jouni.t.suhonen@jyu.fi

spectra are being extended also to other potentially sensitive candidates, as in the case of the ACCESS Collaboration [22].

An additional ingredient in the theoretical analyses of β spectral shapes is the so-called small relativistic NME (sNME) used to fix the measured (partial) half-life in the enhanced SSM [19,20] and the SMM [21]. In spite of its smallness, sNME can influence the (partial) half-lives and shapes of β -electron spectra quite strongly, see [3,17,21]. The sNME gathers its major contributions outside the proton (neutron) valence major shell that contains the proton (neutron) Fermi surface. This makes its calculation particularly hard for the nuclear shell model (NSM), exploited in this work, which typically uses as valence space just the valence major shell for both protons and neutrons.

The sNME can be related to the so-called large vector NME (l-NME) by using the conserved vector current (CVC) hypothesis [12]. The l-NME gathers its major contributions from the valence major shells so that it is reliably calculable in the framework of the NSM. Although this CVC-dictated value of the sNME is an idealization, strictly applicable to an ideal nuclear many-body calculation [12], it still serves as a good reference in our search for a realistic value of the sNME. In our present work we determine the values of the sNME by fitting the experimental partial half-lives (branching ratios) corresponding to the eight β -decay transitions that we have found to depend on the values of g_A and/or sNME. In this case, the dependence of the β spectral shape on the value of sNME stems from the fact that there are always two values (or none at all) of the sNME that reproduce the measured branching of a β transition.

The present article is organized as follows. In Sec. II the adopted theoretical framework is summarized by introducing briefly the β spectral shapes and the related NME, as also their computation using the NSM. Our results are presented and discussed in Sec. III. Conclusions are drawn in Sec. IV.

II. THEORETICAL FRAMEWORK

In this work we discuss only β^- decays which are weak-interaction processes where a neutron transmutes into a proton and an electron and an electron antineutrino ($\bar{\nu}_e$) are emitted within a nuclear environment:

$$n \rightarrow p + e^- + \bar{\nu}_e.$$

In the following, we describe briefly the theory of β -electron spectral shapes, and their connection to the effective value of the weak axial coupling g_A . We also discuss the NME, in particular the sNME and its role in the present calculations. Furthermore, the NSM, alongside its effective interactions and single-particle model spaces are discussed.

A. β spectral shapes

The partial half-life corresponding to a branching ratio of a transition to a particular final state in the daughter isobar can be obtained from the expression

$$t_{1/2} = \kappa / \tilde{C}, \quad (1)$$

where $\kappa = 6289$ s is a collection of natural constants [20] and the integrated shape function reads

$$\tilde{C} = \int_0^{w_0} S(w_e) dw_e, \quad (2)$$

where the shape function $S(w_e)$ can be written as

$$S(w_e) = C(w_e) p w_e (w_0 - w_e)^2 F_0(Z, w_e). \quad (3)$$

In this expression, $F_0(Z, w_e)$, with Z as the proton number of the daughter nucleus, is the usual Fermi function taking into account the final-state Coulomb distortion of the wave function of the emitted electron and

$$w_0 = \frac{W_0}{m_e c^2}, \quad w_e = \frac{W_e}{m_e c^2}, \quad p = \frac{p_e c}{m_e c^2} = \sqrt{w_e^2 - 1} \quad (4)$$

are kinematic quantities scaled dimensionless by the electron rest mass $m_e c^2$. Here, p_e and W_e are the momentum and energy of the emitted electron, respectively, and W_0 is the β endpoint energy, which for the ground-state transitions defines the β -decay Q value. The shape factor $C(w_e)$ contains the Fermi and Gamow-Teller NME for allowed transitions [11] and in general it is a complicated combination of leptonic phase-space factors and NME, as described in detail in [12] and recently in [14,15].

In the current work, we discuss first-forbidden and second-forbidden nonunique β^- -decay transitions and the associated β -spectral shapes $S(w_e)$. The presently discussed first-forbidden β transitions are pseudovector (change in parity) $\Delta J = 1$ (change of one unit of angular momentum) transitions, and the second-forbidden transition, corresponding to the decay of ^{99}Tc , is a $\Delta J = 2$ tensor (no change in parity) transition. All these transitions have both vector and axial-vector components and depend on more than one NME, thus being sensitive to details of nuclear structure through the initial and final nuclear wave functions. For the vector part we adopt the CVC-compatible value $g_V = 1.0$ of the weak vector coupling. In this work, we will refer to the effective g_A^{eff} as simply g_A and it should not be confused with its free-nucleon value $g_A^{\text{free}} = 1.27$.

Our particular aim is to find β spectral shapes that are sensitive to the effective value of g_A . This dependence is enabled by the interference of the vector and axial-vector parts with the mixed vector-axial-vector part in the decomposition

$$S(w_e) = g_V^2 S_V(w_e) + g_A^2 S_A(w_e) + g_V g_A S_{VA}(w_e) \quad (5)$$

of the shape function. Thus far only very few cases with a sizable sensitivity of $S(w_e)$ to the value of g_A have been identified [8,19,20]. Another dependence of $S(w_e)$ can come from the chosen value of sNME [3]. Details related to this chosen value of sNME are highlighted below.

B. β spectral shapes and the value of the sNME

The small relativistic NME (sNME) can play an important role in combined studies of β spectral shapes and branching ratios (partial half-lives) [3,17,20,21]. In these works the sNME has been used as a fitting parameter, together with g_A , in order to fit the experimental β spectral shapes and branching ratios simultaneously. In the nuclear-structure

calculations, the sNME gathers contributions outside the nucleon major shell(s) where the proton and neutron Fermi surfaces lie. Due to the limitation of the NSM valence space to these shells only, the value of the sNME turns out to be unrealistic (practically zero) in the NSM calculations.

In an ideal case (infinite valence spaces, perfect nuclear many-body theory) the value of the sNME is tied to the value of the so-called large vector NME (1-NME) by the CVC hypothesis [12] through the relation

$${}^V \mathcal{M}_{KK-11}^{(0)} = \left(\frac{(-M_n c^2 + M_p c^2 + W_0) \times R}{\hbar c} + \frac{6}{5} \alpha Z \right) \times {}^V \mathcal{M}_{KK0}^{(0)}, \quad (6)$$

where the left side of the equation is the sNME, the last term on the right is the 1-NME, and K denotes the order of forbiddenness, with $K = 1$ ($K = 2$) denoting the first-forbidden (second-forbidden) decays. The quantities M_n and M_p denote neutron and proton masses, respectively. W_0 is the available endpoint energy for the decay, \hbar the reduced Planck constant, α is the fine-structure constant, and c the speed of light. Lastly, Z is the atomic number of the daughter nucleus, and $R = 1.2A^{1/3}$ is the nuclear radius in fm [11], A being the nuclear mass number. The value of the 1-NME can be rather reliably computed by the NSM since the main contributions to it stem from the major shell(s) where the nucleon Fermi surfaces lie. The CVC value of sNME can thus be considered as a good reference for the proper value of the sNME.

In our calculations, we adopt the approach of fitting the sNME such that each individual β^- transition can be reproduced in terms of the branching ratio (partial half-life) accounting for screening, radiative, and atomic exchange corrections. Visible at low electron energies is the atomic exchange correction which was originally derived for allowed β decays [25] and is responsible for the upward tilt seen in all curves. The experimental branching ratios are taken from [23]. There is a quadratic dependence of the computed branching ratios on the value of the sNME and hence two values of the sNME, for each decay transition, reproduce the experimental branching (in some cases there are only complex-conjugate pairs of solution available, meaning that the experimental branching cannot be reproduced by the adopted NSM Hamiltonian). One of these two sNMEs is closer to the CVC value of the sNME and thus offers a way to define the ‘‘optimal’’ β spectral shape: By this hypothesis, choosing always the sNME closer to its CVC value produces the most probable spectral shape for a given β -decay transition. In the following we study how clear is this selection of the ‘‘closer-to-the-CVC’’ value of the sNME, and the dependence of the β spectral shape on this chosen value.

C. Nuclear shell-model calculations

The NSM calculations were performed using the software KSHELL [24] with the Hamiltonians *glekpn* [26] and *jj45pnb* [27]. We have used two different single-particle valence spaces for *glekpn* and *jj45pnb*, as indicated in Table I. In particular, for the *glekpn* valence space we have employed

TABLE I. Single-particle valence spaces and single-particle energies adopted in the present work. The mass ranges are: Set 1 is for $A < 88$, Set 2 is for $A = 88-98$, and Set 3 is for $A = 94-98$.

	glekpn (MeV)			jj45pnb (MeV)
	Set 1	Set 2	Set 3	
$\pi 0f_{7/2}$	-10.480	-8.980	-8.012	-
$\pi 0f_{5/2}$	-5.678	-4.178	-4.197	-14.938
$\pi 1p_{3/2}$	-5.761	-4.261	-2.796	-13.437
$\pi 1p_{1/2}$	-1.693	-1.693	-1.340	-12.0436
$\pi 0g_{9/2}$	-1.423	-1.423	-0.436	-8.9047
$\nu 0g_{9/2}$	-9.306	-9.306	-10.357	-
$\nu 0g_{7/2}$	10.927	10.927	11.622	6.2302
$\nu 1d_{5/2}$	4.220	4.220	5.236	2.4422
$\nu 1d_{3/2}$	7.212	7.217	9.496	2.9448
$\nu 2s_{1/2}$	4.371	4.371	6.710	2.6738
$\nu 0h_{11/2}$	-	-	-	4.3795

three different single-particle energy sets, such that Set 1 is suited for the masses $A < 88$, Set 2 for the mass range $A = 88-98$, and Set 3 for the mass range $A = 94-98$. Set 1 is an adjustment of Set 2 changing only the first three proton single-particle energies.

For all *glekpn* computations the valence spaces have been truncated by including the $\pi 0f_{7/2}$ orbital to be part of the closed core, and the same is true for the $\nu 0g_{9/2}$ orbital. In the case of the *jj45pnb* calculations, due to M -scheme dimensions being in some cases higher than 10^{10} , a truncation was made for $A = 95$ such that the $\pi 0f_{5/2}$ orbital was forced to have from four to six protons, and lastly, for $A = 97$ the truncation consists of allowing up to six neutrons in the $\nu 0h_{11/2}$ orbital and the orbital $\pi 0f_{5/2}$ was forced to have from three to six protons. For all other masses, no truncation was made in the *jj45pnb* calculations.

III. RESULTS

Here, we detail the steps involved in our calculations. First we discuss the electromagnetic observables of the involved states in the light of experimental data. Then the experimental branching ratios of the β -decay transitions of interest are fitted by varying the value of the sNME for each selected value of the axial-vector coupling g_A . We then plot the corresponding β spectral shapes to see if there is any sensitivity of the shapes to the value of sNME and/or g_A .

A. Electromagnetic observables

We probe the reliability of our adopted nuclear wave functions by first computing their electromagnetic properties, namely their electric quadrupole moments Q in units of barn and their magnetic dipole moments μ in units of nuclear magneton μ_N . We compare these computed values, as well as the computed energies, with the available data in Table II. Here, the states are given in column 1 and their experimental excitation energies, quadrupole, and dipole moments in columns 2–4. The corresponding computed excitation energies, quadrupole, and dipole moments are given in columns

TABLE II. Comparison of the experimental and *jj45pnb*-computed and *glekpn*-computed state energies E_{exc} (in units of MeV), electric quadrupole moments Q (in units of barn), and magnetic dipole moments μ (in units of nuclear magneton μ_N). The experimental values are taken from the evaluation [23]. The values in squared brackets denote which set of single-particle energies of *glekpn* was used in the calculation. The adopted effective charges are $e_{\text{eff}}^p = 1.5e$ and $e_{\text{eff}}^n = 0.5e$ and the bare g factors $g_l(p) = 1$, $g_l(n) = 0$, $g_s(p) = 5.585$, and $g_s(n) = -3.826$ were used for the magnetic moments.

Isotope (J^π)	Experimental evaluation			<i>jj45pnb</i>			<i>glekpn</i>		
	E_{exc} (MeV)	Q (barn)	μ (μ_N)	E_{exc} (MeV)	Q (barn)	μ (μ_N)	E_{exc} (MeV)	Q (barn)	μ (μ_N)
^{86}Br (1^-)	0.000	—	—	0.601	+0.079	+1.929	0.614	-0.034	-0.455 [1]
^{86}Kr (2^+)	1.565	—	+2.20(10)	1.614	-0.148	+2.084	1.585	-0.123	+2.984 [1]
^{86}Kr (4^+)	2.250	—	+4.1(6)	2.265	+0.450	+3.966	2.340	+0.347	+3.724 [1]
^{87}Br ($\frac{5}{2}^-$)	0.000	—	—	0.519	-0.016	+2.024	0.000	+0.376	+0.612 [1]
^{87}Kr ($\frac{7}{2}^+$)	1.420	—	—	1.532	-0.024	-0.003	1.707	-0.106	+1.124 [1]
^{87}Kr ($\frac{5}{2}^+$)	0.000	-0.300(3)	-1.022(2)	0.000	-0.295	-1.683	0.000	-0.188	-1.683 [1]
^{87}Kr ($\frac{3}{2}^+$)	0.000	-0.300(3)	-1.022(2)	0.000	-0.295	-1.683	0.000	-0.359	-1.408 [2]
^{87}Rb ($\frac{3}{2}^-$)	0.000	+0.1335(5)	+2.75129(8)	0.000	+0.166	+2.842	0.658	+0.177	+3.255 [2]
^{93}Y ($\frac{1}{2}^-$)	0.000	—	-0.139(1)	0.000	—	-0.266	0.747	—	-0.538 [2]
^{93}Zr ($\frac{3}{2}^+$)	0.267	—	—	0.198	+0.001	-0.042	0.183	-0.108	+0.637 [2]
^{95}Sr ($\frac{1}{2}^+$)	0.000	—	-0.537(2)	0.182	—	-1.650	0.275	—	-0.751 [2]
^{95}Y ($\frac{1}{2}^-$)	0.000	—	-0.16(3)	0.000	—	-0.286	0.646	—	-0.535 [2]
^{95}Y ($\frac{3}{2}^-$)	0.686	—	—	0.308	+0.279	+1.700	0.000	+0.396	+2.146 [2]
^{97}Zr ($\frac{1}{2}^+$)	0.000	—	-0.936(5)	0.000	—	-1.829	0.271	—	-0.757 [2]
^{97}Nb ($\frac{3}{2}^-$)	1.251	—	—	0.925	+0.272	+1.809	0.000	+0.442	+2.174 [2]
^{99}Mo ($\frac{1}{2}^+$)	0.000	—	+0.375(3)	0.202	—	-1.799	0.639	—	-0.835 [3]
^{99}Mo ($\frac{5}{2}^+$)	0.098	—	-0.775(5)	0.222	+0.435	-0.266	0.000	+0.500	+1.062 [3]
^{99}Tc ($\frac{3}{2}^-$)	0.509	—	—	0.696	+0.020	+1.825	0.763	+0.350	+2.255 [3]
^{99}Tc ($\frac{9}{2}^+$)	0.000	-0.129(6)	+5.687(2)	0.112	+0.022	+5.662	0.512	+0.243	+5.416 [3]
^{99}Tc ($\frac{7}{2}^+$)	0.141	—	+4.48(15)	0.000	-0.091	+4.593	0.397	+0.724	+4.715 [3]
^{99}Tc ($\frac{5}{2}^+$)	0.181	—	+3.48(4)	0.063	-0.476	+3.356	0.638	+0.307	+3.393 [3]
^{99}Ru ($\frac{5}{2}^+$)	0.000	+0.079(4)	-0.641(5)	0.037	-0.002	+0.288	0.000	-0.322	+1.083 [3]
^{99}Ru ($\frac{3}{2}^+$)	0.090	+0.231(13)	-0.248(6)	0.000	+0.055	-0.282	0.276	+0.275	+0.569 [3]

5–7 for the *jj45pnb* Hamiltonian and in columns 8–10 for the *glekpn* Hamiltonian.

From Table II one can see that mostly the computed energies of the states are in fair agreement with experiment. Since almost all these states are in odd-mass nuclei, the state density can be quite high even at low excitation energies. This makes the prediction of the correct ground state sometimes quite tricky for the NSM. This can be seen in Table II as a failure of the NSM to predict the correct ground state. On the other hand, this is not a serious flaw since in all these cases the experimentally determined ground state is not far in excitation in the predicted theoretical energy spectrum.

In addition to the state energies, a measure of the quality of the corresponding computed wave functions, relevant for the present purposes, are the electromagnetic moments. From Table II one can see that the two interactions mostly agree in sign for both the electric quadrupole moments Q and magnetic dipole moments μ of the states involved. The signs between the computed and measured moments

differ only in cases where the absolute values of these moments are relatively small, like in the cases of the states $^{99}\text{Mo}(1/2^+, 5/2^+)$ (μ), $^{99}\text{Tc}(9/2^+)$ (Q), and $^{99}\text{Ru}(5/2^+)$ (both μ and Q). However, overall, the correspondence between the computed and measured values of these moments is quite good.

B. Values of the small vector matrix element

As already mentioned above, we use the sNME as a fitting parameter to match, for each selected value of the axial coupling g_A , the computed and measured branching ratios of the β -decay transitions of interest. We obtain two solutions for the value of sNME for each value of g_A , giving two ranges of sNME values corresponding to our adopted range $g_A = 0.8$ – 1.2 . These ranges are compared with the CVC value of the sNME, Eq. (6), in Table III. In this table we give, for each individual β transition (columns 1 and 2), the corresponding experimental Q value and excitation energy in the final nucleus in units of MeV in columns 3 and 4. We also give the

TABLE III. Ranges of the values of the fitted sNME (lower and upper bounds), corresponding to range $g_A = 0.8-1.2$ of the axial coupling, and the CVC value of the sNME for the Hamiltonians $jj45pnb$ (columns 6–8) and $glekpn$ (columns 9–11). The transition is given in columns 1 and 2, and the corresponding measured Q value, excitation energy of the final state, and the branching are given in columns 3–5. The data are taken from the evaluation [23]. The numbers without parentheses (in parentheses) correspond to the sNME range which is considered to be more (less) correlated with the CVC value of the sNME.

Evaluation data					$jj45pnb (\times 10^{-2})$			$glekpn (\times 10^{-2})$		
J_i^π	J_f^π	Q_{exp} (MeV)	E_{exp} (MeV)	Br. (%)	Lower	Upper	CVC	Lower	Upper	CVC
$^{86}\text{Br} (1^-)$	$^{86}\text{Kr} (0^+)$	7.633(3)	0.000	15(8)	+1.55(−0.16)	+2.02(+0.13)	+4.99	+3.40(+1.79)	+3.53(+2.33)	+5.36
$^{87}\text{Br} (\frac{5}{2}^-)$	$^{87}\text{Kr} (\frac{7}{2}^+)$	6.818(3)	1.420	4.8(16)	+1.76(−1.18)	+1.83(−1.00)	+0.50	−1.48(+1.71)	−1.43(+1.76)	+0.06
$^{87}\text{Kr} (\frac{5}{2}^+)$	$^{87}\text{Rb} (\frac{3}{2}^-)$	3.88827(25)	0.000	30.5(22)	+0.57(−0.59)	+0.96(−0.57)	+1.57	−1.20(+0.23)	−0.72(+0.29)	−2.79
$^{93}\text{Y} (\frac{1}{2}^-)$	$^{93}\text{Zr} (\frac{3}{2}^+)$	2.895(10)	0.267	4.9(9)	−0.66(−0.68)	−0.08(−0.48)	+1.35	−0.53(−0.20)	−0.50(−0.07)	−0.61
$^{95}\text{Sr} (\frac{1}{2}^+)$	$^{95}\text{Y} (\frac{3}{2}^-)$	6.090(7)	0.686	8.9(7)	−2.04(+4.21)	−1.62(+4.55)	+1.04	+3.64(+0.40)	+5.02(+3.64)	+6.82
$^{97}\text{Zr} (\frac{1}{2}^+)$	$^{97}\text{Nb} (\frac{3}{2}^-)$	2.659(2)	1.251	3.90(20)	−0.10(−1.41)	+0.10(−1.22)	−0.52	−1.77(−1.20)	−1.31(−0.80)	−3.70 ^a
$^{99}\text{Mo} (\frac{1}{2}^+)$	$^{99}\text{Tc} (\frac{3}{2}^-)$	1.3578(9)	0.509	1.16(2)	−0.50(−1.38)	−0.23(−1.12)	−0.47	−1.70(−0.96)	−1.66(−1.10)	−3.43
$^{99}\text{Tc} (\frac{9}{2}^+)$	$^{99}\text{Ru} (\frac{5}{2}^+)$	0.2975(10)	0.000	99.9984(4)	−8.56(+4.96)	−5.15(+8.33)	−17.1	−3.11(+10.4)	−0.93(+12.4)	+0.80

^aFor this transition, the $glekpn$ Hamiltonian could not reproduce the measured branching ratio for $g_A = 1.2$ thus the ranges are for $g_A = 0.8-1.1$.

measured branching ratio in percents in column 5. The CVC values of the sNME are given in columns 8 and 11 for the Hamiltonians $jj45pnb$ and $glekpn$, respectively. In columns 6 and 7 (columns 9 and 10) we give the lower and upper bounds of the range of the fitted sNME values, corresponding to the range $g_A = 0.8-1.2$ of the axial coupling, for the $jj45pnb$ ($glekpn$) Hamiltonian. Here, the numbers without parentheses (in parentheses) correspond to the range which is considered to be the more (less) compatible one with the CVC value of the sNME.

Taking a look at Table III indicates that there is a clear correlation of the ranges of the fitted sNME values with the CVC value of sNME for the decay of ^{87}Kr for both Hamiltonians, for the decays of ^{97}Zr and ^{99}Mo for the $glekpn$ Hamiltonian, and the decays of ^{86}Br , ^{95}Sr , and ^{99}Tc for the $jj45pnb$ Hamiltonian. In these cases the sign of the CVC value of the sNME clearly defines the preferred range of the fitted sNME values. The rest of the cases are less clear and the assignment of the closer-to-CVC-value range is almost a matter of taste, the decay of ^{93}Y being the most unclear case. In the end, only experimental data on the β spectral shapes, when compared with the corresponding computed shapes, will decide which range of the sNME values will be the more realistic one.

C. β spectral shapes

We have produced the β spectral shapes, corresponding to the shape function $S(w_e)$ of Eq. (3), by adopting the experimental Q values and excitation energies listed in Table III. In addition, the experimental branching ratios of the table (column 5) have been reproduced by the sNME fitting procedure discussed in Sec. III B. Our β -spectral results are summarized in Figs. 1–3. In Fig. 1 the decay transitions $^{86}\text{Br}(1^-) \rightarrow ^{86}\text{Kr}(0^+)$ and $^{87}\text{Br}(5/2^-) \rightarrow ^{87}\text{Kr}(7/2^+)$ are shown. It can clearly be seen that the decay of ^{86}Br depends very strongly on the adopted Hamiltonian, the axial coupling, and the sNME, whereas the decay of ^{87}Br depends quite weakly on all these

three degrees of freedom. For the former decay the strong dependence on the used nuclear Hamiltonian is conspicuous for the closer-to-CVC values of the sNME, whereas there is practically no dependence on the chosen Hamiltonian for the farther sNME values.

In Fig. 2 the β spectral shapes corresponding to the decay transitions $^{87}\text{Kr}(5/2^+) \rightarrow ^{87}\text{Rb}(3/2^-)$, $^{93}\text{Y}(1/2^-) \rightarrow ^{93}\text{Zr}(3/2^+)$, and $^{95}\text{Sr}(1/2^+) \rightarrow ^{95}\text{Y}(3/2^-)$ are depicted. Here, the decays of ^{87}Kr and ^{93}Y depend on the value of g_A and sNME, the latter even strikingly strongly. For the decay of ^{95}Sr there is only a very weak dependence on the value of g_A but a rather strong dependence on the value of the sNME, in particular for the Hamiltonian $jj45pnb$. The decays of ^{93}Y and ^{95}Sr depend strongly on the chosen NSM Hamiltonian, whereas for the decay of ^{87}Kr there is practically no dependence on the chosen Hamiltonian.

In Fig. 3 the β spectral shapes corresponding to the decay transitions $^{97}\text{Zr}(1/2^+) \rightarrow ^{97}\text{Nb}(3/2^-)$, $^{99}\text{Mo}(1/2^+) \rightarrow ^{99}\text{Tc}(3/2^-)$, and $^{99}\text{Tc}(9/2^+) \rightarrow ^{99}\text{Ru}(5/2^+)$ are displayed. The decay of ^{97}Zr shows rather strong dependence on g_A for both Hamiltonians, but strong sNME dependence only for the $jj45pnb$ Hamiltonian. The dependence on the chosen Hamiltonian is notable. For the decay of ^{99}Mo there are strong dependencies on the sNME and the chosen Hamiltonian, whereas there is a notable g_A dependence only for the $jj45pnb$ Hamiltonian. In the case of the ^{99}Tc decay there is a strong dependence on the chosen Hamiltonian and the value of g_A . The $glekpn$ interaction shows strong dependence on the values of sNME, whereas the $jj45pnb$ interaction shows only very moderate sNME dependence.

IV. SUMMARY AND CONCLUSIONS

In the present article we perform a survey of possible forbidden nonunique β -decay transitions which would be sensitive to the (effective) value of the weak axial-vector coupling g_A . This dependence would allow determination of the value

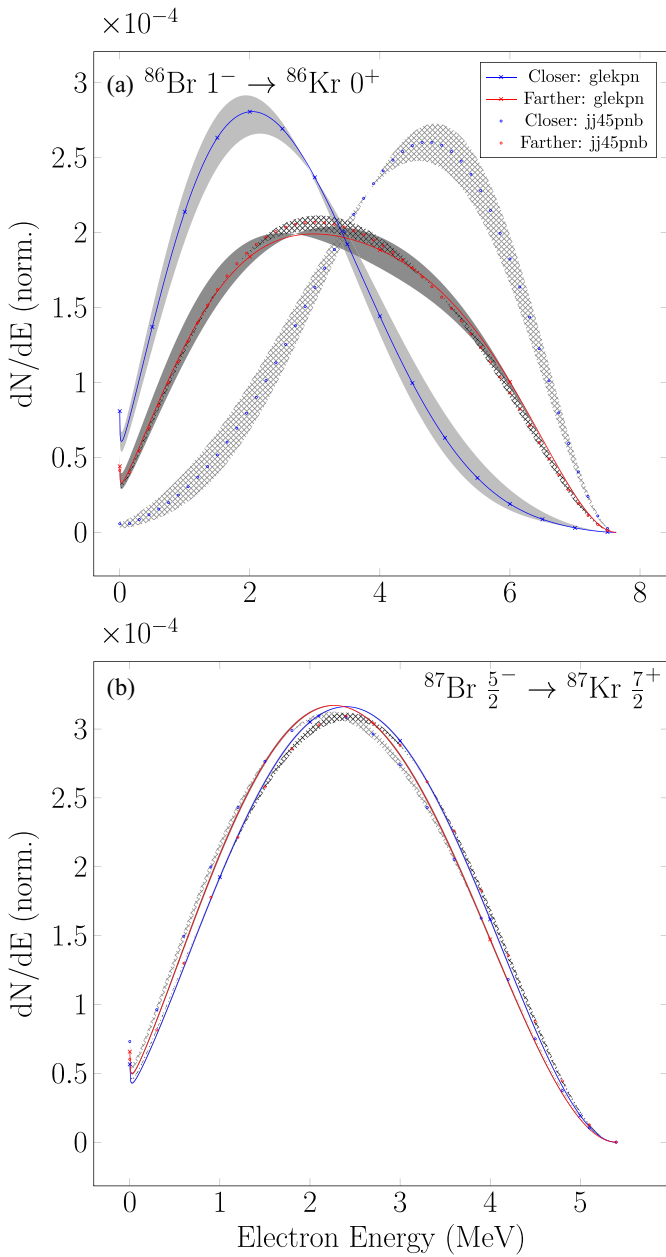


FIG. 1. Computed β spectral shapes of the transitions $^{86}\text{Br}(1^-) \rightarrow ^{86}\text{Kr}(0^+)$ (a) and $^{87}\text{Br}(5/2^-) \rightarrow ^{87}\text{Kr}(7/2^+)$ (b). The crossed-blue (red) curves are those constructed by adopting the value closer to (farther from) to the CVC value of the sNME for each transition. The light (darkened) gray-hatched regions denote the span of the curves corresponding to the range of $g_A = 0.8-1.2$ and their corresponding closer (farther) sNMEs for the *glekpn* Hamiltonian. The corresponding blue and red dotted curves and their light (darkened) gray-hatched regions show the results for the *jj45pnb* interaction. All the areas under the curves have been normalized to unity.

of this coupling in comparisons between the computed and measured electron spectral shapes, in terms of an enhanced spectrum-shape method (SSM) adopted in the present work. This enhanced method exploits the additional dimension of fitting the measured branching ratio of a β transition by using the sNME as a fitting parameter.

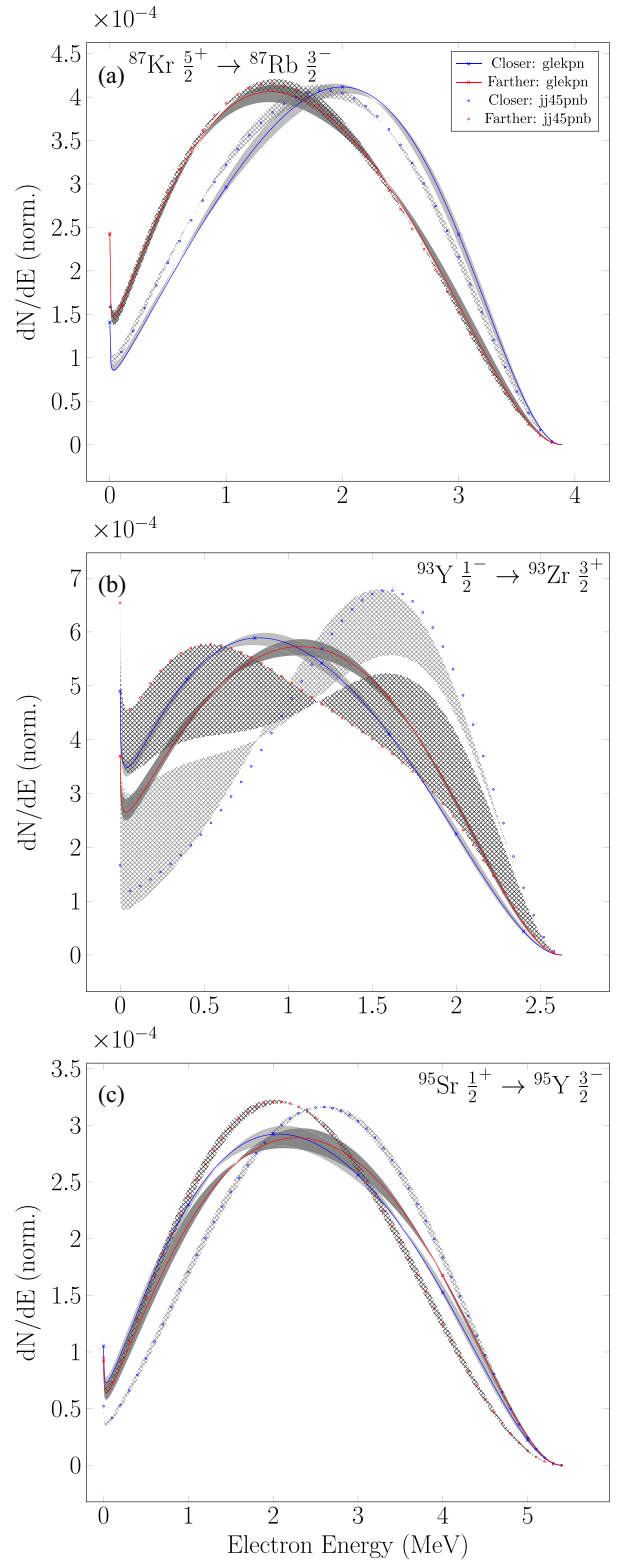


FIG. 2. The same as in Fig. 1 for the transitions $^{87}\text{Kr}(5/2^+) \rightarrow ^{87}\text{Rb}(3/2^-)$ (a), $^{93}\text{Y}(1/2^-) \rightarrow ^{93}\text{Zr}(3/2^+)$ (b), and $^{95}\text{Sr}(1/2^+) \rightarrow ^{95}\text{Y}(3/2^-)$ (c).

Here, we study the nuclear mass region $A = 86-99$ since there are lots of possible decay transitions that have measured branching ratios that are reasonably large in order to

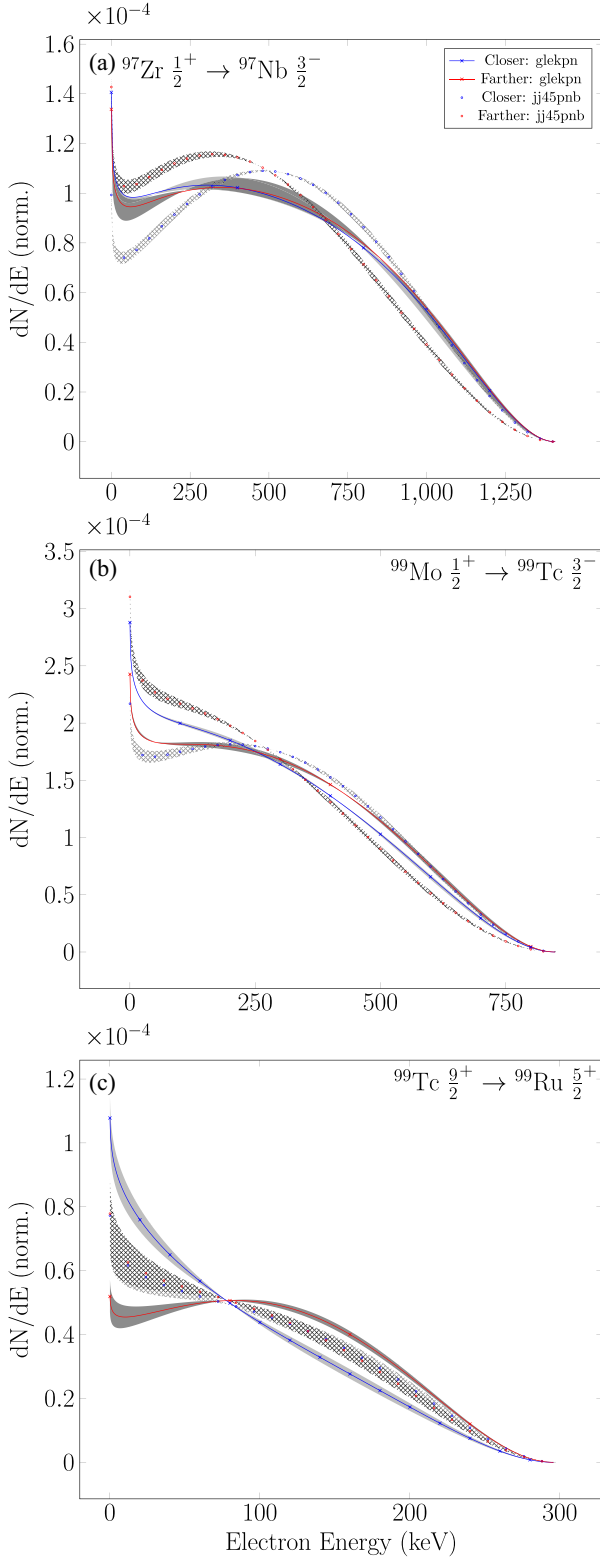


FIG. 3. The same as in Fig. 1 for the transitions $^{97}\text{Zr}(1/2^+) \rightarrow ^{97}\text{Nb}(3/2^-)$ (a), $^{99}\text{Mo}(1/2^+) \rightarrow ^{99}\text{Tc}(3/2^-)$ (b), and $^{99}\text{Tc}(9/2^+) \rightarrow ^{99}\text{Ru}(5/2^+)$ (c).

enable realistic execution of β spectral-shape measurements. In addition, in this mass region there are available two well-established Hamiltonians, *jj45pnb* and *glekpn* of the nuclear

shell model (NSM), which would allow comparison of the results of these two Hamiltonians and a rough estimation of the uncertainties involved in our NSM calculations.

We have found 8 β -decay transitions of potential interest for spectral-shape measurements, the corresponding nuclei ranging from ^{86}Br to ^{99}Tc . The corresponding decay transitions can be grouped in four categories:

Category I includes those transitions which are sensitive to the values of both g_A and sNME. These are the transitions $^{86}\text{Br}(1^-) \rightarrow ^{86}\text{Kr}(0^+)$, $^{87}\text{Kr}(5/2^+) \rightarrow ^{87}\text{Rb}(3/2^-)$, and $^{93}\text{Y}(1/2^-) \rightarrow ^{93}\text{Zr}(3/2^+)$ for both Hamiltonians, and $^{97}\text{Zr}(1/2^+) \rightarrow ^{97}\text{Nb}(3/2^-)$ and $^{99}\text{Mo}(1/2^+) \rightarrow ^{99}\text{Tc}(3/2^-)$ for the *jj45pnb* Hamiltonian, and $^{99}\text{Tc}(9/2^+) \rightarrow ^{99}\text{Ru}(5/2^+)$ for the *glekpn* Hamiltonian.

Category II contains all β transitions that have a strong g_A dependence but a weak sNME dependence. The corresponding transitions are $^{97}\text{Zr}(1/2^+) \rightarrow ^{97}\text{Nb}(3/2^-)$ and $^{99}\text{Mo}(1/2^+) \rightarrow ^{99}\text{Tc}(3/2^-)$ for the *glekpn* Hamiltonian, and $^{99}\text{Tc}(9/2^+) \rightarrow ^{99}\text{Ru}(5/2^+)$ for the *jj45pnb* Hamiltonian.

Category III contains the β transitions that are rather weakly sensitive to g_A but strongly sensitive to sNME. This one transition is $^{95}\text{Sr}(1/2^+) \rightarrow ^{95}\text{Y}(3/2^-)$.

Category IV includes those β transitions that are rather weakly sensitive to both g_A and sNME. This one transition is $^{87}\text{Br}(5/2^-) \rightarrow ^{87}\text{Kr}(7/2^+)$.

All the discussed transitions are first-forbidden nonunique, except for the decay of ^{99}Tc which is second-forbidden nonunique. These β decay transitions are also associated to fission products that contribute notably to the antineutrino flux from nuclear reactors. In particular, the first-forbidden nonunique transitions may play a decisive role in solving the anomalies related to the reactor antineutrino flux [1].

The transition from **Category IV** is interesting mainly as a test of the nuclear-structure calculation, either proving or disproving the shape of the computed β spectral shape. This philosophy is along the lines of the spectral-shape study of the $^{137}\text{Xe}(7/2^-) \rightarrow ^{137}\text{Cs}(7/2^+)$ transition performed by the EXO-200 collaboration in [28]. In this SSM study the measured and computed β spectral shapes showed immaculate agreement, thus verifying the correctness of the corresponding nuclear-structure calculations, since the computed spectral shape of this first-forbidden nonunique transition turned out to be quite independent of the value of the axial-vector coupling.

The transition from **Category III** is important in determining the proper value of the sNME, i.e., whether the fitted value closer to the CVC value of sNME is the right physical choice, as could be anticipated based on the *jj45pnb* values of sNME in Table III. This same strategy is valid also for the β -decay transitions of **Category I**. In addition, the transitions of **Category I** and **Category II** open up a way to assess the effective value of the axial coupling, the ones of **Category II** even more straightforwardly.

Building on the shape decomposition in Eq. (5), we can map the four categories to specific components within this equation: vector (C_V), axial (C_A), and vector-axial (C_{VA}). **Category I** arises under two scenarios: first, when the vector-axial component, with a relevant sNME dependency, is dominant, resulting in a shape influenced by both g_A and sNME; second, when all three components have comparable magnitudes, and

the sensitivity to the sNME in either (or both) the vector or vector-axial components leads to a similar dependence. For **Category II**, the dominance of the axial component or a dominant vector-axial component with weak sNME sensitivity both yield shapes primarily influenced by g_A , albeit with slight sNME sensitivity. **Category III** is defined by a dominant vector component sensitive to sNME variations, making the shape dependent on sNME with minimal g_A influence. Finally, **Category IV** describes cases where a dominant and insensitive vector component to sNME variations results in a shape unaffected by both g_A and sNME.

Properties of many of the discussed β spectral shapes depend more or less also on the adopted Hamiltonian, namely those corresponding to the decays of ^{93}Y , ^{95}Sr , ^{97}Zr , ^{99}Mo , and ^{99}Tc , and also the one corresponding to the closer-to-CVC sNME for ^{86}Br . These decay transitions then open up a way to also test the accuracy of the two widely used NSM Hamiltonians in describing also the β -decay properties in the nuclear-mass region of interest here.

Concerning the experimental aspects, the measurements of the presently discussed β spectral shapes do not need very high precision in the very beginning owing to the large differences in many of the spectra with respect to the sNME and g_A . A challenge for the scintillation-based experimental methods are the short half-lives of the decaying nuclei, excluding ^{99}Tc , ranging from 55 s to 65.9 h. Typically these methods are used for long-lived nuclei, like ^{113}Cd [29] and ^{115}In [30]. Other

possible methods are those based on semiconductor detectors [16] and cryogenic calorimeters [18,22]. Short half-lives may be a challenge also for these type of measurement methods. Further methods are metallic magnetic calorimeters, the decay transition of $^{99}\text{Tc}(9/2^+) \rightarrow ^{99}\text{Ru}(5/2^+)$ having already been measured by Paulsen *et al.* [31] by this method. The short half-lives may be overcome by using radiochemical methods or beams of radioactive nuclei [32–34], like in the ISOLDE facility at CERN. Interesting possibilities offers also the newly developed method employing the Ion Guide Isotope Separator On-Line facility at the Accelerator Laboratory of Jyväskylä [35].

As a final note it should be stated that our calculations indicate that there are a lot of interesting possibilities for future β -decay experiments in the mass region $A = 86\text{--}99$. These experiments would be in a position to shed light on the effective value of the weak axial coupling, on the role of the small relativistic vector matrix element in β -decay calculations, and on the capability of two well-established shell-model Hamiltonians in predicting β -decay properties, in addition to spectroscopic properties, of nuclei in this mass region.

ACKNOWLEDGMENT

We acknowledge the support by CSC–IT Center for Science, Finland, for the generous computational resources.

-
- [1] L. Hayen, J. Kostensalo, N. Severijns, and J. Suhonen, *Phys. Rev. C* **99**, 031301(R) (2019); **100**, 054323 (2019).
 - [2] M. Ramalho, J. Suhonen, J. Kostensalo, G. A. Alcalá, A. Algora, M. Fallot, A. Porta, and A.-A. Zakari-Issoufou, *Phys. Rev. C* **106**, 024315 (2022).
 - [3] M. Ramalho and J. Suhonen, *Phys. Rev. C* **109**, 014326 (2024).
 - [4] J. Suhonen, *Phys. Rev. C* **96**, 055501 (2017).
 - [5] J. Suhonen, *Front. Phys.* **5**, 55 (2019).
 - [6] J. Suhonen and J. Kostensalo, *Front. Phys.* **7**, 29 (2019).
 - [7] J. Engel and J. Menéndez, *Rep. Prog. Phys.* **80**, 046301 (2017).
 - [8] H. Ejiri, J. Suhonen, and K. Zuber, *Phys. Rep.* **797**, 1 (2019).
 - [9] K. Blaum, S. Eliseev, F. A. Danevich, V. I. Tretyak, S. Kovalenko, M. I. Krivoruchenko, Y. N. Novikov, and J. Suhonen, *Rev. Mod. Phys.* **92**, 045007 (2020).
 - [10] M. Agostini, G. Benato, J. A. Detwiler, J. Menéndez, and F. Vissani, *Rev. Mod. Phys.* **95**, 025002 (2023).
 - [11] J. Suhonen, *From Nucleons to Nucleus: Concepts of Microscopic Nuclear Theory* (Springer, Berlin, 2007).
 - [12] H. Behrens and W. Bühring, *Electron Radial Wave Functions and Nuclear Beta-decay (International Series of Monographs on Physics)* (Clarendon Press, Oxford, 1982).
 - [13] J. Kostensalo and J. Suhonen, *Phys. Lett. B* **781**, 480 (2018).
 - [14] M. Haaranen, P. C. Srivastava, and J. Suhonen, *Phys. Rev. C* **93**, 034308 (2016).
 - [15] M. Haaranen, J. Kotila, and J. Suhonen, *Phys. Rev. C* **95**, 024327 (2017).
 - [16] L. Bodenstern-Dresler *et al.* (COBRA Collaboration), *Phys. Lett. B* **800**, 135092 (2020).
 - [17] J. Kostensalo, J. Suhonen, J. Volkmer, S. Zatschler, and K. Zuber, *Phys. Lett. B* **822**, 136652 (2021).
 - [18] A. F. Leder *et al.*, *Phys. Rev. Lett.* **129**, 232502 (2022).
 - [19] A. Kumar, P. C. Srivastava, J. Kostensalo, and J. Suhonen, *Phys. Rev. C* **101**, 064304 (2020).
 - [20] A. Kumar, P. C. Srivastava, and J. Suhonen, *Eur. Phys. J. A* **57**, 225 (2021).
 - [21] J. Kostensalo, E. Lisi, A. Marrone, and J. Suhonen, *Phys. Rev. C* **107**, 055502 (2023).
 - [22] L. Pagnanini *et al.* (ACCESS Collaboration), *Eur. Phys. J. Plus* **138**, 445 (2023).
 - [23] From ENSDF database as of Dec. 2023, version available at <http://www.nndc.bnl.gov/ensarchivals/>.
 - [24] N. Shimizu, T. Mizusaki, Y. Utsuno, and Y. Tsunoda, *Comput. Phys. Commun.* **244**, 372 (2019).
 - [25] O. Nitescu, S. Stoica, and F. Simkovic, *Phys. Rev. C* **107**, 025501 (2023).
 - [26] H. Mach, E. K. Warburton, R. L. Gill, R. F. Casten, J. A. Becker, B. A. Brown, and J. A. Winger, *Phys. Rev. C* **41**, 226 (1990).
 - [27] A. F. Lisetskiy, B. A. Brown, M. Horoi, and H. Grawe, *Phys. Rev. C* **70**, 044314 (2004).
 - [28] S. Al Kharusi *et al.* (EXO-200 Collaboration), *Phys. Rev. Lett.* **124**, 232502 (2020).
 - [29] P. Belli *et al.*, *Phys. Rev. C* **76**, 064603 (2007).
 - [30] L. Pfeiffer, A. P. Mills, E. A. Chandross, and T. Kovacs, *Phys. Rev. C* **19**, 1035 (1979).
 - [31] M. Paulsen *et al.*, [arXiv:2309.14014](https://arxiv.org/abs/2309.14014) [nucl-ex].
 - [32] G. Rudstam *et al.*, *At. Data Nucl. Data Tables* **45**, 239 (1990).
 - [33] A. Algora *et al.*, *Eur. Phys. J. A* **57**, 85 (2021).
 - [34] O. Tengblad *et al.*, *Nucl. Phys. A* **503**, 136 (1989).
 - [35] V. Guadilla *et al.*, *JINST* **19**, P02027 (2024).

V

**HIGH-PRECISION MEASUREMENT OF A LOW Q VALUE FOR
ALLOWED β^- -DECAY OF ^{131}I RELATED TO NEUTRINO MASS
DETERMINATION**

by

Eronen, T and Ge, Z and de Roubin, A and Ramalho, M and Kostensalo, J and
Kotila, J and Beliushkina, O and Delafosse, C and Geldhof, S and Gins, W and
Hukkanen, M and Jokinen, A and Kankainen, A and Moore, I D and Nesterenko, D
A and Stryjczyk, M and Suhonen, J

Physics Letters B **830**, 137135 (2022).

DOI: 10.1016/j.physletb.2022.137135

Reproduced with kind permission of Elsevier.



High-precision measurement of a low Q value for allowed β^- -decay of ^{131}I related to neutrino mass determination



T. Eronen^{a,*}, Z. Ge^{a,*}, A. de Roubin^b, M. Ramalho^a, J. Kostensalo^c, J. Kotila^{a,d,e},
O. Beliuskina^a, C. Delafosse^a, S. Geldhof^{a,1}, W. Gins^a, M. Hukkanen^{a,b}, A. Jokinen^a,
A. Kankainen^a, I.D. Moore^a, D.A. Nesterenko^a, M. Stryjczyk^a, J. Suhonen^{a,*}

^a Department of Physics, University of Jyväskylä, P.O. Box 35, FI-40014, Jyväskylä, Finland

^b Centre d'Etudes Nucléaires de Bordeaux Gradignan, UMR 5797 CNRS/IN2P3 - Université de Bordeaux, 19 Chemin du Solarium, CS 10120, F-33175, Gradignan Cedex, France

^c Natural Resources Institute Finland, Yliopistokatu 6, FI-80130, Joensuu, Finland

^d Finnish Institute for Educational Research, University of Jyväskylä, P.O. Box 35, FI-40014, Jyväskylä, Finland

^e Center for Theoretical Physics, Sloane Physics Laboratory, Yale University, New Haven, CT 06520-8120, USA

ARTICLE INFO

Article history:

Received 5 January 2022

Received in revised form 22 April 2022

Accepted 22 April 2022

Available online 27 April 2022

Editor: D.F. Geesaman

Keywords:

Penning trap

Low Q value

β^- decay

Neutrino mass

ABSTRACT

The ground-state-to-ground-state β^- -decay $^{131}\text{I} (7/2^+) \rightarrow ^{131}\text{Xe} (3/2^+)$ Q value was determined with high precision utilizing the double Penning trap mass spectrometer JYFLTRAP at the IGISOL facility. The Q value of this β^- -decay was found to be $Q = 972.25(19)$ keV through a cyclotron frequency ratio measurement with a relative precision of 1.6×10^{-9} . This was realized using the phase-imaging ion-cyclotron-resonance technique. The new Q value is more than 3 times more precise and 2.3σ higher (1.45 keV) than the value extracted from the Atomic Mass Evaluation 2020. Our measurement confirms that the β^- -decay to the $9/2^+$ excited state at 971.22(13) keV in ^{131}Xe is energetically allowed with a Q value of 1.03(23) keV while the decay to the $7/2^+$ state at 973.11(14) keV was found to be energetically forbidden. Nuclear shell-model calculations with established two-body interactions, alongside an accurate phase-space factor and a statistical analysis of the $\log ft$ values of known allowed β decays, were used to estimate the partial half-life for the low- Q -value transition to the $9/2^+$ state. The half-life was found to be $(1.97^{+2.24}_{-0.89}) \times 10^7$ years, which makes this candidate feasible for neutrino mass searches.

© 2022 The Authors. Published by Elsevier B.V. This is an open access article under the CC BY license (<http://creativecommons.org/licenses/by/4.0/>). Funded by SCOAP³.

1. Introduction

The absolute scale of neutrino mass is one of the big open questions in physics. The neutrino-oscillation experiments have demonstrated that at least two of the three flavors of neutrinos have a non-zero mass and for now there are only upper and lower limits on the neutrino mass provided by experiments that in some cases also depend on theoretical models. Stellar observations combined with cosmological models yield an upper limit on the sum of the neutrino masses, which at this point is ~ 0.12 eV/ c^2 at 95% confidence level [1]. Several approaches to pinpoint the mass of the neutrino, namely nuclear β and double- β decays [2–4], are based on nuclear decay kinematics.

In all of the kinematical approaches, the neutrino mass is determined via precise measurement of the spectral shape distortion close to the endpoint of the spectrum. Only a very small fraction of the events land near the endpoint and thus it is desirable to study a decay with as small Q value as possible [5]. Smaller the Q value, bigger the fraction of events falling near the endpoint. The KATRIN experiment using tritium (^3H) has a ground-state-to-ground-state Q value of 18.6 keV [6] and ^{187}Re has even smaller Q value of about 2.5 keV [7]. ^{163}Ho -nucleus has the lowest known ground-state-to-ground-state electron-capture Q value of about 2.8 keV [8,9]. The rhenium experiment relies on the β transition $^{187}\text{Re}(5/2^+) \rightarrow ^{187}\text{Os}(1/2^-)$ which is of the first-forbidden unique type with the lowest known ground-state-to-ground-state β -decay Q value of $2.492(30)_{\text{stat}}(15)_{\text{sys}}$ keV [7,10]. The Q value of rhenium decay is nearly an order of magnitude smaller than the tritium decay one. Even though all these cases have a very low Q value, they still suffer from the issue that only a very small fraction of decays fall close to the endpoint. In addition, it is necessary to understand the spectrum shape near the endpoint. To detect a

* Corresponding authors.

E-mail addresses: tommieron@jyu.fi (T. Eronen), z.ge@gsi.de (Z. Ge), jouni.t.suhonen@jyu.fi (J. Suhonen).

¹ Present address: GANIL, CEA/DSM-CNRS/IN2P3, 14000 Caen, France.

distortion accounting for the mass of a (anti)neutrino, a substantial amount of events are needed with extremely good background suppression and understanding of the detector systematics.

Quite recently, decays that proceed to excited states in the daughter with an ultra-low Q value (considered to be 1 keV or less) have gained interest. These are of interest for future neutrino mass scale determination experiments [11–20]. The existence of a decay with an ultra-low Q value to an excited state in the daughter was first discovered by Cattadori et al. [21] in the β^- decay of ^{115}In . The intriguing decay branch is the β^- decay of the $9/2^+$ ground state of ^{115}In to the $3/2^+$ state in ^{115}In . The Q value of the decay was confirmed to be less than 1 keV by two Penning trap experiments, JYFLTRAP and Florida State University precision Penning-trap mass spectrometer [22,23]. The existence of a decay branch was experimentally confirmed by HADES underground laboratory with the branching ratio of $1.07(17)\times 10^{-6}$ [22]. Future experiments to utilize these decays for pinpointing the mass of the neutrino would need to take care of the vast background arising from more dominant (usually ground state) decay branches. One possibility is to use de-exciting gamma rays as a gating transition.

More recently, β^- decay of ^{135}Cs was confirmed to be very similar to ^{115}In by a recent JYFLTRAP Q -value measurement. The Q value to the second excited $11/2^-$ state in ^{135}Ba was measured with JYFLTRAP Penning trap mass spectrometer [24,25] and it is equal to 0.44(31) keV [26]. This confirms that the decay is energetically allowed with an ultra-low Q value. The transition is of first-forbidden unique type with a simple universal spectral shape. The decay has not been experimentally confirmed yet but theoretical partial half-life estimate yields a similar branching ratio ($\sim 10^{-6}$) as for ^{115}In decay. Thus, also ^{135}Cs is a potential candidate for antineutrino-mass measurements.

Here, we report on a new β^- decay Q value of ^{131}I . Prior to our measurement, the ground-state-to-ground-state ($7/2^+ \rightarrow 3/2^+$) Q value is known to be 970.80(60) keV [27,28]. There is a $9/2^+$ state in the ^{131}Xe daughter at 971.22(13) keV, which is potentially fed by the β^- decay of ^{131}I [29,30]. The transition is of allowed type, making it a lucrative candidate since this type of transition is expected to have a reasonable branching ratio and a simple spectral shape. With the available data, a Q value of $-0.42(61)$ keV is deduced. Evidently, it is not possible to conclude whether this transition is energetically possible or not.

The β^- decay Q value of the ground state of ^{131}I to the $9/2^+$ state in ^{131}Xe is simply the ground-state-to-ground-state Q value of ^{131}I minus the energy of the excited state. The excitation energy is already known with 130 eV precision [31] while the Q value is known only to 600 eV precision. The focus of this work was to improve the precision of the ground-state-to-ground-state Q value. This is equivalent to mass difference of ^{131}I and ^{131}Xe , which was measured via direct high-precision cyclotron frequency-ratio determination with the double Penning trap JYFLTRAP.

Based on the new Q value, an estimate of the partial half-life and the branching ratio is derived using wave functions obtained from a nuclear shell-model calculation based on a two-body interaction suitable for the presently discussed mass region. In addition, an analysis of three known allowed β decays was performed in order to compare with the result of the shell-model calculation.

2. Experimental method

The Q value of the ground-state-to-ground-state β^- -decay of ^{131}I was measured at the Ion Guide Isotope Separator On-Line facility (IGISOL) with the JYFLTRAP double Penning trap mass spectrometer [25] in the accelerator laboratory of University of Jyväskylä [32,33]. Layout of the facility is shown in Fig. 1. Both the decay parent (^{131}I) and the stable decay daughter (^{131}Xe) ions were simultaneously produced in proton-induced fission reaction.

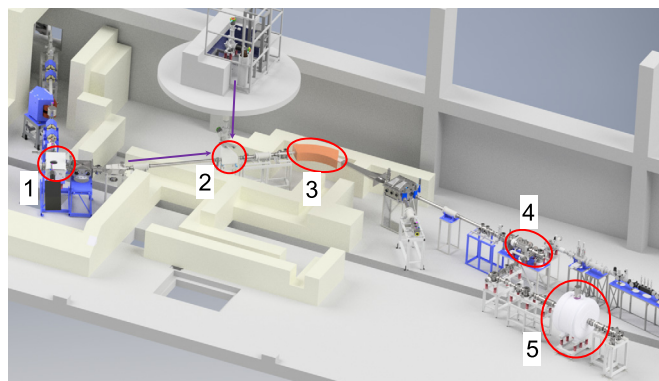


Fig. 1. Layout of the IGISOL facility. The $^{131}\text{I}^+$ and $^{131}\text{Xe}^+$ ions were produced with proton-induced fission reactions at the IGISOL target ion chamber (1). The online beam was selected with an electrostatic kicker (2). The mass number selection was performed with a dipole magnet (3), the ion cooling and bunching in the RFQ cooler-buncher (4) and finally the mass-difference measurement with the JYFLTRAP Penning trap setup (5).

A primary beam of protons with the energy of 30 MeV from the K-130 cyclotron impinged on a uranium target of 15 mg/cm² thickness placed inside a gas cell [34]. The secondary products from the fission reactions were stopped in helium gas and extracted with the help of a sextupole radiofrequency ion guide (SPIG) [35]. Through charge-exchange reactions with helium gas and impurities, most of the extracted products were singly charged. After passing the length of the SPIG, the ions are accelerated with 30 kV and guided through a 55° dipole magnet, which has mass resolving power $M/\Delta M \approx 500$. This is sufficient for separation of different isobars in the secondary beam. After the secondary beam has been isobarically separated, the ions of the chosen mass number $A = 131$ containing $^{131}\text{Xe}^+$, $^{131}\text{I}^+$ and other fission fragments having the same mass number are injected into a radiofrequency quadrupole cooler-buncher (RFQ) [36]. The RFQ is used to accumulate, cool and bunch the ions so they can be efficiently injected into JYFLTRAP double Penning trap setup for the actual Q -value measurement.

JYFLTRAP consists of two cylindrical Penning traps which are both situated inside the same 7-T superconducting solenoid. The first trap, performing as the purification and preparation trap, is filled with helium buffer gas and used to remove isobaric contaminants via the sideband buffer gas cooling technique [37]. This technique alone can usually provide sufficient cleaning with a resolving power $M/\Delta M \approx 10^5$ but in this work, an extra cleaning step was required to separate $^{131}\text{I}^+$ and $^{131}\text{Xe}^+$ ions from each other. To prepare a clean sample containing only one isotope, the Ramsey dipolar cleaning technique was utilized [38]. It is imperative for high precision mass measurement that only one ion species is present in the trap when performing the mass measurement to avoid frequency shifts arising, for example, from ion-ion interactions [39]. In the end, the selection of the ion species was a matter of choosing the suitable excitation frequency to either pass the $^{131}\text{I}^+$ or $^{131}\text{Xe}^+$ for the actual mass measurement.

In Penning trap mass spectrometry, the mass m of an ion with charge q is based on the measurement of the cyclotron frequency

$$\nu_c = \frac{1}{2\pi} \frac{q}{m} B, \quad (1)$$

where B is the magnetic field. The best way to deduce the Q value is to measure the cyclotron frequency ratio of the two ions. In this work, singly charged ions were used and the frequency ratio

$$R = \frac{\nu_c(^{131}\text{Xe}^+)}{\nu_c(^{131}\text{I}^+)} = \frac{m(^{131}\text{I}^+)}{m(^{131}\text{Xe}^+)} \quad (2)$$

determined, where $m(^{131}\text{I}^+)$ and $m(^{131}\text{Xe}^+)$ are the masses of the decay daughter ($^{131}\text{I}^+$) and decay parent ($^{131}\text{Xe}^+$) ions, respectively. The ground-state-to-ground-state β^- Q value of ^{131}I is the atomic mass difference of the parent and daughter

$$Q_{\beta^-}(^{131}\text{I}) = [M(^{131}\text{I}) - M(^{131}\text{Xe})]c^2 \quad (3)$$

and using the frequency ratio from Eq. (2),

$$Q_{\beta^-}(^{131}\text{I}) = (R - 1) [M(^{131}\text{Xe}) - m_e] + \Delta B, \quad (4)$$

where m_e is the mass of an electron and ΔB accounts for the atomic electron binding energy difference (here a few eV).

In this work, the cyclotron frequencies ν_c for the ions were measured using the phase-imaging ion-cyclotron-resonance (PI-ICR) technique [40]. It requires projection of the ion motion in the Penning trap onto a position-sensitive microchannel-plate (MCP) ion detector and provides around 40 times better resolving power than the conventionally used time-of-flight ion-cyclotron-resonance (TOF-ICR) method [40–42]. Measurement scheme 2 described in [41] was applied to directly measure the cyclotron frequency ν_c of the corresponding nuclide.

The cyclotron frequency measurement begins after the ions of interest have been captured into the center of the precision trap. First, coherent components of the magnetron and the axial motions are damped with short RF pulses applied in dipolar configuration. This is followed by the excitation of cyclotron motion using dipolar RF field with the reduced cyclotron frequency (ν_+) to increase the cyclotron radius to about 1 mm. This sets the initial phase of the cyclotron motion.

The next step is the utilization of a quadrupole RF field to convert the cyclotron motion to magnetron motion. For every other measurement cycle the application is done right after the previous step while for every other after a preset longer duration. The cycle with short time interval produces so-called magnetron phase while the longer cycle yields the cyclotron phase. The time difference t of the conversions is called the phase accumulation time. It is known extremely precisely and is the key to high precision frequency determination.

Irrespective of the delay of the conversion excitation, the ions spend same amount of time in the trap before they are extracted towards the MCP detector, which registers the time-of-flight and positions of the ions. The two used time intervals produce two spots of ions on the detector. Combined with a center spot, which is measured without cyclotron and conversion excitations, angles α_- and α_+ for magnetron and cyclotron phases, respectively, are obtained. The time difference between the excitation pulses was chosen to be as close as possible to multiple integer of periods of ion's ν_c frequency (see Eq. (1)) so that the angle difference $\alpha_c = \alpha_+ - \alpha_-$ is as small as possible to minimize systematic shifts to level below 10^{-10} [41]. Finally, the cyclotron frequency is deduced from:

$$\nu_c = \frac{\alpha_c + 2\pi n_c}{2\pi t}, \quad (5)$$

where n_c the number of full revolutions with cyclotron frequency ν_c during the phase accumulation time t .

The cycles with short and long delay before the conversion pulse were alternately applied for a total measurement time of approximately 1 minute with the center spot measured right after. Although the magnetron motion was minimized prior to the measurement and the quadrupole conversion excitation pulse carefully tuned to fully convert the induced cyclotron motion to magnetron, still a tiny fraction of both motions remained. These were taken into account by varying the start of the cyclotron excitation over one magnetron period ($\approx 600 \mu\text{s}$) and the extraction delay over

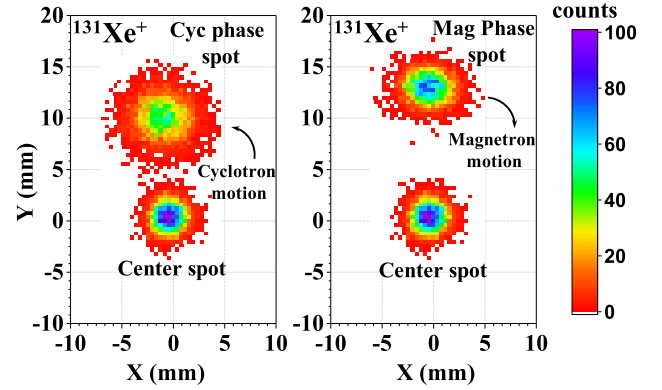


Fig. 2. Ion spots (center, cyclotron phase and magnetron phase) of $^{131}\text{I}^+$ on the 2-dimensional position-sensitive MCP detector after a typical PI-ICR excitation pattern with an accumulation time of 500 ms. The cyclotron phase spot is displayed on the left side and the magnetron phase spot on the right. The angle difference between the two spots relative to the center spot yields α_c of Eq. (5). The color of the pixel represents the number of detected ions.

one cyclotron period ($\approx 0.8 \mu\text{s}$). Five points in each were chosen and thus one full measurement cycle consisted of 25 points for both the magnetron and cyclotron phases, effectively averaging out any residual motion influence. The collection was repeated for 4 times before switching to the other ion species, for which the cycle was repeated. In total, this was repeated for 3.5 hours for accumulation time t of 399 ms and for 16.5 hours for accumulation time of 500 ms (rounded to the nearest integer of period of ν_c). Fig. 2 shows data with 500 ms accumulation time. The quick changing in timescale of a few minutes, not just between the magnetron and cyclotron spots but also between the two ions, ensured that the magnetic field B is nearly identical for the measurement of both ions, minimizing effect of temporal fluctuation of the field.

3. Results and discussion

In total, five sets of data were collected with one using 399 ms of accumulation time and four using 500 ms accumulation time. In each set the measurements of the cyclotron frequencies ν_c of $^{131}\text{Xe}^+$ and $^{131}\text{I}^+$ were interleaved by switching ion species every ≈ 6 minutes. To obtain their cyclotron frequency ratio R , the values of ν_c of $^{131}\text{Xe}^+$ were linearly interpolated to the time of $^{131}\text{I}^+$ measurement. The frequency ratio for each set was obtained by averaging the individual ratios. Fast switching between the two ion species ensured that the temporal fluctuations of the magnetic field had less than 10^{-10} contribution to the uncertainty [43]. Bunches with up to five detected ions were considered in the data analysis to reduce a possible cyclotron frequency shift due to ion-ion interaction [39,43]. The count-rate related frequency shifts were not observed in the analysis. The frequency shifts in the PI-ICR measurement due to ion image distortions, which were well below the statistical uncertainty, were ignored [41]. Since both ions have the same A/q , the mass-dependent systematic shift, which is due to the imperfections of the electric-quadrupolar field in the Penning trap or a misalignment of the electrostatic trapping field with respect to the magnetic field axis, effectively becomes inferior compared to typical statistical uncertainty achieved in the measurement. The uncertainty of the $M(^{131}\text{Xe})$ is only 8 eV/ c^2 and does not contribute to the Q -value uncertainty.

The final frequency ratio was obtained by calculating a weighted mean ratio \bar{R} from the five individual sets. The reduced χ^2 was found to be 1.40, indicating that the statistical uncertainty estimate was too low. To account for this, the uncertainty was expanded by the square root of the reduced chi-squared [44]. The final fre-

Table 1

Potential candidate transitions of ground state of parent nuclei ^{131}I ($7/2^+$) to the excited state of daughter ^{131}Xe with an ultra-low Q value. The first column gives the excited final state of interest for the low Q -value transition. The second column gives decay type. The third column gives the derived experimental decay Q value in units of keV from literature (AME2020) [28] and fourth column lists the Q value from this work. The fifth column gives the experimental excitation energy E^* with the experimental error [29]. The sixth column shows the mass excess (ME) in units of keV/ c^2 from AME2020 and the last column from this work. Spin-parity of the 971.22(13) keV transition has been confirmed experimentally in [30].

Final state in ^{131}Xe	Decay type	Q value (AME2020)	Q value (This work)	E^*	ME (AME2020)	ME (This work)
$9/2^+$	allowed	-0.42(61)	1.03(23)	971.22(13)		
$7/2^+$	allowed	-2.31(62)	-0.86(24)	973.11(14)		
$3/2^+$ (ground state)		970.80(60)	972.25(19)	0	-87442.70(60)	-87441.32(19)

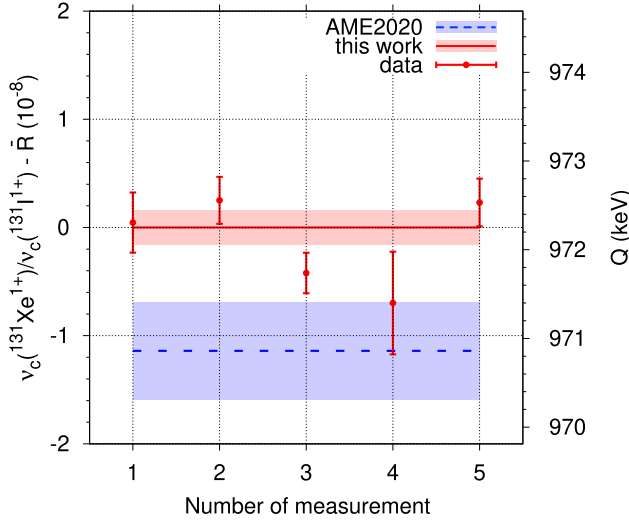


Fig. 3. Cyclotron frequency ratios R of the five sets (points with error bars) and their weighted average compared to the literature value (dashed blue line). The shaded bands show the 1σ uncertainty. The first data point is the set with an accumulation time $t = 399$ ms while the other four have $t = 500$ ms. The left axis shows the frequency ratio with zero being the average frequency ratio from this work and the right axis shows the corresponding Q value.

quency ratio was found to be $\bar{R} = 1.0000079734(16)$. Fig. 3 shows the results of the analysis. Q value for the ground-state-to-ground-state decay and decays to the relevant excited states are tabulated in Table 1 along with the mass excess value of ^{131}I .

The Q value of 972.25(19) keV from this work is more than a factor three more precise than 970.80(60) keV derived from the evaluated masses in AME2020 [27,28]. Also, the Q value is 1.45(63) keV larger. The value in AME2020 originates primarily from the difference between the atomic masses of the parent ^{131}I and that of the daughter ^{131}Xe as listed therein. The ^{131}Xe AME2020 mass value has dominant contribution from a direct Penning trap mass measurement [45], while the adopted AME2020 mass value of ^{131}I was principally derived from a decay measurement of $^{131}\text{I}(\beta^-)^{131}\text{Xe}$ [46,47]. Previous studies have demonstrated that mass values derived in indirect methods, such as decay spectroscopy and nuclear reactions, can suffer from systematic shifts and thus have large discrepancies with values obtained from direct mass measurements [48–50].

The Q values to the excited states near the ground-to-ground-state Q value are obtained by combining the high-precision ground-state-to-ground-state Q value from this work with the excitation energies of the ^{131}Xe states from [29]. The resulting Q values to these low Q value states are given in Table 1 and illustrated in Fig. 4. The decay to the $7/2^+$ state was found to be energetically forbidden at about 4σ while the decay to the $9/2^+$ state is energetically possible with more than 3σ confidence, re-

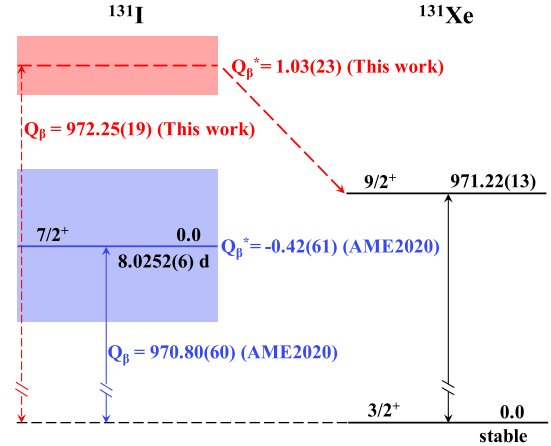


Fig. 4. The ^{131}I ground-state β^- decay to the 971.22(13) keV $9/2^+$ state in ^{131}Xe . The horizontal blue line depicts the level with the Q_{β^-} taken from AME2020 (shaded area shows the 1σ uncertainty) and the red dashed line the Q_{β^-} from this work. The data for the level scheme are adopted from [27–29].

moving the ambiguity of the AME2020-derived Q value whether the decay to the $9/2^+$ state is energetically allowed or not.

The Q value, 1.03(23) keV, is lower than in presently running or planned direct (anti)neutrino mass experiments (the lowest β^- decay Q value is 2.492(30) $_{\text{stat}}(15)_{\text{sys}}$ keV for ^{187}Re and the lowest electron-capture decay Q value is 2.833(30) $_{\text{stat}}(15)_{\text{sys}}$ keV for ^{163}Ho [8]).

To estimate the half-life of this transition, nuclear shell-model (NSM) calculation utilizing the *NuShellX* [51] code with the effective interaction *sn100pn* used to describe ^{132}Sn [52] with ^{100}Sn as a closed core was used. The single-particle model space $1g_{7/2}$, $2d_{5/2}$, $3s_{1/2}$, $2d_{3/2}$ and $1h_{11/2}$ was used for both protons and neutrons. The NSM calculations were able to predict most of the level energies within 100 keV of the corresponding experimental energy below 1 MeV of excitation energy in ^{131}Xe . For the state of interest, $9/2^+$, the computed excitation energy was 937.0 keV, reasonably close to the experimental energy 971.22(13) keV. The dependence of the Q value to the partial half-life of the $7/2^+ \rightarrow 9/2^+$ transition is illustrated in Fig. 5.

Due to the small Q value of this transition, the corresponding partial half-life is extremely sensitive to the exact value of the decay energy, as evident in Fig. 5 where we depict the computed half-life (dashed line) as a function of the Q value. The colored rectangle represents the NSM-predicted partial half-life (vertical span of the rectangle) for the $9/2^+$ transition, taking into account the 1σ error in the presently measured Q value (horizontal span of the rectangle). The NSM-predicted half-life reads $(1.97^{+2.24}_{-0.89}) \times 10^7$ years.

In order to see how reasonable the half-life prediction of the NSM is, an analysis of the measured $\log ft$ values of the well-known allowed transitions to the low-lying $7/2^+$ and to two $5/2^+$

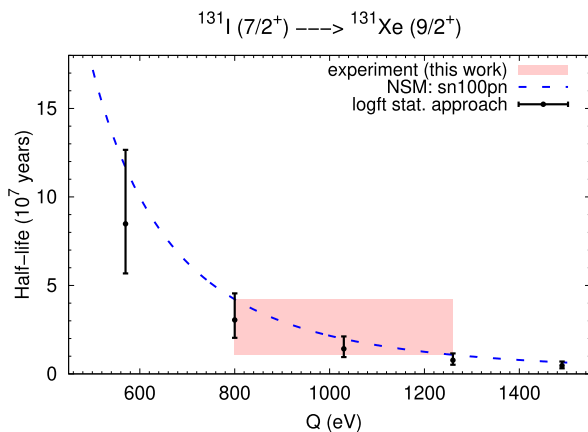


Fig. 5. Shell-model computed half-life as a function of the Q value (dashed line in blue) and the corresponding predicted half-life range for the decay to the $9/2^+$ state (colored rectangle). The points with uncertainties in black are estimates of the half-life assuming the measured Q value 1.03 keV (central point) and its 1σ (points next to the central point) and 2σ errors (points on the extreme left and right), based on a $\log ft$ value deduced using the allowed β transitions to the lower three states in ^{131}Xe (statistical approach, see the text).

states in ^{131}Xe was performed. In this analysis the average of the known $\log ft$ values with their sample standard deviation were used to deduce $\log ft = 6.86(17)$ for the transition to the $9/2^+$ state, in accordance with the NSM calculations. This is called the “statistical approach”. The obtained $\log ft$ was then converted to half-life using five values of phase-space factors, calculated for the central value $Q = 1.03$ keV and its 1σ deviations, $Q = 0.80, 1.26$ keV, and 2σ deviations, $Q = 0.57, 1.49$ keV, as shown by the black points in Fig. 5. In the calculation of phase-space factors exact Dirac wave functions with finite nuclear size and electron screening were used in a similar manner previously employed in the case of $\beta^-\beta^-$ decay [53]. The intrinsic uncertainties in the phase-space calculations come from the uncertainty in the nuclear radius and effective charge. However, these uncertainties cause less than 1 percent error in the phase-space factors so that the only non-negligible error comes from the uncertainty in the $\log ft$ value. In Fig. 5, the 1σ error limits of the deduced $\log ft$ are shown as black vertical bars where the error bars are solely from the $\log ft$ standard deviation by the statistical approach. As can be seen, the results agree within error bars with the NSM-computed partial half-life for the $9/2^+$ -state transition.

In conclusion, a low Q -value transition was searched for in the β^- decay of ^{131}I to states in ^{131}Xe . Such a low- Q -value transition to the $9/2^+$ state at 971.22(13) keV was now verified by a precise Penning-trap measurement of the mass difference of the two nuclei involved while the transition to the $7/2^+$ state was found to have negative Q value. It should be noted that the energy of the $9/2^+$ state was recently reported to be 972.8(1) keV in [30]. However, this and other energies deviate significantly from the evaluated values [29]. Although we are quite confident in using the evaluated energy of 971.22(13) keV, it is clear that a dedicated, high-precision measurement of the $9/2^+$ state energy is needed to remove any ambiguity.

The decay $7/2^+ \rightarrow 9/2^+$ is of allowed type and from the emitted electron spectrum point of view, the transition has a simple universal shape and thus would serve well as a direct electron antineutrino-mass probe. Unfortunately, the estimated partial half-life is so long that the expected decay branch is on the order of 10^{-10} , dominated by β^- decay to $5/2^+$ state at 364.490 keV with $\sim 89\%$ branch. Only time will tell whether future detector technology can overcome the branching problem and lead to a realizable antineutrino-mass experiment on ^{131}I .

Declaration of competing interest

The authors declare that they have no known competing financial interests or personal relationships that could have appeared to influence the work reported in this paper.

Acknowledgements

We acknowledge the support by the Academy of Finland under the Finnish Centre of Excellence Programme 2012–2017 (Nuclear and Accelerator Based Physics Research at JYFL) and projects No. 306980, 312544, 275389, 284516, 295207, 314733, 318043, 327629 and 320062. The support by the EU Horizon 2020 research and innovation program under grant No. 771036 (ERC CoG MAIDEN) is acknowledged.

References

- [1] Planck Collaboration, N. Aghanim, Y. Akrami, M. Ashdown, J. Aumont, C. Baccigalupi, M. Ballardini, A.J. Banday, R.B. Barreiro, N. Bartolo, S. Basak, R. Battye, K. Benabed, J.P. Bernard, M. Bersanelli, P. Bielewicz, J.J. Bock, J.R. Bond, J. Borrill, F.R. Bouchet, F. Boulanger, M. Bucher, C. Burigana, R.C. Butler, E. Calabrese, J.F. Cardoso, J. Carron, A. Challinor, H.C. Chiang, J. Chluba, L.P.L. Colombo, C. Combet, D. Contreras, B.P. Crill, F. Cuttaia, P. de Bernardis, G. de Zotti, J. Delabrouille, J.M. Delouis, E.D. Valentino, J.M. Diego, O. Doré, M. Douspis, A. Ducuc, X. Dupac, S. Dusini, G. Efstathiou, F. Elsner, T.A. Enßlin, H.K. Eriksen, Y. Fantaye, M. Farhang, J. Fergusson, R. Fernandez-Cobos, F. Finelli, F. Forastieri, M. Frailis, A.A. Fraisse, E. Franceschi, A. Frolov, S. Galeotta, S. Galli, K. Ganga, R.T. Génova-Santos, M. Gerbino, T. Ghosh, J. González-Nuevo, K.M. Górski, S. Gratton, A. Gruppuso, J.E. Gudmundsson, J. Hamann, W. Handley, F.K. Hansen, D. Herranz, S.R. Hildebrandt, E. Hivon, Z. Huang, A.H. Jaffe, W.C. Jones, A. Karakci, E. Keihänen, R. Keskitalo, K. Kiiveri, J. Kim, T.S. Kisner, L. Knox, N. Krachmalnicoff, M. Kunz, H. Kurki-Suonio, G. Lagache, J.M. Lamarre, A. Lasenby, M. Lattanzi, C.R. Lawrence, M.L. Jeune, P. Lemos, J. Lesgourgues, F. Levrier, A. Lewis, M. Liguori, P.B. Lilje, M. Lilley, V. Lindholm, M. López-Cañiego, P.M. Lubin, Y.Z. Ma, J.F. Macías-Pérez, G. Maggio, D. Maino, N. Mandolesi, A. Mangilli, A. Marcos-Caballero, M. Maris, P.G. Martin, M. Martinelli, E. Martínez-González, S. Matarrese, N. Mauri, J.D. McEwen, P.R. Meinhold, A. Melchiorri, A. Mennella, M. Migliaccio, M. Millea, S. Mitra, M.A. Miville-Deschênes, D. Molinari, L. Montier, G. Morgante, A. Moss, P. Natoli, H.U. Nørgaard-Nielsen, L. Pagano, D. Paoletti, B. Partridge, G. Patanchon, H.V. Peiris, F. Perrotta, V. Pettorino, F. Piacentini, L. Polastri, G. Polenta, J.L. Puget, J.P. Rachen, M. Reinecke, M. Remazeilles, A. Renzi, G. Rocha, C. Rosset, G. Roudier, J.A. Rubiño-Martín, B. Ruiz-Granados, L. Salvati, M. Sandri, M. Savelainen, D. Scott, E.P.S. Shellard, C. Sirignano, G. Sirri, L.D. Spencer, R. Sunyaev, A.S. Suur-Uuski, J.A. Tauber, D. Tavagnacco, M. Tenti, L. Toffolatti, M. Tomasi, T. Trombetti, L. Valenziano, J. Valiviita, B.V. Tent, L. Vibert, P. Vielva, F. Villa, N. Vittorio, B.D. Wandelt, I.K. Wehus, M. White, S.D.M. White, A. Zacchei, A. Zonca, Planck 2018 results, *Astron. Astrophys.* 641 (2020) A6, <https://doi.org/10.1051/0004-6361/201833910>.
- [2] J. Suhonen, O. Civitarese, Weak-interaction and nuclear-structure aspects of nuclear double beta decay, *Phys. Rep.* 300 (3–4) (1998) 123–214, [https://doi.org/10.1016/S0370-1573\(97\)00087-2](https://doi.org/10.1016/S0370-1573(97)00087-2).
- [3] F.T. Avignone, S.R. Elliott, J. Engel, Double beta decay, Majorana neutrinos, and neutrino mass, *Rev. Mod. Phys.* 80 (2) (2008) 481–516, <https://doi.org/10.1103/RevModPhys.80.481>, arXiv:0708.1033.
- [4] H. Ejiri, J. Suhonen, K. Zuber, Neutrino–nuclear responses for astro-neutrinos, single beta decays and double beta decays, *Phys. Rep.* 797 (2019) 1–102, <https://doi.org/10.1016/j.physrep.2018.12.001>.
- [5] E. Ferri, D. Bagliani, M. Biasotti, G. Ceruti, D. Corsini, M. Favrezi, F. Gatti, A. Giachero, C. Gotti, C. Kilbourne, A. Kling, M. Maino, P. Manfrinetti, A. Nucciotti, G. Pessina, G. Pizzigoni, M. Ribeiro Gomes, M. Sisti, The status of the MARE experiment with 187Re and 163Ho isotopes, *Phys. Proc.* 61 (August 2015) 227–231, <https://doi.org/10.1016/j.phpro.2014.12.037>.
- [6] E.G. Myers, A. Wagner, H. Kracke, B.A. Wesson, Atomic masses of tritium and helium-3, *Phys. Rev. Lett.* 114 (1) (2015), <https://doi.org/10.1103/PhysRevLett.114.013003>.
- [7] D.A. Nesterenko, S. Eliseev, K. Blaum, M. Block, S. Chenmarev, A. Dörr, C. Droese, P.E. Filianin, M. Goncharov, E. Minaya Ramirez, Y.N. Novikov, L. Schweikhard, V.V. Simon, Direct determination of the atomic mass difference of Re 187 and Os 187 for neutrino physics and cosmochronology, *Phys. Rev. C, Nucl. Phys.* 90 (4) (2014) 042501, <https://doi.org/10.1103/PhysRevC.90.042501>.
- [8] S. Eliseev, K. Blaum, M. Block, S. Chenmarev, H. Dorrer, C.E. Düllmann, C. Enss, P.E. Filianin, L. Gastaldo, M. Goncharov, U. Köster, F. Lautenschläger, Y.N. Novikov, A. Rischka, R.X. Schüssler, L. Schweikhard, A. Türler, Direct measurement of the mass difference of ^{163}Ho and ^{163}Dy solves the Q -value puzzle for the neutrino mass determination, *Phys. Rev. Lett.* 115 (6) (2015) 62501, <https://doi.org/10.1103/PhysRevLett.115.062501>, arXiv:1604.04210.

- [9] P.C. Ranitzsch, C. Hassel, M. Wegner, D. Hengstler, S. Kempf, A. Fleischmann, C. Enss, L. Gastaldo, A. Herlert, K. Johnston, Characterization of the Ho 163 electron capture spectrum: a step towards the electron neutrino mass determination, *Phys. Rev. Lett.* 119 (12) (2017), <https://doi.org/10.1103/PhysRevLett.119.122501>.
- [10] M. Shamsuzzoha Basunia, Nuclear data sheets for A=193, *Nucl. Data Sheets* 143 (2017) 1–381, <https://doi.org/10.1016/j.nds.2017.08.001>.
- [11] J. Kopp, A. Merle, Ultralow Q values for neutrino mass measurements, *Phys. Rev. C, Nucl. Phys.* 81 (4) (2010) 1, <https://doi.org/10.1103/PhysRevC.81.045501>, arXiv:0911.3329.
- [12] S. Eliseev, C. Böhm, D. Beck, K. Blaum, M. Breitenfeldt, V.N. Fedosseev, S. George, F. Herfurth, A. Herlert, H.J. Kluge, M. Kowalska, D. Lunney, S. Naimi, D. Neidherr, Y.N. Novikov, M. Rosenbusch, L. Schweikhard, S. Schwarz, M. Seeliverstov, K. Zuber, Direct mass measurements of ^{194}Hg and ^{194}Au : a new route to the neutrino mass determination?, *Phys. Lett. B: Nucl. Elem. Part. High-Ener. Phys.* 693 (4) (2010) 426–429, <https://doi.org/10.1016/j.physletb.2010.08.071>, <http://www.sciencedirect.com/science/article/B6TVN-50XS6CB-3/2/e50e7350cb45d005a90ae8b4b2c98c1b>.
- [13] M. Haaranen, J. Suhonen, Beta decay of ^{115}Cd and its possible ultra-low Q-value branch, *Eur. Phys. J. A* 49 (7) (2013) 1–9, <https://doi.org/10.1140/epja/i2013-13093->.
- [14] J. Suhonen, Theoretical studies of rare weak processes in nuclei, *Phys. Scr.* 89 (5) (2014) 54032, <https://doi.org/10.1088/0031-8949/89/5/054032>.
- [15] A. Welker, P. Filianin, N.A. Althubiti, D. Atanasov, K. Blaum, T.E. Cocolios, S. Eliseev, F. Herfurth, S. Kreim, D. Lunney, V. Manea, D. Neidherr, Y. Novikov, M. Rosenbusch, L. Schweikhard, F. Wienholtz, R.N. Wolf, K. Zuber, Precision electron-capture energy in ^{202}Pb and its relevance for neutrino mass determination, *Eur. Phys. J. A* 53 (7) (2017) 14–17, <https://doi.org/10.1140/epja/i2017-12345-y>.
- [16] J. Karthein, D. Atanasov, K. Blaum, S. Eliseev, P. Filianin, D. Lunney, V. Manea, M. Mougeot, D. Neidherr, Y. Novikov, L. Schweikhard, A. Welker, F. Wienholtz, K. Zuber, Direct decay-energy measurement as a route to the neutrino mass, *Hyperfine Interact.* 240 (1) (2019) 1–9, <https://doi.org/10.1007/s10751-019-1601-z>, arXiv:1905.05510.
- [17] N.D. Gamage, R. Bhandari, M. Horana Gamage, R. Sandler, M. Redshaw, Identification and investigation of possible ultra-low Q value β decay candidates, *Hyperfine Interact.* 240 (1) (2019), <https://doi.org/10.1007/s10751-019-1588-5>.
- [18] R. Sandler, G. Bollen, N.D. Gamage, A. Hamaker, C. Izzo, D. Puentes, M. Redshaw, R. Ringle, I. Yandow, Investigation of the potential ultralow Q-value β -decay candidates Sr 89 and Ba 139 using Penning trap mass spectrometry, *Phys. Rev. C* 100 (2) (2019) 1, <https://doi.org/10.1103/PhysRevC.100.024309>, arXiv:1906.03335.
- [19] Z. Ge, T. Eronen, A. de Roubin, D.A. Nesterenko, M. Hukkanen, O. Beliuskina, R. de Groote, S. Geldhof, W. Gins, A. Kankainen, A. Koszorús, J. Kotila, J. Kostensalo, I.D. Moore, A. Raggio, S. Rinta-Antila, J. Suhonen, V. Virtanen, A.P. Weaver, A. Zadornaya, A. Jokinen, Direct measurement of the mass difference of ^{72}As - ^{72}Ge rules out ^{72}As as a promising β -decay candidate to determine the neutrino mass, *Phys. Rev. C* 103 (2021) 065502, <https://doi.org/10.1103/PhysRevC.103.065502>.
- [20] Z. Ge, T. Eronen, K.S. Tyrin, J. Kotila, J. Kostensalo, D.A. Nesterenko, O. Beliuskina, R. de Groote, A. de Roubin, S. Geldhof, W. Gins, M. Hukkanen, A. Jokinen, A. Kankainen, A. Koszorús, M.I. Krivoruchenko, S. Kujanpää, I.D. Moore, A. Raggio, S. Rinta-Antila, J. Suhonen, V. Virtanen, A.P. Weaver, A. Zadornaya, ^{159}Dy electron-capture: a new candidate for neutrino mass determination, *Phys. Rev. Lett.* 127 (2021) 272301, <https://doi.org/10.1103/PhysRevLett.127.272301>.
- [21] C.M. Cattadori, M. De Deo, M. Laubenstein, L. Pandola, V.I. Tretyak, Observation of β decay of ^{115}In to the first excited level of ^{115}Sn , *Nucl. Phys. A* 748 (1–2) (2005) 333–347, <https://doi.org/10.1016/j.nuclphysa.2004.10.025>.
- [22] J.S. Wieslander, J. Suhonen, T. Eronen, M. Hult, V.V. Elomaa, A. Jokinen, G. Marissens, M. Miasazek, M.T. Mustonen, S. Rahaman, C. Weber, J. Äystö, Smallest known Q value of any nuclear decay: the rare β -decay of $\text{In}115(9/2^+) \rightarrow \text{Sn}115(3/2^+)$, *Phys. Rev. Lett.* 103 (12) (2009) 122501, <https://doi.org/10.1103/PhysRevLett.103.122501>.
- [23] B.J. Mount, M. Redshaw, E.G. Myers, Q value of $\text{In}115 \rightarrow \text{Sn}115(3/2^+)$: the lowest known energy β decay, *Phys. Rev. Lett.* 103 (12) (2009) 122502, <https://doi.org/10.1103/PhysRevLett.103.122502>.
- [24] A. Kankainen, T. Eronen, D. Nesterenko, A. de Roubin, M. Vilén, Recent experiments at the JYFLTRAP Penning trap, *Hyperfine Interact.* 241 (1) (2020) 43, <https://doi.org/10.1007/s10751-020-01711-5>.
- [25] T. Eronen, J.C. Hardy, High-precision Q_{EC} -value measurements for superallowed decays, *Eur. Phys. J. A* 48 (4) (2012) 1–8, <https://doi.org/10.1140/epja/i2012-12048-y>.
- [26] A. De Roubin, J. Kostensalo, T. Eronen, L. Canete, R.P. De Groote, A. Jokinen, A. Kankainen, D.A. Nesterenko, I.D. Moore, S. Rinta-Antila, J. Suhonen, M. Vilén, High-precision Q-value Measurement confirms the potential of Cs 135 for absolute antineutrino mass scale determination, *Phys. Rev. Lett.* 124 (22) (2020) 1, <https://doi.org/10.1103/PhysRevLett.124.222503>, arXiv:2002.08282.
- [27] W. Huang, M. Wang, F. Kondev, G. Audi, S. Naimi, The AME 2020 atomic mass evaluation (I). Evaluation of input data, and adjustment procedures*, *Chin. Phys. C* 45 (3) (2021) 030002, <https://doi.org/10.1088/1674-1137/abdbb0>.
- [28] M. Wang, W. Huang, F. Kondev, G. Audi, S. Naimi, The AME 2020 atomic mass evaluation (II). Tables, graphs and references*, *Chin. Phys. C* 45 (3) (2021) 030003, <https://doi.org/10.1088/1674-1137/abddaf>.
- [29] National nuclear data center, Available at <https://www.nndc.bnl.gov/>, 2021, 2020/4/7.
- [30] R. Banik, S. Bhattacharyya, S. Biswas, S. Bhattacharya, G. Mukherjee, S. Rajban-shi, S. Dar, S. Nandi, S. Ali, S. Chatterjee, S. Das, S.D. Gupta, S.S. Ghugre, A. Goswami, A. Lemasson, D. Mondal, S. Mukhopadhyay, H. Pai, S. Pal, D. Pandit, R. Raut, P. Ray, M. Rejmund, S. Samanta, Revealing multiple band structures in ^{131}Xe from α -induced reactions, *Phys. Rev. C* 101 (4) (2020) 044306, <https://doi.org/10.1103/physrevc.101.044306>.
- [31] Y. Khazov, I. Mitropolsky, A. Rodionov, Nuclear data sheets for A = 131, *Nucl. Data Sheets* 107 (11) (2006) 2715–2930, <https://doi.org/10.1016/j.nds.2006.10.001>.
- [32] I.D. Moore, T. Eronen, D. Gorelov, J. Hakala, A. Jokinen, A. Kankainen, V.S. Kolhinen, J. Koponen, H. Penttilä, I. Pohjalainen, M. Reponen, J. Rissanen, A. Saastamoinen, S. Rinta-Antila, V. Sonnenschein, J. Äystö, Towards commissioning the new IGISOL-4 facility, *Nucl. Instrum. Methods Phys. Res., Sect. B, Beam Interact. Mater. Atoms* 317 (PART B) (2013) 208–213, <https://doi.org/10.1016/j.nimb.2013.06.036>, <http://www.sciencedirect.com/science/article/pii/S0168583X13007143>.
- [33] V.S. Kolhinen, T. Eronen, D. Gorelov, J. Hakala, A. Jokinen, K. Jokiranta, A. Kankainen, M. Koikkalainen, J. Koponen, H. Kulmala, M. Lantz, A. Mattera, I.D. Moore, H. Penttilä, T. Pikkarainen, I. Pohjalainen, M. Reponen, S. Rinta-Antila, J. Rissanen, C. Rodríguez Triguero, K. Rytönen, A. Saastamoinen, A. Solders, V. Sonnenschein, J. Äystö, Recommissioning of JYFLTRAP at the new IGISOL-4 facility, *Nucl. Instrum. Methods Phys. Res., Sect. B, Beam Interact. Mater. Atoms* 317 (PART B) (2013) 506–509, <https://doi.org/10.1016/j.nimb.2013.07.050>.
- [34] H. Penttilä, D. Gorelov, V.V. Elomaa, T. Eronen, U. Hager, J. Hakala, A. Jokinen, A. Kankainen, P. Karvonen, I.D. Moore, J. Parkkonen, K. Peräjärvi, I. Pohjalainen, S. Rahaman, S. Rinta-Antila, J. Rissanen, V.A. Rubchenya, A. Saastamoinen, V. Simutkin, T. Sonoda, C. Weber, A. Voss, J. Äystö, Independent isotopic yields in 25 MeV and 50 MeV proton-induced fission of natU, *Eur. Phys. J. A* 52 (4) (2016) 104, <https://doi.org/10.1140/epja/i2016-16104-4>.
- [35] P. Karvonen, I.D. Moore, T. Sonoda, T. Kessler, H. Penttilä, K. Peräjärvi, P. Ronkanen, J. Äystö, A sextupole ion beam guide to improve the efficiency and beam quality at IGISOL, *Nucl. Instrum. Methods Phys. Res., Sect. B, Beam Interact. Mater. Atoms* 266 (21) (2008) 4794–4807, <https://doi.org/10.1016/j.nimb.2008.07.022>, <http://www.sciencedirect.com/science/article/B6TJN-4T2S8KR-1/2/1d7624cd369335096dcb1fd81a410fea>.
- [36] A. Nieminen, J. Huikari, A. Jokinen, J. Äystö, P. Campbell, E.C. Cochrane, Beam cooler for low-energy radioactive ions, *Nucl. Instrum. Methods Phys. Res., Sect. A, Accel. Spectrom. Detect. Assoc. Equip.* 469 (2) (2001) 244–253, [https://doi.org/10.1016/S0168-9002\(00\)00750-6](https://doi.org/10.1016/S0168-9002(00)00750-6), <http://www.sciencedirect.com/science/article/B6TJM-43PGJKX-C/1/93d5587efba5cfe8571b63228952dab8>.
- [37] G. Savard, S. Becker, G. Bollen, H.J. Kluge, R.B. Moore, T. Otto, L. Schweikhard, H. Stolzenberg, U. Wiess, A new cooling technique for heavy ions in a Penning trap, *Phys. Lett. A* 158 (5) (1991) 247–252, [https://doi.org/10.1016/0375-9601\(91\)91008-2](https://doi.org/10.1016/0375-9601(91)91008-2).
- [38] T. Eronen, V.V. Elomaa, U. Hager, J. Hakala, A. Jokinen, A. Kankainen, S. Rahaman, J. Rissanen, C. Weber, J. Äystö, JYFLTRAP: mass spectrometry and isomerically clean beams, *Acta Phys. Pol. B* 39 (2) (2008) 445–455, <https://www.actaphys.uj.edu.pl/R/39/2/445.pdf>.
- [39] A. Kellerbauer, K. Blaum, G. Bollen, F. Herfurth, H.J. Kluge, M. Kuckein, E. Sauvan, C. Scheidenberger, L. Schweikhard, From direct to absolute mass measurements: a study of the accuracy of ISOLTRAP, *Eur. Phys. J. D* 22 (1) (2003) 53–64, <https://doi.org/10.1140/epjd/e2002-00222-0>.
- [40] D.A. Nesterenko, T. Eronen, A. Kankainen, L. Canete, A. Jokinen, I.D. Moore, H. Penttilä, S. Rinta-Antila, A. de Roubin, M. Vilen, Phase-imaging ion-cyclotron-resonance technique at the JYFLTRAP double Penning trap mass spectrometer, *Eur. Phys. J. A* 54 (9) (2018) 0, <https://doi.org/10.1140/epja/i2018-12589-y>.
- [41] S. Eliseev, K. Blaum, M. Block, A. Dörr, C. Droese, T. Eronen, M. Goncharov, M. Höcker, J. Ketter, E.M. Ramirez, D.A. Nesterenko, Y.N. Novikov, L. Schweikhard, A phase-imaging technique for cyclotron-frequency measurements, *Appl. Phys. B, Lasers Opt.* 114 (1–2) (2014) 107–128, <https://doi.org/10.1007/s00340-013-5621-0>.
- [42] S. Eliseev, K. Blaum, M. Block, C. Droese, M. Goncharov, E. Minaya Ramirez, D.A. Nesterenko, Y.N. Novikov, L. Schweikhard, Phase-imaging ion-cyclotron-resonance measurements for short-lived nuclides, *Phys. Rev. Lett.* 110 (8) (2013) 82501, <https://doi.org/10.1103/PhysRevLett.110.082501>.
- [43] C. Roux, K. Blaum, M. Block, C. Droese, S. Eliseev, M. Goncharov, F. Herfurth, E.M. Ramirez, D.A. Nesterenko, Y.N. Novikov, L. Schweikhard, Data analysis of Q-value measurements for double-electron capture with SHIPTRAP, *Eur. Phys. J. D* 67 (7) (2013) 1–9, <https://doi.org/10.1140/epjd/e2013-40110-x>.
- [44] R.T. Birge, The calculation of errors by the method of least squares, *Phys. Rev.* 40 (2) (1932) 207–227, <https://doi.org/10.1103/PhysRev.40.207>.
- [45] M. Höcker, R. Rana, E.G. Myers, Atomic masses of ^{82}Kr and $^{131,134}\text{Xe}$, *Phys. Rev. A* 88 (5) (2013) 52502, <https://doi.org/10.1103/PhysRevA.88.052502>.
- [46] N. Verster, G. Nijgh, R. van Lieshout, C. Bakker, Measurement of the radiations from ^{131}I and ^{131}Xe with a lens type beta-ray spectrometer, *Physica* 17 (7) (1951) 637–657, [https://doi.org/10.1016/0031-8914\(51\)90048-1](https://doi.org/10.1016/0031-8914(51)90048-1).

- [47] D. Rose, G. Hinman, L.G. Lang, Internal conversion in i^{131} , Phys. Rev. 86 (1952) 863–865, <https://doi.org/10.1103/PhysRev.86.863>.
- [48] J.C. Hardy, L.C. Carraz, B. Jonson, P.G. Hansen, The essential decay of pandemonium: a demonstration of errors in complex beta-decay schemes, Phys. Lett. B 71 (2) (1977) 307–310, [https://doi.org/10.1016/0370-2693\(77\)90223-4](https://doi.org/10.1016/0370-2693(77)90223-4).
- [49] S. Eliseev, D. Nesterenko, K. Blaum, M. Block, C. Droese, F. Herfurth, E. Minaya Ramirez, Y.N. Novikov, L. Schweikhard, K. Zuber, Q values for neutrinoless double-electron capture in ^{96}Ru , ^{162}Er , and ^{168}Yb , Phys. Rev. C, Nucl. Phys. 83 (3) (2011) 38501, <https://doi.org/10.1103/PhysRevC.83.038501>.
- [50] D.A. Nesterenko, L. Canete, T. Eronen, A. Jokinen, A. Kankainen, Y.N. Novikov, S. Rinta-Antila, A. de Roubin, M. Vilen, High-precision measurement of the mass difference between ^{102}Pd and ^{102}Ru , Int. J. Mass Spectrom. 435 (2019) 204–208, <https://doi.org/10.1016/j.ijms.2018.10.038>.
- [51] B. Brown, W. Rae, The shell-model code NuShellX@MSU, Nucl. Data Sheets 120 (2014) 115–118, <https://doi.org/10.1016/j.nds.2014.07.022>.
- [52] B.A. Brown, N.J. Stone, J.R. Stone, I.S. Towner, M. Hjorth-Jensen, Magnetic moments of the 2 states around ^{132}Sn , Phys. Rev. C 71 (4) (2005), <https://doi.org/10.1103/physrevc.71.044317>.
- [53] J. Kotila, F. Iachello, Phase-space factors for double- β decay, Phys. Rev. C 85 (2012) 034316, <https://doi.org/10.1103/PhysRevC.85.034316>.

VI

β^- DECAY Q-VALUE MEASUREMENT OF ^{136}CS AND ITS IMPLICATIONS FOR NEUTRINO STUDIES

by

Ge, Z and Eronen, T and de Roubin, A and Ramalho, M and Kostensalo, J and
Kotila, J and Suhonen, J and Nesterenko, D A and Kankainen, A and Ascher, P
and Beliuskina, O and Flayol, M and Gerbaux, M and Grevy, S and Hukkanen, M
and Husson, A and Jaries, A and Jokinen, A and Moore, I D and Pirinen, P and
Romero, J and Stryczyk, M and Virtanen, V and Zadvornaya, A

Phys. Rev. C **108**, 4, 045502 (2023).

DOI: 10.1103/PhysRevC.108.045502

Reproduced with kind permission of American Physical Society.

β^- decay Q -value measurement of ^{136}Cs and its implications for neutrino studies

Z. Ge^{1,2,*}, T. Eronen^{2,†}, A. de Roubin^{3,‡}, M. Ramalho², J. Kostensalo⁴, J. Kotila^{2,5,6}, J. Suhonen^{2,§},
 D. A. Nesterenko², A. Kankainen², P. Ascher³, O. Beliuskina², M. Flayol³, M. Gerbaux³, S. Grévy³,
 M. Hukkanen^{2,3}, A. Husson³, A. Jaries², A. Jokinen², I. D. Moore², P. Pirinen², J. Romero^{2,7},
 M. Stryczyk², V. Virtanen², and A. Zadornaya^{2,||}

¹GSI Helmholtzzentrum für Schwerionenforschung GmbH, 64291 Darmstadt, Germany

²Department of Physics, University of Jyväskylä, P.O. Box 35, FI-40014, Jyväskylä, Finland

³Université de Bordeaux, CNRS/IN2P3, LP2I Bordeaux, UMR 5797, F-33170 Gradignan, France

⁴Natural Resources Institute Finland, Yliopistokatu 6B, FI-80100, Joensuu, Finland

⁵Finnish Institute for Educational Research, University of Jyväskylä, P.O. Box 35, FI-40014, Jyväskylä, Finland

⁶Center for Theoretical Physics, Sloane Physics Laboratory, Yale University, New Haven, Connecticut 06520-8120, USA

⁷Department of Physics, University of Liverpool, Liverpool L69 7ZE, United Kingdom



(Received 7 June 2023; accepted 19 September 2023; published 11 October 2023)

The β^- decay Q value of ^{136}Cs ($J^\pi = 5^+$, $t_{1/2} \approx 13$ d) was measured with the JYFLTRAP Penning trap setup at the Ion Guide Isotope Separator On-Line facility of the University of Jyväskylä, Finland. The monoisotopic samples required in the measurements were prepared with a new scheme utilized for the cleaning, based on the coupling of dipolar excitation with Ramsey's method of time-separated oscillatory fields and the phase-imaging ion-cyclotron-resonance technique. The Q value is determined to be 2536.83(45) keV, which is ≈ 4 times more precise and 11.4(20) keV ($\approx 6\sigma$) smaller than the adopted value in the most recent Atomic Mass Evaluation AME2020. The daughter, ^{136}Ba , has a 4^+ state at 2544.481(24) keV and a 3^- state at 2532.653(23) keV, both of which can potentially be ultralow Q -value end states for the ^{136}Cs decay. With our new ground-to-ground state Q value, the decay energies to these two states become $-7.65(45)$ keV and $4.18(45)$ keV, respectively. The former is confirmed to be negative at the level of $\approx 17\sigma$, which verifies that this transition is not a suitable candidate for neutrino mass determination. On the other hand, the slightly negative Q value makes this transition an interesting candidate for the study of virtual β - γ transitions. The decay to the 3^- state is validated to have a positive low Q value which makes it a viable candidate for neutrino mass determination. For this transition, we obtained a shell-model-based half-life estimate of $2.1_{-0.8}^{+1.6} \times 10^{12}$ yr. Furthermore, the newly determined low reaction threshold of 79.08(54) keV for the charged-current $\nu_e + ^{136}\text{Xe} (0^+) \rightarrow ^{136}\text{Cs}^* + e^-$ neutrino capture process is used to update the cross sections for a set of neutrino energies relevant to solar ^7Be , pep, and CNO neutrinos. Based on our shell-model calculations, the new lower threshold shows event rates of 2–4 percent higher than the old threshold for several final states reached by the different species of solar neutrinos.

DOI: [10.1103/PhysRevC.108.045502](https://doi.org/10.1103/PhysRevC.108.045502)

I. INTRODUCTION

The standard model (SM) predicts that the neutrino is massless, and how neutrinos acquire their small masses, verified by the neutrino-oscillation experiments, is consequently a matter of great theoretical interest and may be evidence of new physics beyond the SM [1–3]. Assessing the neutrino mass scale has been an outstanding task for particle physics, as the absolute value of the neutrino mass would provide an important parameter to extend the SM of particle physics and

to understand the origin of fermion masses beyond the Higgs mechanism. The neutrinoless double β decay experiments aim to probe if neutrinos are of Dirac or Majorana nature and to measure the effective Majorana neutrino mass [4–6]. This method is, however, nuclear-model dependent and strongly relies on the calculation of the involved nuclear matrix elements, sensitive to the details of the nuclear wave functions describing the initial, intermediate, and final nuclear states of the process [6]. Complementary ways to probe the involved wave functions have been devised, like the nuclear muon capture, charge-exchange, and double charge-exchange reactions [6]. Nevertheless, β^- -decay or electron-capture (EC) spectrum end-point study remains currently the only laboratory method to provide a model-independent measurement of the absolute scale of the (anti)neutrino mass. In these experiments the most sensitive upper limits on the mass of the electron neutrino m_{ν_e} have been achieved by investigating the end point of the β^- electron spectrum. The most stringent upper limit of $0.8 \text{ eV}/c^2$ [90% confidence level (C.L.)] for the

*Corresponding author: z.ge@gsi.de

†Corresponding author: tommi.eronen@jyu.fi

‡Present address: KU Leuven, Instituut voor Kern- en Stralingsfysica, B-3001 Leuven, Belgium.

§Corresponding author: jouni.t.suhonen@jyu.fi

||Present address: II. Physikalisches Institut, Justus-Liebig-Universität Gießen, 35392 Gießen, Germany.

electron-antineutrino mass is obtained by studying the tritium decay in the KATRIN (KARlsruhe TRitium Neutrino) experiment [7], and an upper limit of $150 \text{ eV}/c^2$ (95% C.L.) is obtained for the electron-neutrino mass, as achieved by studying the EC of ^{163}Ho in the ECHO experiment [8]. In these decay experiments, as small as possible Q value of the decay is essential to partially balance the limitation on the statistics when looking for the tiny (anti)neutrino-mass generated distortion close to the end-point energy [9,10]. For the β -decay experiments the fraction of decays in a given energy interval ΔE below the end-point Q value is proportional to $(\Delta E/Q)^3$, whereas for the EC this dependence on the Q value can be even more drastic especially in the case when the Q value is close to an atomic excitation level [11,12]. The preference for lower Q values is based on the fact that the fraction of decays in a given energy interval ΔE below the end-point will be increased with a lower Q value.

Up to now, only ground-state-to-ground-state (gs-to-gs) decay cases of ^3H , ^{187}Re (β^- decay), and ^{163}Ho (electron capture), having the lowest known gs-to-gs Q values, have been used for direct neutrino-mass-determination experiments. The β^- decay of tritium, $^3\text{H}(1/2^+) \rightarrow ^3\text{He}(1/2^+)$, which is of the allowed type (a Fermi and/or Gamow-Teller transition) with a Q value ($Q_{\beta^-}^0$) of $\approx 18.6 \text{ keV}$ [13], is utilized to measure the effective electron antineutrino mass. In an EC transition, like $^{163}\text{Ho} + e^- \rightarrow ^{163}\text{Dy}^* + \nu_e$, one can determine the effective electron neutrino mass from the analysis of the endpoint region of the excitation energy spectrum of the daughter atom ^{163}Dy , whose Q_{EC} is $\approx 2.8 \text{ keV}$.

The possibility to utilize transitions to excited final states has recently attracted a lot of attention, as reviewed in [14]. Intensive search for isotopes featuring β^- /EC transitions from ground-state-to-excited-states (gs-to-es) with a positive low Q value, preferably ultralow ($<1 \text{ keV}$), has recently been carried out [11,12,15–24]. From the technology point of view, suitable detectors are available as described in [25]. It is imperative to search for nuclides that could be used for competitive experiments using gs-to-es decays. In addition to the slightly positive Q values, the slightly negative Q values can also be of interest in seeking for a new type of transition process, like the virtual radiative “detour” transitions (RDT). A recent study of this type of transition in ^{59}Ni was carried out in Ref. [26,27], where a virtual transition via a state 26 keV higher than allowed by the Q value of the transition was found to contribute about 4% to the experimental gamma spectrum. This result highlights that a slightly energetically forbidden transition will open a door to the possibility to study RDTs. Since the probability of such a detour transition is proportional to $(E^* - E_\gamma)^{-2}$ [26], where E_γ is the energy of the emitted gamma ray, a transition with an ultra-low negative Q value would make the RDT a relatively strong channel and thus easier to detect.

Special attention is given to possible alterations in neutrino-capture cross sections of low-energy neutrinos, for example those from the sun, by the more precise Q -value measurements. Of interest are the charged-current $\nu_e + ^{136}\text{Xe}(0^+) \rightarrow ^{136}\text{Cs}^* + e^-$ neutrino-capture cross sections for the solar ^7Be , pep, and CNO neutrinos where our improved threshold value could alter the cross sections and thus the

detection potential of these neutrinos in xenon-based solar-neutrino observatories [28].

In summary, a precise and accurate determination of the transition Q value is extremely important to validate the possible further usage of low Q -value-decay candidate transitions in the context of searches for the absolute (anti)neutrino mass scale or for radiative “detour” transitions. Also implications for the low-energy solar-neutrino detection could potentially be of relevance. The allowed transition $^{136}\text{Cs}(5^+, t_{1/2} \approx 13 \text{ d}) \rightarrow ^{136}\text{Ba}^*(4^+, 2544.481(24) \text{ keV}$ [29–32]), is of paramount interest for the antineutrino-mass studies because of its small gs-to-es Q value $Q_{\beta^-}^*$ ($= Q_{\beta^-}^0 - E^*$) of $3.7(19) \text{ keV}$ [33]. This transition is proposed to be one of the most promising candidates for neutrino mass determination [24]. The $Q_{\beta^-}^*$ value for this transition can be deduced from the sub-keV-precision energy-level E^* data in [32] and the gs-to-gs Q value of ^{136}Cs in AME2020 [33]. The gs-to-gs Q value of ^{136}Cs in AME2020 is evaluated primarily using data from two $^{136}\text{Cs}(\beta^-) ^{136}\text{Ba}$ -decay experiments performed more than 60 years ago [34,35]. Previous studies have already demonstrated that Q values derived in indirect methods, such as decay spectroscopy, show large discrepancies with those from direct mass measurements and can be inaccurate over a wide range of mass numbers [20,36,37]. The AME2020 Q value with its large uncertainty of 1.9 keV , and its possible inaccuracy, requires verification to unambiguously identify energetically allowed or forbidden low- Q transitions. To confirm whether there are β^- -decay transitions from ^{136}Cs that can serve as potential candidates for future antineutrino-mass determination experiments or be eligible for studies of RDTs, the gs-to-gs Q value needs to be measured directly with a sub-keV uncertainty.

Penning trap mass spectrometry (PTMS) is the leading technique for accurate and precise mass and Q -value determination. It relies on the determination of the cyclotron frequency ratio of parent and daughter ions, from which the mass difference can be extracted. In this article, we report on the first-time direct determination of the gs-to-gs β^- -decay Q value of ^{136}Cs with the JYFLTRAP PTMS. A method based on utilization of a dipolar radiofrequency (RF) excitation of ion motion with time-separated oscillatory fields in the precision trap coupled with the phase-imaging ion-cyclotron-resonance (PI-ICR) technique, is used to prepare monoisotopic ions to ensure a contaminant-free high-precision Q -value determination. The new scheme allows for an efficient isobaric ion separation of ^{136}Cs from the small mass-difference ($90 \text{ keV}/c^2$) contaminant of ^{136}Xe , and isomeric ion separation of ^{136}Cs from its co-produced low-lying isomeric state ($t_{1/2} \approx 17.5 \text{ s}$) at 518 keV .

II. EXPERIMENTAL METHOD

The measurement was performed at the Ion Guide Isotope Separator On-Line facility (IGISOL) [38] with the JYFLTRAP double Penning trap mass spectrometer [39,40] at the University of Jyväskylä, Finland. A schematic view of the experimental setup is shown in Fig. 1. The two ion species of the decay pair, ^{136}Cs and ^{136}Ba , were produced by irradiating a natural uranium target foil with a few μA proton

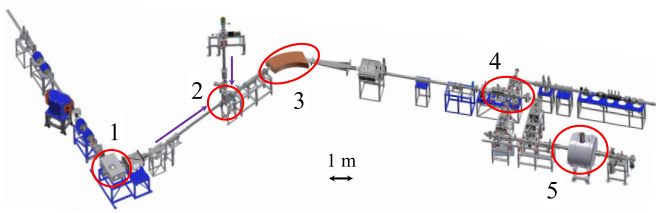


FIG. 1. Schematic view of the IGISOL facility. The $^{136}\text{Cs}^+$ and $^{136}\text{Ba}^+$ ions were produced with proton-induced fission reactions on a natural uranium target within the IGISOL target chamber (1). The online beam was selected with an electrostatic kicker (2) and the dipole magnet (3) was used to transport only ions with $A/q = 136$. The ion cooling and bunching was carried out in the RFQ cooler-buncher (4) and the final Q value and mass measurement was performed with the JYFLTRAP Penning trap setup (5).

beam at 30 MeV from the K-130 cyclotron. The produced ions were stopped and thermalized in a helium-filled gas cell, and extracted out with the gas flow and electric fields via a sextupole ion guide [40]. The extracted ions were accelerated to 30 keV of energy and transported further to the 55° dipole magnet having a mass resolving power of $M/\Delta M \approx 500$. This allows isobaric separation to select only ions with $A/q = 136$, including ^{136}Cs , ^{136m}Cs , ^{136}Xe , ^{136}Ba , ^{136}Te , and ^{136}I that are all produced in the fission reaction. The ions are then delivered to a radiofrequency quadrupole cooler-buncher [41], where they are accumulated, cooled and bunched prior to sending the bunches to the JYFLTRAP double Penning trap mass spectrometer for further purification and the final mass-difference measurements.

JYFLTRAP consists of two cylindrical Penning traps in a 7 T magnetic field. The first trap (purification trap) is filled with helium buffer gas and is used for isobaric purification via the buffer-gas cooling technique [45]. This technique can provide a mass purification with a resolving power of around 10^5 . For higher mass resolving power, the Ramsey cleaning method [42] can be employed. Figure 2 shows the schematic diagram of the steps employed prior to the actual mass and Q -value measurements in the second trap (precision trap).

In this experiment, a purified sample of decay-daughter ions $^{136}\text{Ba}^+$ was prepared with the buffer-gas cooling tech-

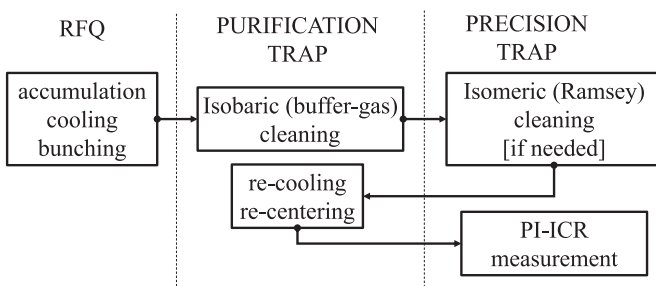


FIG. 2. Schematic of the measurement cycle at JYFLTRAP [39,42–44]. The purification trap is used for isobaric cleaning, and it is often sufficient to provide contaminant-free samples in most of the cases studied. The precision trap is used for further isomeric cleaning when higher resolving power is needed and final high-precision mass or Q -value measurements.

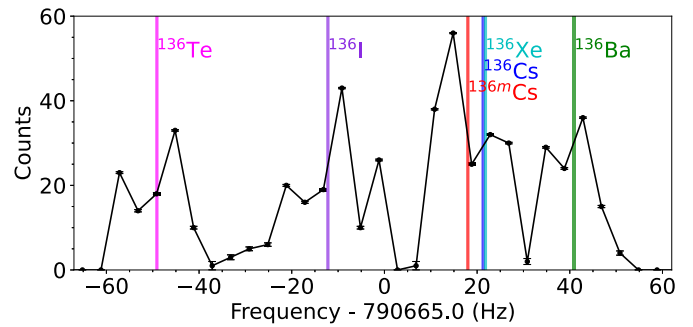


FIG. 3. Detected number of ions downstream from the PTMS as a function of quadrupole excitation frequency in the purification trap. The vertical lines in various colors indicate the excitation frequency to be applied for the selection of the corresponding ion species of singly charged ions of mass $A = 136$.

nique, which was enough to remove all other ion species. This is shown in Fig. 3, where the mass-sensitive quadrupole excitation frequency was scanned over the resonance frequencies of the $A/q = 136$ ion species.

For the preparation of clean samples of $^{136}\text{Cs}^+$ decay-parent ions, higher resolving power is needed. As indicated in Fig. 3, the selection frequencies to center ions of ^{136}Cs , ^{136m}Cs , ^{136}Xe are too close to completely separate them from each other. In this case, the Ramsey cleaning technique [42] is employed right after the sideband buffer-gas cooling. Due to the closeness in mass of $^{136}\text{Cs}^+$ to both $^{136m}\text{Cs}^+$ and $^{136}\text{Xe}^+$, it is still challenging by the use of the conventional Ramsey cleaning technique [42] to completely purify the ion sample of $^{136}\text{Cs}^+$. Here, we introduce a new cleaning scheme, which relies on scanning the dipolar excitation (so-called cleaning excitation) frequency over the ν_+ frequency of the ion species present in the precision trap while applying the phase-imaging ion-cyclotron-resonance (PI-ICR) technique [43,44] to identify which ions are ultimately transmitted.

The dipolar excitation was applied as two 22-ms fringes interrupted for 762 ms. Depending on the applied frequency, the ions are left with different cyclotron motion amplitude. If this amplitude is high enough, the ions will hit the electrode of the diaphragm between the two traps in the subsequent transfer back to the first trap for recooling and centering. To assess the composition of the remaining ion bunch, the ions are transferred again to the precision trap where the PI-ICR method is utilized.

The phase accumulation time in the PI-ICR identification was chosen to be 458 ms. This allowed sufficient angular separation to unambiguously observe all three ion species. Figure 4 shows the dipolar excitation scan while gating on the well-resolved spots of different species. Setting the excitation frequency to maximally transmit $^{136}\text{Cs}^+$ ions, the other two are, if not completely, at least heavily suppressed (contamination ratio of less than 2%). After the verification, the cleaning settings are locked and the final mass measurement with the PI-ICR technique commenced. The actual PI-ICR mass measurement was performed with phase accumulation times chosen such that the spots of different ions did not overlap and thus interfere with spot position fitting.

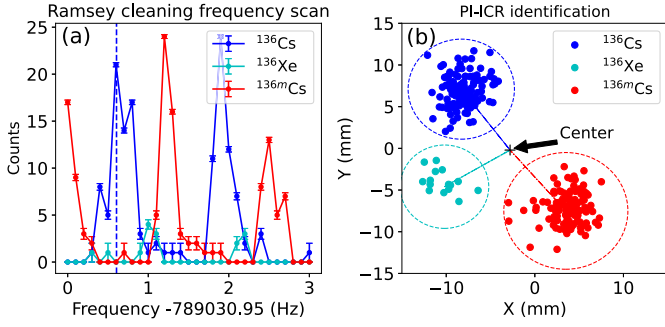


FIG. 4. (a) Ramsey-type dipole excitation frequency scan with a 22 ms (On) - 762 ms (Off) - 22 ms (On) excitation pattern in the second trap filtered by the positional gates shown in (b) using the PI-ICR identification (458 ms phase accumulation time) plot. The used angular gates are highlighted. The vertical dashed line shows the chosen optimal frequency to transmit ^{136}Cs ions while suppressing the others.

The PI-ICR technique used in this work for the Q value measurement is the state-of-the-art Penning trap mass measurement technique for short-lived ions [43,46,47]. This technique allows extraction of the free-space ion-cyclotron frequency

$$\nu_c = \frac{1}{2\pi} \frac{q}{m} B, \quad (1)$$

where q is the charge of the ion, m the mass, and B the magnetic field of the trap, through observation of the final motional phase of the ions. The measurement begins by initial excitation of cyclotron motion of the ions with a short (≈ 1 ms) dipolar pulse at the ν_+ frequency. This is followed by a cyclotron-to-magnetron motion quadrupolar conversion pulse at frequency ν_c . Finally, ions are extracted from the trap to be detected with the position-sensitive MCP detector.

The quadrupolar conversion pulse needs to be applied with two different delay times while keeping the overall cycle identical. One short delay is used to record the so-called magnetron phase and the other, longer, for the cyclotron phase. The delay difference of these settings define the phase-accumulation time t_{acc} . The cycle is described in detail in [43,44]. The phase angle detected between the two cycles with respect to the center spot is $\alpha_c = \alpha_+ - \alpha_-$, where α_+ and α_- are the polar angles of the cyclotron and magnetron motion phases. The cyclotron frequency ν_c is derived from

$$\nu_c = \frac{\alpha_c + 2\pi n_c}{2\pi t_{acc}}, \quad (2)$$

where n_c is the number of complete revolutions of the measured ions during the phase accumulation time t_{acc} . Two different accumulation times, 458 ms and 428 ms, were used in this measurement. These times were chosen to ensure contaminant ions (especially ^{136m}Cs and ^{136}Xe for ^{136}Cs frequency determination) do not appear on the same angle with the ion of interest in case of leakage from the trap.

The excitation time was fine-tuned to be multiple integers of ν_c period such that the angle α_c did not exceed a few degrees. This reduces the shift in the ν_c measurement due to the conversion of the cyclotron motion to magnetron motion

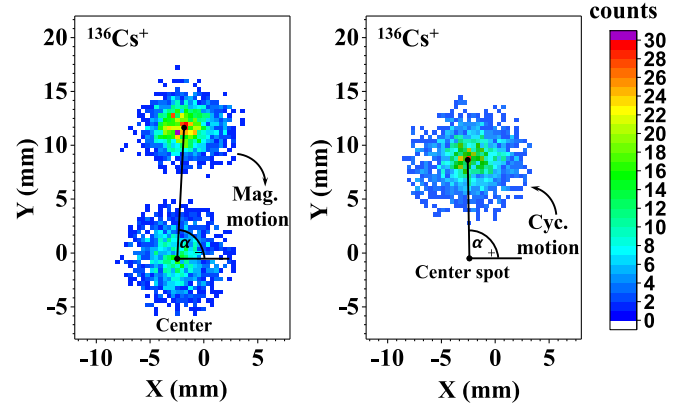


FIG. 5. $^{136}\text{Cs}^+$ ion spots of center, cyclotron phase and magnetron phase on the two-dimensional position-sensitive MCP detector after a PI-ICR excitation pattern with an accumulation time of 458 ms. The magnetron phase spot along with a center spot is illustrated on the left and the cyclotron phase spot on the right. The cyclotron frequency ν_c is deduced from angle difference between the two spots relative to the center spot. The color bar indicates the number of detected ions for each pixel.

and the possible distortion of the ion-motion projection onto the detector to a level well below 10^{-10} [46]. Additionally, the start time of the initial cyclotron motion excitation was scanned over one magnetron period and the extraction delay was varied over one cyclotron period to account for any residual magnetron and cyclotron motion that could shift the different spots. An example of phase spots collected is shown in Fig. 5. In total, ≈ 13 h of data was collected in interleaved ν_c measurements of $^{136}\text{Cs}^+$ and $^{136}\text{Ba}^+$ ions.

The Q_{β^-} value can be derived using the cyclotron frequency ratio of the measured ion pair:

$$Q_{\beta^-} = (M_p - M_d)c^2 = (R - 1)(M_d - qm_e)c^2 + (R \cdot B_d - B_p), \quad (3)$$

where M_p and M_d are the masses of the parent ($^{136}\text{Cs}^+$) and daughter ($^{136}\text{Ba}^+$) atoms, respectively, and R their cyclotron frequency ratio ($\frac{\nu_{c,d}}{\nu_{c,m}}$) for singly charged ions ($q = 1$). m_e is the mass of an electron. B_p and B_d are the electron binding energies of the parent and daughter atoms, which are neglected as it is on the order of a few eV [48] and R is off from unity by less than 10^{-4} . Since both the parent and daughter have the same A/q , mass-dependent shifts effectively become inferior compared to the statistical uncertainty achieved in the measurements. Moreover, due to the very small relative mass difference of the parent and daughter ($\Delta M/M < 10^{-4}$), the contribution of the uncertainty to the Q value from the mass uncertainty of the reference (daughter), 0.24 keV/ c^2 , can be neglected.

III. RESULTS AND DISCUSSION

In total, 13.5 h of PI-ICR measurement data with two different accumulation times were recorded. The full sequence, consisting of measurement of magnetron phase, cyclotron phase, and center spots required about 3 min to complete.

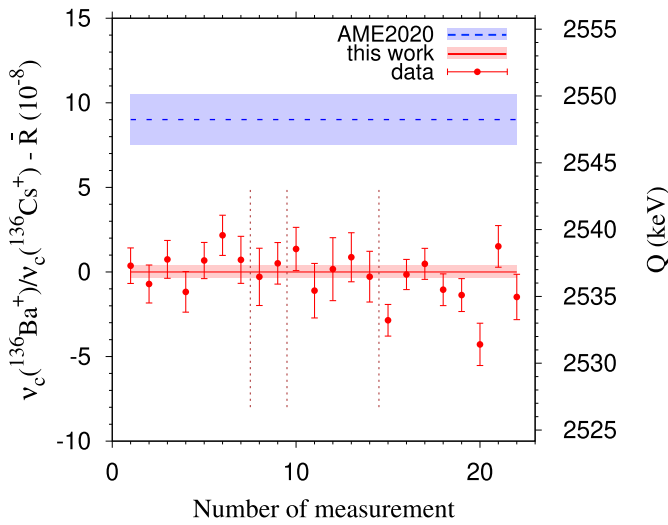


FIG. 6. The deviation (left axis) of the individually measured cyclotron frequency ratios R [$\nu_c(^{136}\text{Ba}^+)/\nu_c(^{136}\text{Cs}^+)$] from the measured value \bar{R} and (right axis) Q values in this work compared to value adopted from AME2020 [33,52]. The red points with uncertainties are measured individual data collected in four different time slots, which are separated with vertical brown dashed lines. The weighted average value from this work $\bar{R} = 1.000\,020\,039\,1(35)$ is illustrated by the horizontal solid red line with its 1σ uncertainty band. The dashed blue line is the value in AME2020 with its 1σ uncertainty area shaded in blue.

This was sequentially repeated for both ion species $^{136}\text{Cs}^+$ and $^{136}\text{Ba}^+$. In the analysis, the position of each spot was fitted with the maximum-likelihood method. A few rounds were summed to have a few tens of detected ions for fitting. The phase angles were calculated accordingly based on the determined positions of the phases to deduce the ν_c frequency of each ion species. The ν_c of the daughter $^{136}\text{Ba}^+$ as a reference was linearly interpolated to the time of the measurement of the parent $^{136}\text{Cs}^+$ to deduce the cyclotron frequency ratio R . Ion bunches containing no more than five detected ions were considered in the data analysis in order to reduce a possible cyclotron frequency shift due to ion-ion interactions [49,50]. The count-rate related frequency shifts were not observed in the analysis. The temporal fluctuation of the magnetic field has been measured to be $\delta_B(\nu_c)/\nu_c = \Delta t \times 2.01(25) \times 10^{-12} \text{ min}$ [44], where Δt is the time interval between two consecutive reference measurements. Contribution of temporal fluctuations of the magnetic field to the final frequency ratio uncertainty was less than 10^{-10} . The frequency shifts in the PI-ICR measurement due to ion image distortions, which were well below the statistical uncertainty, were ignored in the calculation of the final uncertainty. The weighted mean ratio \bar{R} of all single ratios was calculated along with the inner and outer errors to deduce the Birge ratio [51]. The maximum of the inner and outer errors was taken as the weight to calculate \bar{R} . The determination of Q_{β^-} from \bar{R} depends on the measured cyclotron frequency ν_c via Eq. (3). In Fig. 6, results of the analysis including all data with comparison to literature values are demonstrated. The final frequency ratio \bar{R} with its uncertainty as well as the corresponding Q value

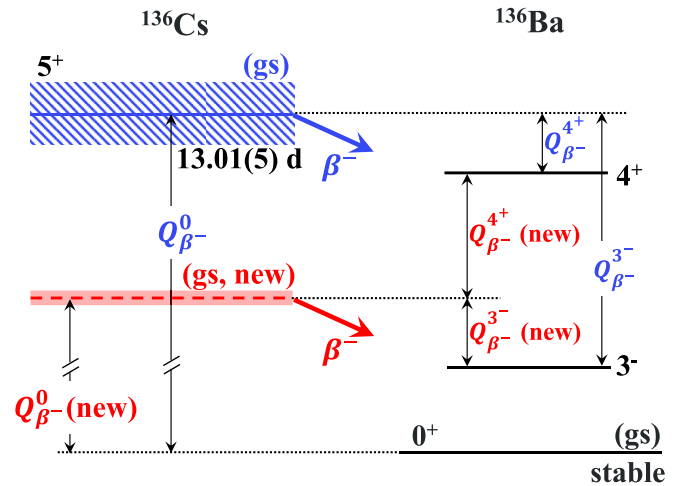


FIG. 7. Partial decay diagram for the ^{136}Cs ground state to ground state and possible ultralow Q -value excited states of 4^+ and 3^- in ^{136}Ba using Q values from AME2020 [33,52] in comparison to this work. The levels drawn with solid lines show the excited states with the Q values from AME2020 and dashed lines from the refined Q values in this work (new). The hatched and shaded areas (in blue for the 3^- and in red for the 4^+ state) illustrate the corresponding 1σ uncertainty in the Q values. Table II lists the Q values in detail.

are $\bar{R} = 1.000\,020\,039\,1(35)$ and $Q_{\beta^-} = 2536.83(45)$ keV, respectively.

A comparison of our results with the literature values is tabulated in Table I. The mass excess of the parent nucleus ^{136}Cs (5^+) was deduced to be $-86350.09(54)$ keV. The gs-to-gs Q value ($Q_{\beta^-}^0$), determined to be $2536.83(45)$ keV from this work, is ≈ 4 times more precise than that derived from the evaluated masses in AME2020 [33,52]. The new $Q_{\beta^-}^0$ value has a deviation of $-11.4(20)$ keV from the AME2020 value and is $\approx 6\sigma$ smaller. The high-precision β^- decay energy from this work, together with the nuclear energy level data from [32] of the excited states of ^{136}Ba as tabulated in Table II, were used to determine gs-to-es Q value ($Q_{\beta^-}^*$) of these two states, see Fig. 7. The calculated Q values of potential candidate transitions of the ground state of parent nuclei ^{136}Cs to the excited states of daughter ^{136}Ba are tabulated in Table II. Our results confirm that the decay of the ground state of ^{136}Cs to the 4^+ excited state in ^{136}Ba with an excitation energy of $2544.481(24)$ keV is energetically forbidden. The Q_{β^-} value is negative with $\approx 17\sigma$ confidence. The decay channel to the 3^- excited state at $2532.653(23)$ keV, having a refined Q value of $4.18(45)$ keV, is energetically allowed and serves as a possible low Q -value transition to be used for neutrino-mass determination. The unexpectedly large deviation of the $Q_{\beta^-}^0$, which lowers the gs-to-es Q value of $15.5(19)$ keV by more than 10 keV for the excited state of $2532.653(23)$ keV, makes the decay to this state of considerable interest.

The partial half-life of the transition, which is of first-forbidden unique type, can be estimated with a microscopic nuclear model. It depends on the Q value through a phase-space factor and on nuclear structure through the involved nuclear matrix element (NME). The relevant NME was calculated using the nuclear shell model in the full $0g_{9/2} -$

TABLE I. Mean cyclotron frequency ratio \bar{R} between the daughter ^{136}Ba (0^+) and parent ^{136}Cs (5^+) nuclei, Q_{β^-} values (in keV) and the mass excess (in keV/ c^2) of parent nuclei determined in this work in comparison with the AME2020 values [33].

	\bar{R}	Q_{β^-}	mass excess [^{136}Cs (5^+) _{gs}]
AME2020		2548.2(19)	-86338.9(19)
This work	1.000 020 039 1(35)	2536.83(45)	-86350.09(54)

$1d - 2s - 0h_{11/2}$ model space using the effective interaction SN100PN [53]. The calculation was carried out using the shell-model code NUSHELLX@MSU [54]. To account for the well-known problem of the shell model, underestimation of the half-lives of β -decay transitions [55], we adopt an effective value of the axial-vector coupling constant $g_A^{\text{eff}} = 1$, while the 1σ uncertainties related to the shell-model calculation are estimated by varying g_A^{eff} between 0.8 and 1.2 (see, e.g., [55]). The phase-space factor was calculated using exact Dirac electron wave functions with finite nuclear size and electron screening as was previously done for double β decays [56] and allowed β decay [21]. The used formalism for calculating phase-space factors for first-forbidden unique transitions was adopted from [57]. The resulting theoretical half-life estimate is $2.1_{-0.8}^{+1.6} \times 10^{12}$ yr. The half-life as a function of Q value is presented in Fig. 8. The best estimate corresponds to a branching ratio of about $1.7 \times 10^{-12}\%$.

As an isotope which undergoes double β decay, ^{136}Xe is particularly well suited as a target for study of the charged-current (CC) neutrino capture process $\nu_e + ^{136}\text{Xe}(0^+) \rightarrow ^{136}\text{Cs}^* + e^-$ [58,59]. It features a low reaction threshold of $Q = 90.3(19)$ keV (mass difference from AME2020 [33,52]) and a relatively large cross section due to the sizable Gamow-Teller transition strengths connecting the 0^+ ^{136}Xe ground state and the lowest-lying 1^+ excited states of ^{136}Cs . The signal generated in the detector is the combination of the outgoing electron and any γ rays or conversion electrons emitted as the Cs nucleus relaxes to its ground state. Recently, many new low-lying states in ^{136}Cs have been identified, several of which are isomeric and potentially can be used in filtering events [60]. As the reaction threshold Q of ^{136}Xe is low enough (lowest among all naturally occurring isotope of xenon), this reaction can be used to search for neutrinos from the solar carbon-nitrogen-oxygen (CNO) cycle [61,62], and can also provide a unique measurement of ^7Be neutrinos, which may enable novel measurements of temperature of the solar core [63]. With the mass excess of ^{136}Cs from our measurements combined with the precise mass value of ^{136}Xe

measured at FSU Penning trap [33,52,64], we refined the Q value to be 79.1(5) keV. This value is 11.2(19) keV lower than the evaluated value from AME2020, which will increase the solar neutrino capture rates in the CC neutrino capture process. The same final state of ^{136}Cs with a lower Q value will indicate a higher sensitivity to search for CC absorption of MeV-scale fermionic dark matter on nuclei as well [61,65].

The $\nu_e + ^{136}\text{Xe}(0^+) \rightarrow ^{136}\text{Cs}^* + e^-$ neutrino capture process to the two lowest-lying 1^+ states of ^{136}Cs has been studied earlier in Ref. [28]. The wave functions of the initial and final states were computed in the nuclear shell model. Here, we update the cross sections with the new Q value for a set of neutrino energies relevant to solar ^7Be , pep, and CNO neutrinos. The results are shown in Table III. The new lower threshold will result in event rates roughly two to four percent higher than the old threshold for the given final states and listed species of solar neutrinos.

IV. CONCLUSION

A new scheme of preparing monoisotopic samples of ^{136}Cs and ^{136}Ba , based on the coupling of the Ramsey cleaning method and the PI-ICR technique to enhance the separation capability of JYFLTRAP, has been employed. A direct high-precision gs-to-gs β^- decay Q -value measurement of $^{136}\text{Cs}(5^+) \rightarrow ^{136}\text{Ba}(0^+)$ was performed using the PI-ICR technique at the JYFLTRAP double Penning trap mass spectrometer. A Q value of 2536.83(45) keV was obtained and its precision is improved by a factor of four. A discrepancy of around 6 standard deviations is found compared to the adopted value in the AME2020. We confirm that one of the two potential ultralow Q -value β^- -decay transitions, $^{136}\text{Cs}(5^+) \rightarrow ^{136}\text{Ba}^*[4^+, 2544.481(24)$ keV], is energetically forbidden at the 17σ level. A new Q value of $-7.65(45)$ keV was measured for this transition. This is more than a factor of three smaller than the Q value of -26 keV for the transition in ^{59}Ni , resulting in 9 times stronger transition probability for the detour transition. While the negative Q values exclude

TABLE II. Potential candidate transitions of initial state of parent nucleus ^{136}Cs (5^+ , ground state), to the excited states of daughter ^{136}Ba with ultralow Q values. The first column gives the spin and parity of the excited final state of ^{136}Ba for the low Q -value transition. The second column gives the decay type. The third column gives the derived decay $Q_{\beta^-}^*$ value in units of keV from literature (Lit.) [33] and the fourth column from this work (new). The fifth column gives the experimental excitation energy with the experimental uncertainty [32] in units of keV. The last column shows the confidence (σ) of the Q value being nonzero. A negative value indicates a negative Q value. “1st FU” represents first forbidden unique.

Final state of ^{136}Ba	Decay type	$Q_{\beta^-}^*$ (Lit.)	$Q_{\beta^-}^*$ (new)	E^*	$Q/\delta Q$ (new)
4^+	allowed	3.7(19)	$-7.65(45)$	2544.481(24)	-17
3^-	1st FU	15.5(19)	4.18(45)	2532.653(23)	9

TABLE III. Total cross sections of the $\nu_e + {}^{136}\text{Xe}(0^+) \rightarrow {}^{136}\text{Cs}^* + e^-$ neutrino capture process for the two lowest-lying 1^+ final states of ${}^{136}\text{Cs}$ (column 1) with discrete neutrino energies (column 2) in a range relevant to solar ${}^7\text{Be}$, pep, and CNO neutrinos. Results are shown for the new threshold 79.08 keV (column 3) and the old threshold 90 keV as used in Ref. [28] (column 4). The calculations were made in the nuclear shell model as described in Ref. [28].

Final state	E_ν (MeV)	NEW σ_{tot} (cm ²) ($Q = 79.08$ keV)	OLD σ_{tot} (cm ²) ($Q = 90$ keV)
1_1^+ (590 keV)	0.7	1.16×10^{-44}	1.12×10^{-44}
	0.8	1.57×10^{-44}	1.52×10^{-44}
	0.9	2.06×10^{-44}	2.00×10^{-44}
	1.0	2.60×10^{-44}	2.54×10^{-44}
	1.1	3.21×10^{-44}	3.14×10^{-44}
	1.2	3.88×10^{-44}	3.80×10^{-44}
	1.3	4.60×10^{-44}	4.52×10^{-44}
1_2^+ (890 keV)	1.0	7.57×10^{-45}	7.32×10^{-45}
	1.1	1.01×10^{-44}	9.82×10^{-45}
	1.2	1.30×10^{-44}	1.27×10^{-44}
	1.3	1.63×10^{-44}	1.59×10^{-44}
	1.4	1.99×10^{-44}	1.95×10^{-44}
	1.5	2.39×10^{-44}	2.34×10^{-44}
	1.6	2.81×10^{-44}	2.76×10^{-44}
1.7	3.27×10^{-44}	3.22×10^{-44}	

the use of this transition to study neutrino mass, the small negative Q values could make it a candidate for the study of β - γ detour transitions proceeding via virtual states. Our results underline the need to measure the Q values to high precision. Not only for the sake of better precision, but, as seen here, existing data can simply be significantly off. For a long-term project building a detector utilizing gs-to-es transitions to measure the mass of a neutrino, it is imperative to know the decay with high accuracy. Moreover, we verify that another transition, ${}^{136}\text{Cs}(5^+) \rightarrow {}^{136}\text{Ba}^*[3^-, 2532.653(23) \text{ keV}]$, as a first-forbidden unique transition with a simple universal spectral shape, is positively allowed at a level of 9σ with a

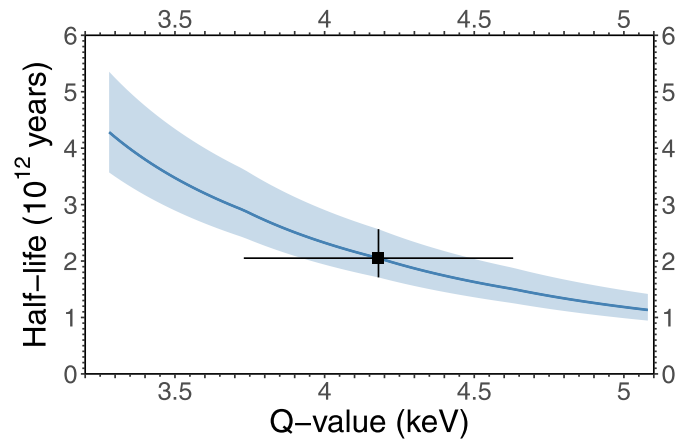


FIG. 8. Theoretical estimate for the partial half-life of the first-forbidden unique transition ${}^{136}\text{Cs}(5_{\text{gs}}^+) \rightarrow {}^{136}\text{Ba}(3^-)$ with a Q -value of 4.18(45) keV. The shaded area represents a 1σ uncertainty for a given Q value, while the horizontal error bar represents the 1σ uncertainty of the Q value, and the vertical error bar the 1σ nuclear structure uncertainty for the best estimate of the Q value.

small low Q value and thus is a possible candidate for future neutrino mass determination experiment. The refined mass difference of ground states of ${}^{136}\text{Xe}$ and ${}^{136}\text{Cs}$ indicates a higher sensitivity of ${}^{136}\text{Xe}$ as a target for study of charged-current (CC) neutrino capture processes.

ACKNOWLEDGMENTS

We acknowledge the staff of the Accelerator Laboratory of University of Jyväskylä (JYFL-ACCLAB) for providing stable online beam. We thank the support by the Academy of Finland under the Finnish Centre of Excellence Programme 2012–2017 (Nuclear and Accelerator Based Physics Research at JYFL) and Projects No. 306980, No. 312544, No. 275389, No. 284516, No. 295207, No. 314733, No. 315179, No. 327629, No. 320062, No. 354589, and No. 345869. The support by the EU Horizon 2020 research and innovation program under Grant no. 771036 (ERC CoG MAIDEN) is acknowledged. This project has received funding from the European Union’s Horizon 2020 research and innovation programme under Grant Agreement No. 861198–LISA–H2020–MSCA–ITN–2019.

[1] Y. Fukuda, T. Hayakawa, E. Ichihara, K. Inoue, K. Ishihara, H. Ishino, Y. Itow, T. Kajita, J. Kameda, S. Kasuga *et al.*, *Phys. Rev. Lett.* **81**, 1562 (1998).
 [2] Q. R. Ahmad, R. C. Allen, T. C. Andersen, J. D. Anglin, J. C. Barton, E. W. Beier, M. Bercovitch, J. Bigu, S. D. Biller, R. A. Black, I. Blevis *et al.*, *Phys. Rev. Lett.* **89**, 011301 (2002).
 [3] M. Gerbino and M. Lattanzi, *Front. Phys.* **5**, 70 (2018).
 [4] J. Suhonen and O. Civitarese, *Phys. Rep.* **300**, 123 (1998).
 [5] F. T. Avignone, S. R. Elliott, and J. Engel, *Rev. Mod. Phys.* **80**, 481 (2008).
 [6] H. Ejiri, J. Suhonen, and K. Zuber, *Phys. Rep.* **797**, 1 (2019).
 [7] M. Aker, A. Beglarian, J. Behrens, A. Berlev, U. Besserer, B. Bieringer, F. Block, B. Bornschein, L. Bornschein, M. Böttcher *et al.*, *Nat. Phys.* **18**, 160 (2022).
 [8] C. Velte, F. Ahrens, A. Barth, K. Blaum, M. Braß, M. Door, H. Dorrer, C. E. Düllmann, S. Eliseev, C. Enss *et al.*, *Eur. Phys. J. C* **79**, 1026 (2019).
 [9] A. B. McDonald, G. Drexlin, V. Hannen, S. Mertens, and C. Weinheimer, *Adv. High Energy Phys.* **2013**, 293986 (2013).
 [10] E. Ferri, D. Bagliani, M. Biasotti, G. Ceruti, D. Corsini, M. Faverzani, F. Gatti, A. Giachero, C. Gotti, C. Kilbourne, A. Kling, M. Maino, P. Manfrinetti, A. Nucciotti, G. Pessina, G. Pizzigoni, M. Ribeiro Gomes, and M. Sisti, *Phys. Proc.* **61**, 227 (2015).

- [11] Z. Ge, T. Eronen, A. de Roubin, K. Tyrin, L. Canete, S. Geldhof, A. Jokinen, A. Kankainen, J. Kostensalo, J. Kotila *et al.*, *Phys. Lett. B* **832**, 137226 (2022).
- [12] Z. Ge, T. Eronen, K. S. Tyrin, J. Kotila, J. Kostensalo, D. A. Nesterenko, O. Beliuskina, R. de Groote, A. de Roubin *et al.*, *Phys. Rev. Lett.* **127**, 272301 (2021).
- [13] E. G. Myers, A. Wagner, H. Kracke, and B. A. Wesson, *Phys. Rev. Lett.* **114**, 013003 (2015).
- [14] M. Redshaw, *Eur. Phys. J. A* **59**, 18 (2023).
- [15] M. Haaranen and J. Suhonen, *Eur. Phys. J. A* **49**, 93 (2013).
- [16] J. Suhonen, *Phys. Scr.* **89**, 054032 (2014).
- [17] R. Sandler, G. Bollen, N. D. Gamage, A. Hamaker, C. Izzo, D. Puentes, M. Redshaw, R. Ringle, and I. Yandow, *Phys. Rev. C* **100**, 024309 (2019).
- [18] J. Karthein, D. Atanasov, K. Blaum, S. Eliseev, P. Filianin, D. Lunney, V. Manea, M. Mougeot, D. Neidherr, Y. Novikov *et al.*, *Hyperfine Interact.* **240**, 61 (2019).
- [19] A. De Roubin, J. Kostensalo, T. Eronen, L. Canete, R. P. De Groote, A. Jokinen, A. Kankainen, D. A. Nesterenko, I. D. Moore *et al.*, *Phys. Rev. Lett.* **124**, 222503 (2020).
- [20] Z. Ge, T. Eronen, A. de Roubin, D. A. Nesterenko, M. Hukkanen, O. Beliuskina, R. de Groote, S. Geldhof, W. Gins, A. Kankainen *et al.*, *Phys. Rev. C* **103**, 065502 (2021).
- [21] T. Eronen, Z. Ge, A. de Roubin, M. Ramalho, J. Kostensalo, J. Kotila, O. Beliuskina, C. Delafosse, S. Geldhof, W. Gins *et al.*, *Phys. Lett. B* **830**, 137135 (2022).
- [22] Z. Ge, T. Eronen, A. de Roubin, J. Kostensalo, J. Suhonen, D. A. Nesterenko, O. Beliuskina, R. de Groote, C. Delafosse, S. Geldhof *et al.*, *Phys. Rev. C* **106**, 015502 (2022).
- [23] M. Ramalho, Z. Ge, T. Eronen, D. A. Nesterenko, J. Jaatinen, A. Jokinen, A. Kankainen, J. Kostensalo, J. Kotila, M. I. Krivoruchenko *et al.*, *Phys. Rev. C* **106**, 015501 (2022).
- [24] D. K. Keblbeck, R. Bhandari, N. D. Gamage, M. Horana Gamage, K. G. Leach, X. Mougeot, and M. Redshaw, *Phys. Rev. C* **107**, 015504 (2023).
- [25] L. Gastaldo, *J. Low Temp. Phys.* **209**, 804 (2022).
- [26] C. L. Longmire, *Phys. Rev.* **75**, 15 (1949).
- [27] M. Pfützner, K. Pachucki, and J. Żylicz, *Phys. Rev. C* **92**, 044305 (2015).
- [28] S. Haselschwardt, B. Lenardo, P. Pirinen, and J. Suhonen, *Phys. Rev. D* **102**, 072009 (2020).
- [29] M. M. Al-Hamidi, A. M. Demidov, M. M. Dyufani, M. S. El-Ahrash, I. V. Mikhailov, D. M. Rateb, S. M. Sergiwa, A. M. Shermit, and S. M. Zlitni, *Yad. Fiz.* **57**, 545 (1994).
- [30] S. Mukhopadhyay, M. Scheck, B. Crider, S. N. Choudry, E. Elhami, E. Peters, M. T. McEllistrem, J. N. Orce, and S. W. Yates, *Phys. Rev. C* **78**, 034317 (2008).
- [31] I. Dioszegi, C. Maraczy, and A. Veres, *Nucl. Phys. A* **438**, 395 (1985).
- [32] National Nuclear Data Center, available at <https://www.nndc.bnl.gov/> (2020/4/7).
- [33] M. Wang, W. Huang, F. Kondev, G. Audi, and S. Naimi, *Chin. Phys. C* **45**, 030003 (2021).
- [34] J. L. Olsen and G. D. O'Kelley, *Phys. Rev.* **95**, 1539 (1954).
- [35] R. Reising and B. Pate, *Nucl. Phys.* **65**, 609 (1965).
- [36] D. Fink, J. Barea, D. Beck, K. Blaum, C. Böhm, C. Borgmann, M. Breitenfeldt, F. Herfurth, A. Herlert, J. Kotila *et al.*, *Phys. Rev. Lett.* **108**, 062502 (2012).
- [37] D. A. Nesterenko, L. Canete, T. Eronen, A. Jokinen, A. Kankainen, Y. N. Novikov, S. Rinta-Antila, A. de Roubin, and M. Vilen, *Int. J. Mass Spectrom.* **435**, 204 (2019).
- [38] I. D. Moore, T. Eronen, D. Gorelov, J. Hakala, A. Jokinen, A. Kankainen, V. S. Kolhinen, J. Koponen, H. Penttilä, and I. Pohjalainen, *Nucl. Instrum. Methods Phys. Res. B* **317**, 208 (2013).
- [39] T. Eronen, V. S. Kolhinen, V. V. Elomaa *et al.*, *Eur. Phys. J. A* **48**, 46 (2012).
- [40] P. Karvonen, I. D. Moore, T. Sonoda, T. Kessler, H. Penttilä, K. Peräjärvi, P. Ronkanen, and J. Äystö, *Nucl. Instrum. Methods Phys. Res. B* **266**, 4794 (2008).
- [41] A. Nieminen, J. Huikari, A. Jokinen, J. Äystö, P. Campbell, and E. C. Cochran, *Nucl. Instrum. Methods Phys. Res. A* **469**, 244 (2001).
- [42] T. Eronen, V. V. Elomaa, U. Hager, J. Hakala, A. Jokinen, A. Kankainen, S. Rahaman, J. Rissanen, C. Weber, and J. Äystö, *Acta Phys. Pol. B* **39**, 445 (2008).
- [43] D. A. Nesterenko, T. Eronen, A. Kankainen, L. Canete, A. Jokinen, I. D. Moore, H. Penttilä, S. Rinta-Antila, A. de Roubin, and M. Vilen, *Eur. Phys. J. A* **54**, 154 (2018).
- [44] D. A. Nesterenko, T. Eronen, Z. Ge, A. Kankainen, and M. Vilen, *Eur. Phys. J. A* **57**, 302 (2021).
- [45] G. Savard, S. Becker, G. Bollen, H. J. Kluge, R. B. Moore, T. Otto, L. Schweikhard, H. Stolzenberg, and U. Wiess, *Phys. Lett. A* **158**, 247 (1991).
- [46] S. Eliseev, K. Blaum, M. Block, A. Dörr, C. Droese, T. Eronen, M. Goncharov, M. Höcker, J. Ketter, E. M. Ramirez, D. A. Nesterenko, Y. N. Novikov, and L. Schweikhard, *Appl. Phys. B* **114**, 107 (2014).
- [47] S. Eliseev, K. Blaum, M. Block, C. Droese, M. Goncharov, E. Minaya Ramirez, D. A. Nesterenko, Y. N. Novikov, and L. Schweikhard, *Phys. Rev. Lett.* **110**, 082501 (2013).
- [48] A. Kramida, Yu. Ralchenko, J. Reader, and NIST ASD Team, NIST Atomic Spectra Database (ver. 5.8), available online at <https://physics.nist.gov/asd> [2021, January 19], National Institute of Standards and Technology, Gaithersburg, MD (2020).
- [49] A. Kellerbauer, K. Blaum, G. Bollen, F. Herfurth, H. J. Kluge, M. Kuckein, E. Sauvan, C. Scheidenberger, and L. Schweikhard, *Euro. Phys. J. D* **22**, 53 (2003).
- [50] C. Roux, K. Blaum, M. Block, C. Droese, S. Eliseev, M. Goncharov, F. Herfurth, E. M. Ramirez, D. A. Nesterenko, Y. N. Novikov, and L. Schweikhard, *Eur. Phys. J. D* **67**, 146 (2013).
- [51] R. T. Birge, *Phys. Rev.* **40**, 207 (1932).
- [52] W. Huang, M. Wang, F. Kondev, G. Audi, and S. Naimi, *Chin. Phys. C* **45**, 030002 (2021).
- [53] B. A. Brown, N. J. Stone, J. R. Stone, I. S. Towner, and M. Hjorth-Jensen, *Phys. Rev. C* **71**, 044317 (2005).
- [54] B. Brown and W. Rae, *Nucl. Data Sheets* **120**, 115 (2014).
- [55] J. T. Suhonen, *Front. Phys.* **5**, 55 (2017).
- [56] J. Kotila and F. Iachello, *Phys. Rev. C* **85**, 034316 (2012).
- [57] N. Gove and M. Martin, *At. Data Nucl. Data Tables* **10**, 205 (1971).
- [58] R. Davis, D. S. Harmer, and K. C. Hoffman, *Phys. Rev. Lett.* **20**, 1205 (1968).
- [59] R. S. Raghavan, *Phys. Rev. Lett.* **78**, 3618 (1997).
- [60] S. J. Haselschwardt, B. G. Lenardo, T. Daniels, S. W. Finch, F. Q. L. Friesen, C. R. Howell, C. R. Malone, E. Mancil, and W. Tornow, *Phys. Rev. Lett.* **131**, 052502 (2023).

- [61] J. L. Newstead, L. E. Strigari, and R. F. Lang, [Phys. Rev. D **99**, 043006 \(2019\)](#).
- [62] S. Appel, Z. Bagdasarian, D. Basilico, G. Bellini, J. Benziger, R. Biondi, B. Caccianiga, F. Calaprice, A. Caminata, P. Cavalcante *et al.*, [Phys. Rev. Lett. **129**, 252701 \(2022\)](#).
- [63] J. N. Bahcall, [Phys. Rev. D **49**, 3923 \(1994\)](#).
- [64] M. Redshaw, E. Wingfield, J. McDaniel, and E. G. Myers, [Phys. Rev. Lett. **98**, 053003 \(2007\)](#).
- [65] J. A. Dror, G. Elor, and R. McGehee, [Phys. Rev. Lett. **124**, 181301 \(2020\)](#).